ABSTRACT

Title of Document: REACTION RATES AND TEXTURAL DEVELOPMENT OF HYDROLYSIS REACTIONS IN THE SYSTEM MgO-SiO_2-H_2O

Ryan J. Kerrigan, Ph.D., 2011

Directed By: Professor Philip Candela and Associate Research Scientist Philip Piccoli,, Department of Geology

Experiments in the simplified systems MgO-SiO_2-H_2O (MSH) and MgO-SiO_2-H_2O-CO_2 (MSHC) have been conducted by using hydrothermal diamond anvil cells to investigate reaction rates and the resulting textures at temperatures and pressures consistent with the temperatures and pressures of the Earth's crust. The conditions and simplified systems of the experiments serve as approximations for geologic environments wherein magnesium-rich rocks (i.e., mafic, ultramafic, and magnesium-rich carbonate rocks) are hydrothermally altered by silica-rich fluids. The hydrolysis reaction rates and textures that result from the irreversible interactions of olivine and magnesite with aqueous fluids in the presence of quartz have been characterized.

Reaction rates have been determined by a new approach developed during this study, which uses *in situ* observation of reactant volume loss to determine the growth

rate of the products of hydrolysis reactions. In addition, some experiments were analyzed by real-time synchrotron radiation analysis to identify the phases in the reactions and to provide semi-quantitative constraints on the kinetic data. Experiments performed in this study resulted in the development of several textural varieties. Talc grown during this study exhibited both fibrous and platy habits, textural variations that appeared to be controlled by: variations in the density of the aqueous phase, surface area of starting materials, rate of temperature increase, and the presence of strong chemical gradients. The primary growth of fibrous talc in these experiments demonstrates that the production of fibrous talc does not require the pseudomorphism of a fibrous precursor as previously suggested.

REACTION RATES AND TEXTURAL DEVELOPMENT OF HYDROLYSIS REACTIONS IN THE SYSTEM MgO-SiO_2-H_2O

By

Ryan J. Kerrigan

Dissertation submitted to the Faculty of the Graduate School of the
University of Maryland, College Park, in partial fulfillment
of the requirements for the degree of
Doctor of Philosophy
2011

Advisory Committee:
Professor Philip Candela, Chair
Associate Research Scientist Philip Piccoli, Co-Chair
Associate Professor Mark Frank
Professor Bruce James
Professor Ann Wylie

Acknowledgements

I would like to thank Philip Candela and Philip Piccoli for providing advice and support throughout the course of this project, and, in particularly, for their continued patience. Andrew Campbell provided much appreciated guidance in research and teaching. I thank Dr. Ann Wylie for the use of her lab during this study and her expertise related to fibrous materials. I would also like to thank Dr. Mark Frank for introducing me to synchrotron radiation and help particularly at the onset of Ph.D. studies. I thank Dr. Bruce James for serving as the Dean's representative on my committee.

I would also like to thank: Dan Earnest for introducing me to the hydrothermal diamond anvil cell; Kim Allison of the R. J. Lee group for help with TEM work; Sanjit Ghose and Zhiquiang Chen of BNL-NSLS for support during synchrotron analyzes; Rebecca Fischer, Daniel Hawkins, and Zoltan Zajacz for aiding in synchrotron analyses; Dorothy Brown for being the most helpful person I have encountered at this university; Debbie Pruett for help with graduating paperwork; Todd Karwoski for IT support; Jason Hunter, Stacia Gordon, and Fawna Korhonen, thank you for listening; to my roommates, my fellow graduate students (past and present), the Bruins, the Celtics, the Pats, and the Red Sox for welcomed distractions; and, especially, to my family for their unwavering support and unconditional love.

Most importantly, to Jessica Miller, you are my best friend and you have supported me throughout this process. You are amazing and I am lucky to have found you.

Table of Contents

List of Tables

List of Figures

Chapter 1: Dissertation Overview

Introduction: Fundamental Objectives

Talc deposits of economic importance are primarily formed in three ways: hydrothermal processes (produced by hot ascendant, aqueous phases or brines produced by a variety of processes), contact metamorphism, and metasomatism caused by regional metamorphism (Van Gosen et al., 2004). All of these processes involve the interaction of a silica-rich fluid and a magnesium-rich rock. A common result of this alteration in greenschist to amphibolite facies is a massive, talc-rich soapstone.

The literature in this field is extensive with respect to the phase equilibria and thermodynamics of these systems, but there is a noticeable void in investigations related to reaction rates and textural development. This study attempts to partially fill that void by developing a new experimental method to study reaction rates while observing the development of various textural morphologies.

Application of Novel Analytical Techniques to Old Problems

The abundance of magnesium-rich rocks within the crust of the Earth makes them critically important to understanding the Earth as a dynamic system. The chemical systems $MgO\text{-}SiO_2\text{-}H_2O$ (MSH) and $MgO\text{-}SiO_2\text{-}H_2O\text{-}CO_2$ (MSHC) can serve as simplified approximations to natural systems for the examination of how rocks behave under crustal conditions. Most previous investigations have employed conventional experimental methods (i.e., externally-heated pressure vessels in

resistance furnaces, batch-flow reactors, etc.) which require the examination of post-experiment materials to infer the nature of reactions. This study provides the description of a new method of examining reactants, *in situ*, by using the hydrothermal diamond anvil cell to infer the growth rates of reaction products while examining textural development.

Diamond anvil cells (DAC) allow for experimentation while samples are observed and analyzed *in situ* by various spectroscopic methods. Although the DAC has been in existence since the late 1950's (Jamieson et al., 1959; Weir et al., 1959), early DAC apparatus were not optimal for the study of fluid/mineral interactions. In the early 90's, the hydrothermal diamond anvil cell (HDAC) was developed. This study uses one specific HDAC model, referred to as a Bassett-type HDAC. It provided an improved ability to examine fluids and fluid/mineral interactions at elevated pressure and temperatures (Bassett et al., 1993). Using the advantages of *in situ* observation of fluid/mineral interactions, this study has developed a method to infer the growth rates of reaction products by monitoring and determining the mass-loss of reactants.

Recent studies have used *in situ* observation via HDAC experimentation to monitor mineral cross-sectional area changes to determine the aqueous solubility of minerals (Wang et al., 2004; Audétat and Keppler, 2005; Manning et al., 2008; Gross, 2009; Mysen, 2009). This technique, referred to as optical weighing (or more accurately referred to herein as *in situ* mass determination), was first introduced by Matthews and Davis (1999) and provides estimations of the mass of objects that are too small to be measured accurately by analytical balances. The techniques of

conventional solubility studies (i.e., methods employing weight loss or fluid extraction) and the *in situ* techniques of the HDAC have considerable procedural differences but yield similar results.

The technique of *in situ* mass determination by the estimation of reactant or product volumes is based on the measurement of changes in mineral cross-sectional area and can be used to infer reaction product growth rates, given certain assumptions. Experiments have been conducted that monitor the volume change of reactant quartz as it dissolves in the aqueous phase and thereby reacts with a magnesium-rich phase in the chamber of the HDAC. The solubility of quartz, determined by methods of *in situ* mass loss by using the HDAC, has been reported by Wang et al. (2004) and Gross (2009) with results similar to studies that used conventional techniques. Building upon the work of these studies, experiments conducted in this study represent the first report of reaction product growth rates using this novel, indirect method of determination.

Dissertation Structure and Content

This dissertation is written in four chapters. The first chapter provides an overview of the document. The second chapter offers background on a variety of topics necessary for the understanding of material presented in later chapters. An in-depth discussion of the use and errors associated with HDAC experimentation is also included. Chapters three and four are manuscripts presenting the results and implications of experiments conducted in two related chemical systems. The appendices, both written and electronic, include material that is too lengthy to incorporate into the body of the document.

Chapter 2: Review of Pertinent Studies and Procedural Variables

Introduction and Geologic Context

During large-scale tectonic collisions, mafic and ultramafic portions of the oceanic crust are commonly obducted and included into the regional metamorphic sequence of metasedimentary rocks as slivers, juxtaposing magnesium-rich ultramafic rocks and magnesium-poor, silica-rich rocks (Sanford, 1982). Strong chemical potential gradients are therefore created within this tectonically-produced stratigraphy, and at temperatures sufficient for significant reaction, the tectonically interleaved ultramafic rocks can react irreversibly with the surrounding country rock and their associated fluids. The metasomatic alteration of these ultramafic bodies by aqueous fluids results in blackwall zones. Blackwall zones are characterized by an 'onion skin' morphology of nearly monomineralic or bimineralic zones of alteration dictated largely by the silica and magnesium content (Read, 1934; Phillips and Hess, 1936; Evans and Trommsdorff, 1974; and Sanford, 1982). A characteristic of blackwall zones is the strong chemical potential gradients that drive the diffusion of silica and magnesium (Sanford, 1982). Silica from a quartz-bearing country rock will diffuse into the core of the ultramafic body, which is characterized by a lower chemical potential of silica. Chemical potential gradients drive the transport of silica and other constituents as the system strives towards equilibrium. The experiments presented in this research model the conditions that may prevail in the generation of blackwall zones and related rocks that may form by the reaction of ultramafic material with silica-rich aqueous fluids. In these experiments, water is in excess and

is near saturation with respect to quartz. Diffusive flow into the core of the single crystal of olivine (or magnesite) becomes the rate limiting step of reactions and limits the achievement of equilibrium of the system during experiments in this study, analogous to what has been reported regarding natural occurrences (Read, 1934; Phillips and Hess, 1936; Evans and Trommsdorff, 1974; and Sanford, 1982).

Alteration of Mafic and Ultramafic Rocks

Although the oceanic crust comprises predominantly mafic rocks, ultramafic rocks can be found along slow to ultra-slow spreading ridges where material from the upper mantle is exhumed during episodes of low magmatic supply (Andreani et al., 2007). The hydrothermal alteration of peridotite in the oceanic lithosphere can occur at temperatures of 600-800 °C, and continue below 350 °C producing zones of alteration, and non-equilibrium alteration assemblages (Janecky and Seyfried, 1986). The products of the hydrothermal alteration of peridotite include hydrous magnesium silicate phases (e.g. anthophyllite, serpentine, talc) as well as other phases. Altered oceanic crust containing these hydrous phases can be transported to convergent zones, where the oceanic crust will be subducted and dehydrated. The dehydration of oceanic crust can lead to the hydration of the peridotitic mantle wedge producing new hydrous magnesium silicate assemblages. Chapter three addresses the reaction rates and resulting textures observed under these conditions.

Alteration of Magnesium-rich Carbonates

Chapter four addresses reactions between magnesium-rich carbonates (i.e., magnesite) and silica-rich fluids under mid-crustal conditions by using the simplified

system MSHC. Common rocks that fall into the chemical MSHC system are dunites, serpentinites, steatites, ophicarbonates, and magnesite deposits. The experiments of chapter four focus on the hydrothermal alteration of magnesite deposits, their decarbonation, and the development of talc deposits ± olivine and magnesite.

Magnesite deposits, volumetrically minor compared to other carbonate deposits (i.e., calcite, aragonite, and dolomite), can occur as large monomineralic bodies (Aharon, 1988; Pohl, 1990; Abu-Jaber and Kimberley, 1992). Large deposits of magnesite commonly occur as either sedimentary beds or as carbonated ultramafic rocks. The latter occurrence has seen resurgence in examination due to the attractive possibility of sequestering excess atmospheric carbon dioxide in ultramafic bodies deep within the crust via hydraulic carbonation (Oelkers et al., 2008). There has also been considerable interest in magnesite over the past twenty years as a number of studies have suggested that magnesite is the major stable carbonate phase in the mantle (Katsura et al., 1991; Beillmann et al., 1993; Gillet, 1993; Isshiki et al., 2004). Magnesite is thought to be stable as deep as the lower mantle (Isshiki et al., 2004), but significant decarbonation can occur along subduction zone geotherms (Molina and Poli, 2000). As carbonated ultramafic rocks are subducted and travel toward the mantle, they commonly experience hydrothermal alteration via fluids containing excess silica; chapter four addresses the reaction rates and resulting textures observed under these conditions.

Hydrothermally altered magnesite deposits that have experienced an influx of silica-rich fluids can undergo a variety of physical and chemical changes. If a silica-rich fluid is in excess, a number of hydrous silicate phases can form in equilibrium

with magnesite (e.g., talc, anthophyllite, and serpentine) (Greenwood, 1967; Johannes, 1969; Aharon, 1988; Pohl, 1990; Abu-Jaber, 1992).

The reactions examined in chapter four between natural magnesium-rich carbonates and silica-rich fluids (i.e., magnesite + quartz + water) at mid-crustal conditions (~180-860 MPa and 400-765 °C), may occur during the subduction of magnesium-rich carbonates as well as ophicarbonates. The subduction of carbonates has been postulated as the primary method of delivering carbon dioxide to the mantle (Becker and Altherr, 1992). Understanding the conditions that allow for the preservation of magnesite during subduction and the rates at which decarbonation may occur can yield insight into the global carbon cycle.

High Aspect Ratio Minerals

This study has produced an uncommon, fibrous habit of talc. To the best of my knowledge, the primary growth of fibrous talc has not been reported in the literature. The following section provides a description of high aspect ratio minerals and their postulated mechanisms of growth. Amphibole and serpentine minerals, chemically similar to talc, are widely reported in a fibrous habit. Fibrous talc, on the other hand, is uncommon in natural systems, and its origin has been explained by the replacement of fibrous/asbestiform amphiboles and/or serpentines during retrograde metamorphism (Stemple and Brindley, 1960; Ross et al., 1968; Sanford, 1981; Greenwood, 1998; Ferrari and Viti, 2010). The production of fibrous talc in this study demonstrates that the growth of talc after amphibole and/or serpentine is not necessary for the production of a fibrous habit. Fibrous talc is not considered to be asbestos and the effects of fibrous talc on the human respiratory system remain

uncertain (Beard et al., 2001). The results of this study will be used to predict the conditions under which fibrous talc may form in nature.

Mechanisms for High Aspect Ratio Mineral Growth

The development of high aspect ratio mineral habits is due to preferentially inhibiting growth along specific crystallographic axes or by preferentially promoting growth along one crystallographic axis. The most common growth mechanism invoked for the formation of high aspect ratio mineral habits is associated with one-dimensional tension (e.g. faults, fractures, intersecting regional and local stresses) (Zoltai, 1981; Ahn and Busek, 1991). This has been explained as a relief of stresses in one direction rather than the creation of one-dimensional tension. Synthetic fibers that form under one-dimensional tension can grow almost instantaneously, and under some conditions fibers may grow just as rapidly (Zoltai, 1981).

Rapid crystallization due to supersaturation can result in many crystal nucleation sites and if each of the nucleation sites survive to produce an individual crystal, dense nucleation may inhibit growth on the plane parallel to the nucleation surface, prompting growth in one direction (Zoltai, 1981). Veblen (1980) found microstructures that strongly suggest that the primary mechanism of fiber formation in asbestos is separation along the grain boundaries between individual crystallites.

Talc most commonly crystallizes in a platy habit and only rarely crystallizes in a fibrous form. When talc exhibits a fibrous habit it has been attributed to pseudomorphism of preexisting fibrous minerals such as amphibole or serpentine minerals (Stemple and Brindley, 1960; Ross et al., 1968; Greenwood, 1998). Often coexisting with fibrous talc are transitional fibers that have a mixed mineralogy and

represent incomplete pseudomorphism of the primary mineral. Transitional fibers have been cited as evidence for the pseudomorphism of preexisting fibrous minerals to generate fibrous talc (Stemple and Brindley, 1960; Wylie and Huggins, 1980, Sanford, 1981).

Synthetic fibers (sometimes referred to as *whiskers*) are commonly grown by directionally restricting the supply of the material needed for growth (Walker and Zoltai, 1979). The promotion of growth in only one crystallographic direction could be due to strong gradients in the nutrients required to grow the fibers. Uniaxial growth requires ideal conditions that will permit growth on one crystal face but will not allow growth in other directions; this can be difficult to achieve in the laboratory setting (Zoltai, 1981).

Health Issues

When some types of asbestos are inhaled by animals, the asbestos can become lodged in the lung and can cause asbestosis (scarring of the lungs), lung cancer and malignant mesothelioma, as well as other harmful pulmonary issues (VanGosen et al., 2004). The detrimental effects inflicted by asbestos have been attributed to the properties of the asbestiform crystallization habit, surface charge and/or magnesium content (Palekar et al., 1979).

Talc is mined for use as an ingredient in paint, ceramics, rubber, insecticides, roofing, paper and crayons. Its most familiar use is in talcum powder. Although fibrous talc is uncommon, trace quantities are present in most talc deposits. In a few deposits, fibrous talc is a major component (e.g. Gouverneur Talc District, NY) (Wylie et al., 1997). The earliest mention of fibrous talc in the literature is by

MacAdam (1886), who describes fibrous talc used to make paper. Fibrous talc in nature is usually found together with asbestiform minerals. Recently, the incorporation of fibrous talc in crayons generated worry for health officials and consumers because of the mineral's similarities in composition and habit to some types of asbestos (Beard et al., 2001). Analysis of available data suggests that there is no solid evidence linking talc to human carcinoma (Wylie et al., 1997; Wylie and Verkouteren, 2000). The scope of this study does not include potential health effects of talc, but this study may aid in locating and identifying deposits containing fibrous talc so they can be further studied.

Kinetics within the MgO-SiO_2-H_2O±CO_2 System

The following section describes the constraints governing the reaction rates determined in this study. There have been several studies addressing the kinetics of the hydration of magnesium-rich rocks under conditions similar to those in this study (Martin and Fyfe, 1970; Moody, 1976; Sanford, 1981; Wegner and Ernest, 1983; Janecky and Seyfried, 1986; Normand et al., 2002). These studies agree on a number of issues related to reactions in these settings: (1) the rates are geologically fast; (2) the rate limiting factor in nature is the availability of water in the system transported by intergranular diffusion; (3) the reactions rates are initially interface-controlled; (4) once all nucleation sites have been occupied on the surface of the minerals, the rate becomes diffusion-controlled. The topics addressed by these studies are addressed in the following discussion.

Basic Kinetics Principles

A rate equation for a given reaction will depend on the complexity of the reaction. Some of the simpler rate equations describe homogeneous reactions (i.e. reaction where all reactants and products are part of a single phase) and can provide a basis for more complex heterogeneous reactions (i.e., reactions involving multiple phases). Most reactions in geology involve multiple phases and are governed by heterogeneous reactions rate equations. These equations will involve the addition of terms to describe the behavior of crystal nucleation, the reaction interface, and mass (or heat) transfer.

Rate equations, often referred to as rate laws, commonly express the relationship of the rate of a reaction to the rate constant and the concentration of the reactants. The rate constant is a numerical representation of proportionality between the reaction rate and the concentrations of the reactants. The units of the rate constant will depend on the form of the rate law used. Rate equations can describe elementary reactions (i.e., reactions that proceed as written without intermediate steps) and overall reactions (i.e., reactions that proceed as a series of elementary steps but are commonly expressed as only the initial reactants and final products). The following equations (Eq. 2.1 - 2.7) are applicable to homogeneous reaction and form the basis for the more complex heterogeneous reactions. The simplest form of a rate equation describes a zero-order homogeneous reaction:

$$\frac{dC}{dt} = k \qquad \textbf{Eq. 2.1}$$

$$C = C° + k \cdot t \qquad \textbf{Eq. 2.2}$$

where C is concentration, C° is initial concentration, t is time and k is the rate constant. The ‘rate’ of this equation is given by the change in concentration divide by an expressed length of time. A zero-order reaction will produce a linear relationship between the change in concentration over a change in time. The zero-order rate law can explain many simple reactions where the rate is independent of reactant concentration.

The order of a reaction expresses how the product of the reaction will respond to changes in the concentration of the reactants. As seen above (Eq. 2.2), zero-order reactions are independent of changes to the reactant concentration, but as the order increases so does the influence of the reactant concentration. First-order reactions can be expressed as follows:

$$\frac{dC}{dt} = -k \cdot C \qquad \textbf{Eq. 2.3}$$

$$C = C^{\circ} \cdot e^{-k \cdot t} \qquad \textbf{Eq. 2.4}$$

$$\ln C = -k \cdot t + \ln C^{\circ} \qquad \textbf{Eq. 2.5}$$

First-order reactions will have a 1 to 1 relationship between a reactant concentration and the product concentration. If the starting concentration of a first-order reactant is doubled, then the resulting products will be doubled by the reaction. As the reaction order continues to increase, so does the effect of the starting concentration of the reactant. Equation 2.7 shows how higher-order (greater than 1) reactions can be treated:

$$\frac{dC}{dt} = -k \cdot C^{n} \qquad \textbf{Eq. 2.6}$$

$$\frac{1}{C^{n-1}} = (n-1) \cdot k \cdot t + \frac{1}{C^{\circ n-1}} \qquad \textbf{Eq. 2.7}$$

where *n* is the order of the reaction. The order of the reaction does not have to be a whole number. For heterogeneous reactions the order of the reaction will be the sum of reaction orders of each elementary step that describe the overall reaction.

When rate laws are applied to the non-ideal problems encountered in geology, additional factors and variables must be considered. The dependence of reaction rate on temperature can be seen in the Arrhenius equation (Eq. 2.8 and 2.9):

$$k = A \cdot e^{-\frac{E_{app}}{RT}} \qquad \textbf{Eq. 2.8}$$

$$\ln k = -\left(\frac{E_{app}}{R}\right) \cdot \left(\frac{1}{T}\right) + \ln A \qquad \textbf{Eq. 2.9}$$

where A is a pre-exponential factor that encompasses a number of variables and depends on the frequency of atomic interaction, E_{app} is the apparent activation energy and R is the ideal gas constant. The activation energy of a reaction is a numerical representation of an energetic barrier that the overall reaction must overcome for the reaction to proceed. The form of Equation 2.9 makes it possible to find the activation energy by plotting ln*k* vs. 1/T; the slope of the line produced will equal the apparent activation energy divided by the ideal gas constant.

Lasaga (1998) put forth a comprehensive rate equation (Eq. 2.10), that was later revised by Cama et al. (2000), which addresses the kinetics of geologically relevant heterogeneous reactions by incorporating terms to account for the interactions of mineral surfaces and fluids. Equation 2.10 covers many of the

important parameters that must be considered to understand the kinetics of a geologic system:

$$Rate = k \cdot A_{\min} \cdot e^{-E_{app}/RT} \cdot a_{H^+}^{n_{H^+}} \cdot \prod_i a_i^{n_i} \cdot g(I) \cdot f(\Delta G_r)$$

Eq. 2.10

where k is the rate constant, A_{min} is the reactive surface area of the mineral, E_{app} is the apparent activation energy of the overall reaction, R is the gas constant, T is the absolute temperature, a_i and a_{H+} are the activities in solution of species i and H^+, respectively, n_i and n_{H+} are the orders of the reaction with respect to these species, g(I) is a function of the ionic strength (I) and $f(\Delta G_r)$ is a function of the Gibbs free energy of the reaction. Note that the rate approaches zero as the ΔG_r approaches zero. The pH dependence of the dissolution/precipitation reactions is represented by the term $a_{H^+}^{n_{H^+}}$ in Equation 2.10. This general rate law (Eq. 2.10) can be applied to the growth and dissolution of minerals. The first portion is concerned with the temperature dependence (Arrhenius behavior) as well as the effects of surface areas. The second portion of the equation deals with the addition of various activities of catalytic or inhibiting agents and the last portion of Equation 2.10 incorporates the thermodynamic deviation from equilibrium.

An abbreviated version of Equation 2.10 is presented in chapter three with some discussion of how this equation can aid in understanding the results of experiments conducted during this study. The increased growth rates observed during increases in temperature can be attributed to the Arrhenius equation portion of the

equation ($\exp(-E_{app}/RT)$). The deviation from thermodynamic equilibrium is the driving force for reaction and as equilibrium is approached, reaction rate decreases. Additional factors play a role in the reaction rates observed. At the onset of the isothermal reactions, the rate limiting step is interface-controlled (i.e., the controlling factor of the reaction rate is the attachment or detachment of atoms to or from the surface of a phase). Once reactive surfaces have become occupied by crystal nuclei the reaction becomes diffusion controlled (i.e., the controlling factor of the reaction rate is the transport of atoms to the reaction interface). Order of the reaction (n_i) will be highly dependent on the nature of nucleation and morphology of the minerals produced. Christian (2002) has found that the order of the reaction will double in diffusion controlled reactions if fibers are being produced instead of plates, although the reaction rates reported in chapters three and four are not consistent with this behavior.

In each set of experiments conducted (quartz + olivine + fluid or quartz + magnesite + fluid), the assemblage of starting materials is thermodynamically unstable at the conditions studied. The growth of talc in experiments occurs most frequently on the surface of the magnesium-rich phase, but also on the gasket walls. The preferential nucleation of run products on a magnesium-rich phase likely results from one or more of the following factors: (1) the dissolution of magnesium-rich phase is the rate limiting step, and, as dissolved species become available, they are used to nucleate a reaction product; (2) the dissolved magnesium species diffuse too slowly to escape the immediate vicinity of the magnesium-rich phase grain; or (3) the surface of the magnesium-rich phase is energetically favorable for the nucleation of

the run products. In many experimental runs, dense growth of run products on the surface of the magnesium-rich phase can ‘armor’ the magnesium-rich phase and isolates the core, making it difficult for further contribution to the reactions. Martin and Fyfe (1970) also report this phenomenon. Dungan (1977) observed the similar processes in natural samples that have undergone olivine hydration. This behavior has been observed in the reactions of this study, particularly in isothermal experiments but in experiments that involve varied temperature steps, thermally activated reactions are initiated, reactivating reaction.

Characterization of Experimental Variables

Overview of the Hydrothermal Diamond Anvil Cell

The diamond anvil cell (DAC) has been in existence since the late 1950’s and has been used to study the behavior of substances at elevated temperature and pressure (Jamieson et al., 1959; Weir et al., 1959). The introduction of gaskets to confine the samples (Van Valkenburg, 1964) and the establishment of fluid/mineral reaction experiments (Van Valkenburg, 1971) have expanded the abilities of the diamond anvil cell. The hydrothermal diamond anvil cell (HDAC), also referred to as a Bassett-type HDAC, was developed by William A. Bassett to analyze fluids and fluid/mineral interactions at elevated pressure and temperatures (Bassett et al., 1993). The HDAC is a modification of a previous design developed by Merrill and Bassett (1974); the 1993 model is similar but 3 to 4 times larger. Several modifications were made to the standard DAC design to construct an appropriate vessel for geochemical investigations involving fluid/mineral interactions. Larger diamonds (~1.5-1.0 culet face, ~1/8 carat) are used, which allows for larger volumes of fluids and/or minerals

to be within the experimental charge; this modification reduces the maximum pressure that can be achieved. Additionally, the use of a hydrothermal pressurization system confined by a rhenium (or iridium) gasket and heated by an external heat source was a new approach to DAC experimentation. This design results in a more homogeneous pressure and temperature over the sample for volumes on the order of ~0.007-0.07 mm^3.

The ranges of temperature and pressure that can be attained by using the HDAC are -190 to 1200 °C and up to 2.5 GPa, respectively (Bassett et al., 1993). Gaskets are cut from metal foil; they have a center hole, which acts as the walls of the chamber, and confines the sample between the diamonds. The hardness and rigidity of rhenium metal and iridium metal at high temperatures make them suitable gasket material and preferable to the typical DAC gasket material (i.e., molybdenum or steel). The diamonds are placed on tungsten carbide (WC) seats wrapped with molybdenum wires (0.010 inches, 254 microns in diameter), which act as resistance heaters for the HDAC. Each molybdenum wire was connected to an autotranformer which controlled the voltage and, therefore, the current that flowed through the molybdenum wire heaters. Heat is transferred to the sample chamber via conduction through the tungsten carbide seats and the diamonds (Bassett et al., 1993). The wrapped tungsten carbide seats are positioned on ceramic washers to minimize heat conduction to other portions of the cell. The use of molybdenum wraps allows low power (~150 Watts) to produce high temperatures (~1000°C) (Bassett, 2003). The molybdenum wire readily oxidizes at high temperatures; therefore, the HDAC assembly is enclosed with a metal sleeve, and a gaseous solution of argon with 5%

hydrogen is continually flowed through the interior of the apparatus. The hydrogen is necessary to convert any excess oxygen to water. The diamonds, tungsten carbide seats, molybdenum wire and ceramic washers are fixed into place on an adjustable seat with SiO_2-Al_2O_3-ZrO_2-based cement. The cemented assembly can be manipulated by three screws at its base that allow the user to adjust the positioning and alignment of the diamonds. A chomel-alumel, type-K, thermocouple is cemented to each of the diamonds in such a way that the join of the thermocouple is in direct contact with the diamond, juxtaposed to the culet face. Diamond's high thermal conductivity makes the temperature measurement a good proxy for the chamber temperature. The majority of the 'exoskeleton' of the HDAC (post, platens and sleeve) is made out of stainless steel with the exception of the base, which is made of brass. The two halves of the HDAC fit together on three posts, which are fastened together with screws. The screws are tightened to provide a confining force. Bellville springs are placed under the screws and accommodate additional pressure brought on by the thermal expansion of the steel exoskeleton during experiments.

Before the gasket is set in place, the diamonds were alignmented by observing the interference fringes. When the diamonds were pressed together they showed the extent of the misalignment by producing interference fringes on the diamond faces. Adjusting the diamonds to minimize interference fringes, until the fringes are absent, ensures the diamond faces are parallel. A rhenium gasket is placed on the bottom diamond and held in place with silicon-based caulk. The dimensions of the gaskets in this study range in thickness from 125 to 250 μm. The gasket aperture, which acts as the wall of the chamber, ranged in size from 250 to 600 μm. The solid

starting materials (i.e. the minerals) are placed into the chamber first; these minerals are on average approximately 100 μm · 50 μm · 50 μm ($l \cdot w \cdot h$). Droplets of an aqueous solution (H_2O, HCl, etc.) were added to the chamber, and the cell is closed, enclosing a bubble of air with the solution. Experiments conducted at the University of Maryland were performed on the stage of a Leitz polarizing microscope which had a 1/3 inch type IT CCD camera mounted to collect video. A second video camera records the temperature monitor. These two video feeds are routed to a computer for capture with the video of the temperature monitor as a smaller 'picture-in-picture' on the recorded video. Windows Movie Maker is used for any post-production editing needed for the final video.

The chamber and its contents can be considered to be subjected to an internal hydraulic pressure consistent with the equation of state (EOS) of pure water, if some reasonable assumptions are made. The aqueous solutions used in this study were deionized water or hydrochloric acid of low concentration (10 – 0.1 milli-molality (m*m*)). The hydrochloric acid solutions can be considered to have, nominally, the same properties as water in terms of density, thermal expansivity and compressibility. Experiments presented in chapter four incorporate magnesite as one of the starting materials, which upon reaching elevated temperatures and pressures decarbonated, adding carbon dioxide, and changing the chemistry and physical properties of the aqueous solution. Although carbon dioxide addition was minimal (up to 0.09 mole fraction carbon dioxide) iterative calculations were made to adjust for the changes in physical properties of the fluid (Bakker, 2003). Upon heating, the liquid and vapor are in equilibrium and will travel up the 2-phase boundary line of water and steam. The

vapor bubble changes its size due to the thermal expansivity/compressibility of the vapor or fluid until homogenization is reached. Homogenization occurs when the expansion of one of the phases overtakes the other and the sample moves off the 2-phase boundary and into a 1-phase field. If the sample chamber has a proportion of liquid to vapor equal to or greater than 2 to 1, the bubble will shrink, and the sample will move into the liquid stability field (Bassett et al., 1993).

Use of the EOS of water to calculate the pressure of the sample requires the assumption that the chamber remains isovolumetric. The sample chamber is thought to change dimensions when exposed to elevated pressure and temperature. Above 600 °C, the chamber's internal pressure causes the rhenium gasket to deform via hydrolytic weakening (Burchard et al., 2003). Gasket deformation can be minimized (but not eliminated) by careful preparation of pristine gaskets, pre-indentation of gaskets prior to experimental runs, proper design of experiments to avoid overpressures created by some chemical reactions and exact assembly of equipment/experiments. A discussion of gasket deformation and the effects it will have on experimental conditions is presented in a subsequent section of this chapter.

Pressure and Temperature Calibrations

Pressure calibrations of the EOS of water in HDAC experiments have been performed by using the: α - β quartz transition (Shen et al. 1993); tetragonal to cubic phase transition in $BaTiO_3$ (Haselton et al. 1995; Chou 2007); shifts in the A1 raman modes of quartz (Bassett et al. 1996; Schmidt and Ziemann 2000); monoclinic to cubic transition in $Pb_3(PO_4)_2$ (monoclinic/trigonal); and tetragonal to cubic phase transition in $PbTiO_3$ (Chou 2007). Bassett et al. (1996) suggested that, when all of the

uncertainties are propagated, pressure determination based on the EOS of water is accurate to within 1% at temperatures and pressures up to 1000 °C and 0.5 GPa, respectively.

The accuracy of the pressure determination depends, in part, on the accuracy of the temperature measurements. Type-K thermocouples, used in this work, have an accuracy ("tolerance" in the thermocouple literature) of 2.2 °C below 293 °C, and above 293 °C, it is 0.75% of the temperature. The uncertainty in temperature measurements affects the perceived temperature of liquid-vapor homogenization of the fluid, and therefore adds uncertainty to the determined density isochore of the experiment. Figure 2.1 demonstrates the effects uncertainty of the liquid-vapor homogenization temperature will have on the density of the fluid and the resulting pressure estimate, for the case at 600 °C, based on the EOS of pure water. Figure 2.1 shows two groups of three lines, with the three lines corresponding to the reported temperature, and the upper and low limits. The lines are plotted with respect to their homogenization temperatures on the x-axis, with the black lines corresponding to the left y-axis (density, $g \cdot cm^{-3}$) and the gray lines corresponding to the right y-axis (resulting pressure in MPa, at 600 °C). During this study, liquid-vapor homogenization temperatures ranged from 100 °C to 300 °C. Low homogenization temperatures (<175 °C) were determined to have less than ±1% uncertainty in the resulting pressure. The uncertainty in pressure will increase at higher liquid-vapor homogenization temperatures to ±2% variation in pressure at 300 °C. The uncertainty in temperature of liquid-vapor homogenization temperatures closer to the critical point of water will lead to an uncertainty in the pressure determinations of up to

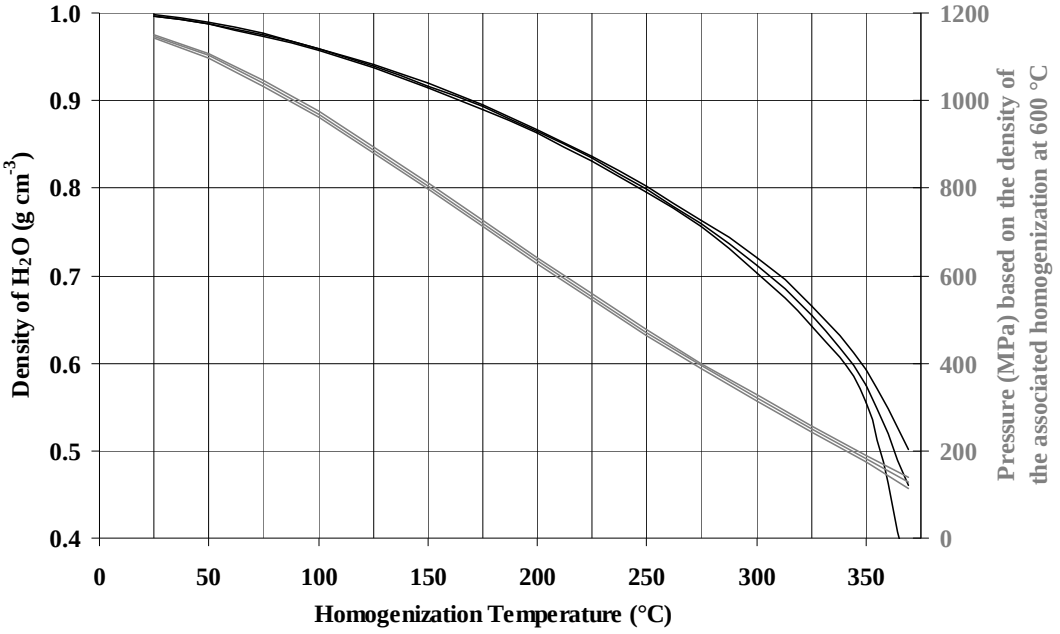

Figure 2.1 The uncertainty in fluid density and pressure based on uncertainty of the homogenization temperature. The two groups of lines are plotted with respect to the reported liquid-vapor homogenization temperature, the upper limit on temperature, and lower limit on temperature, given the uncertainty of the reported temperature. Black lines are plotted with respect to density (g · cm^{-3}), gray lines represent the resulting pressures (MPa) at 600 °C.

±10%. The higher variation closer to the critical point is due to the larger uncertainty in temperature and the increased change in the density isochore slopes as they wrap around the critical point.

Temperature calibrations were conducted by observing melting points and phase transitions of well-known substances at atmospheric pressure. Bassett et al. (1993) used $NaNO_3$ and NaCl melting points and found that precision was ±0.1 °C between -110 °C and 380 °C with an accuracy of ±0.5 °C over that same range, and temperature precision is ±0.5 °C at -190 °C to -110 °C or above 380 °C, with an accuracy of ±1.5 °C over that same range. Temperature calibrations conducted at the University of Maryland (UMD) differ slightly (see Table 2.1). Calibrations at UMD

measured the temperatures of the melting points of NaCl (800.5 °C), CsCl (645 °C) and $NaNO_3$ (307 °C) and also the bcc to fcc transition in CsCl (479 °C), all at 1 atm (Table 2.1). The hydrothermal diamond anvil cells used in this study required a temperature correction factor of 1.0085 to raise the temperature value given by the thermocouple readouts ('temperature observed') to the actual temperature inside the chamber ('true temperature').

Table 2.1. Temperature (°C) Calibration in the HDAC

		$T_{Reference}$	$T_{Observed}$	2σ	N	$(T_{Ref} - T_{Ob})$
$NaNO_3$	m. p.*	307	306.8	0.8	11	0.2
CsCl	bcc↔fcc**	479	476.3	2.4	11	2.7
	m. p.*	645	641.4	1.3	17	3.6
NaCl	m. p.*	800.5	793.7	1.5	26	6.8

True Temperature = Temperature observed **x** 1.0085

* m. p. - Melting Points from Lide (2000)
** bcc↔fcc - CsCl phase transition from Menary et al. (1951)

Gasket Deformation

A difficult obstacle accompanying HDAC experimentation is the deformation of the rhenium gasket at elevated temperatures and pressures. Gasket deformation during experiments results in volume changes of the cell, which will change the isochoric behavior of the aqueous fluid. Pre-indenting gaskets can reduce deformation, but does not eliminate it. Most HDAC studies, not concerned with kinetics, determine the aqueous fluid density after deforming the gasket by cycling the cell through significant changes in temperature before beginning the experiment. Gasket pre-indention was performed in the experiments described; however, cycling

of the cell through significant changes in temperature is not possible in kinetics experimentation.

Bassett et al. (1993) performed measurements to quantify the volume changes associated with gasket deformation in the HDAC. The variation of distance in the z direction (i.e., between the anvil faces) was less than 0.5%, and in the lateral directions (i.e., gasket aperture diameter), they found that change was negligible. The rhenium gaskets used in this study have all exhibited deformation during the experiments. If no volume change is assumed, once the sample has homogenized, the density of the solution will stay on an isochoric pathway to higher pressures and temperatures, based on the equation of state of the solution (Wagner and Pruss, 2002; Bakker, 2003). This assumption is the basis for the calculation of the hydraulic pressure in the HDAC.

Experiments conducted at the University of Maryland were documented by using a video recording system in order to provide a record of reaction progress. Videos were analyzed after the experiments and cross-sectional areas of various components were measured to monitor changes during the experiment. Greater detail of these measurements is provided in chapters three and four. Cross-sectional area of the chamber aperture was measured from recorded videos at regular time intervals (generally 10 minutes) for the duration of an experiment. Gasket deformation, resulting from ductile flow of the gaskets, is most pronounced when temperature is increased. The rhenium deforms in response to the compressive stress applied to the gasket by the diamonds. The force is imposed by the assembly screws and is accentuated by thermal expansion of the steel assembly and the rhenium gasket at

elevated temperatures. As temperature was increased, the ductile flow of the rhenium gasket was visible in recorded experiments as a migration of the chamber walls towards the center of the cell, thereby decreasing the volume of the cell and increasing the density of the aqueous fluid. Gasket expansion can also occur as a response to the hydrostatic pressure of the experimental charge, but is thought to be minimal.

At late stages in some experiments the growth of reaction products, which frequently occurred on the gasket walls, would obscure measurements, giving the appearance of a smaller aperture. In addition, growth of the reaction products dispersed throughout the cell can block light transmitted through the chamber aperture, leading to underestimations of the cross-sectional area. Given these limitations, measurements of gasket aperture dimensions in these experiments are consistent with most of the deformation being accommodated in the first thirty minutes of an experiment (Table 2.2 and Appendix A-1). For these reasons, measurements of the chamber aperture in this study were only conducted for the first hour of the experiments. After the first hour, chamber measurements were assumed to be equal to the measurement taken at the one hour mark. Values in Table 2.2 demonstrate that, in most cases, the majority of the inferred deformation of the gasket occurs at least within the first hour of the experiment. In experiments that are contrary to this, an examination of the experiments (images in Appendix B-2 and C-2, and videos in Appendix D), shows that each of these experiments had extensive growth which obscured chamber measurements, leading to questionable results.

Experiment	isothermal or stepwise	Max T (°C)	Chamber volume decrease from initial	Chamber volume decrease in 1st hour	Chamber volume decrease post-1st hour	Estimated change in the z direction	Retrograde density: Actual - Predicted
plate dominated							
06-09-07	isothermal	655	15.49%	98.64%	1.36%	1.52%	-0.12
11-04-09	stepwise	615	5.70%	83.55%	16.45%	0.55%	-0.19
fiber dominated							
09-05-07	isothermal	640	3.72%	75.02%	24.98%	0.40%	-0.60
06-10-07	isothermal	655	25.15%	98.23%	1.77%	1.87%	-0.03
08-25-09	stepwise	765	5.84%	100.29%	-0.29%	0.91%	-0.09
both plates and fibers							
08-29-07	isothermal	600	2.85%	96.75%	3.25%	0.28%	-0.03
02-24-08	isothermal	550	11.33%	37.24%	62.76%	1.21%	-0.14
12-02-09	stepwise	615	7.37%	88.34%	11.66%	0.83%	-0.07
03-02-10	stepwise	615	9.70%	37.16%	62.84%	1.08%	-0.05

Table 2.2. Table of select run conditions, volume and density calculations. Chamber volume calculations were determined by monitoring changes in the chamber aperture. 'Isothermal' or 'stepwise' indicates the thermal condition of the experiment (stepwise = temperature vary in a stepwise fashion). 'Max T' represents the maximum temperature reached by the experiment. 'Chamber volume decrease in 1st hour' is the chamber volume decrease observed during the first hour of the experiment as a percent of the total volume decrease. 'Chamber volume decrease post-1st hour' is remaining chamber volume decrease experienced. 'Estimated change in the z direction' is the change in chamber height due to the volume change (%). The last column reports the difference between the predicted aqueous fluid density change estimated by the volume measurements and the observed retrograde density achieved.

Determining the magnitude of chamber volume change seen in the lateral dimensions allows for a rough estimate of change along the 'z' direction (i.e., the thickness of the rhenium foil in the plane perpendicular to the image). If all the deformed rhenium, caused by the indentation of the diamond, flowed towards the center of the chamber, a calculation can be made for the maximum amount of indentation. These values do not exceed a 1.87% decrease in rhenium foil thickness. Post-experiment secondary electron images (found in Appendices B-3 and C-3) illustrate that the deformation of the gasket is not limited to only flowing in towards the aperture opening: rhenium deformation can be detected on the outer edge of the diamond indentation, consistent with flow of the rhenium away from the gasket aperture as the gasket indents. The estimates of 'z' direction presented in Table 2.2 can account for rhenium flowing toward the center of the cell but not away from the center, therefore values must be thought of as lower limits on the 'z' direction deformation.

The major contributor to the flow of the rhenium gasket is thermal expansion of the HDAC apparatus. Thermal expansion of the assembly was also evident in experiments examined by synchrotron radiation x-ray diffraction (SR-XRD). Experiment conducted at Brookhaven National Laboratories - National Synchrotron Light Source (BNL-NSLS) used SR-XRD to identify phases involved in reactions and provide semi-quantitative reaction rate data (SR-XRD results are discussed in Chapters three and four). During SR-XRD examination, the HDAC apparatus was placed with the diamond culet faces perpendicular to the beam. As the HDAC increased in temperature, the assembly thermally (and potentially the stage)

expanded, moving the chamber above the path of the beam as the stage remained stationary. This 'drift' away from the beam required realignment of the chamber center for the first half hour of experimentation until thermal expansion slowed. Figure 2.2 displays the movement of the cell, with respect to the beam, during a representative experiment. The values provide in Figure 2.2 were the result of determining the center of the chamber at different times during an experiment. The experiment was brought to a temperature 400 °C, where it was held isothermally for ~140 minutes. The graph displays movement of the HDAC but after the first 30 minutes the assembly stabilizes and little thermal expansion can be detected. Similar patterns were observed for most experiments conducted at BNL-NSLS.

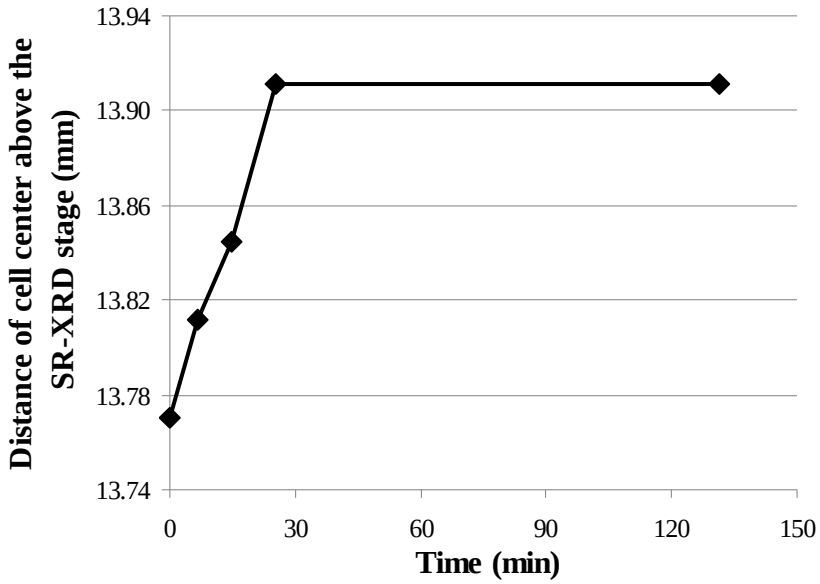

Figure 2.2 Change in position of the HDAC apparatus in the SR-XRD hutch due to thermal expansion (during experiment Run 37). See text for details and discussion.

Error Related to *In Situ* Mass Loss Determinations

A portion of this study describes a novel method of determining the growth rates of reaction products by using *in situ* observation and measuring reactant mass loss. The technique of *in situ* mass loss determinations uses image analysis of objects (phases of known density), by measuring their cross-sectional areas, extrapolating measurements to volumes, and then, masses. Although the technique of *in situ* mass loss has not been used to infer reaction product growth rates before, it has been employed to determine the solubility of minerals in aqueous fluids (Wang et al., 2004; Manning et al., 2008; Gross, 2009; Mysen, 2009). While a more in-depth description of the technique is provided in chapters three and four, a discussion of the errors related to this technique has been provided here to aid in assessment of the data presented in subsequent chapters.

The technique of *in situ* mass determination was first developed by Matthews and Davis (1999) to provide mass estimations of zircon grains that are below the precision of analytical balances. Matthews and Davis (1999) massed ellipsoidal zircon grains, ranging in size from 100-300 µm along the long axis of the grain, with an analytical microbalance, then using image analysis, they determined the mass of each grain for direct comparison. They found that the masses determined by *in situ* mass determination deviated from the balanced mass by ±10%, with a precision of ±1 µg. Gross (2009) tested these results on euhedral grains of quartz by processing images using a crystal computational program, and determined a coefficient of variation (CV) of the measurements of ~1%. Wang et al. (2004) was the first to determine mass loss of minerals reacting in an aqueous fluid using the *in-situ*

technique. They assumed the error of the measured quartz grain equal to one pixel of the image analyzed (or 0.535 µm per pixel); this translates into ±0.0043 µg change in mass or a 10% change in the determined solubility of quartz in their study.

The first step in making *in situ* mass loss determinations was to generate a series of screen capture images from the videos of recorded experiments at specific time intervals. Once the screen capture images were acquired, measurements of the cross-sectional area of the chamber, quartz and magnesium-rich phase were made by using the image processing software ImageJ®. These measurements were made in triplicate and the precision of those measurements was calculated, along with the CV and maximum CV, for each set of experiments (Table 2.3 and Appendices B-1 and C-1). Table 2.3 present the CV and maximum CV for all experiments presented in this study at the time of prograde homogenization. In both sets of experiments, the largest measured cross-sectional areas, the chamber, had the highest precision, or the lowest coefficient of variation and the smallest measured cross-sectional areas, the quartz,

	CV	**Max CV**
Olivine Experiments		
Chamber Volume	0.22%	0.56%
Quartz Volume	0.51%	0.98%
Olivine Volume	0.34%	0.51%
Magnesite Experiments		
Chamber Volume	0.14%	0.32%
Quartz Volume	0.51%	0.74%
Magnesite Volume	0.34%	0.63%

Table 2.3. Precision of *in situ* mass loss determinations expressed as the coefficient of variation (CV) of the triplicate measurements made at the time of prograde homogenization and the maximum coefficient of variation (Max. CV).

had the lowest precision, or the highest coefficient of variation. The smallest measured cross-sectional areas, the quartz, had the lowest precision, and the highest coefficient of variation (reaching a maximum of 9% CV at later stages of experiments), in part due to quartz dissolving to a small volume.

Measurements of the cross-sectional area of the objects of interest were collected and modeled as idealized shapes that closely matched the actual shape in order to calculate the volume. The chamber is treated as an ideal right circular cylinder with the thickness of the gasket being the third axis for volume. The quartz and olivine grains are treated as ideal ellipsoids with a 2:1:1 axis ratio. The magnesite starting material, a microcrystalline magnesite aggregate, had a natural parting of ~50 µm, that exhibited a ~2:1 right elliptical cylinder morphology, and because of this the magnesite volume was modeled differently from quartz and olivine. Only grains exhibiting the described morphologies were chosen as starting materials. For all mineral grains, once the cross-sectional area is determined, the area is treated as an idealized 2:1 ellipse and the two principal axes are found. The quartz and olivine grains had a third axis that could be approximated as equal to the short axis of the area ellipse. The third axis for magnesite was determined to be the natural parting of the microcrystalline rock at ~50 µm. Careful selection of the starting materials shapes was intentional and imperative in order to facilitate calculation of model volumes of the idealized shapes. In an attempt to evaluate the effect of shapes on volume calculations (and subsequently solubilities), the length of the longest axis (these are the diameter of curved shapes and the length of blocky shapes of the longest axis of the idealized shapes) has been plotted against the calculated volumes (Figure 2.3).

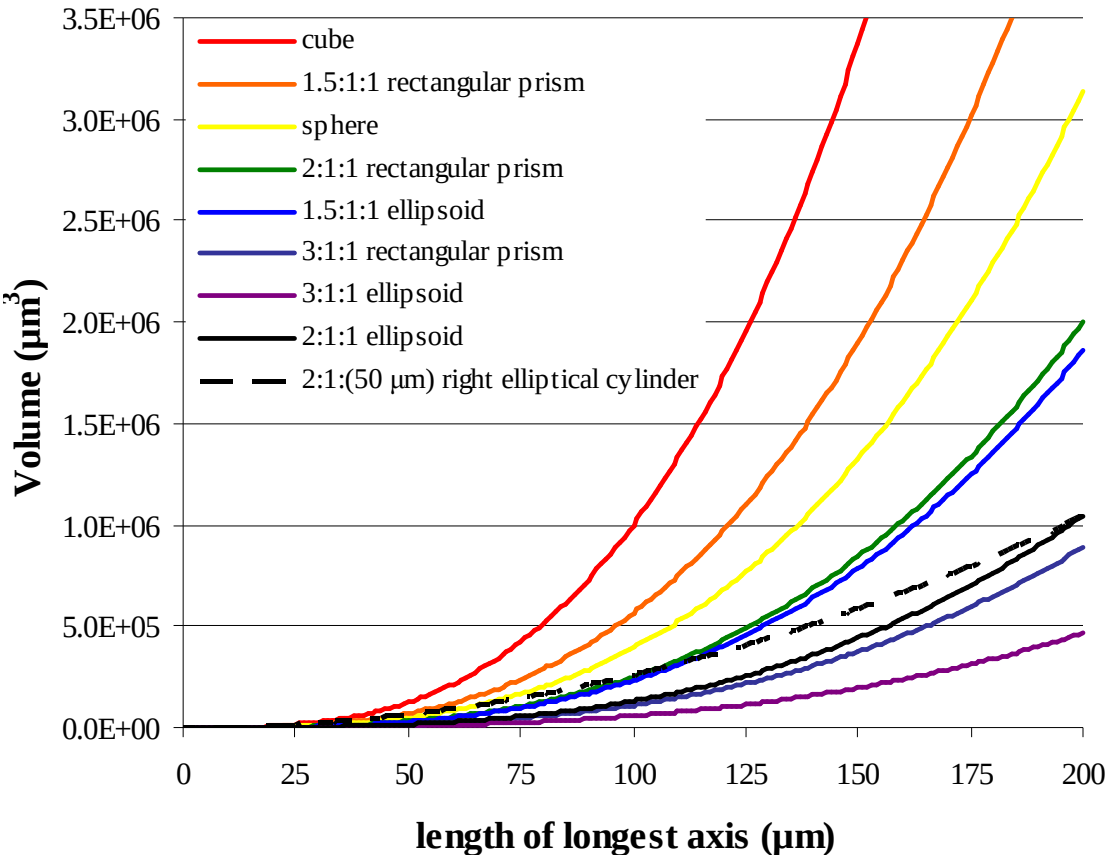

Figure 2.3 Volume change of various shapes as a function of length of the longest axis. Shapes used in this study are shown by the black solid line for olivine and quartz, and the black dashed line for magnesite.

The solid black line represents the idealized shape exhibited for the olivine and quartz grains. The dashed black line represents the idealized shape exhibited by magnesite grains and is modeled by holding the height of the right elliptical cylinder constant (at 50 µm), but it is plotted a function of its longest elliptical diameter to facilitate ease in comparison. Figure 2.3 demonstrates that if the mineral grains were poorly chosen (that is, not representing idealized shapes), and/or could better be described by another morphology, the results can be systematically skewed.

The accuracy of *in situ* mass loss measurements was evaluated by considering the cross-sectional area measurements to have an accuracy equal to one pixel, the

same manner proposed by Wang et al. (2004). The images collected as part of this study were higher resolution than those of Wang et al. (2004), with one pixel equaling 0.461 µm compared to their pixel length of 0.535 µm. Figure 2.4 shows the measurement accuracy of the estimated mass of quartz grains of various sizes. Figure 2.4 was drawn for a quartz grain with a 2:1:1 ellipsoidal morphology, and shows the error in mass of the grain, if the volume of the modeled grain is decreased by one

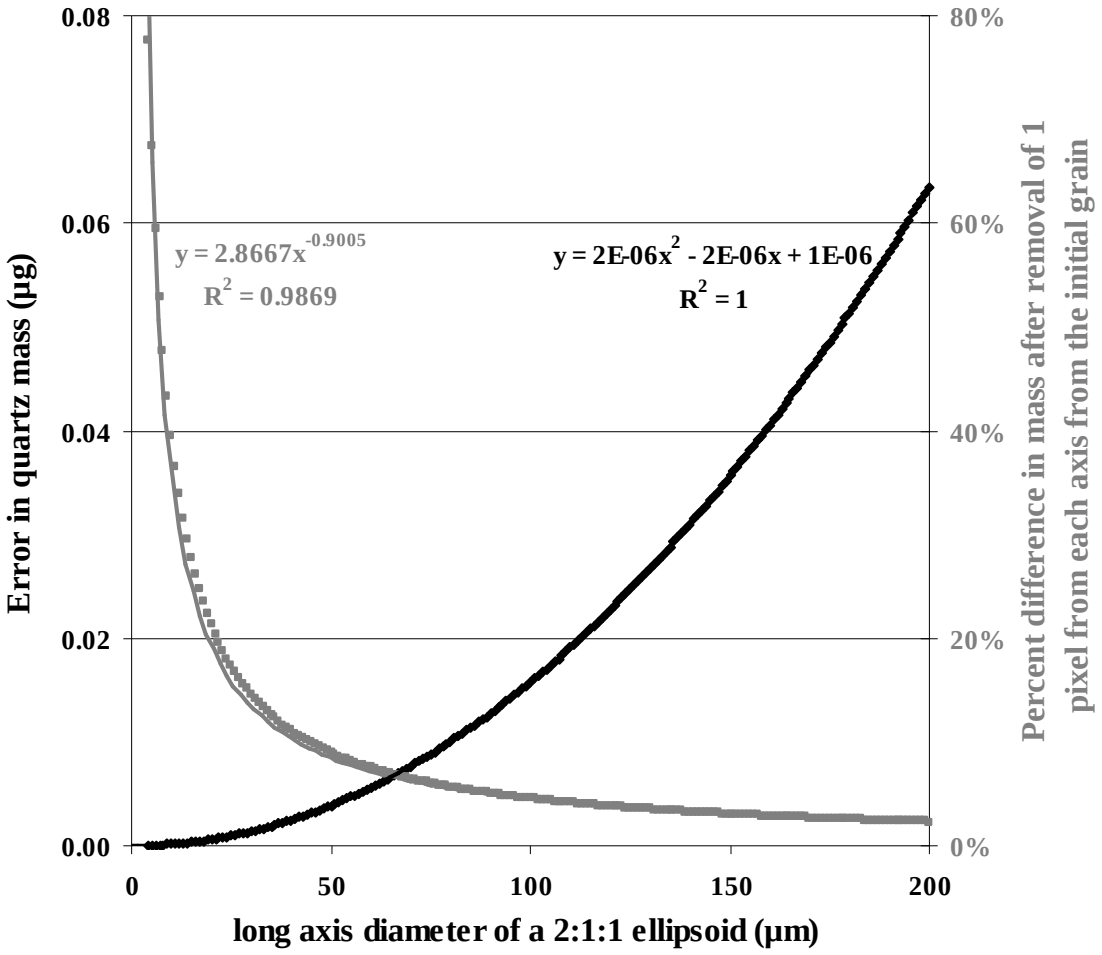

Figure 2.4 Accuracy of cross-sectional area measurements of an ideal 2:1:1 ellipsoid of quartz. The x-axis is the diameter of the long axis of a 2:1:1 ellipsoid. The black line shows the calculated error in quartz mass. The gray line shows the change in quartz mass when one pixel length is removed from each of the three principal axes, represented as a percentage of change from the initial grain mass.

pixel on each of the principal axes of the ellipsoid. The error is represented as mass (in µg) and as the percent error from the initial grain mass (before pixel subtraction). Error in quartz measurements will result in incorrect estimations of talc produced and, therefore, incorrect talc growth rates. For example, for a quartz grain with a longest axis diameter of ~180 µm (the upper limit of quartz grains used), the error in quartz mass is 0.05 µg (or $8.3 \cdot 10^{-10}$ moles of quartz). Projecting that error forward by assuming all the quartz is consumed during the production of talc, this amount of quartz error would result in a uncertainty of $3.3 \cdot 10^{-10}$ moles of talc produced. In representative experiments described in this study, $\sim 3.3 * 10^{-9}$ moles of talc are produced, and given the uncertainty described above, this results in a difference of 9.8%. This example would be an upper limit of error because as experiments proceed the quartz dissolves, decreasing in size, and the associated error decreases as well.

If the same error calculations are made for the volume of the cell, the volume of the cell and the mass of water calculated will vary by 0.75% for a 300 µm diameter chamber with a rhenium foil thickness of 150 µm with the chamber filled with water with density of $0.85\ g \cdot cm^{-3}$. This is equal to ~65000 μm^3 or 0.05 µg of water under those conditions. The mass of water error calculations take into effect the volume occupied by minerals; without minerals present in the cell, the percent difference is 0.64%.

Aqueous Solutions and Minerals at Elevated Temperature and Pressure

The speciation of dissolved components was not determined during this study but to understand the potential reaction pathways, it is necessary to review the results of previous studies of related dissolved chemical speciation. To understand the nature of dissolved species within the presented experiments it is necessary to rely on previous studies that have determined these parameters under similar conditions.

H_2O-HCl Aqueous Solutions

All experiments incorporate an aqueous fluid, loaded into the cell with minerals, sealed in the chamber, and raised to elevated temperatures and pressures. As noted above, careful characterization of the fluid is required to determine the pressure within the experimental chamber. Water is both the pressure medium in the chamber and the main agent of chemical transport of dissolved species. As temperature increases, the chemical properties of water change, importantly including the ionic dissociation of water. Figure 2.5 shows the ionic dissociation of water at various densities and temperature at a pressure of 200 MPa. As temperature rises, the ionic dissociation of water into H^+ and OH^- species increases; each isochoric line presented in Figure 2.5 represent the neutral pH for the given conditions.

A set of experiments in this study was conducted by using aqueous solutions containing hydrochloric acid (see Chapter three for additional discussion). Hydrochloric acid solutions used in this study ranged from 0.1-10 m*m* hydrochloric acid yielding aqueous solutions with pH=4 and 2, respectively, at 25°C. At these low concentrations of hydrochloric acid any deviations of the physical properties of the aqueous solution from pure deionized water are insignificant. However, using

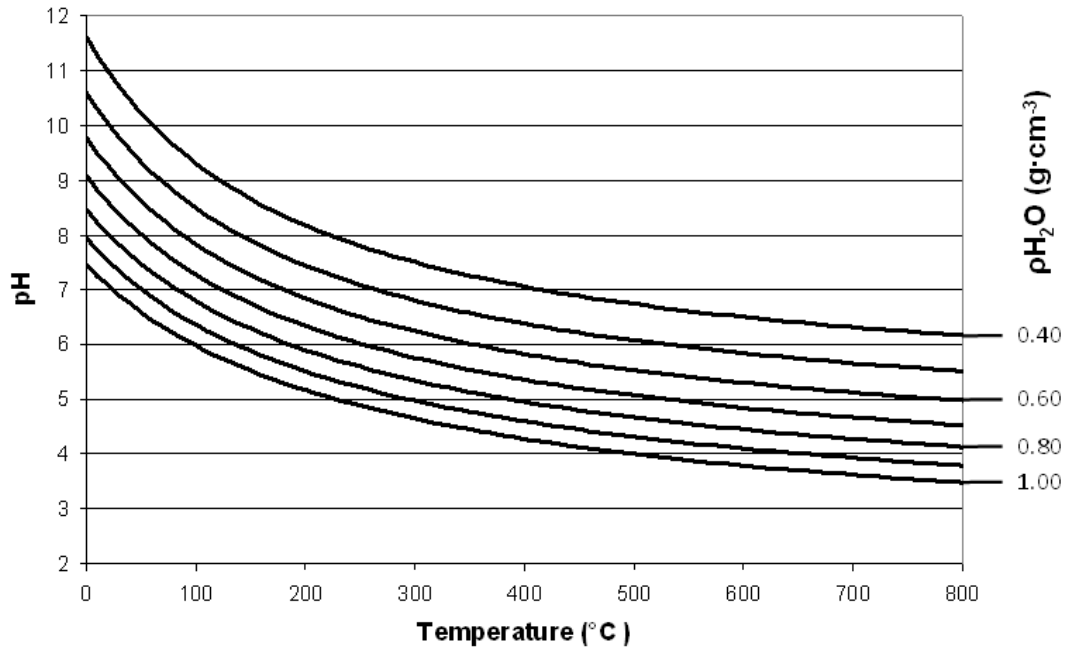

Figure 2.5 Neutral pH of H_2O at various densities and temperatures (at 200 MPa).

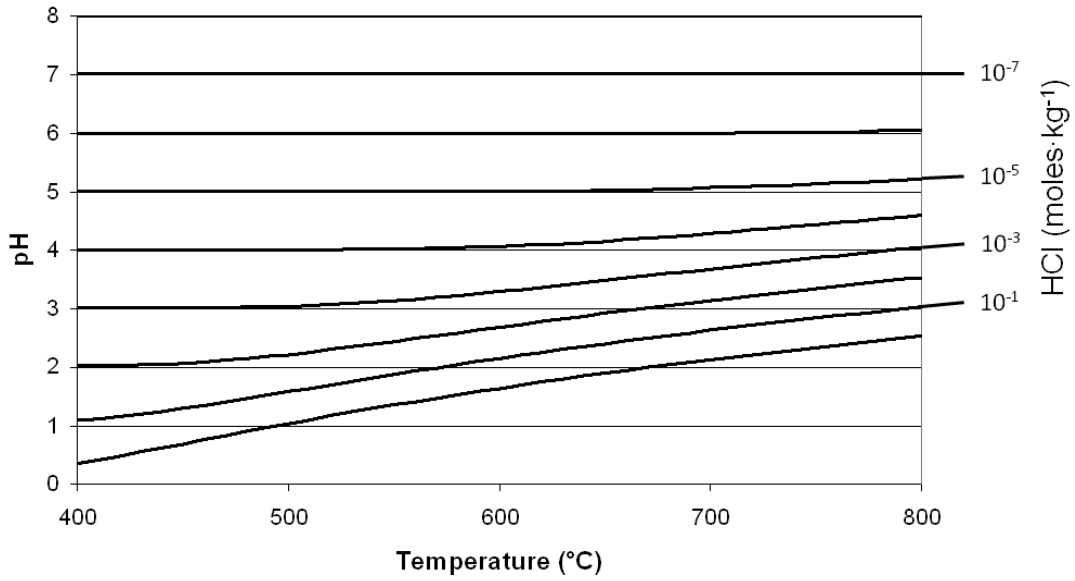

Figure 2.6 Change in pH for HCl solutions with increasing temperature (at 200 MPa).

hydrochloric acid solutions in these experiments introduces chloride, and chloride complexes will dominate over hydroxyl complexes (Hemley et al., 1977a). Chloride complexes can act as catalysts, allowing the system to reach equilibrium faster than

normally would occur. Hydrochloric acid appeared to exhibit no catalytic function in the experiments presented in this study (Chapter three). Figure 2.6 provides a representation of the changes to the pH of hydrochloric acid solutions given variations in concentration and temperature.

H_2O-CO_2 Aqueous Solutions

A set of experiments in this study was conducted by using the mineral magnesite ($MgCO_3$) as one of the starting materials. As reactions progressed, magnesite decarbonated as magnesium was consumed during the production of talc ($Mg_3Si_4O_{10}(OH)_2$), and carbon dioxide was added to the aqueous fluid (see Chapter four). The addition of carbon dioxide to the aqueous fluid will change the physical properties of the aqueous fluid, particularly the density of the fluid, and therefore the pressure within the chamber. During an analysis of each experiment, estimates of the carbon dioxide content of the aqueous fluid were iteratively calculated. Adjustment to the density and resulting pressures, due to the addition of carbon dioxide, were made by using the program FLUIDS developed by Bakker (2003).

Mineral Dissolution

Quartz constituted a part of the starting assemblage for all experiments in this study. The knowledge of quartz solubility in aqueous fluids at elevated temperatures and pressures is an important foundation for this study. As temperature and pressure are increased during experiments, quartz decreases in volume as it dissolves into the aqueous fluid. Measurements taken during the experiments monitored the size decrease and estimate the amount of silica dissolved in the aqueous fluid, with respect

to quartz saturation. All silica in excess of quartz saturation is assumed to be consumed by the production of silicate reaction products. Therefore, the accuracy of estimated quartz saturation will affect various aspects of the results determined in Chapters three and four, in particular for the growth rates of the reaction products.

Quartz readily dissolves in pure water at elevated pressures and temperatures (Manning, 1994). The speciation of silica in silica-rich fluids has been well studied (Manning, 1994; Newton and Manning, 2002; Zotov and Keppler, 2002; Gerya et al., 2005; Newton and Manning, 2009; Mysen, 2010). Below 600°C and 600-800 MPa, orthosilicic acid (H_4SiO_4) is the dominant species of dissolved silica. At higher temperatures and pressures, polymerization occurs and H_4SiO_4 monomers and $H_6Si_2O_7$ (or pyrosilic acid) dimers.

Methods similar to the methods of this study (estimating mineral dissolution by way of *in situ* mass loss evidence) have been employed to determine the solubility of quartz in water, at elevated pressures and temperatures by monitoring quartz volume changes (Wang et al., 2004; Gross, 2009). Their results matched well the experimental results of Manning (1994) up to 370 °C. In conditions above 370 °C, once quartz saturation was reached, the abraded quartz grains begin to facet, resulting in inaccurate estimations. The experiments of Gross (2009) began with euhedral grains of quartz and used crystal volume computation software, which yielded volumes of faceted minerals, to determine quartz volumes. Gross (2009) confirmed the quartz saturation determined in the experiments of Manning (1994) and Gerya et al. (2005) at temperatures between 300 °C and 635 °C (with a reported error of 5.6%). Most experiments conducted during this study did not exhibit faceting of the

quartz grain inferring that, in these experiments, quartz saturation is not reach but is buffered just below quartz saturation as reaction products remove silica from the aqueous solution.

In experiments that involved the decarbonation of magnesite, the addition of carbon dioxide increased the solubility of quartz. Figure 2.5 presents quartz saturation, expressed in molality (moles $\cdot$ kg^{-1}), for various density isochores of water and H_2O-CO_2 fluids of 0.05 and 0.1 mole fraction of carbon dioxide (Manning, 1994; Akinfiev and Diamond, 2009). The upper limit of carbon dioxide mole fraction reached by experiments was ~0.092 (see Chapter four). The effects of carbon dioxide addition to the aqueous fluid correlate well with the absolute mole fraction of carbon dioxide. For example, when the carbon dioxide mole fraction of the fluid is 0.10, the increase in quartz saturation is approximately 10%. The relationship is dependent on the density of the fluid and will vary; therefore, must be calculated on a case by case basis.

The dissolution of magnesite and olivine will produce dissolved species of magnesium within the aqueous fluid (and silica in the case of olivine). In pure water systems Mg^{2+} is the dominant species of magnesium at the conditions of these experiments. In experiment involving hydrochloric acid, chloride complexes can play an important role in the speciation of magnesium. Above ~500°C and 200 MPa, the most common dissolved species for magnesium is $MgCl_2^0$. Below these temperatures, $MgCl^+$ and Mg^{2+} become more important (Hemley et al., 1977a; Frantz and Popp, 1979). Hydrochloric acid was not used in experiments with magnesite as a starting material due to the reactivity of these phases at room temperature and pressure.

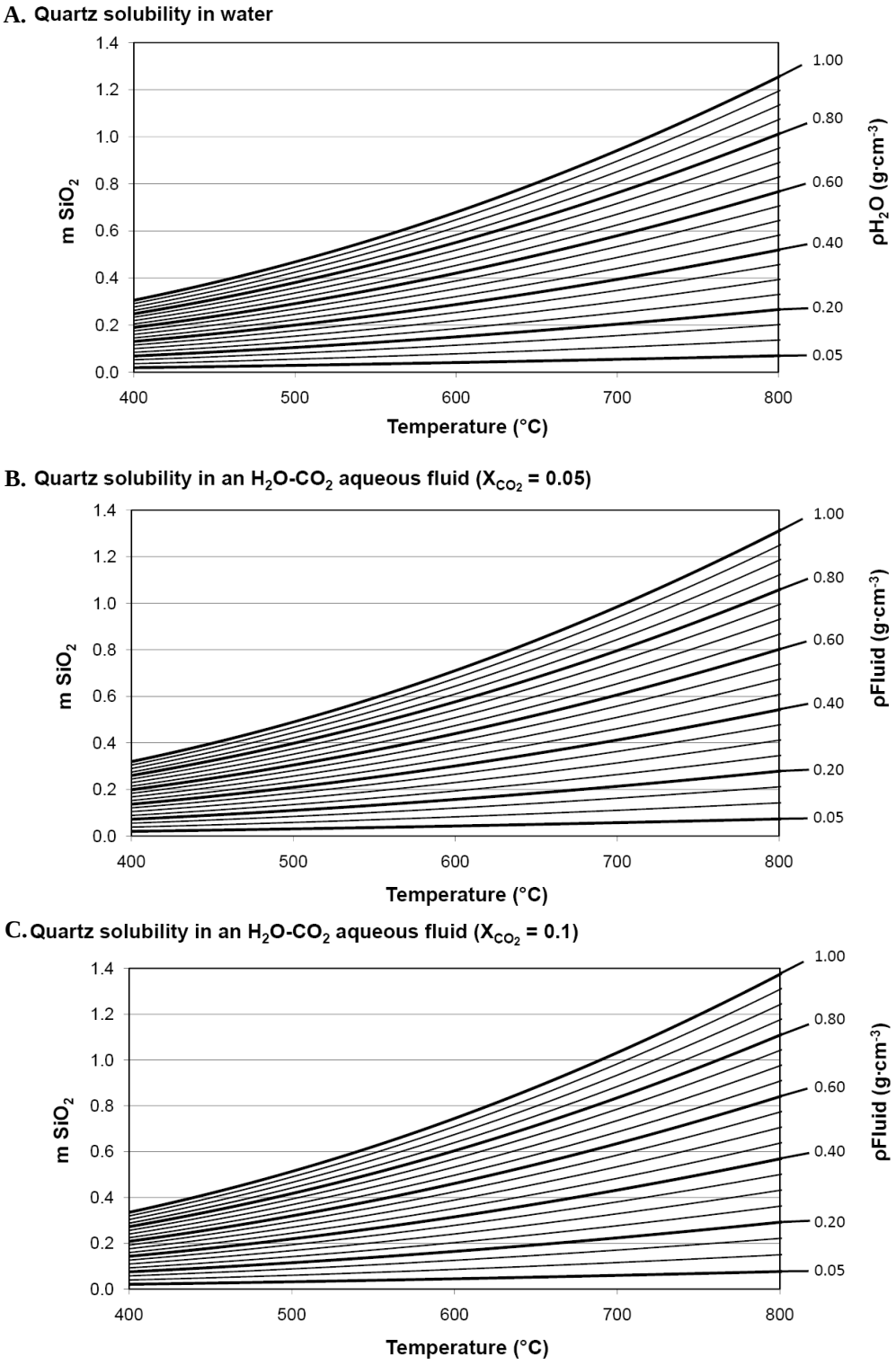

Figure 2.7 Concentration of SiO_2 at quartz saturation over temperature as a function of the density of pure water (A) (after Manning, 1994) and mole fractions carbon dioxide of 0.05 (B) and 0.1 (C) (Akinfiev and Diamond, 2009).

Talc Mineralogy

Talc ($Mg_3Si_4O_{10}(OH)_2$), a hydrous magnesium silicate, is the primary reaction product of experiments conducted during this study. Talc is produced by the hydrolysis of magnesium-rich minerals. It commonly forms a platy habit, but rarely is found in a fibrous habit. Experiments conducted in this study produced both habits of talc, and in some cases, they coexisted. The habits appeared to be dependent on the specific conditions (e.g. P, T) of the experiments (as discussed in the subsequent chapters). The following discussion has been provided to introduce the properties, chemistry, and crystal structure of talc.

The physical properties of talc make it an important economic resource used in the production of papers, paints, crayons, ceramics, and cosmetics (particularly, baby powder). The chemistry and crystal structure of talc are responsible for the unique properties, such as: hardness, perfect cleavage, hydrophobicity, and organophilicity. Talc is a phyllosilicate (or sheet silicate) composed of TOT (tetrahedral-octohedral-tetrahedral) sheets bound by van der Waals forces. The sheets are composed of a layer of magnesium oxide octahedra that sits between two layers of rings of silica tetrahedra with hydroxyl ions positioned in the center of the interlinked silica rings (Figure 2.8).

Talc forms monoclinic (2/m) or triclinic (bar 1) pseudohexagonal crystals, most commonly in a platy habit. The crystallographic axes of the talc are aligned with the *c* axis parallel to the short axis of the plates and the other crystallographic axes are within the plane of the plates. Talc fibers are the high aspect ratio form and can exhibit a cylindrical to ribbon habit with aspect ratios greater than 100. The

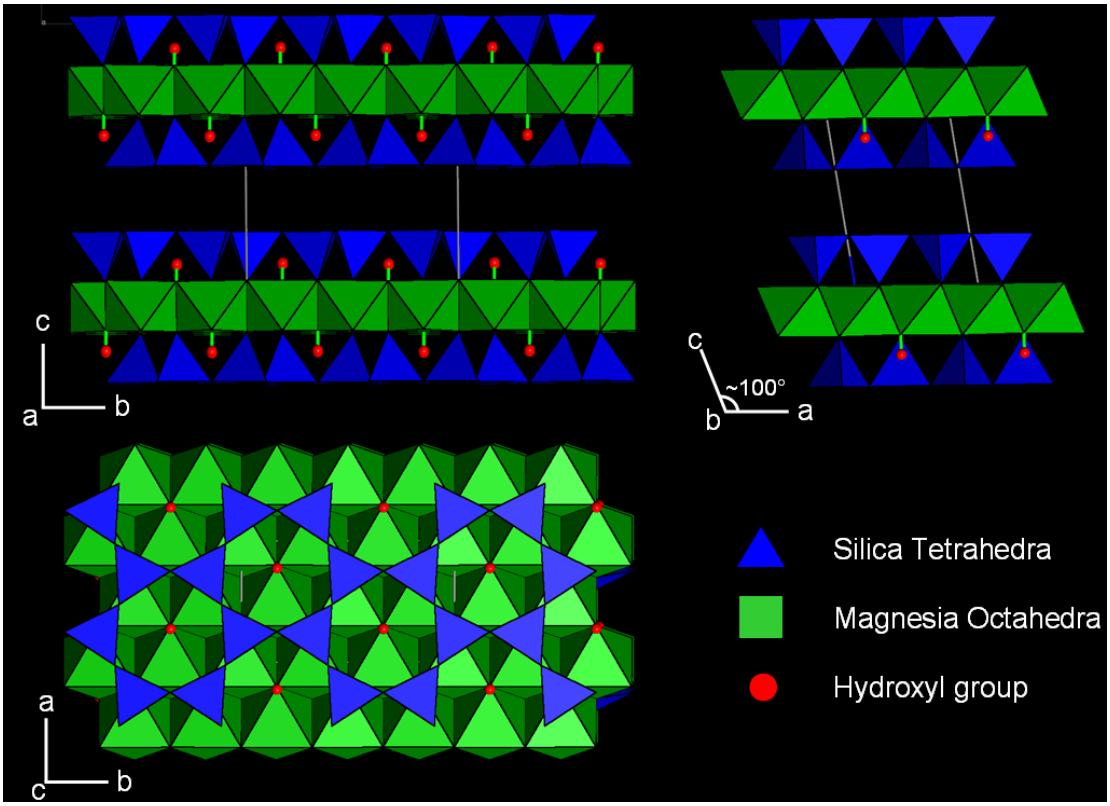

Figure 2.8. The crystal structure of talc.

crystallographic axes of talc fibers are aligned with the *a* axis parallel to the length of the fiber and the other axes perpendicular to the long axis. When talc has been found in a fibrous habit, its origin has been attributed the pseudomorphism of preexisting fibrous minerals, such as amphiboles or serpentines. Several studies have examined talc crystallography associated with fibrous talc produced by pseudomorphism after anthophyllite and bipyroboles (Velben and Buseck, 1980), or after tremolite (Stemple and Brindley, 1960). In those studies, the *b* axis of the preexisting mineral was interpreted to remain unchanged through pseudomorphism, but the *a* axis of the resulting fibrous talc formed parallel to the c axis of the preexisting mineral. The *c* axis of the preexisting single to multi-chained silicate is parallel to the chains; during pseudomorphism a reorganization of the structure occurs, and connects those chains

into sheets. Bose and Ganguly (1994) observed similar axial relationships in talc dehydration to enstatite: the *a* axis of the talc within the plane of the sheet and parallel to the c axis of the resulting enstatite.

Talc fibers produced during this study were examined by transmission electron microscopy (TEM) to investigate the internal structure and morphology of the fibers. Figure 2.9 is a TEM image of a talc fiber which shows the internal structure as represented by two sets of lines showing the lattice of talc. Talc is commonly monoclinic with a β angle (angle between the *a* and *c* axes) ~100 degrees. The sets of lines represent the crystallographic axes of the talc fiber and intersect at

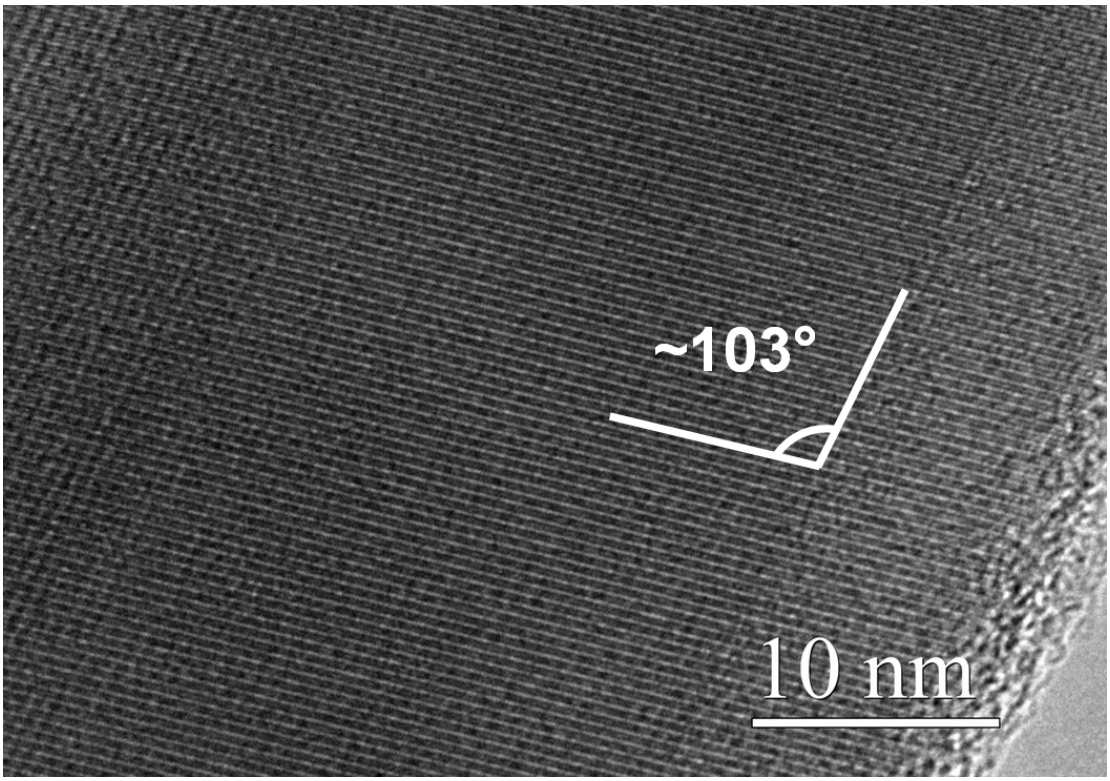

Figure 2.9. Transmission electron microscopy image of a talc fiber.

103 degrees, slightly higher than anticipated but that could be due to the fiber being slightly angled with respect to the plane of the image. When talc is triclinic, the α, β, and γ angles are not equal but most have the alpha as 90 degrees. All reports of talc fiber crystallography have maintained that the c-axis is perpendicular to the length of the fiber (Stemple and Brindley, 1960; Velben and Buseck, 1980). If the fiber in Figure 2.9 is monoclinic, then the axis parallel to the length of the fiber must be the a-axis. If the fiber is triclinic, the axis parallel to the length of the fiber could be either the *a* or *b* axis. Structural refinements to define the crystal system were not attempted, and this work would shed little light on that topic.

Chapter 3: Olivine + Quartz + Water ± HCl at Mid-crustal Conditions in the Hydrothermal Diamond Anvil Cell: Controls on the Growth of Fibrous Talc

Abstract

Most talc deposits are formed by metasomatism of dolostone or ultramafic rocks during metamorphism or hydrothermal alteration. Talc in these deposits generally exhibits a platy morphology; rarely, it can exhibit a fibrous habit. In previous studies, the origin of fibrous talc has been explained by the replacement of fibrous amphiboles during retrograde metamorphism. In this study, experiments have been performed in the MgO-FeO-SiO_2-H_2O-HCl system to investigate textural development and reaction rates of hydrolysis reactions by using a hydrothermal diamond anvil cell (HDAC) apparatus. In experiments, quartz and olivine were reacted irreversibly in aqueous media with the subsequent production of fibrous talc without any apparent amphibole or serpentine precursor. San Carlos olivine (Fo_{90}) + Brazilian quartz + aqueous fluid (deionized water or 0.1 - 10 m*m* HCl) were added to the HDAC and brought to temperatures of 400 - 655 ºC and pressures of 0.1-1.2 GPa for a duration of 2-6 hours. Most experiments were isothermally (± 3 °C); some experiments experienced a second temperature increase of 50 °C after a predetermined duration, where they held at the higher temperature for the remainder of the experiment. One set of experiments was video recorded to provide a visual record of reaction progress; a second set of experiments was recorded via *in situ* synchrotron x-ray diffraction. Vapor-liquid homogenization temperatures were

recorded before and after the experiments to determine the prograde and retrograde isochores, respectively. All experiments produced talc as the only new phase. Experiments can be separated into three groups based on the morphology of run products talc: (1) experiments producing only talc plates; (2) experiments producing only talc fibers; and, (3) experiments producing both talc plates and fibers. Experiments in this study demonstrate that the growth of fibrous talc does not require a fibrous precursor.

In experiments that produced only talc plates, quartz grains commonly exhibited faceting once talc coated the olivine grain, restricting the supply of nutrients for talc growth. In experiments producing fibrous talc (± platy talc), the quartz grain rarely exhibited faceting. The talc fibers (aspect ratios ≥ 25:1; average lengths ~40 µm) grew on the surface of the olivine and on the gasket walls. Growth rates were determined by a visual estimation of quartz mass loss assuming all silica in excess of quartz saturation was consumed by talc production. Maximum talc growth rates in these experiments ranged from 10^{-11} to 10^{-13} moles per second or 10^{-5} to 10^{-6} moles per second per square meter. Results of experiments in this study suggest that the mechanism for talc fiber growth is related to initial nucleation density of talc on the respective substrate and the degree of supersaturation related to pressure decreases. The large surface area of olivine (relative to quartz), an increase in the density of the aqueous fluid, and the chemical isolation of olivine by talc armoring, are all factors that appear to play a role in the production of only platy talc. Decreases in aqueous fluid density (resulting changes in pressure and silica saturation with respect to

quartz) and lower olivine surface areas (relative to quartz) are conditions common to experiments that produced fibrous talc.

Introduction

Hypotheses for the formation of most talc-bearing assemblages commonly require the interaction of silica-rich fluids and magnesium-rich rocks. These hypotheses invoke contact metamorphism, metasomatism, or other related hydrothermal processes (Van Gosen et al., 2004) that produce hydrous magnesium silicate phases (e.g., anthophyllite, serpentine, talc). This study examines the textual development and reaction rates during olivine hydrolysis by silica-rich fluids. These experiments were designed to shed light upon the hydration of ultramafic rock by hydrothermal fluids at mid-crustal conditions, particularly those that result in the formation of talc-bearing assemblages.

Talc occurs most commonly in a platy habit, but it can occur, more rarely, in a fibrous habit. Experiments conducted during this study produced plates and fibers of talc. Due to the confusing, and sometimes contradictory nature of the literature surrounding the terminology of high aspect ratio minerals, a compilation of terms is presented here (Table 3.1). Many authors have attributed the fibrous habit of talc to the pseudomorphism of preexisting fibers such as amphibole or serpentine minerals, as evidenced by the presence of transitional fibers (Stemple and Brindley, 1960; Ross et al., 1968; Wylie and Huggins, 1980; Sanford, 1981; Ferrari and Viti, 2010). Fibrous talc is not considered to be asbestos, and the effects of fibrous talc on the human respiratory system remain uncertain (Beard et al., 2001). The production of

Table 3.1. Definitions of terms related to high aspect ratio minerals. Compiled from MacAdam, 1886; Walker and Zoltai, 1979; Zoltai, 1981; Leake et al., 1997; Bailey et al., 2003, Wylie (personal communication), 2008.	
Acicular	A needle-like mineral habit.
Asbestiform	Having the habit of asbestos including: (1) hair-like, elongate fibers with polygonal, circular, or irregular cross sections usually less than 0.5 µm in width, and exceptionally smooth faces; (2) higher tensile strength, more flexibility and usually more durability than the same mineral crystallized in other habits; (3) crystallization in bundles of parallel fibrils randomly oriented around the fiber axis and easily separable by hand pressure.
Asbestos	A commercial term describing certain silicates belonging to the serpentine and amphibole mineral groups that have crystallized in an asbestiform habit. Minerals commonly mined as asbestos include chrysotile, asbestiform riebeckite (crocidolite), asbestiform grunerite (amosite), asbestiform anthophyllite, asbestiform tremolite, and asbestiform actinolite (some times included in this group are winchite, eckermanite and edenite).
Asbestos Fibers	Fibrils and fibril bundles of asbestos. They have the following characteristics when viewed by light microscopy: (1) Mean aspect ratios ranging from 20:1 to 100:1 or higher for fibers longer than 5 µm (2) Very thin fibrils, usually less than 0.5 µm in width, (3) Parallel fibers occurring in bundles and (4) One or more of the following: fiber bundles displaying splayed ends, matted masses of individual fibers and/or fibers showing curvature.
Fiber	A high aspect ratio mineral particle, ranging from 20:1 to 100:1 (but can be higher), but may not possess other properties of asbestos.
Fibrous	Having the appearance of being composed of fibers.
Fibril	The smallest single fiber making up an asbestos fiber bundle. Fibril widths are generally less than 0.5 µm.
Transitional Fibers	Fibers of mixed mineralogy, sometimes referred to as composite fibers.

fibrous talc in the presented experiments reveals that the growth of fibrous talc does not require a preexisting fibrous mineral.

One hypothesis for the primary growth of minerals with a high-aspect ratio can be ascribed to preferential growth along one crystallographic axis or the inhibition of growth along other crystallographic axes. Uniaxial growth requires conditions where one crystal face is supersaturated while other crystal faces remain below saturation; this can be difficult to achieve in the laboratory setting (Zoltai, 1981). One growth mechanism invoked for the formation of chrysotile asbestos involves growth in zones of local dilation (Zoltai, 1981; Ahn and Busek, 1991; Virta, 2002). Synthetic fibers are commonly grown by directionally manipulating the supply

of the material needed for growth, promoting uniaxial growth (Walker and Zoltai, 1979). Uniaxial growth may occur in settings of extremely rapid crystallization due to supersaturation, a condition that results in a high nucleation density. If each of the nucleation sites survives to produce an individual crystal, dense nucleation may inhibit additional growth within the plane parallel to the nucleation surface, prompting growth in one direction (Zoltai, 1981). Inhibiting growth on two axes can be achieved by well-defined grain boundaries of densely packed nuclei. The conditions of these experiments leading to the growth of fibrous talc are evaluated to establish their contribution to talc morphology.

Many experimental and theoretical studies have been conducted to investigate the thermodynamics and phase equilibria in the MgO-SiO_2-H_2O (MSH) system (Bowen and Tuttle, 1949; Fyfe, 1962; Greenwood, 1963; Greenwood, 1971; Zen, 1971; Bricker et al., 1973; Chernosky, 1976; Zen and Chernosky, 1976; Evans, 1977; Hemley et al., 1977a; Hemley et al., 1977b; Chernosky and Autio, 1979; Day and Halbach, 1979; Chernosky et al., 1985; Day et al., 1985; Berman et al., 1986; Hemingway, 1991), and other studies have addressed the related dehydration reactions (Brindley and Hayami, 1963; Wegner and Ernst, 1983; Bose and Ganguly, 1994; Pawley, 1998). To the best of my knowledge, no studies have addressed the textural development of talc under mid-crustal conditions.

Further, few experimental and field studies have examined the rates of hydration reactions of ultramafic rocks (Martin and Fyfe, 1970; Moody, 1976; Sanford, 1981; Wegner and Ernst, 1983; Janecky and Seyfried, 1986; Normand et al., 2002). These studies, taken together, suggest that: (1) the rates of the pertinent

reactions are geologically fast; (2) the rate limiting factor, in nature, is the availability of water transported by intergranular diffusion; (3) the reactions rates are initially interface controlled reactions; (4) once all nucleation sites have been occupied on the surface of the olivine, the rate becomes diffusion controlled; (5) the rate of olivine hydrolysis can be modeled by using a first order rate law. These studies all infer results from the run products *post facto*; few studies have collected data during the course of the alteration reactions. Techniques developed during this study allows for the *in situ* observation of reactions to assess reaction rates and textural development in this system.

The Bassett-type hydrothermal diamond anvil cell (HDAC), an apparatus optimized for *in situ* observation of hydrothermal reactions at crustal conditions, has been used in recent investigations to examine the rates of mineral dissolution and precipitation (montmorillonite dehydration - Huang et al., 1994; quartz dissolution - Wang et al., 2004; rutile solubility - Audétat and Keppler, 2005; Mn-doped zinc silicate precipitation - Takesue et al., 2007; rutile solubility - Manning et al., 2008; solubility and structure of Na-rich melts - Mysen, 2009). Some studies use *in situ* observation via HDAC experimentation to monitor reactant and product cross-sectional area changes to determine reaction rates. This technique, referred to as optical weighing (or the more accurately referred to here as, *in situ* mass determination), was first introduced by Matthews and Davis (1999) and provides mass estimations of objects that are below the precision of analytical balances. *In situ* mass loss determinations have been used, in conjunction with the HDAC experimentation, to estimate aqueous quartz solubility at elevated pressures and

temperatures by monitoring quartz volume changes (Wang et al., 2004; Gross, 2009). Their results matched well the experimental results of Manning (1994) up to 370 °C. Above 370 °C the abraded quartz grains begin to facet, resulting in somewhat less accurate estimations. The experiments of Gross (2009) began with euhedral grains of quartz and used crystal volume computation software, which yielded volumes of faceted minerals to determine quartz volumes. Gross (2009) confirmed the silica saturation with respect to quartz determined in the experiments of Manning (1994) and Gerya et al. (2005) at temperatures between 300 °C and 635 °C (with a reported error of 5.6%). The techniques of conventional solubility studies (i.e., methods employing weight loss or fluid extraction) and the *in situ* methods of the HDAC have considerable procedural differences but yield similar results.

Experiments conducted were designed to determine the controls of textural development and rate of olivine hydrolysis. Chemical and morphological characterization of starting materials and reaction products combined with *in situ* observation of experiments provides insight to controlling mechanisms in these reactions. The experiments of this study produced talc of varying habit which correlated to specific experimental conditions such as, fluid density, surface area of starting materials, temperature and pressure, initial rise in temperature, and changes in pressure. Fibrous growth of talc in not common and few studies have investigated its origin. The results of experiments conducted in this study suggest that the mechanism for the growth of fibrous talc is related to: (1) initial nucleation density, (2) chemical gradients, or (3) degree of supersaturation related to pressure decreases. It is unclear

if one of these factors plays a larger role or if it is necessary for all three to work in concert for the production of fibrous talc.

Experimental Methods

Starting Materials, Apparatus and Procedures

Starting materials used in this study consisted of single crystal inclusion-free Brazilian quartz, San Carlos olivine (Fo_{90}), and H_2O-HCl aqueous solutions ranging from deionized H_2O to 10 m*m* HCl solutions. Crystalline starting materials were characterized by using synchrotron x-ray diffraction at Brookhaven National Laboratory - National Synchrotron Light Source (BNL-NSLS) and energy dispersive spectroscopy on a JEOL JXA-8900 electron probe microanalyzer at the University of Maryland Nanocenter. Starting minerals were crushed, sieved (38-90 μm), cleaned in multiple deionized water and isopropyl alcohol baths, and then air-dried. Minerals used were chosen based on roundness, with ellipsoidal grains preferred (near an aspect ratio of 2:1) to allow for simpler calculation of grain volume. One quartz grain, one olivine grain (both grains having length · width · height of approximately 100 μm · 50 μm · 50 μm) and an H_2O-HCl fluid were loaded into the cylindrical chamber of the hydrothermal diamond anvil cell (diameter 250-300 μm, and height 150-250 μm). During loading, a small air bubble was retained for the purpose of ensuring liquid-vapor homogenization. The mass of the starting materials was not measured by using an analytical balance because of the small sample size. Instead, the masses of the grains were determined indirectly by the method of 'optical weighing' first developed by Matthews and Davis (1999).

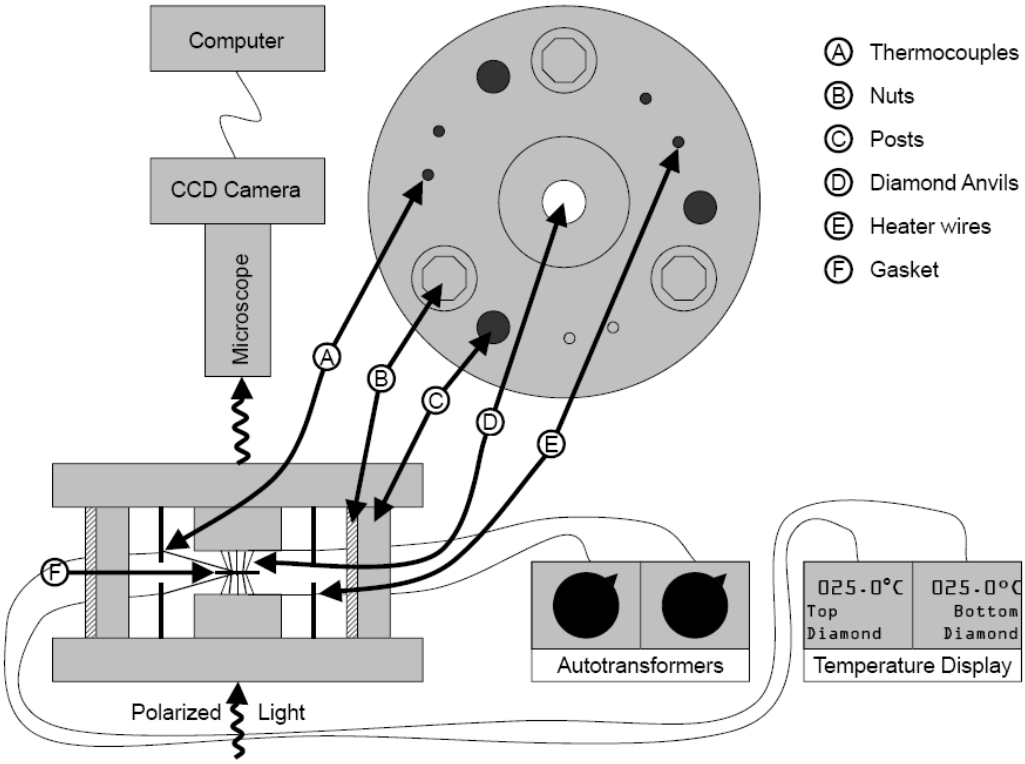

Figure 3.1 Schematic of the Bassett-type hydrothermal diamond anvil cell (HDAC). Diagram not to scale.

In the HDAC (Fig. 3.1), two diamonds with 1.0-1.5 mm culets form the bottom and top of the experimental chamber. The gasket, a 150-250 μm thick rhenium foil with a 250-300 μm diameter hole, acts as the walls of the chamber, creating a cylindrical chamber volume of ~10^7 μm^3. Each diamond was placed on a tungsten carbide seat that was wrapped with molybdenum wire (254 μm diameter) which functioned as the external resistance heaters. The tungsten carbide seats are adjustable allowing for easy alignment of the diamonds. Each molybdenum wire was connected to an autotranformer which controlled the voltage and, therefore, the current that flowed through the molybdenum wire heaters. K-type thermocouples were positioned such that the join was just below the culet face and in direct contact

with the diamond. The diamonds, molybdenum wire heaters and thermocouples were cemented in place to the tungsten carbide seat with Resbond^{TM} 940 LE cement. The two halves of the HDAC fit together along three posts. They are secured together with screws tightened to apply a uniaxial stress. Bellville springs were placed under the screws to accommodate the thermal expansion of the steel assembly during experiments. When fully assembled, a stainless steel sheath enclosed the cell and a gaseous solution of argon with 5% hydrogen continually flowed through the interior of the apparatus to avoid oxidation of heating components and diamonds.

Temperature calibrations were conducted with the cell open to the argon-hydrogen medium to determine the melting points of sodium nitrate ($NaNO_3$, T_m = 306.8 °C), cesium chloride (CsCl, T_m = 645.0 °C) and sodium chloride (NaCl, T_m = 800.5 °C) at room pressure. The use of cesium chloride allowed for a secondary calibration by using the bcc→fcc phase transition which occurs at 479 °C. Temperature calibrations indicated that observed temperatures were systematically lower by 0.85 % (measurements having a 2σ = 1.4 °C).

Pressures were determined by the initial liquid-vapor homogenization temperature and isochores for the pure water system, in conjunction with the experiment temperature (Bassett et al. 1993; Wagner and Pruss, 2002). Due to the low concentration of hydrochloric acid in the aqueous fluid, behavior of the experimental fluid was not expected to deviate significantly from that of pure water. Initial aqueous fluid densities ranged from 0.57 to 0.99 g · cm^{-3}, leading to isochoric pressure-temperature paths that lie within the envelope of reasonable geothermobars for the continental crust (Fig. 3.2). Figure 3.2 shows temperature and pressure ranges for

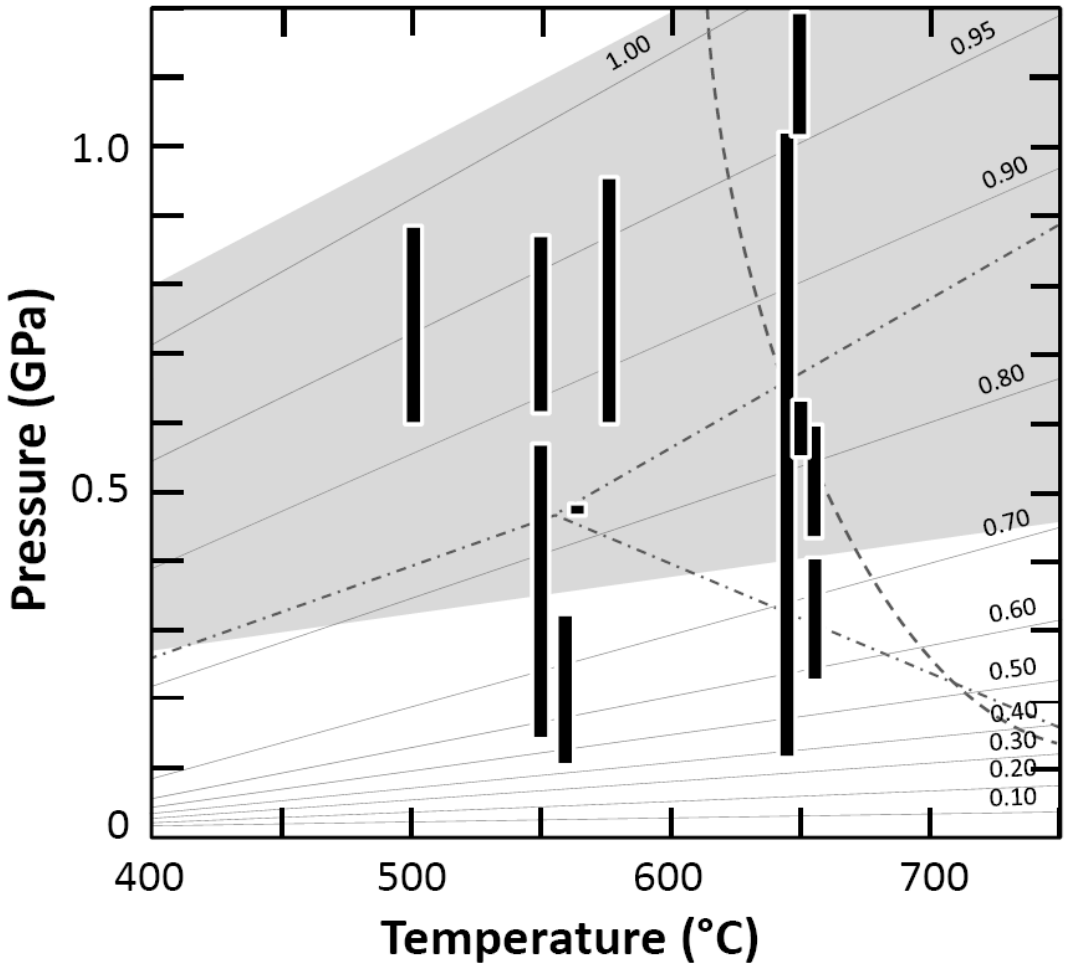

Figure 3.2 Pressure-temperature diagram showing the isochores of pure water (solid lines labeled in $g \cdot cm^{-3}$), a range of geothermobars for continental crust (shaded area), the aluminum silicate triple point with univariant equilibria (dot-dash lines), the haplogranite minimum melt (dash line) and the pressure-temperature conditions of the HDAC experiments (black blocks). Blocks are represented by the maximum temperature and the pressure as determined the prograde and retrograde isochores. The uncertainty of the experiments is narrower than the width of the boxes. Experimental summaries can be found in Table 3.2. Isochores are from Wagner and Pruss (2002), geothermal and geobaric constraints from Rudnick et al. (1998) and Stein (1995), and the minimum melt from Johannes and Holtz (1996).

Experiment	Starting Materials	Ramp-up time (sec)	Ramp-up rate (°C sec^{-1})	Max P up (MPa)	Max P down (MPa)	ΔP (MPa)	T Max / duration (°C / hrs)	Δρ (g cm^{-3})
Plate dominated experiments								
06-09-07	Ol+Qtz+0.1mMHCl	72	4.9	373	596	223	655/3.13	0.1137
07-09-07	Ol+Qtz+0.1mMHCl	30	8.2	255	547	292	550/5.92	0.1626
Run 18	Ol+Qtz+0.1mMHCl	n/a	-	607	879	272	400/1.55, 500/0.5	0.0028
Run 23	Ol+Qtz+1mMHCl	n/a	-	866	677	-189	550/2.97	-0.0528
Plate and fibers experiments								
08-23-07	Ol+Qtz+0.1mMHCl	32	8.5	311	116	-195	560/3.35	-0.2514
08-29-07	Ol+Qtz+0.1mMHCl	32.0	10.2	396	369	-27	600/4.85	-0.0164
02-24-08	Ol+Qtz+0.1mMHCl	30	7.1	180	135	-45	550/3.46	-0.0758
08-27-08	Ol+Qtz+10mMHCl	60	5.5	480	472	-8	565/2.61	-0.0037
Run 13	Ol+Qtz+0.1mMHCl	n/a	-	633	556	-77	600/1.97, 650/1.23	-0.0303
Run 11	Ol+Qtz+H2O	n/a	-	1205	1024	-181	600/1.82, 650/0.75	-0.0393
Fiber dominated experiments								
09-05-07	Ol+Qtz+H2O	71	7.6	1031	119	-912	640/2.82	-0.5643
06-10-07	Ol+Qtz+0.1mMHCl	46	6.7	228	405.7	177.7	655/3.77	0.1505

Table 3.2. Conditions and data from experiments. Experiments conducted at NSLS-BNL begin with the word 'Run.' Ramp-up time represents the time taken from the homogenization to reach the target temperature. 'Max P up' and 'Max P down' are the maximum pressure attained by the experiment as determined by the isochoric relationships of the prograde and retrograde liquid-vapor homogenizations, respectively. 'T Max' is the maximum temperature reached by the experiment, for most, the temperature was held at one temperature (target temperature = maximum temperature). Experiments that experienced a second temperature step, are denoted by a second temperature/duration (additional conditions and data can be found in Appendix B-1).

Experiment	Fluid Vol. (μm^3)	Quartz Vol. (μm^3)	Olivine Vol. (μm^3)	Ol Vol. /Qtz Vol.	Faceted Quartz	Max growth rate (mol sec^{-1})	Max growth rate (mol sec^{-1} m^{-2})
Plate dominated experiments							
06-09-07	1.71E+07 (±1.17E+05)	6.55E+05 (±9.65E+03)	6.11E+05 (±5.58E+03)	0.93	yes	8.60E-12	3.36E-05
07-09-07	1.26E+07 (±6.10E+04)	5.21E+05 (±6.47E+03)	5.07E+05 (±2.34E+03)	0.97	yes	5.16E-12	2.34E-05
Run 18	-	-	-	-	yes	-	-
Run 23	-	-	-	-	no	-	-
Plate and fibers experiments							
08-23-07	1.66E+07 (±4.97E+04)	1.17E+06 (±1.09E+04)	1.10E+06 (±7.00E+03)	0.95	no	9.24E-12	3.09E-05
08-29-07	1.59E+07 (±9.61E+04)	9.20E+05 (±1.55E+04)	7.09E+05 (±3.77E+03)	0.77	no	1.89E-11	6.92E-05
02-24-08	1.65E+07 (±1.21E+05)	1.53E+06 (±1.91E+04)	1.19E+06 (±1.10E+03)	0.78	no	1.82E-12	6.08E-06
08-27-08	1.28E+07 (±6.00E+04)	1.15E+06 (±1.13E+04)	5.30E+05 (±3.57E+03)	0.46	no	9.01E-12	3.67E-05
Run 13	-	-	-	-	yes	-	-
Run 11	-	-	-	-	yes	-	-
Fiber dominated experiments							
09-05-07	1.80E+07 (±1.11E+05)	1.07E+06 (±2.18E+04)	6.75E+05 (±4.60E+03)	0.63	no	2.59E-11	9.03E-05
06-10-07	1.25E+07 (±1.13E+05)	6.10E+05 (±8.86E+03)	6.32E+05 (±7.85E+03)	1.04	no	4.71E-11	2.10E-04

Table 3.2. (cont.) Fluid, quartz (Qtz) and olivine (Ol) volume determinations and errors are discussed in the text.

each experiment (data summarized in Table 3.2 and Appendix B-1) and their relationships to the isochores of pure water, the geothermobars, the aluminum silicate triple point (and associated univariant reactions), and the minimum melt of haplogranite.

Errors in pressure determinations can be attributed to the accuracy of the measured homogenization temperature, gasket deformation, and potential leakage of the aqueous fluid. Bassett et al. (1993) quantified gasket deformation; measured variation in the 'z' distance (i.e., between the anvil faces) as less than 0.5 %, and in the lateral directions (i.e., gasket diameter) it was found to be negligible. The minimum average deformation in the 'z' direction of the gasket in this study was determined to be ~1.0 %. The lateral deformation was determined to average ~5.0 %. In most HDAC studies, not concerned with kinetics, the aqueous fluid density is often determined after deforming the gasket by cycling the cell through significant changes in temperature before beginning the experiment. Gasket pre-indention was performed before experiments; however, cycling of the cell through significant changes in temperature is not possible in kinetics experimentation. Retrograde homogenization (i.e., the homogenization at the end of the experiment) was attained and exhibited varied density changes for each experiment.

After temperature was increased to the target temperature, most experiments were held isothermally (±3 °C) for the duration of the experiment. In three experiments, the temperature was increased approximately midway through the experiment (by 50 or 100 °C) to investigate thermal effects on the reaction rate (experimental conditions available in Table 3.2 and Appendix B-1). The amount of

time between the initial increase in temperature from the homogenization temperature to the target temperature of the experiment, or the 'ramp-up' time, was varied in some experiments to evaluate its effect on reaction product morphology. Ramp-up times were also affected by the magnitude of the temperature increase required to reach the target temperature: these values translate to a ramp-up rate from 5 to 10 °C · sec^{-1}.

Synchrotron Radiation X-ray Diffraction

A series of experiments were preformed and analyzed by *in situ* synchrotron x-ray diffraction (SR-XRD) at Brookhaven National Laboratories National Synchrotron Light Source (BNL-NSLS). Experiments were performed by using beamline X17C. During experiments, the cell was positioned with 25 µm diameter x-ray beam (wavelength = 0.4066 Å) located on the olivine grain for the duration of the experiments; this is the main location of talc growth. SR-XRD spectra were collected consecutively during the experiment at exposures of 200 seconds, with occasional longer exposures (600 sec.). Representative results from one of these experiments are displayed in Figure 3.3. Gaps in time are accounted for by the length of exposures, repositioning of the cell due to thermal expansion of the apparatus, or for visual inspection of the chamber.

The olivine starting materials were single crystals of olivine, and therefore the diffraction was manifested as points on the 2-D diffraction image (representative examples of these can be found in Appendices B-4 and C-4). In contrast, the reaction products grew in random crystallographic directions producing diffraction rings. Post-experiment reduction of the diffraction patterns was conducted by using the programs Fit-2d® and Peak Fit®. The diffraction points produced by the olivine and diamonds

were removed from the patterns before integration, leaving behind only the rings produced by the reaction products. Occasionally, rhenium peaks are present in the diffraction patterns as thermal expansion of the HDAC caused the cell to drift away from the intended site of analysis. After masking, integration, and background reduction, the resulting patterns were of talc, and the occasional rhenium.

Talc [002], [006] and [-332] hkl diffraction peaks were monitored because of their strong signal and their isolation from potentially interfering peaks. These three talc peaks were evaluated individually by determining their intensity and finding the area beneath the peak (an example of the method is graphically represented in Figure 3.4 is shown for the talc [002] peak). The peak area determinations can serve as a

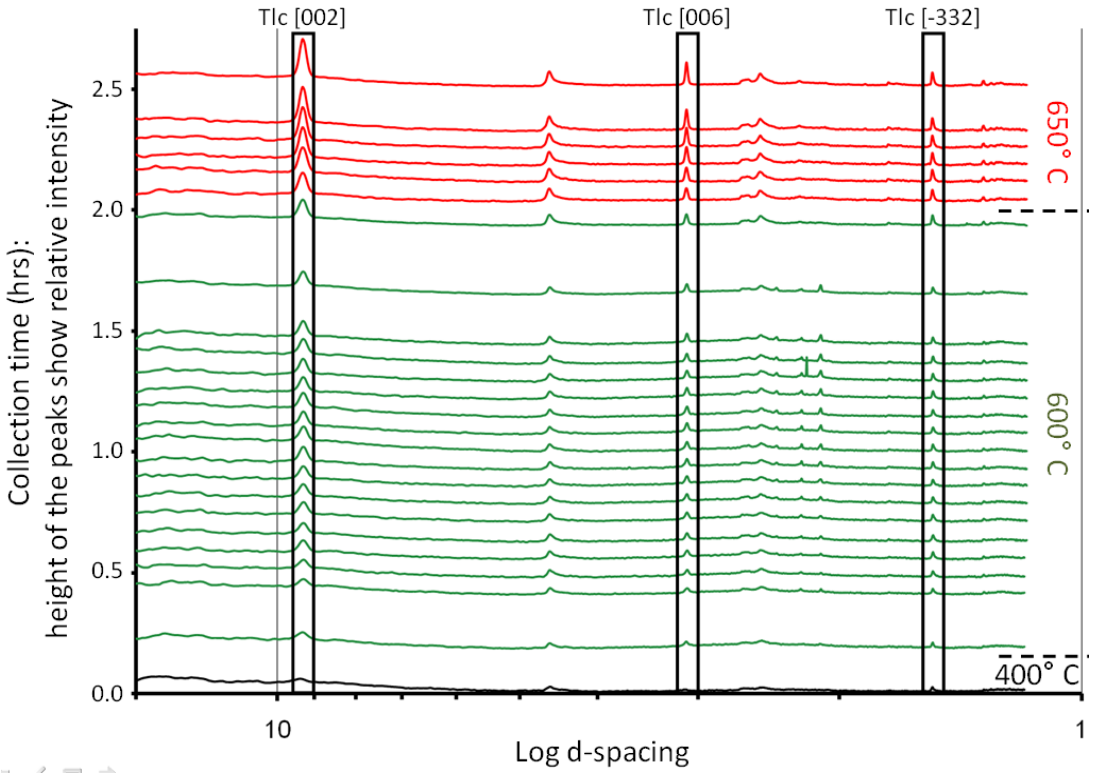

Figure 3.3. Synchrotron x-ray diffraction spectra for experiment 'Run 11' plotted as Log d-spacing versus time. Background has been reduced and diffraction points from the single crystal of olivine have been removed showing only the reaction product peaks with occasional rhenium peaks. Dashed lines on the right axis denote increases in temperature. Boxes indicate the location of peaks used for peak area analysis.

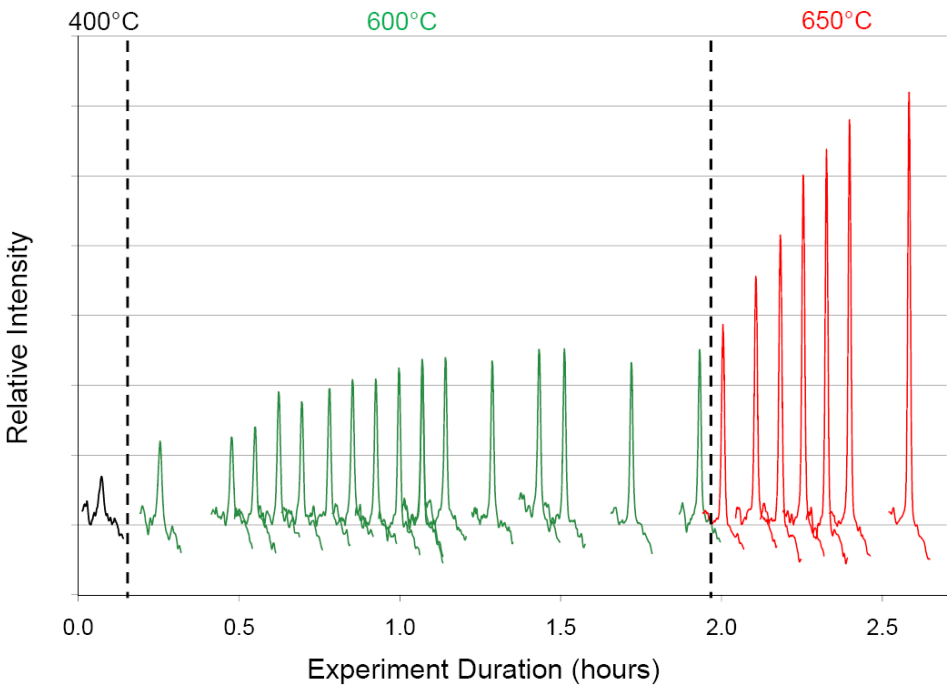

Figure 3.4. Synchrotron x-ray diffraction spectra for 'Run 11' showing only the region of d-spacing related to the talc [002] reflection (d-spacing region 11-8 Å). Relative intensity of the peaks is plotted as a function of run duration.

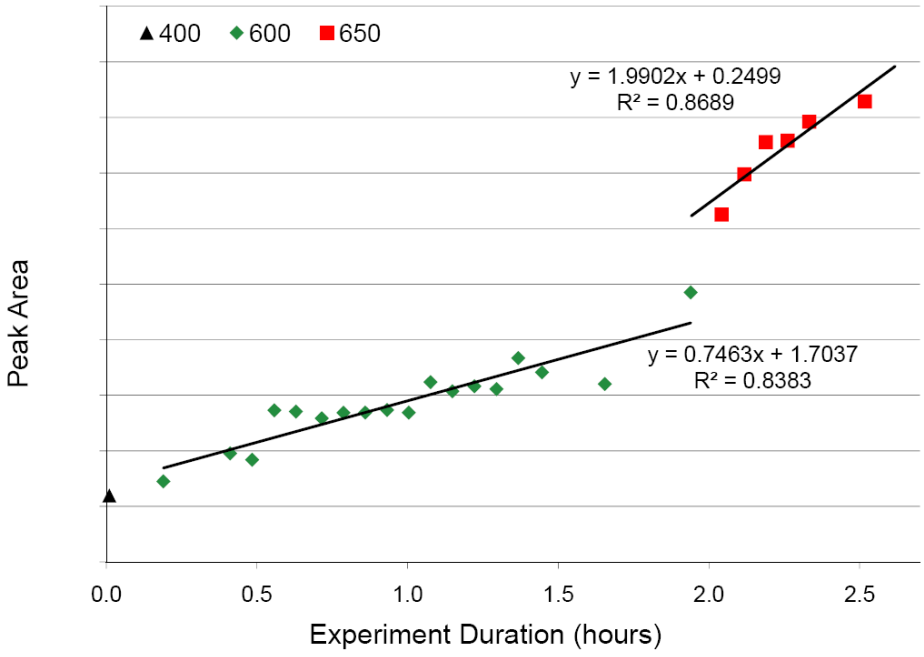

Figure 3.5. Relative peak areas from synchrotron x-ray diffraction for 'Run 11' showing the sum of peak areas underneath the talc [002], [006] and [-332] peaks as a function of run duration.

semi-quantitative proxy for phase abundance (Davidson et al., 2008). Summing the peak areas for an individual spectrum and plotting the relative peak heights versus time collected provided a qualitative view of the reaction rates (Fig. 3.5). Quantitative abundances cannot be determined by this method because analysis only monitors local changes in the path of the beam which can only capture ~ 0.5 % of the chamber volume; further, drift of the cell led to sampling of different volumes elements of the cell over time. However, using SR-XRD in conjunction with visual observation experimentation allows for *in situ* phase identification and confirmation of the lack of intermediate reaction products.

In Situ Mass Loss Determination

Experiments performed at the University of Maryland were conducted on the stage of a polarizing microscope equipped with a 1/3 inch type IT CCD camera to collect video. Windows Movie Maker® was used for post-production editing (representative videos can be found with supplementary material). Post-experiment analysis required the generation of screen capture images from the recorded experiment at known time intervals. The screen capture images were created at the onset of each temperature increase, 1 minute after the temperature increase was initiated, and then every 10 minutes throughout the experiments. Image analysis software (ImageJ®) was used to determine the area of the chamber, olivine and quartz in pixels. Pixel areas measured were then converted to areas (1 $pixel^2$ = 0.2 μm^2). Wang et al. (2004) assume a measuring error of one pixel which translates into an error in the quartz solubility of ~10 %. Cross-sectional area measurements were made in triplicate for each image. These measurements resulted in precisions ranging

from 0.3-2.0 % coefficients of variation. Measured precision led to uncertainty in quartz solubility of ~10 %, which will translate to uncertainty in the estimation of talc produced by 5-15 %, depending on size of chamber, density of fluid and other contributing errors.

As the experiments progressed, reaction products grew on the olivine and on the gasket wall, adding uncertainty to the area determinations of these objects. Measurements of the olivine grain were only determined at the beginning of the experiments; at later stages of the experiment talc production on the olivine grain surface made accurate measurements impossible. Any volume decrease of the olivine grain was assumed to be commensurate with the estimated amount of talc produced. Measurements of the chamber area were determined for the first hour of the experiment; after the first hour, the majority of gasket deformation has been accommodated and talc growth obscures measurement of the chamber area. All chamber area values after the first hour of the experiment were held constant at the last measured area value. No reaction products grew on the quartz or the diamond faces; quartz area was measured throughout the experiments. In most experiments that only produced platy talc, after some duration at elevated temperature and pressure, quartz dissolution ceased and the quartz grain began to facet. The faceting of the quartz grain led to, in some cases, an apparent increase in quartz area.

The volumetric morphology of quartz and olivine were modeled as idealized ellipsoids with aspect ratios of 2:1. Measured pixel areas were reduced to find the lengths of the two principal elliptical axes. The third dimension of the ellipsoids (the z-direction) was considered to be equal to the short axis. Only grains that exhibited an

aspect ratio of approximately 2:1:1 and exhibited ellipsoidal morphology were considered for starting materials. Given mineral densities, the estimation of grain volume from cross sectional area allowed for the determination of the mineral mass.

The volume of the chamber was determined by measuring the area of the chamber (the edge of the rhenium gasket aperture) and combining it with the known thickness of the rhenium foil (in this study, either 150 or 250 μm). The volumes of the grains are subtracted from the volume of the cell at the time of liquid-vapor homogenization, when the density of the aqueous fluid is known, to estimate the mass of the aqueous fluid. If no aqueous fluid escapes from the chamber during experimentation, the mass of the aqueous fluid will only change as hydrous phases are produced and destroyed. For example, water is consumed in the reaction:

$$5\ SiO_2 + 3\ Mg_2SiO_4 + 2\ H_2O = 2\ Mg_3Si_4O_{10}(OH)_2. \qquad \textbf{Eq. 3.1}$$

Changes in the mass of the aqueous fluid can be estimated by the estimated talc growth and the reaction stoichiometry.

The estimated mass of the aqueous fluid and the determined number of moles of silica in the aqueous fluid (as estimated by quartz volume reduction), were used to calculate the apparent molality of silica in aqueous solution at any time. The apparent molality of silica was then compared to the experimentally determined quartz solubility (Manning, 1994). All dissolved silica in excess of quartz saturation was considered to be consumed by talc growth (Eq. 3.1) allowing for the determination of the number of moles of talc produced in the reaction at any time. For every 2.5 moles of silica in excess of quartz saturation, 1 mole of talc was produced. As the reaction progressed, water and olivine were consumed. Consumption of water via talc growth

changed the density of the aqueous fluid. The density of the fluid was also affected by changes in the chamber volume. Density changes of the aqueous fluid were iteratively recalculated based on water consumption and chamber volume change. Density changes of the aqueous fluid effect the determination of pressure and quartz saturation; with these adjusted values talc growth was calculated.

Results

Synchrotron X-ray Diffraction Analysis

In all SR-XRD analyses, talc is the only detectable mineral produced during experiments. Talc diffraction peaks were visible in the first spectrum acquired at the target temperature for all experiments analyzed by SR-XRD. Monitoring changes in talc diffraction intensity permits a semi-quantitative assessment of talc growth rate.

Results from a representative experiment ('Run 11') conducted at BNL-NSLS are shown in Figures 3.3-3.5. Ramp-up times, volumes and growth rates were not determined for experiments conducted at BNL-NSLS (Table 3.2). Figure 3.3 shows 24 consecutively collected spectra from a single experiment. Results are plotted with respect to the 2θ angles (incident beam = 0.4066 Å) versus intensity but also stacked on the y-axis as a function of time collected. All peaks visible in Figure 3.3 have been identified as talc or rhenium (from the edge of the gasket as the cell moved via thermal expansion). No quartz peaks were produced during SR-XRD analysis because quartz was not within the volume of the beam. The first spectrum was collected at 400 °C and a talc signal was detected. Temperature was increased to 600 °C and the talc diffraction increases in intensity. After 120 minutes at 600 °C, the

temperature was increased by 50 °C. Increases in temperature were accompanied with increased talc growth rate; inferred by increased talc diffraction intensity.

Figure 3.4 displays the 24 spectra collected during Run 11 shown in Figure 3.3, but focusing primarily on the d-spacing region of the talc [002] peak (i.e., 8 to 11 Å; talc [002] = 9.55 Å). The peaks are plotted as intensity with respect to time. The talc [002] peak exhibited an immediate increase in intensity with each temperature increase. When the experiments were held at each temperature step, over time, the peak intensity stabilized as talc growth rate decreased. Figure 3.5 represents the sum of the peak areas for the talc [002], [006] and [-332] hkl peaks as a function of time. Data demonstrate that as a significant amount of talc is produced, the reaction rate drops at each temperature step, consistent with an approach to equilibrium. A quantitative approach to peak area analysis is not available due to uncertainties in exact beam location with respect to the reactants and products. Using SR-XRD in conjunction with HDAC experimental methods allows for relative phase abundance determinations and positive identification of phases present during reactions.

Experiment Monitored by Video Analysis

Using *in situ* mass loss determinations we are able to provide estimates of talc growth rates while monitoring the development of various textures. The experiments evaluated by this technique were held isothermally at temperatures ranging from 550 to 655 °C with maximum pressures ranging from 0.12 to 1.0 GPa. The duration of experiments ranged from 2.6 to 5.9 hours. Experimental conditions of each experiment are shown in Figure 3.2 and listed in Table 3.2 and Appendix B-1. During each experiment, the initial increase in temperature was accompanied by an

immediate decrease in quartz volume as quartz dissolves. Screen captures from representative experiments are shown in Figure 3.6 and Appendix B-2.

SR-XRD analyses demonstrate that talc is immediately produced once temperature is elevated; talc growth is also evident from the change in opacity of the olivine. The olivine, which was initially transparent, changes its opacity during the initial rise in temperature as talc nucleated on its surface. Talc nucleates on the olivine and gasket walls. After the initial decrease in apparent quartz volume, the rate of apparent volume change decreased as the aqueous fluid approached quartz saturation. The consumption of quartz corresponded to the predicted quartz saturation

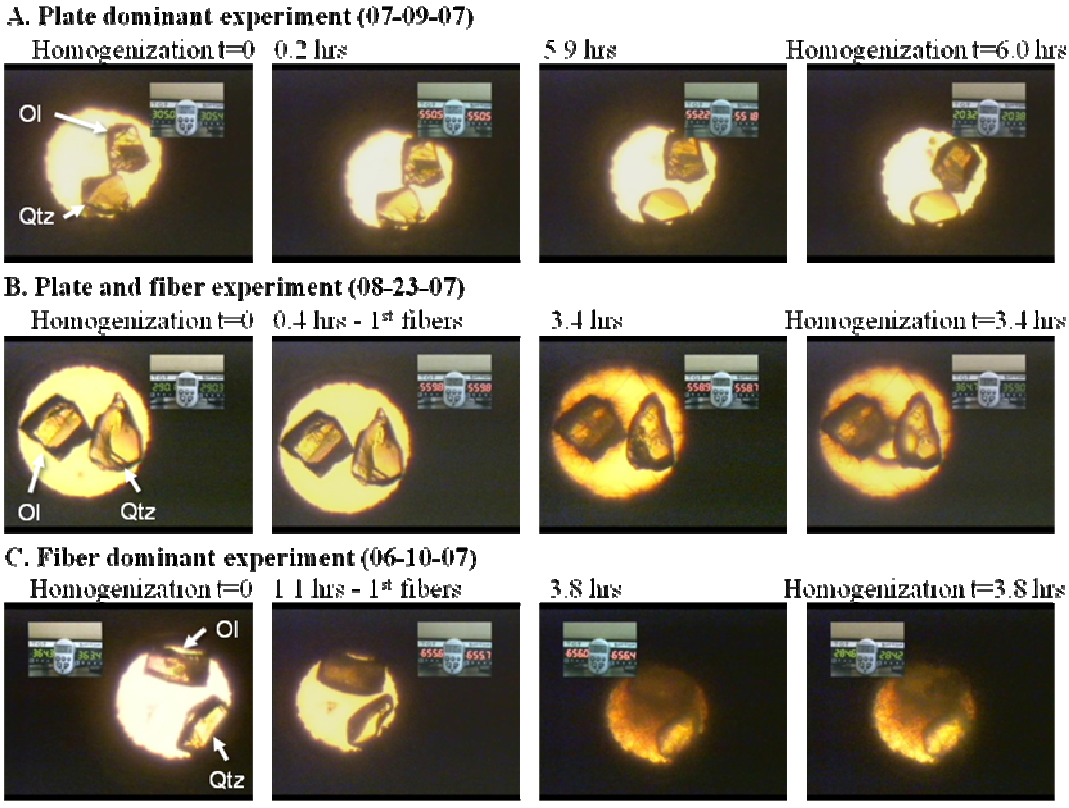

Figure 3.6. Images from videos of three experiments (A) producing only platy talc (experiment 07-09-07) (B) producing platy and fibrous talc coexisting (experiment 08-23-07) and (C) producing only fibrous talc (experiment 06-10-07). Horizontal field of view for each image is 590 µm.

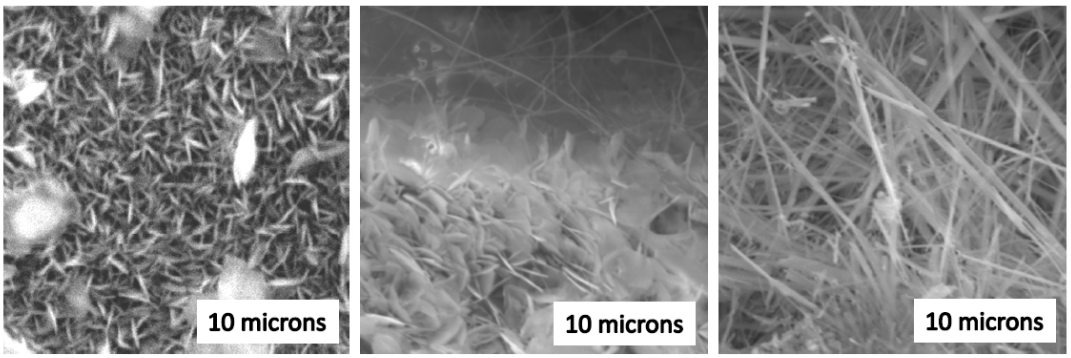

Figure 3.7. Representative secondary electron images of the three textural classes produced by the experiments: (A) platy talc, (B) both platy and fibrous talc and (C) fibrous talc.

of the aqueous fluid within the first 30 minutes of the experiments; several experiments reached quartz saturation within minutes of achieving the target temperature. In most cases, it is thought that the aqueous fluid approaches, but does not achieve, quartz saturation, because silica is continuously being removed from the aqueous fluid to produce talc. This assumption appears to hold true for all experiments except for those that produce only platy talc, where it is common for the quartz grain to facet. Fibers of talc extended into the fluid volume providing additional growth surfaces outside the initial nucleation surfaces (i.e., the surface of the olivine and gasket walls). Continued growth of talc results in continued dissolution of quartz as silica approaches quartz saturation but it is removed from the fluid via talc production.

The determination of talc growth rates is based on the apparent change in quartz volume, the estimated amount of fluid, and the predicted silica saturation with respect to quartz. Maximum talc growth rates range 10^{-11} - 10^{-13} moles per second (Table 3.2 and Appendix B-1). The surface area available for talc nucleation is

estimated by calculating the olivine and gasket wall surface areas; these were the only surfaces of talc nucleation. Knowledge of the surface area provides growth rates ranging from 10^{-5} - 10^{-6} moles per second per square meter. The growth rates determined by *in situ* mass loss are well within the limits necessary for an order of magnitude evaluation of the rates. However, the data suggest that the slower growth rates correspond to the lower temperature experiments (Fig. 3.8C). Variable concentrations of hydrochloric acid were use during this study to investigate its effects as a catalyst. Results from this study suggest that hydrochloric acid does not appear to exhibit an effect on the growth rate of talc within the limits of concentration studied.

Talc Morphology

After each experiment was completed, the run products were inspected by polarized light microscopy and by secondary electron microscopy. The reaction products have been split into three groups based on the nature of the final morphology of the talc: platy talc, fibrous talc and experiments where both platy and fibrous talc coexisted (see Figs. 3.6 and 3.7). In experiments that produced platy talc and no talc fibers, talc habit was in the form of pseudohexagonal platelets ranging from sub-micron to 8 µm lengths on the long axes of the plates, with sub-micron thicknesses (Figs. 3.6A and 3.7A). The talc plates developed with the short axis of the plate parallel, to sub-parallel, to the growth surface with random orientations on the other two mineral axes. Experiments that produced platy talc without the presence of talc fibers often exhibited a faceting of the quartz grain. As the olivine surface became armored by talc, the release rate of magnesium decreased. Further, as olivine became

chemically isolated, quartz saturation was reached. Under conditions of restricted supply of magnesium from decreased dissolution of olivine, the silica concentration in the aqueous fluid increased toward quartz saturation, allowing quartz to recrystallize.

Experiments in the 'fibrous' group exhibited only fibrous talc in post-experiment analysis. *In situ* and post-experiment images of the fibrous experiments are shown in Figures 3.6C and 3.7C. Fibers of talc grew to lengths up to 50 µm with widths ranging from tens of nanometers to 1 µm. Fibers grew with the long axis perpendicular to sub-perpendicular to the growth surface. Fibers were numerous ($\sim 10^3$ - 10^6) and commonly resulted in mats of fibers throughout the chamber. In many cases, numerous fibers appear to radiate from a common point on the growth surface. The first appearance of fibrous talc, based on visual evidence, varied from minutes to as much as an hour after reaching the target temperature. The third category included experiments that produced coexisting platy and fibrous talc. The mineral habits displayed the same morphological features previously mentioned but with fewer fibers ($\sim 10^2$ - 10^3).

Discussion

Integration of data from the experiments permits an evaluation of textural development and rate of hydrolysis of olivine in the presence of a silica-rich fluid at mid-crustal pressure and temperatures. Direct measurement of the dissolved species has not been attained because of the wealth of data available in the literature. Specific conditions resulting in varied habits of talc have been evaluated to understand their effects on the nucleation and growth during olivine hydrolysis.

Many experimental factors were examined to determine if they exhibited control of the growth rate of talc measured or its resulting morphology. Isobaric pressure levels of experiments (i.e., high or low pressure) did not appear to affect the growth rates or resulting textures of the experiments, although fluctuations in pressure brought on by density changes may exhibit control on talc textures produced (discussed below). The temperature of the isothermal experiments or the amount temperature increases in the polythermal experiments did not appear to affect the textures but higher temperatures did result in faster growth rates. In addition, the rate at which the temperature was increased, or the ramp-up time, was examined but no observable trend could be seen between rate or texture of the reactions. Both reaction rate and talc morphology were independent of the duration of the experiments.

Based on available data, the main factors that appear to contribute to the textural development and the rate of olivine hydrolysis are considered to be: the changes in aqueous fluid density (resulting from changes in pressure and silica saturation with respect to quartz), the relative surface area relationships of starting materials, the experiment's temperature and pressure, and the changes in temperature and pressure.

In the four experiments that produced only platy talc, reactions ceased after the olivine was chemically isolated from reaction by the armoring of the olivine surface by talc. This was inferred from the observed faceting of quartz in the later stages of the experiments. The attainment of quartz saturation is the simplest explanation for the faceting of quartz. SR-XRD confirms that under these conditions there was still olivine present in the charge. For experiments that produced fibrous

talc there is no evidence to suggest that the armoring became thick enough for the reactions to cease.

Under isothermal conditions, reaction rates decreased upon approaching equilibrium. The rate of mineral dissolution and precipitation increased when the temperature increased. This progression was particularly evident in experiments that included an increase in temperature (runs 11, 13 and 18). Each of these experiments was examined via SR-XRD for phase identification and to track relative phase abundance. The growth rates increased with increasing temperature which is evidenced by the rate of increase of talc peak areas (Fig. 3.5). At a given temperature, talc growth rates decrease over time, consistent with an approach to equilibrium.

Trends in the data are consistent with a generalized rate law:

$$Rate = k_o \cdot e^{\frac{-E_a}{RT}} \cdot f(\Delta\mu_r) \cdot f(c_i^{n_i}). \qquad \textbf{Eq. 3.2}$$

simplified after Lasaga (1998), where k_o is a constant, E_a is the activation energy, R is the ideal gas constant, T is the absolute temperature, $\Delta\mu_r$ is the difference in chemical potential between the products and reactants, and $f(c_i^{ni})$ is a function of the concentration of species in aqueous solution, c_i, and n_i is the order of the reaction. The increased growth rates observed during increases in temperature are commensurate with the Arrhenius term in the equation ($\exp(-E_a/RT)$). ($\Delta\mu_r$) is controlled by the difference in chemical potentials between the reactants (olivine, quartz, and water) and the products (talc). Reactions slow as olivine is increasingly isolated from the system by talc armoring.

Factors Controlling of Mineral Habit

Experiments in this study produced fibrous talc, platy talc or a combination of both textural varieties. A number of experimental conditions/parameters were examined to investigate their relative contributions to textural development. In previous studies, the presence of fibrous talc has been explained by talc pseudomorphism after other, more common, fibrous minerals such as amphiboles and chysotile (Stemple and Brindley, 1960; Ross et al., 1968; Wylie and Huggins, 1980; Ferrari and Viti, 2010). This study tests the hypotheses that fibrous talc may result from: changes in aqueous fluid density (resulting changes in pressure and silica saturation with respect to quartz), surface area relationships of starting materials, and the temperature and pressure.

Changes in aqueous fluid density occur during HDAC experiments and result in changes in internal pressure that may affect nucleation and growth. These changes in pressure are shown in Figure 3.2 as the vertical length of the black boxes and are listed in Table 3.2 and Appendix B-1. Changes in aqueous fluid density can be brought about by minor seepage of aqueous fluid out of the cell through the gasket/diamond interface, by changes in the chamber volume via gasket deformation, or by chemical reaction.

Deformation of the rhenium gaskets is visible in recorded experiments and is apparent in post-experiment analysis by light and electron microscopy. Gaskets were pre-indented to provide a proper sealing surface and to minimize gasket deformation during experiments. Homogenization temperatures showed a range of prograde and retrograde isochores from 0.99 to 0.39 g cm^{-3}. Most experiment density changes did

not exceed ~0.25 g cm^{-3} with one exception (Table 3.2 and Fig. 3.8A). Gasket deformation decreases the volume of the chamber, increasing the density of the aqueous fluid and increasing the internal pressure. Gasket relaxation due to thermal expansion of the rhenium or by response to the internal pressure is manifested by an increase in the chamber diameter, but this relaxation never exceeds the initial gasket diameter. Analysis of post-experiment videos demonstrates that the majority of gasket deformation occurs within the first 30 minutes at the target temperature of the experiment.

In experiments that decreased in density, some leakage must have occurred, but it cannot be pervasive because homogenization was achieved upon decreasing temperature. It is thought that during the initial increase in temperature some aqueous fluid may escape before the chamber is completely sealed by thermal expansion.

Most of the experiments that exhibited an increase in aqueous fluid density resulted in the development of platy talc (Fig. 3.8A). Conversely, most experiments that exhibited a decrease in aqueous fluid density produced fibrous talc. The decrease in aqueous fluid density resulted in a decrease in pressure, and therefore a decrease in the solubility of quartz in the aqueous fluid (Manning, 1994). Supersaturation with respect to quartz has been invoked to explain fibrous growth of other minerals (Zoltai, 1981). Data suggests that these conditions are favorable for the growth of talc in a fibrous habit.

Three factors appear to play a role in the production of only platy talc or the inhibition of fibrous talc. First, experiments that exhibit an increase in aqueous fluid density commonly result in the production of only platy talc (Fig. 3.8A). Second,

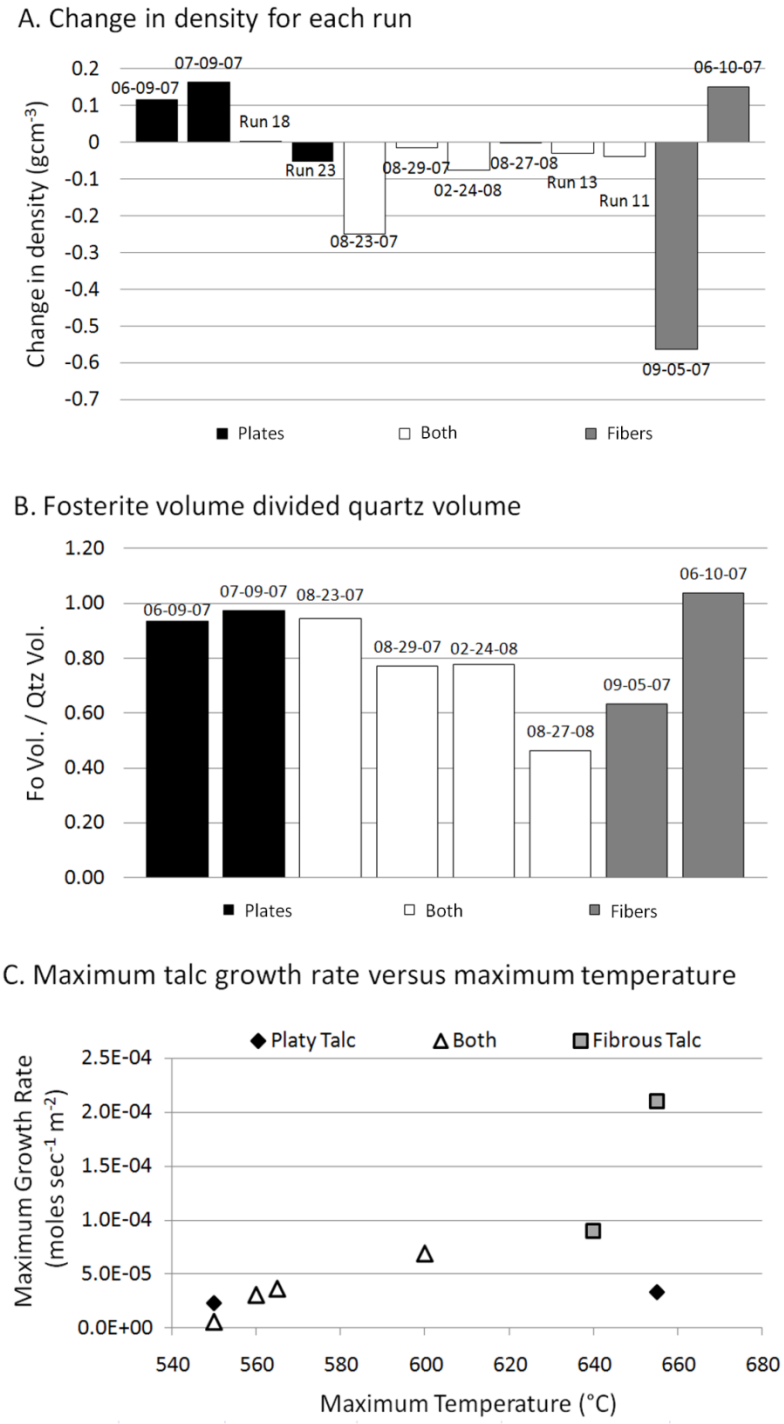

Figure 3.8. Comparison of select experimental conditions: (A) change in density for all experiments presented in this study, (B) olivine/quartz ratio (by volume), and (C) talc growth rate versus maximum experimental temperature. Note: for B and C the SR-XRD experiments do not have available data; see Table 3.2 and Appendix B-1 for all values.

when the olivine surface area is large, relative to the quartz surface area, it is more likely that only platy talc with be produced during the experiment (Fig. 3.8B). Large olivine surface areas will provide ample sites for talc nucleation in its common platy form. Third, armoring of the olivine by talc chemically isolates the olivine from the aqueous fluid, making diffusive transport of magnesium difficult. During armoring, the development of fibers is less likely because the nutrients are not available for this form of rapid growth. Some armoring of the olivine grain is exhibited by experiments producing fibrous talc, but the nature of the intergranular boundaries must allow for continued diffusive transport of magnesium. The nucleation density of fibers could be lower, relative to those experiments producing platy talc, because armoring does not appear to inhibit the diffusive transport of magnesium the same way.

Conclusions

Platy talc is a common hydrothermal alteration product of dolostone and ultramafic rocks. Rarely, it can exhibit a fibrous habit, a characteristic that has been previously explained by the replacement of fibrous amphiboles during retrograde metamorphism. This study presents experiments developed to investigate textural relationships and reaction rates of talc-producing reactions by using a hydrothermal diamond anvil cell (HDAC) apparatus. Quartz and olivine were reacted irreversibly in aqueous media (0.1 - 10 m*m* HCl) to produce fibrous talc (without any apparent amphibole precursor) as well as the more common platy talc. Experiments were run at temperatures of 400 - 655 ºC and pressures of 0.1-1.2 GPa for a duration of 2-6 hours. Vapor-liquid homogenization temperatures were recorded before and after the experiments to determine the prograde and retrograde isochores, respectively. Run

products can be separated into three groups based on morphology of the talc produced: talc plates; talc fibers; or, both.

Experimental results demonstrate that the growth of fibrous talc does not require a fibrous phase as a precursor. Talc fibers (aspect ratios $\geq$ 25:1; average lengths ~40 µm) grew on the surface of the olivine and on the gasket walls. Maximum talc growth rates of fibrous talc, determined by estimates of quartz mass loss, ranged from 10^{-11} to 10^{-13} moles per second or 10^{-5} to 10^{-6} moles per second per square meter. Experiments that produced only talc plates commonly exhibited faceting of the quartz grain, suggesting that the supply of magnesium from the dissolution of olivine was inhibited, whereas experiments producing fibrous talc (± platy talc) rarely exhibited faceting of the quartz grain.

These data appear to be consistent with the mechanism of talc fiber growth being related to initial nucleation density of talc on the respective substrate, as well as the degree of supersaturation related to pressure decreases. The large surface area of olivine (relative to quartz), an increase in the density of the aqueous fluid, and the chemical isolation of olivine by talc armoring, are all conditions that appear to favor the production of only platy talc. Decreases in aqueous fluid density (resulting changes in pressure and silica saturation with respect to quartz) and lower olivine surface areas (relative to quartz) are conditions common to experiments that produced fibrous talc. These tentative conclusions represent a consistent hypothesis that supersaturation and surface area constraints may be the main factors contributing talc morphology.

Chapter 4: Magnesite Decarbonation and Talc Growth in the Presence of Silica-rich Fluids at Mid-crustal Pressures and Temperatures

Abstract

The system MgO-SiO_2-H_2O-CO_2 (MSHC) has been investigated in order to study the irreversible decarbonation of magnesite and the subsequent production of talc in the presence of a silica-rich aqueous fluid. Hydrothermal experiments containing magnesite + quartz + water under temperatures and pressures corresponding generally from greenschist to amphibolite facies (up to 765 °C and 1 GPa) were conducted in Bassett-type hydrothermal diamond anvil cells (HDAC). One set of experiments was video recorded to provide a visual record of reaction progress; a second set of experiments was recorded via *in situ* synchrotron radiation x-ray diffraction (SR-XRD).

The starting materials consist of ellipsoidal grains of magnesite and quartz (~0.1 · 0.05 · 0.05 mm) in deionized water. The sample chamber is confined by the two diamonds (1-1.5 mm culet) and a rhenium gasket (~0.3 mm diameter hole, 0.15-0.25 mm thick). Most experiments experienced temperatures and pressures that progressively increased, step-wise, through 465 - 765 °C and 0.1 - 1 GPa, with several isothermal steps of 30-90 minutes in duration. Some experiments were returned to 465 °C before quench. Four of the twelve experiments were held isothermally at elevated temperatures. Images of digitally recorded experiments were analyzed by using *in situ* mass loss determinations to monitor apparent changes of

mineral proportions over time. *In situ* SR-XRD, provides phase identification and insight to relative abundance changes of reactants and products.

With increasing temperature, magnesite decarbonation accompanies quartz dissolution and talc precipitation. At each temperature step, reaction rates increased abruptly concomitant with the rise in temperature. Subsequently, reaction rates decreased consistent with an approach to equilibrium (Greenwood, 1967; Johannes, 1969). After being held at a constant temperature for 30-90 minutes, the temperature was increased, and the cycle was repeated. After the complete consumption of quartz, olivine began to form at the expense of magnesite and talc. In experiments that experienced a final temperature step, back down to 465 °C, precipitation of magnesite occurred. Decarbonation of magnesite added carbon dioxide to the fluid, reaching estimated concentration of 0.01 to 0.09 mole fraction.

The results of this paper suggest that if dissolved silica only approaches quartz saturation and is constantly being removed from the fluid to be incorporated in the reaction product, the quartz grain will not facet, and therefore the methods of mass loss estimations are valid. Results from experiments suggest that the mechanism for talc fiber growth is related to: (1) conditions affecting initial nucleation density (i.e., surface area of starting materials and rate of temperature increase), and (2) degree of supersaturation related to pressure decreases. It is unclear whether one factor plays a larger role than others or if they are all working, in concert to produce this unique talc habit. Some experiments produced the primary crystallization of fibrous talc, a rare habit of the mineral. Previous studies have suggested that the growth of fibrous talc is due to the pseudomorphism of preexisting fibrous minerals. Experiments in this study

demonstrate that preexisting fibrous minerals are not necessary as a precursor of fibrous talc.

Introduction

Common rocks which fall into the chemical system MgO-SiO_2-H_2O-CO_2 (MSHC) include dunites, serpentinites, steatites, ophicarbonates, and magnesium-rich carbonates. Magnesite deposits can occur as large monomineralic bodies (Aharon, 1988; Pohl, 1990; Abu-Jaber and Kimberley, 1992) taking the form of either sedimentary beds or carbonated ultramafic rocks. There has been considerable interest in magnesite over the past twenty years as magnesite could serve as a repository for atmospheric carbon dioxide (Oelkers et al., 2008), and further, it appears to be an important carbonate phase in the mantle (Katsura et al., 1991; Beillmann et al., 1993; Gillet, 1993; Isshiki et al., 2004). Additionally, upon subduction, carbonated ultramafic rocks may undergo hydrothermal alteration via silica-bearing aqueous fluids; this study addresses the reaction rates and textures that result from some of the interactions that can occur between magnesite and aqueous fluids.

The reaction of silica-bearing fluids with magnesite can result in the formation of hydrous silicate phases including talc, anthophyllite, and serpentine (Greenwood, 1967; Johannes, 1969; Aharon, 1988; Pohl, 1990; Abu-Jaber, 1992). Talc, in particular, occurs most commonly in a platy habit, but can occur, more rarely, in a fibrous habit. Experiments conducted during this study produced plates and fibers of talc. Many authors have attributed the fibrous habit of talc to the pseudomorphism of preexisting fibers such as amphibole or serpentine minerals, as evidenced by the

presence of transitional fibers (Stemple and Brindley, 1960; Ross et al., 1968; Wylie and Huggins, 1980; Sanford, 1981; Ferrari and Viti, 2010). Fibrous talc is not considered to be asbestos and the effects of fibrous talc on the human respiratory system remain uncertain (Beard et al., 2001). The primary growth of minerals with a high-aspect ratio has been ascribed to preferential growth along one crystallographic axis or the inhibition of growth along other crystallographic axes (Zoltai, 1981). Building upon the work presented in Chapter three, experiments presented will demonstrate that production of fibrous talc does not require a preexisting fibrous mineral and test hypotheses related to the conditions of formation of fibrous talc.

Previous Work

Experimental investigations of the MSHC system have determined the phase relationships at crustal conditions (Greenwood, 1967; Johannes, 1969); a compilation of phase relations is presented in Figure 4.1. These studies have examined phase equilibria with little attention paid to the textural development and reaction rates. More recently, experimental studies on magnesite have focused on its stability in the mantle, as it is thought to be the stable mantle carbonate phase (Gillet, 1993; Fiquet et al., 2002; Skorodumova et al., 2005; Takafuji et al., 2006; Litasov et al., 2008).

The experiments were conducted by using the Bassett-type hydrothermal diamond anvil cell (HDAC) to monitor *in situ* reactions in the MSHC system. Methods of *in situ* mass loss described in Chapter three have been employed in this study to determine reaction rates while simultaneously observing the development of mineral textures. The solubility of quartz in H_2O and H_2O-CO_2 fluids at crustal conditions has been determined in conventional mineral solubility studies (i.e.,

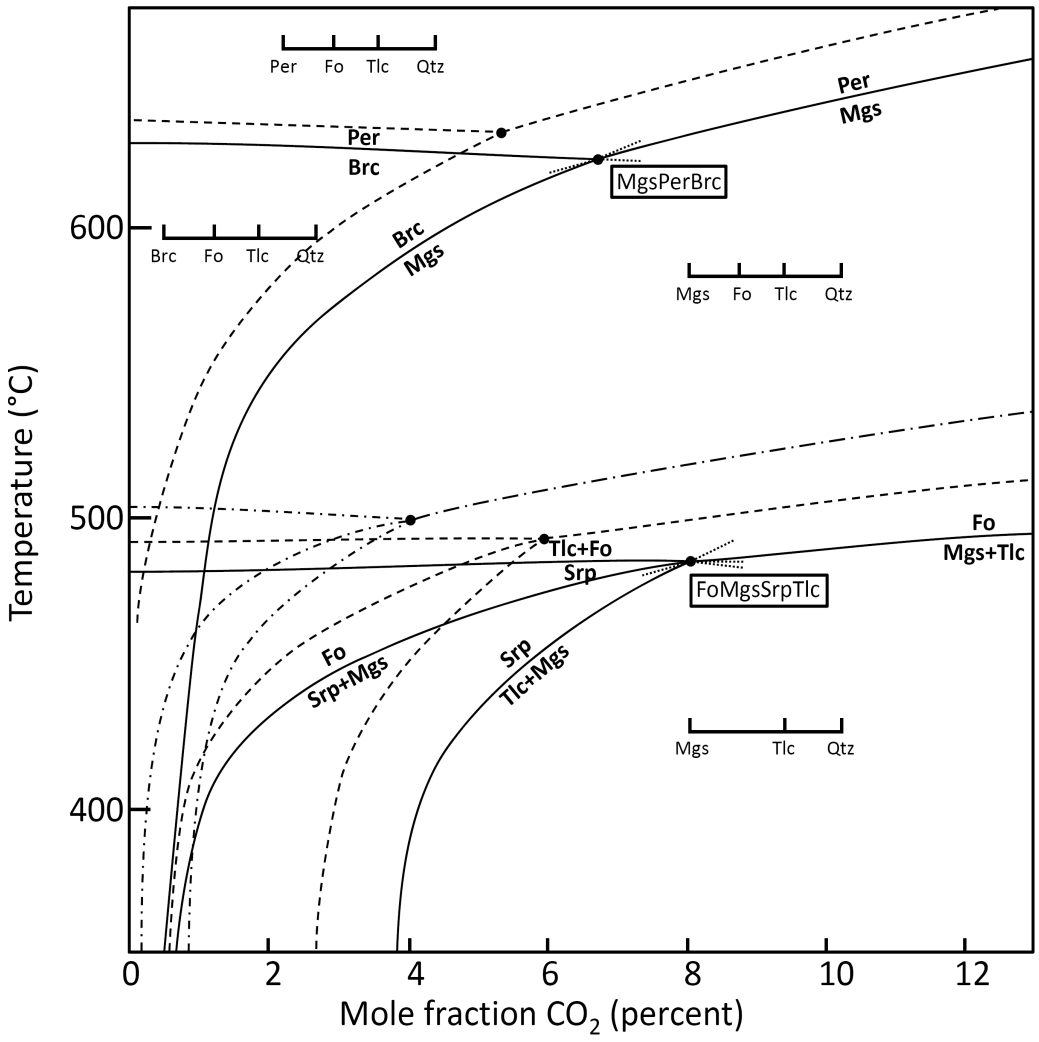

Figure 4.1. Isobaric equilibria for the system MgO-SiO_2-H_2O-CO_2 represented in the mole percent carbon dioxide vs. temperature field (solid line = 100 MPa, dash line = 200 MPa, and dash-dot = 400 MPa). Metastable extensions are shown for the 100 MPa isobaric equilibria as dotted lines. Mineral phases that can appear in divariant fields are marked on the horizontal lines with Mgs (or Brc, or Per when applicable) and Qtz as end members. Mineral phases present at invariant points are listed in boxes. Abreviations: Brc, brucite $Mg(OH)_2$; Fo, forsterite Mg_2SiO_4; Mgs, magnesite $Mg(CO)_2$; Per, periclase MgO; Qtz, quartz SiO_2; Srp, serpentine $Mg_3Si_2O_5(OH)_4$; and Tlc, talc $Mg_3Si_4O_{10}(OH)_2$. Modified after Johannes (1969) and Greenwood (1967).

methods employing weight loss or fluid extraction) (Kennedy, 1950; Manning, 1994; Aranovich and Newton, 1999; Newton and Manning, 2000; Akinfiev and Diamond, 2009). The techniques of conventional solubility studies and the *in situ* methods of the HDAC have considerable procedural differences but yield similar results.

In situ mass loss determinations have been used, in conjunction with the HDAC experimentation, to estimate quartz saturation in water at elevated pressures and temperatures by monitoring quartz volume changes (Wang et al., 2004; Gross, 2009). Both studies reported complications involving quartz volume estimates arising from quartz faceting. In the present experiments, continued growth of run products buffered the concentration of dissolved silica just below quartz saturation. If dissolved silica only approaches quartz saturation and is being removed from the aqueous fluid by reaction product precipitation, the quartz grain will not facet.

Experimental Methods

Starting Materials, Apparatus and Procedures

Experiments were conducted by using the Bassett-type hydrothermal diamond anvil cell (HDAC). The starting materials consisted of: single crystal, inclusion-free, Brazilian quartz; natural, microcrystalline magnesite from the Westvaco Mine, CA; and deionized water. Crystalline starting materials were characterized by synchrotron radiation x-ray diffraction at Brookhaven National Laboratory - National Synchrotron Light Source (BNL-NSLS) and energy dispersive spectroscopy on a JEOL JXA-8900 electron probe microanalyzer at the University of Maryland Nanocenter. Experimental set-up and procedures related to the HDAC apparatus, and mineral

selection, preparation and loading follow the convention described in Chapters two and three.

Initial pressures were determined from the prograde liquid-vapor homogenization temperature and isochores for the pure water system, in conjunction with the experiment temperature (Bassett et al. 1993; Wagner and Pruss, 2002). The decarbonation of magnesite led to the addition of carbon dioxide to the fluid; corrections are made iteratively to account for pressure changes (Bakker, 2003). Carbon dioxide estimates are determined by modeling magnesite decarbonation to compensate for the estimated amount of talc grown. Due to the low final mole fraction carbon dioxide (maximum estimated mole fraction of CO_2 = 0.09), most pressure corrections for the resulting H_2O-CO_2 fluid are small. Initial aqueous fluid densities for the experiments ranged from 0.79 to 0.92 g · cm^{-3}, leading to isochoric pressure-temperature paths that lie within the envelope of reasonable geothermobars for the continental crust (Fig. 4.2). Error in pressure determination can be attributed to the accuracy of homogenization temperature measurements and changes to the density of the aqueous fluid density brought on by gasket deformation, chemical changes to the aqueous fluid, or fluid leakage. All gaskets were pre-indented to minimize deformation during experiments. Retrograde homogenization of the fluid was attained in all experiments and all exhibited some change in density.

Most experiments (8 of 12) experienced a stepwise increase of temperature; some experiments (4 of 12) were performed isothermally (±3 °C), after a transient increase in temperature up to run conditions. In experiments with several temperature steps, each experiment was brought to an initial target temperature of 465 °C after the

initial, or prograde, liquid-vapor homogenization, and held for 60-90 minutes. Temperature was then increased, stepwise, at 50 °C intervals, until complete consumption of the quartz was achieved. Experiments were held at each temperature step for 30 minutes, with the exception of the steps at 465 and 615 °C, which were held for 60-90 minutes. The stepwise increase in temperature and the associated pressures, based on the range of prograde isochoric pathways, are graphically represented in Figure 4.2; additional experimental conditions can be found in Table

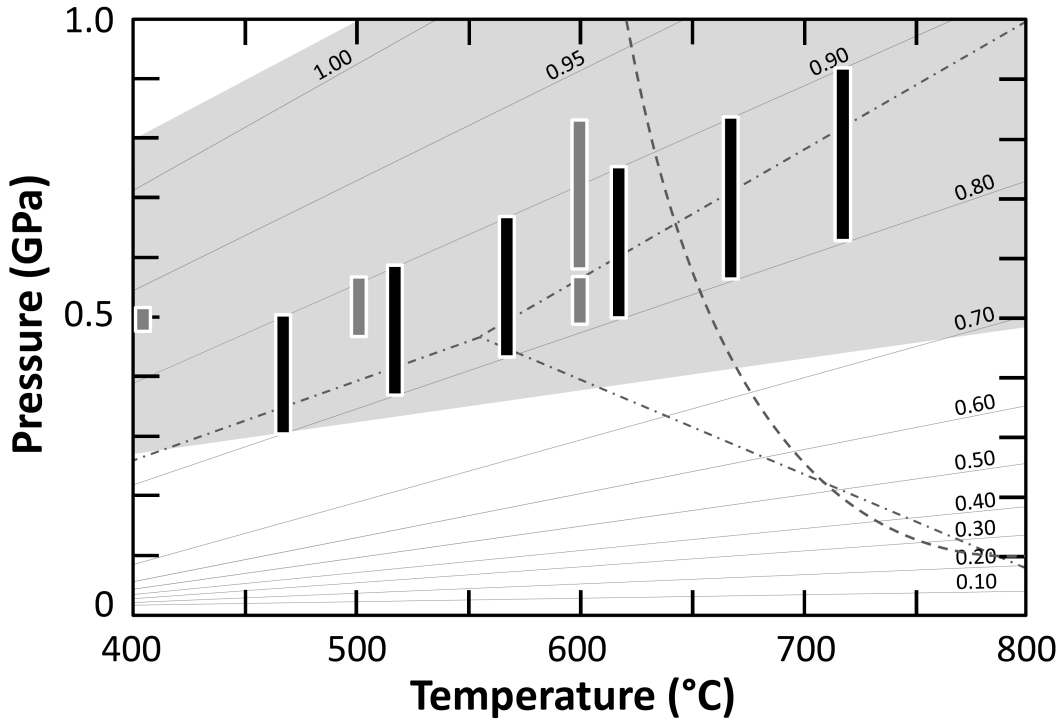

Figure 4.2. Temperature-pressure diagram showing the conditions of temperature step of experiments (black blocks) and isothermal experiments (gray blocks), pressure is based off of the liquid-vapor homogenization of experiments. Also plotted are the isochores of pure water (solid lines; Wagner and Pruss, 2002), the field of geothermobars for continental crust (shaded area; Rudnick et al., 1998; and Stein,1995), the minimum melt of a haplogranite (dashed line; Johannes and Holtz, 1996), and the aluminosilicate triple point with univariant lines (dot-dash lines).

Experiment	Ramp-up time (sec)	Ramp-up rate (°C · sec^{-1})	Max P up (MPa)	Max P down (MPa)	ΔP (MPa)	T Max (°C)	Duration (hours)	Δρ (g ·cm^{-3})	Max CO_2 (mole percent)
plate dominated									
11-04-09	30	7.7	547	297	-250	615	5.00	-0.143	4.7%
08-06-10	28	7.9	374	560	186	515	2.00	0.080	1.1%
Run 27	-	-	686	381	-305	615	5.67	-0.135	-
Run 32	-	-	466	561	95	500	3.60	0.036	-
Run 33	-	-	490	565	75	600	3.55	0.032	-
Run 37	-	-	472	516	45	400	2.45	0.015	-
fiber dominated									
08-25-09	120	2.2	857	722	-135	765	5.67	-0.045	9.2%
05-11-10	40	5.4	432	181	-251	565	2.02	-0.199	3.5%
both									
12-02-09	45	6.3	725	687	-38	615	4.00	-0.012	4.3%
03-02-10	50	5.1	627	696	69	615	3.07	0.024	4.0%
06-23-10	90	3.3	779	553	-226	615	4.10	-0.078	6.5%
Run 36	-	-	575	822	247	600	6.03	0.080	-

Table 4.1. Conditions and data from experiments in the MSHC system. Experiments conducted at NSLS-BNL begin with the word 'Run.' Ramp-up time represents the time taken from the homogenization temperature to reach the target temperature. 'Max P up' and 'Max P down' are the maximum pressure attained by the experiment as determined by the isochoric relationships of the prograde and retrograde liquid-vapor homogenizations, respectively. 'T Max' is the maximum temperature reached by the experiment.

Experiment	Fluid volume (μm^3)	Qtz volume (μm^3)	Mgs volume (μm^3)	Mgs/Qtz Surface area ratio	Qtz consumption (hours)	1st fiber appearance (hours)	Talc growth rate (moles · sec^{-1})	Talc growth rate (moles · sec^{-1} · m^{-2})
plate dominated								
11-04-09	9.45E+06 (±4.87E-03)	6.90E+05 (±2.78E-03)	2.18E+06 (±1.76E-04)	2.07	2.07	-	1.76E-11	6.47E-05
08-06-10	1.66E+07 (±3.25E-03)	2.65E+05 (±1.32E-02)	1.30E+06 (±3.66E-03)	2.33	1.90	-	7.87E-13	2.63E-06
Run 27	-	-	-	-	-	-	-	-
Run 32	-	-	-	-	-	-	-	-
Run 33	-	-	-	-	-	-	-	-
Run 37	-	-	-	-	-	-	-	-
fiber dominated								
08-25-09	9.24E+06 (±4.37E-03)	1.37E+06 (±1.80E-03)	1.20E+06 (±7.15E-03)	0.72	3.95	1.73	8.60E-12	4.03E-05
05-11-10	9.74E+06 (±3.57E-03)	4.96E+05 (±1.22E-03)	1.16E+06 (±3.29E-03)	1.37	1.95	0.43	1.78E-12	8.34E-06
both								
12-02-09	9.98E+06 (±9.23E-03)	6.67E+05 (±8.39E-02)	1.35E+06 (±2.42E-03)	1.31	3.25	2.67	4.82E-11	2.15E-04
03-02-10	9.83E+06 (±4.76E-03)	5.86E+05 (±3.82E-02)	1.52E+06 (±3.29E-03)	1.61	2.77	2.08	2.52E-12	1.07E-05
06-23-10	6.29E+06 (±5.99E-03)	7.80E+05 (±2.55E-02)	7.76E+05 (±5.75E-03)	0.68	-	2.61	9.45E-12	5.70E-05
Run 36	-	-	-	-	-	-	-	-

Table 4.1. (cont.) Data from experiments conducted at University of Maryland and analyzed by *in situ* mass loss. Fluid, quartz (Qtz) and magnesite (Mgs) volume determinations and errors are discussed in the text.

4.1. Two experiments (08-25-09 and 12-02-09) had a final thermal stage, reducing temperature to 465 °C to attain reversals. Four experiments were held isothermally through the duration of the experiment. Each of these experiments were conducted at BNL-NSLS and held at 400, 500, or 600 °C, while being analyzed by *in situ* synchrotron radiation x-ray diffraction. The amount of time during the initial temperature increase from the homogenization temperature to the initial temperature step at 465 °C, or the 'ramp-up' time, was varied in some experiments to evaluate its effect on reaction product morphology; these values, as expressed as increase rate, ranged from 2 to 8 °C sec^{-1}.

Synchrotron Radiation X-ray Diffraction

A series of experiments were performed and analyzed by *in situ* synchrotron-radiation x-ray diffraction (SR-XRD), at Brookhaven National Laboratories National Synchrotron Light Source (BNL-NSLS) at beamline X17C. During the experiments, the cell was positioned such that the 25 µm diameter x-ray beam (wavelength = 0.4066 Å) was located on the magnesite grain for the duration of the experiments. SR-XRD spectra were collected for 100 seconds exposures in a continuous fashion for the duration of the experiments. Spectra were integrated using Fit2D® and backgrounds were removed using Peak Fit®.

Once spectra had been reduced, all peaks were identified as magnesite, talc, olivine, rhenium (from the gasket), or from the plastic sealing the Ar/H atmosphere of the cell. Characteristic peaks of the reactants and products were isolated from the spectra and peak area changes were monitored. Specifically, the magnesite [018] and [116] (two overlapping peaks, d-spacing = 1.7 Å), olivine [021] (d-spacing = 3.9 Å)

and talc [002] (d-spacing = 9.3 Å) diffraction peaks were monitored because of their high intensity and their isolation from interfering peaks (quartz was never in the path of the x-ray beam). Reactants and products exhibited no preferred crystallographic orientation in the collected spectra. The peak area determinations can serve as a semi-quantitative proxy for phase abundance (Davidson et al., 2008). Higher intensities indicate an increase in phase abundance along the path of the beam. The characteristic peak areas were summed and the sum was used as a relative measure of the quantity of reactants and products. Each phase can be represented as a percent of the total signal and monitored over time to evaluate relative abundance as reactions progress.

In Situ Mass Loss Determination

Experiments performed at the University of Maryland were conducted on the stage of a polarizing microscope equipped with a 1/3" type IT CCD camera to collect video. Windows Movie Maker® was used for post-production editing (see Appendix D). Videos, resulting screen capture images, measurements of chamber and mineral dimensions, and treatment of dimension data were attained and processed by the methods described in Chapters two and three. Measurements of the magnesite grain and the chamber aperture were only determined for the early stages of experiments because as reactions progressed growth of the run products obscured measurement as described in Chapters two and three. Cross-sectional area measurements for the quartz grain were made in triplicate for each image; these measurements resulted in an average coefficient of variation of 1.13%. As quartz volume decreased and approaches complete dissolution, precision decreases. The standard deviation does not vary significantly from the previous measurements, but its relation to the

measured areas leads to larger coefficients of variation, up to 9%. Propagating the error due to replicate measurements (precision) led to errors in quartz solubility of ~10 % which will lead to errors in the estimation of talc produced of ~5 to 15 %. Errors in talc production estimates are dependent on size of chamber, density of fluid and temperature and pressure.

The volumes of the grains are subtracted from the volume of the cell at the time of liquid-vapor homogenization, when the density of the aqueous fluid is known, to estimate the mass of the aqueous fluid. If no aqueous fluid escapes from the chamber during experimentation, the mass of the aqueous fluid will only change as hydrous and carbonate phases are produced and destroyed. As talc is produced water is consumed and carbon dioxide is produced in the reaction:

$$4\ SiO_2 + 3\ MgCO_3 + H_2O = Mg_3Si_4O_{10}(OH)_2 + 3\ CO_2. \qquad \textbf{Eq. 4.1}$$

Once quartz was fully consumed, talc reacts with magnesite to produce olivine:

$$Mg_3Si_4O_{10}(OH)_2 + 5\ MgCO_3 = 4\ Mg_2SiO_4 + H_2O + 5\ CO_2. \qquad \textbf{Eq. 4.2}$$

In experiments 08-25-09 and 12-02-09, after complete destruction of the quartz, the temperature was lowered to 465 °C, and reversals were achieved (expressed by reversing the direction of Equation 4.2). Changes in the mass of the aqueous fluid can be estimated by monitoring talc growth and the reaction stoichiometry. Once the quartz grain has been consumed, any changes to the aqueous fluid chemistry can not be measured by the methods employed in this study, therefore, most experiments were halted after complete quartz dissolution.

The estimated mass of the aqueous fluid and the determined moles of silica in the aqueous fluid (as estimated by quartz size reduction), were used to calculate the

apparent molality of silica. The apparent molality of silica was then compared to the experimentally determined quartz solubility (Manning, 1994). All dissolved silica in excess of quartz saturation was considered to be consumed by talc growth (Eq. 4.1), allowing for the determination of the number of moles of talc produced in the reaction at any time. For every 4 moles of silica in excess of quartz saturation, 1 mole of talc was grown. Consumption of water and liberation of carbon dioxide via talc growth and magnesite decarbonation, respectively, will change the density and composition of the aqueous fluid. Density changes of the aqueous fluid were iteratively recalculated based on water consumption and the addition of carbon dioxide. Density and chemistry changes of the aqueous fluid effect the determination of pressure and quartz saturation limits. Adjusted values of density and mole fraction carbon dioxide allow for the calculation of a new quartz saturation, more suitable for H_2O/CO_2 aqueous fluids, using the relationships of Akinfiev and Diamond (2009).

Results

Synchrotron X-ray Diffraction Analysis

The use of SR-XRD in conjunction with HDAC experiments, allowed for the positive identification of reaction products throughout the duration of the experiments. This allowed the monitoring of relative phase abundances by evaluating peak area changes. Talc diffraction peaks were visible in the first spectrum acquired at the target temperature for all experiments analyzed by SR-XRD. As reactions progressed, talc diffraction intensified as magnesite diffraction diminished. Once the quartz grain was fully consumed, talc began to react with magnesite to produce

olivine. Monitoring changes in diffraction intensity of reactant and products permitted the qualitative analysis of the reaction rate.

Results from a representative experiment (Run 27) conducted at BNL-NSLS are displayed in Figure 4.3. This experiment experienced multiple temperature step increases, as indicated in the methods section. All peaks have been identified as being from magnesite (the primary location of analysis), talc (the initial growth product), olivine (the final growth product after the consumption of quartz), rhenium (from the edge of the gasket), and from the plastic enclosing the argon gas (5% hydrogen) atmosphere of the HDAC. To achieve an atmosphere of argon gas (5% hydrogen) openings in the HDAC must be blocked by a clear, high-temperature plastic. One main diffraction peak is produced from the plastic (~4.5 ° 2θ, d-spacing ~5.2 Å), during spectra reduction that signal is subtracted from each spectrum. During heating, the HDAC assembly expanded as the steel apparatus thermally equilibrated. Expansion of the apparatus accounts for the occasional rhenium diffraction peak. Gaps in collections present in Figure 4.3 are due to the duration of each collection, repositioning the HDAC back to the intended site of analysis or entry into the hutch for visual inspection of the cell contents. By design, quartz was excluded from the beam path. Experiments monitored with optical microscopy demonstrated that no growth occurs on the quartz grain.

Diffraction peak areas for the characteristic peaks of magnesite, olivine, and talc were monitored throughout Run 27 with results presented in Figure 4.4 as each mineral's signal as a percent of the total signal collected (i.e., the sum of magnesite [018] & [116], olivine [021], and talc [002] peak areas). At the start of Run 27 (25

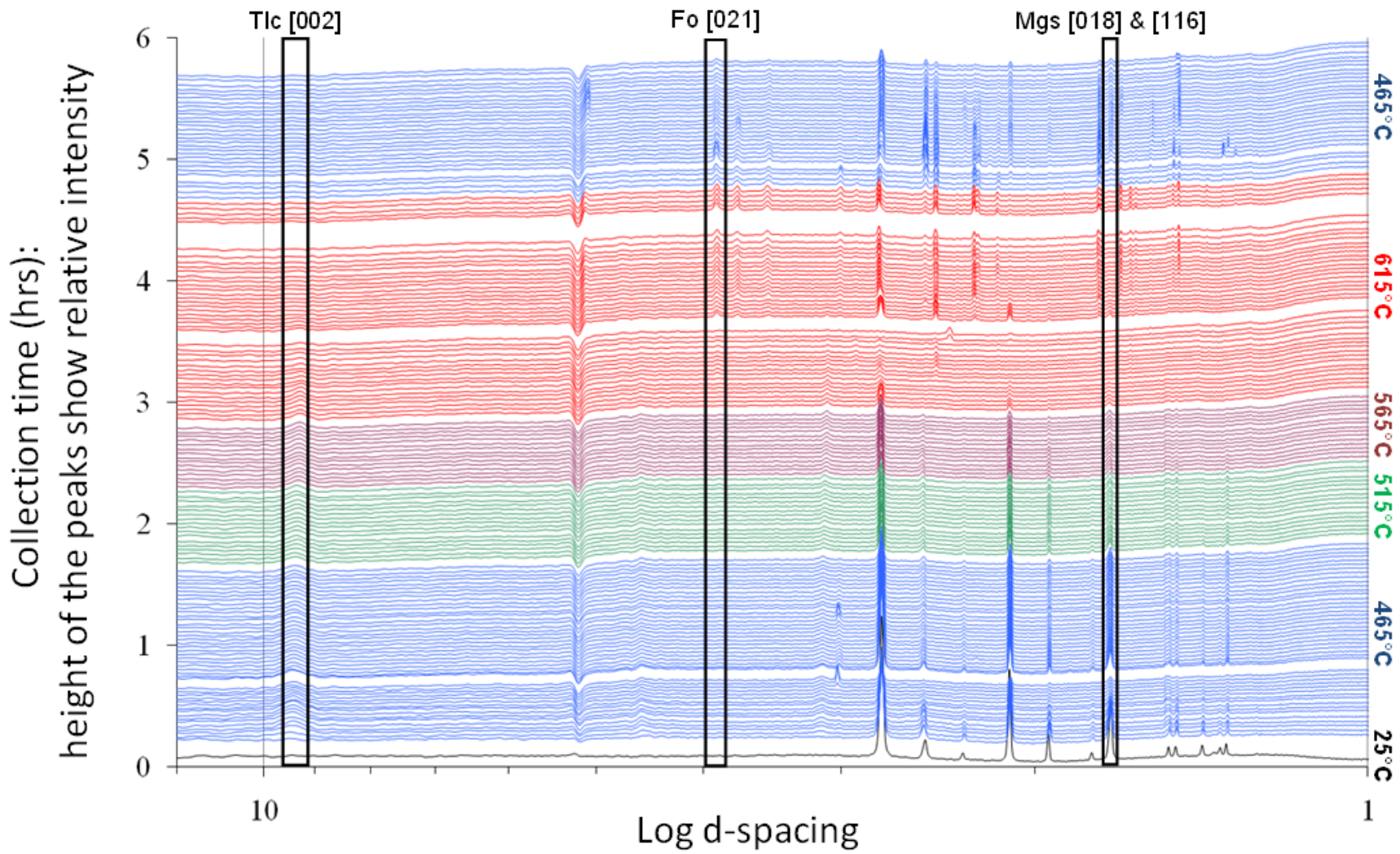
Tlc [002]
Fo [021]
Mgs [018] & [116]
Collection time (hrs):
height of the peaks show relative intensity
0
1
2
3
4
5
6
10
1
Log d-spacing
465°C
615°C
565°C
515°C
465°C
25°C

Figure 4.3. Synchrotron radiation x-ray diffraction spectra for an experiment containing magnesite + quartz + water, plotted as a function of Log d-spacing versus collection time and relative intensity. Colors denote different temperature steps as indicated on the right axis. Boxes indicate the locations of peaks used for peak area analysis.

°C), the only diffracting reactant, or product, in the path of the beam is magnesite, but because of residual background signals, other phases erroneously appear to be present in low amounts in Figure 4.4. The background reduction procedure is unable to remove all background signal from the collected spectra, so the 'peak areas' at those 2θ return results that suggest low levels of talc and olivine. The 25 μm diameter synchrotron beam can only captures 0.7% of the chamber volume. The incidence path of the beam will greatly affect the apparent relative phase abundances, as determined by peak area changes. For example, as the cell migrates due to thermal expansion, the path of incident beam will move from the center of the magnesite grain to the edge of the grain. Movement to the edge of the grain will produce a more intense signal of reaction products as the beam intersects more of the outer surface of the ellipsoidal grain where the majority of growth is occurring. When the cell is repositioned, so that the incidence path of the beam returns to the center of the magnesite grain, relative abundances appear to reset, as evidence by the flipping of the signal seen at 0.8 and 3.5 hours in Figure 4.4. Uncertainties in peak area analyses lead to only semi-quantitative conclusions about reaction rates; however, these data demonstrate relative phase abundances and provide positive identification of reactant and products throughout the experiments.

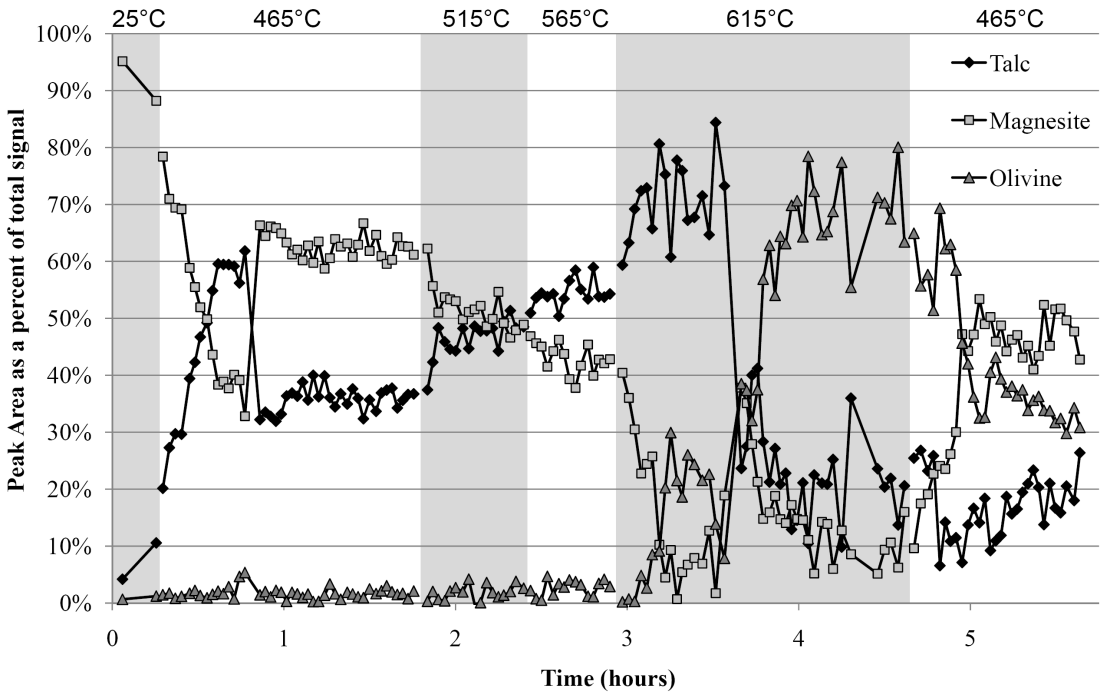

Figure 4.4. Peak area normalized to the total signal versus time for characteristic peaks of magnesite, talc, and olivine. Locations represented in Figure 4.3. See text for discussion.

Although qualitative, general trends can be identified using the analysis of SR-XRD peak area changes (Fig. 4.4). At the initial increase in temperature, magnesite signal decreases as the talc signal increases. Talc diffraction continues to intensify with more talc growth, at the expense of magnesite (plus quartz and water), until the talc signal reaches ~70% of the phase abundance relative to magnesite and olivine. As talc reaches ~70% abundance, the olivine signal begins to rise, and all quartz is consumed at this stage of the experiment. At 615ºC, with quartz no longer present, and the relative abundance of olivine rises at the expense talc and magnesite. The last temperature step of the experiment, at 465ºC, olivine is no longer stable and talc and magnesite are created at the expense of olivine.

Experiments Monitored by Video Analysis

Textural development of talc was observed and growth rates were determined by using *in situ* mass loss determination techniques. The experiments as part of this study experienced a stepwise increase in temperature, ranging from 465 to 765 °C with maximum pressures ranging from 0.43 to 0.86 GPa. The durations of the experiments ranged from 2.0 to 5.6 hours. Quartz was completely consumed in these experiments with one exception (experiment 06-23-10). Some experiments were left at elevated temperature and pressure after complete quartz consumption in order to investigate olivine growth textures (experiments 08-25-09, 11-04-09, and 12-02-09). Other experiments were terminated immediately following complete quartz consumption to preserve talc textures (experiments 03-02-09, 05-11-09, and 08-06-10). Several experiments experienced a final temperature decrease down to 465 °C in an attempt to evaluate back reactions (experiments 08-25-09 and 11-04-09). Experimental conditions can be found in Figure 4.2 and Table 4.1. Screen captures and secondary electron images from representative experiments are shown in Figure 4.5 (also Appendices C-2 and C-3).

After the prograde liquid-vapor homogenization was determined, experiments were brought to the first temperature step (465 °C) and held isothermally for 60-90 min. The initial increase in temperature was accompanied by an immediate decrease in quartz volume as it dissolves into the aqueous fluid. Occasionally, loading of the starting materials would result in some contact between the magnesite and quartz grains, producing a dusting of microcrystalline magnesite on the surface of the quartz. The magnesite dusting on the surface of the quartz grain is immediately shed by the

A. Plate dominated (experiment 11-04-09)

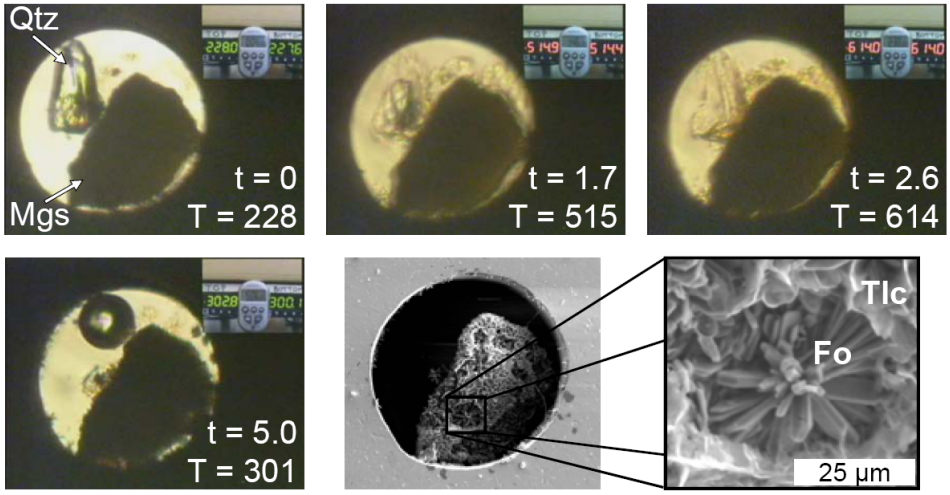

B. Fiber dominated (experiment 08-25-09)

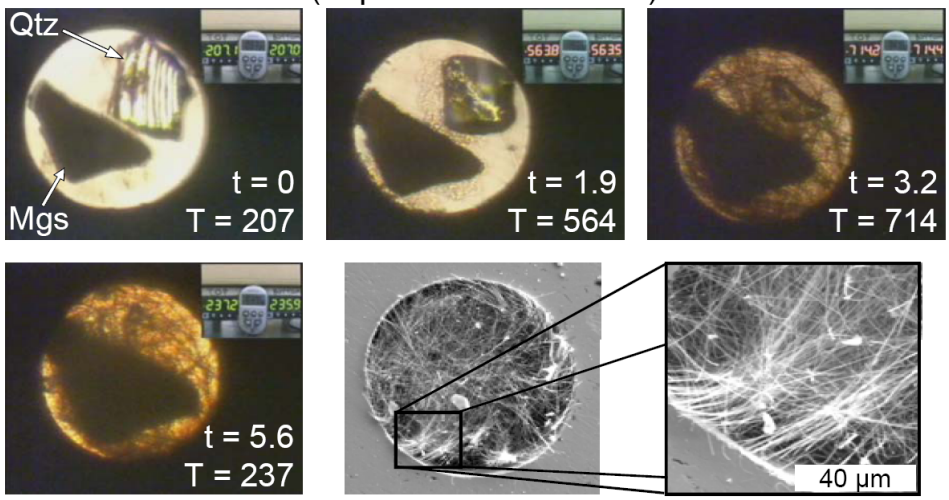

C. Both plates and fibers (experiment 12-02-09)

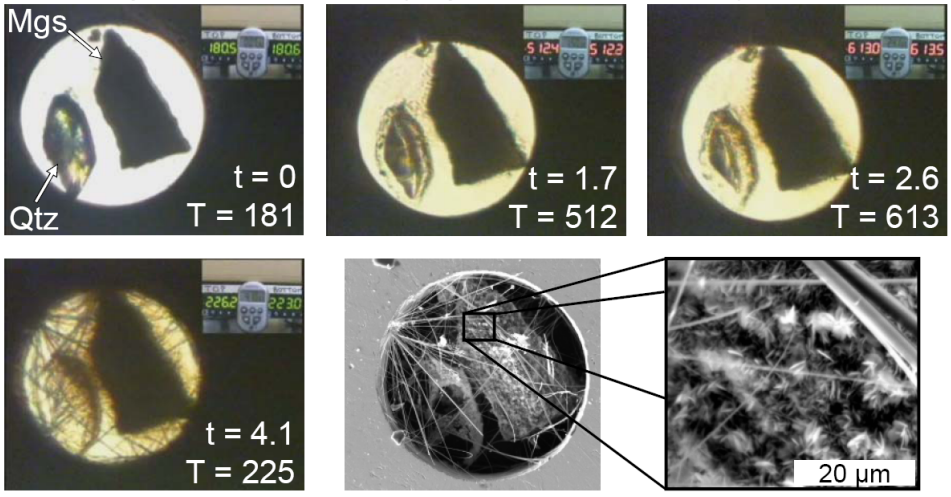

Figure 4.5. Screen capture images from videos of three experiments with secondary electron images of run products. The chamber aperture in each image is ~310 µm in diameter. All experiments experienced a stepwise increase in temperature and pressure (see Table 4.1 and Appendix C-1). Time (hrs) and temperature (°C) is listed in the bottom right of each screen capture image. **A.** Experiment producing only talc of a platy habit (experiment 11-04-09): this experiment was held at elevated conditions for 3 hours after the quartz grain had been consumed. The development of olivine florets can be seen the secondary electron images. **B.** experiment producing only fibrous talc (experiment 08-25-09): the dense mat of fibrous talc obscures the relic magnesite grain in secondary electron images, no detectable talc plates are present. **C.** experiment producing both talc plates and fibers (experiment 12-02-09): halo produced by quartz-magnesite contact during loading is evident in images. Post experiment analysis of the haloes suggests they were completely converted to plates of talc.

quartz as rapid quartz dissolution begins at the first temperature step. Figures 4.5 A and C show the effect of the dusting, which appear as 'haloes' surrounding the quartz. Imaging of run products suggests the 'dusting' is completely converted to talc. There is no direct correlation between the presence of magnesite dustings and the rate of reaction or the development of particular mineral habits.

The magnitude of quartz volume decrease suggests that quartz readily dissolved into the aqueous fluid and the dissolved silica approached quartz saturation within minutes. Figure 4.6 presents the dissolved silica molality in excess of quartz saturation and talc growth rates, with respect to time and temperature, for three representative experiments. These calculations demonstrate that dissolved silica in the aqueous fluid is immediately in excess of quartz saturation upon reaching the first temperature step at 465 °C, indicating that talc growth is immediate. This observation is in agreement with the presence of talc diffraction peaks in SR-XRD in spectra collected during the first 100 seconds at the first temperature step. Given that silica is likely to be removed from aqueous solution upon the production of talc, the silica

A. Experiment 11-04-09 (plate dominated)

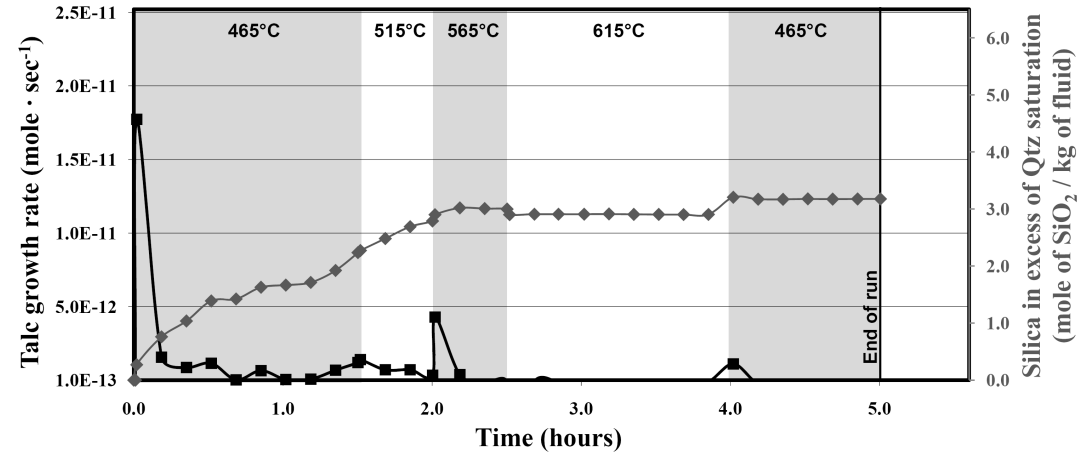

B. Experiment 08-25-09 (fiber dominated)

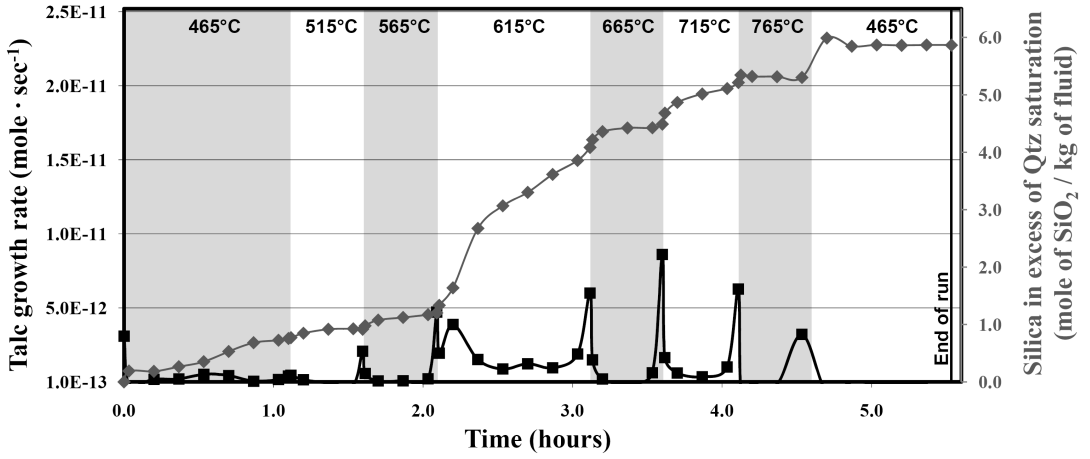

C. Experiment 12-02-09 (both plates and fibers present)

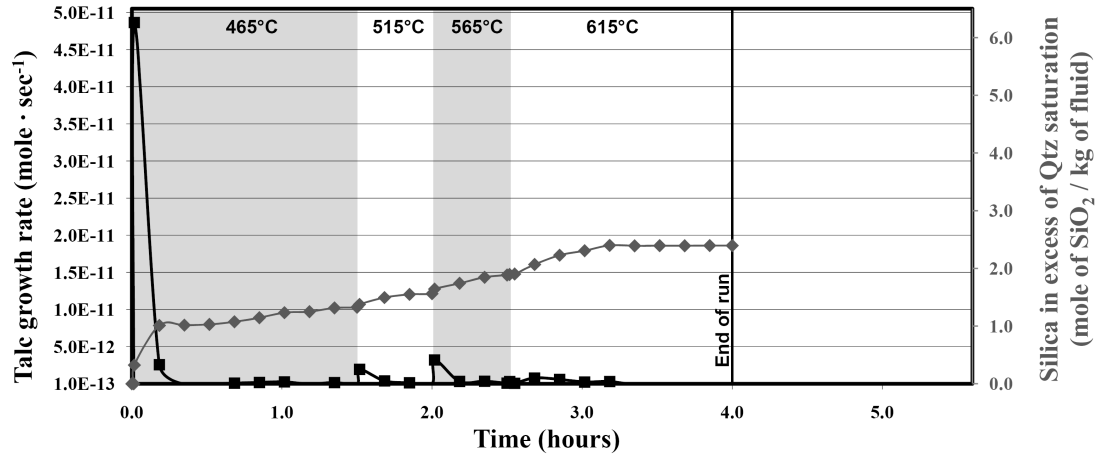

Figure 4.6. *In situ* mass loss data for three experiments: **A.** Experiment 11-04-09 produced platy without the presence of fibers, **B.** Experiment 08-25-09 produced fibrous talc without the presence of plates, and **C.** Experiment 12-02-09 produced both platy and fibrous talc. The x-axis is time (hours), the left y-axis is talc growth rate (moles sec^{-1}) represented by the square symbols, the right y-axis is the apparent molality of silica in excess of quartz saturation as measured by quartz volume changes. The mass of the fluid is estimated using the prograde density of the fluid. Shaded area segregate different temperature steps with respect to time with a solid vertical line denoting the end of the experimental run. Photomicrographs and secondary electron images for these experiments can be found in Figure 4.5, and Appendices C-2 and C-3.

concentration is probably maintained just below quartz saturation, as evidenced by continued quartz dissolution. Talc nucleates on the magnesite and gasket walls. With each step increase in temperature, an immediate reduction in quartz volume was observed as talc grew in the experiment (see Fig. 4.6). The rate of quartz volume change decreased as a function of reaction progress at a given temperature step interval. After the prescribed duration at the temperature step, the temperature was increased to the next temperature step and the cycle of quartz dissolution began again as a new, higher quartz saturation was approached and rapid thermally activated reaction progressed. The continued growth of talc at the expense of magnesite, continued until the quartz grain was completely consumed.

As reactions progressed, water and magnesite were consumed in the production of talc. For each mole of talc grown, one mole of water was consumed and three moles of carbon dioxide entered the fluid. The fluid composition was, therefore, continually changing. Estimations of the carbon dioxide content of the aqueous fluid were based on the estimations of talc grown and the required amount of magnesite destruction. As the aqueous fluid increased in carbon dioxide content, the pressure change according to the H_2O-CO_2 equations of state (Bakker, 2003). Knowing the

mole fraction of carbon dioxide in the fluid, the new density of aqueous fluid and the new pressure allowed for the determination of a corrected value of quartz saturation (Akinfiev and Diamond, 2009). Increased carbon dioxide concentration of the aqueous fluid increases the solubility of silica with respect to quartz. The calculated mole fraction of carbon dioxide in the aqueous fluid did not exceed 0.092. The magnitude of changes in density, pressure and quartz saturation due to the presence of carbon dioxide were highly dependent on the initial density of the aqueous fluid, the peak conditions reached, and the amount of quartz consumed during talc production and, therefore, were unique to each experiment (Fig. 4.1). Once the quartz was consumed, talc and magnesite began to react to produced olivine. Without quartz, reaction progress could no longer be monitored.

Iterative calculations that model the behavior of mineral/fluid interactions in the HDAC allowed for determination of the amount of talc growth throughout experiments. Talc growth rates were calculated from the rate of destruction of quartz and the appropriate stoichiometric coefficients (Fig. 4.6). Calculated talc growth rates in these experiments range from 10^{-11} to10^{-13} moles per second. At each temperature step increase, a spike in the growth rate was followed by a decrease in growth rate as the reaction proceeded isothermally. Talc growth was restricted to the surface of the magnesite grain and the walls of the gasket. Maximum talc growth rates in these experiments range from 10^{-4} to10^{-6} mole sec^{-1} m^{-2}, where the area was taken as the area of the substrate upon which the crystals grew. Talc growth was also observed on the small magnesite fragments, but such growth was unaccounted for by these measurements. Growth of talc occurs without any apparent intermediate products,

based on the results of the experiments conducted at BNL-NSLS wherein reaction progress was followed by way of in-situ x-ray diffraction

Morphology of Reaction Products

After each experiment was completed, the run products were inspected by polarized light microscopy and scanning electron microscopy. The reaction products have been split into three groups based on the nature of the final morphology of the talc in the experimental charge: platy talc, fibrous talc and experiments where both platy and fibrous talc coexisted (Fig. 4.5, and Appendices C-2 and C-3). In experiments that produced talc plates without talc fibers, talc was in the form of pseudohexagonal platelets ranging from less than a micrometer to 8 µm lengths along the long axis, with sub-micrometer thicknesses (Fig. 4.5A). The talc platelets developed with the short axis parallel to sub-parallel, to the growth surface with random orientations on the other mineral axes.

Experiments in the 'fibrous' group exhibited only fibrous talc. *In situ* and post-experiment images of the fibrous talc experiments are shown in Figure 4.5B. Fibers of talc grew to lengths up to 50 µm with widths ranging from tens of nanometers to 1 µm. Fibers grow with the long axis perpendicular to sub-perpendicular to the growth surface. Fibers grown were numerous (~10^3 - 10^6) and commonly resulted in mats of fibers throughout the chamber radiating from the magnesite grain and the gasket walls. Secondary electron images in Figure 4.5B display a mat of talc fibers so thick that the relic magnesite grain is difficult to identify. The first 'visible' appearance of fibrous talc, based on *in situ* optical microscopy, varied from 0.5 hrs to as much as 2.7 hours after the initial rise in

temperature. Previous evidence discussed demonstrates that talc growth was initiated immediately upon reaching the target temperature. The morphology of the talc during nucleation is uncertain; if platy talc were initially present in the experiments of the fibrous talc group, it was either overgrown or destroyed. The nature of talc nuclei is not detectable by the methods employed in this study. The third group of experiments is experiments that produced both platy and fibrous talc coexisting with each other (Fig. 4.5C). The mineral habits displayed the same morphological features previously mentioned but with fewer fibers (~10^2 - 10^3).

Experiments held at elevated temperatures and pressures after the complete consumption of quartz produced forsterite. Forsterite was identified by SR-XRD and was present in the secondary electron image as orthorhombic tablets radiating from points in 'floret' morphology (Fig. 4.5A). Multiple florets comprising forsterite crystals are present, presumably nucleating at a single point, consuming talc and magnesite, and producing both water and carbon dioxide as a by-product (Eq. 4.2). The tablets of forsterite reach maximum dimensions up to 25 microns in length and 8 microns in thickness.

Experiments 08-25-09, 11-04-09, and Run 27 experienced a final, reduced temperature step at 465 °C, and crystallized magnesite, consistent with the phase relations in Figure 4.1 (Greenwood, 1967; Johannes, 1969). This regenerated magnesite crystallized as equally distributed, euhedral rhombohedra, most noticeably in the secondary electron image of Run 27 (Appendix C-3). Large (~25 µm) magnesite rhombohedra were present in Run 27, in experiments 08-25-09, 11-04-09, magnesite was sparse and the few located are on the micron scale.

Discussion

Factors Controlling Mineral Habit

Experiments in this study have produced fibrous talc, platy talc or both. Platy talc is, by far, the most common form of the mineral; talc rarely grows in a fibrous habit. In previous studies, the presence of fibrous talc has been explained by talc pseudomorphism after other, more common, fibrous minerals such as amphibole and serpentine (Stemple and Brindley, 1960; Ross et al., 1968; Wylie and Huggins, 1980; Sanford, 1982). In this study, the hypotheses are tested that fibrous talc may result from: changes in fluid density (resulting changes in pressure and silica saturation with respect to quartz); relative surface area of starting materials; experiment temperature; the effect of carbon dioxide pressure; and the rate of the initial temperature increase.

Changes in fluid density occur during HDAC experiments and result in changes in internal pressure that may affect nucleation and growth. Changes in fluid density are brought about by: minor seepage of fluid out of the cell through the gasket/diamond interface; changes in the chamber volume via gasket deformation; or, chemical reaction. Prograde isochores of experiments ranged in density from 0.799 to 0.923 $g \cdot cm^{-3}$. Attainment of retrograde liquid-vapor homogenization revealed a change in the density of the aqueous fluid; retrograde homogenization values ranged from 0.599 to 0.938 $g \cdot cm^{-3}$. Experiments with density changes greater than 0.2 $g \cdot cm^{-3}$ have not been considered here due to their excessive loss of fluid.

Gaskets are pre-indented to provide a proper sealing surface and to minimize gasket deformation during experiments. However, gasket deformation is exhibited by all runs and commonly occurs as a 5-6 % decrease in chamber volume within the first

30 minutes of each experiment and then stabilizes. This volume change will result in a density change. In these experiments the average density was approximately 0.85 g $\cdot$ cm^{-3}, and the density change due to a volume decrease of 5-6 % represents an increase in density by approximately 5.5-6.5 %.

Chemical reactions can also be responsible for fluid density change. For each mole of talc grown, one mole of water is removed from the fluid and three moles of carbon dioxide enters the fluid. Also, in experiments that produced olivine, for every mole of olivine grown, 0.25 moles of water and 1.25 moles of carbon dioxide enter the fluid. Mass balance predicts a higher density fluid at the end of the experiment; this is not the case in many experiments. In some experiments, the density decreased with time, and therefore some leakage must have occurred but can not have been extensive because homogenization was achieved upon decreasing temperature at the end of the experiment.

Most experiments that resulted in fluid density increases generally failed to develop fibrous talc. Conversely, most experiments that resulted in fluid density decreases most often produced fibrous talc. The relationship of aqueous fluid density change to the talc morphology was also reported by the study on the carbon dioxide-free system (Chapter three), with respect to olivine-quartz-water reactions under similar conditions. Decreases in the density of the aqueous fluid will lead to decreases in the solubility of quartz, producing a supersaturated fluid; a condition often leading to the growth of fibrous minerals (Zoltai, 1981). Not all of the experiments are consistent with this hypothesis concerning the relationship between a decrease in aqueous fluid density and the production of fibers (Fig. 4.7A and Table 4.1); but this

study tentatively concludes from these results, that supersaturation explains at least some of the occurrences of fiber growth. That is, density changes may be one of a number of factors potentially responsible for controlling talc mineral habit.

Based on trend in the available data, three factors appear to play a role controlling the habit of talc. Experiments that exhibited an increase in fluid density commonly resulted in the production of only platy talc (Fig. 4.7A). The second factor inhibiting fiber growth (or promoting platy growth) is the relative magnesite surface area with respect to quartz. When the magnesite surface area is large, relative to quartz, it is more likely that only platy talc will be produced (Fig. 4.7B). The third factor is the rate of temperature increase from the homogenization temperature to the first temperature step, or the ramp-up rate. Experiments producing only platy talc have had faster ramp-up times than experiments producing fibrous talc (Fig. 4.7C).

Both surface area and ramp-up time may influence the textural development of talc although their effects can not be discriminated from the data presented here. Larger magnesite surface areas may provide sites for talc nucleation during the initial rise in temperature. Apparently, when the proportion of magnesite surface area, relative to the volume of the system, is below some critical value, the combined rate of nucleation and growth of fibers is greater than the rate of growth of the talc plates. For fast ramp-up times, the starting materials will spend less time in any given arbitrary temperature interval, and because nucleation rate is temperature dependent, fewer nuclei will be produced compared to slower ramp-up times. How this will affect the nucleation and growth of platy versus fibrous talc is unclear. Finally, it should be noted, that all run product growth in these experiments has been into ‘open

A.

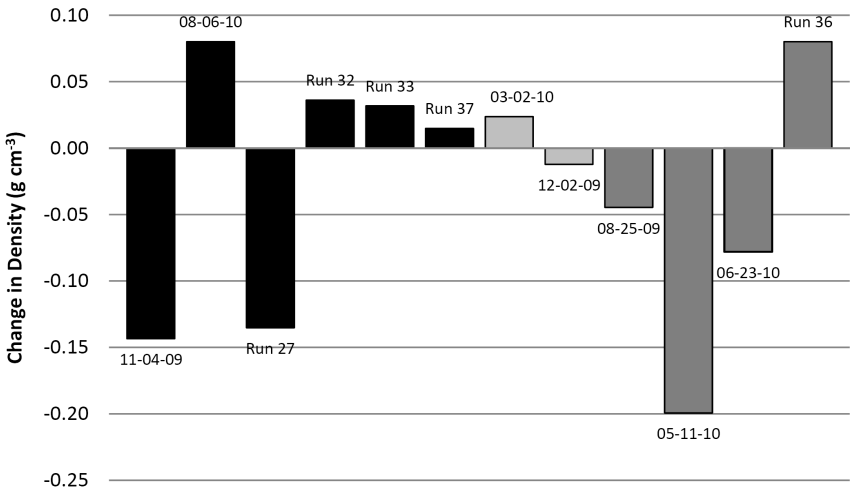
Change in Density (g cm-3)
0.10
0.05
0.00
-0.05
-0.10
-0.15
-0.20
-0.25
08-06-10
Run 32
Run 33
Run 37
03-02-10
Run 36
12-02-09
08-25-09
06-23-10
11-04-09
Run 27
05-11-10

B.

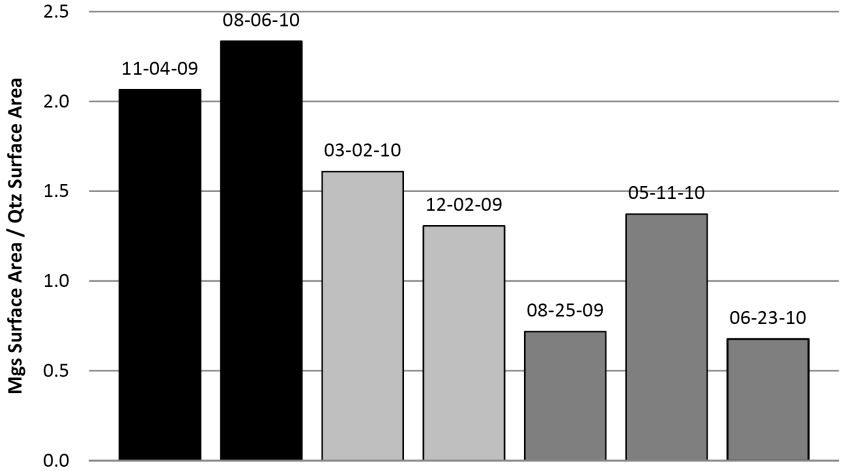
Mgs Surface Area / Qtz Surface Area
2.5
2.0
1.5
1.0
0.5
0.0
11-04-09
08-06-10
03-02-10
12-02-09
08-25-09
05-11-10
06-23-10

C.

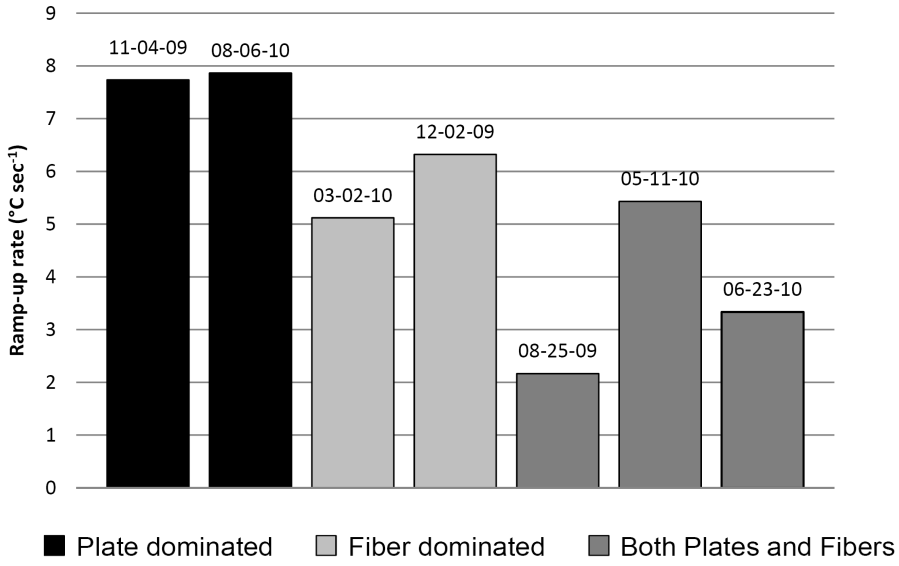
Ramp-up rate (°C sec-1)
9
8
7
6
5
4
3
2
1
0
11-04-09
08-06-10
03-02-10
12-02-09
08-25-09
05-11-10
06-23-10
Plate dominated
Fiber dominated
Both Plates and Fibers

Figure 4.7. Comparison of experimental conditions for: **A.** change in density (based on difference in prograde and retrograde liquid-vapor homogenization isochores); **B.** magnesite surface area divide by quartz surface area (area obtained at prograde homogenization); **C.** Ramp-up temperature from the prograde homogenization temperature to the first temperature step (465 °C).

space.' That is, fiber growth in these experiments, occurred in a simulated, aqueous fluid-filled, pore; this factor cannot be excluded in the formation of fibrous talc.

Conclusions

Growth rates are inferred by quartz dissolution and the dissolved silica required for talc production. Maximum talc growth rates in these experiments are ~10^{-11} - 10^{-13} moles second^{-1} (~10^{-4} - 10^{-6} moles second^{-1} meters^{-2}). These reaction rates would yield maximum transformation times for a 5 mm magnesite grain of ~$10^{0.5}$ to $10^{2.5}$ days. The fastest rates would be reserved for natural settings where magnesite bodies experience a vast in-flux of fluid or an abrupt thermal change (e.g., crack-seal settings or emplacement of an intrusive body).

Rapid reaction rates accompany temperature increases then begin to decrease as equilibrium is approached. Silica removed from the aqueous fluid, consumed in the production of talc, is replenished by additional quartz dissolution, holding the fluid near quartz saturation. Once quartz is destroyed, talc and magnesite react to form olivine. The reactions observed, Mgs + Qtz + fluid → Tlc, Tlc + Mgs → Fo + fluid and Fo + fluid → Mgs + Tlc are consistent with the equilibrium phase relations found by Johannes (1969). This novel method allows for real-time, *in situ* monitoring of mineral-fluid interactions, developments reaction textures and the determination of reaction rates.

Although talc is common, fibrous talc is rare. Previous studies have suggested that fibrous talc requires a fibrous precursor; however, these results demonstrate that the growth of fibrous talc does not require a fibrous precursor. The question remains, why is fibrous talc not more common in nature? Clearly, the specific conditions that generated fibrous talc in these experiments do not commonly occur in talc-forming environments. The tentative conclusions of this study are that fibrous talc formation may be promoted by density (or pressure) decrease, surface area constraints, or growth in open pores, conditions that apparently, do not commonly occur during talc growth.

Chapter 5: Synthesis

Reaction rates have been determined by a new approach, developed during this study, which uses *in situ* observation of reactant mass loss to infer the growth rate of the products of hydrolysis reactions and also allows observations of textural development. During this study, experiments have been conducted in two related systems. The differences between the two systems allow for the evaluation of additional variables not addressed in their chapters.

Contributions to Understanding Reaction Rates in the MgO-SiO_2-H_2O±CO_2 System

Maximum talc growth rates in each set of experiments ranged from 10^{-11} to 10^{-13} moles $\cdot$ sec^{-1}. Whereas the reported growth rates of talc are consistent, the reaction time required to transform an equal volume of the magnesium-rich phases (either olivine, if considered to be forsterite, or magnesite) will differ because of the magnesium content and the densities of each of the phases. To transform a 5 mm diameter grain of forsterite to talc, given the determined reaction rates, would require ~9 to 900 days, depending on growth rates. Whereas, to transform an equal volume of magnesite to talc, it would require ~4 to 400 days.

The similarity of the talc growth rates in the two sets of experiments indicates that the dissolution of the magnesium-rich phases is either not the rate limiting step or that the release of magnesium by dissolution of these phases is virtually at the same rate under the conditions investigated. The latter is unlikely as it is thought that the decarbonation of the microcrystalline aggregate of a carbonate mineral would be

faster than the hydrolysis of single crystal fragments of olivine. The data also suggest that the morphology of talc, whether fibrous or platy, does not appear to affect appreciably the growth rate of talc.

Contributions to Understanding Textural Development

Talc grown during this study exhibited both fibrous and platy habits. Based on available data, these textural variations that may to be controlled by: variations of the aqueous fluid density, surface area of starting materials, rate of initial temperature increase, or the occurrence of growth into open space. Decreases in aqueous fluid density (resulting changes in pressure and quartz solubility), slow initial rise in temperature, and lower magnesium-rich reactant surface areas (relative to quartz) were conditions common to experiments that produced fibrous talc. Although it could not be distinguished whether one of these factors was more important than others, whether these factors must coincide, or if an additional constraint, not measured during this study, is the principle factor controlling talc habit. The primary growth of fibrous talc in these experiments demonstrates that the production of fibrous talc does not require the pseudomorphism of a fibrous precursor as it had previously been explained. Although talc is common, fibrous talc is rare. Clearly, the specific conditions that generated fibrous talc in these experiments do not commonly occur in talc-forming environments. The tentative conclusions of this study is that fibrous talc formation may be promoted by density (or pressure) decrease, surface area constraints, or growth in open pores, conditions that apparently, do not commonly occur during talc growth.

Appendices

Appendix A – Supplementary Data for Chapter Two

A-1. Chamber Area and Predicted Density Changes in Experiments.

This appendix provides graphs of the measured cross-sectional area of the chamber aperture (in pixels, shown in black) as a function of time, for selected experiments. Also plotted on the graphs are the estimated density changes of the fluid (in $g \cdot cm^{-3}$, in gray). The density of the fluid is measure at the beginning of experiments, the prograde homogenization, and at the end, the retrograde homogenization (provided for experiment above the graph). Using the cross-sectional area of the chamber aperture and the height of the gasket, we can find the volume occupied by the fluid. If no fluid escapes, the only changes to density will be the change of the cell volume. These plots show the estimated density change due to chamber volume change.

Experiments with talc dominantly platy

Experiment 06-09-07: prograde density = 0.70, retrograde density =0.82

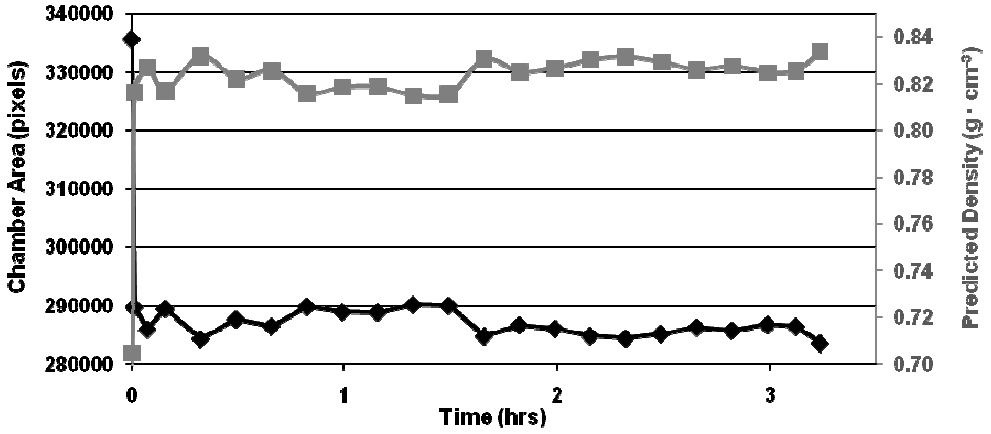

Experiment 11-04-09: prodgrade density = 0.82, retrograde density = 0.68

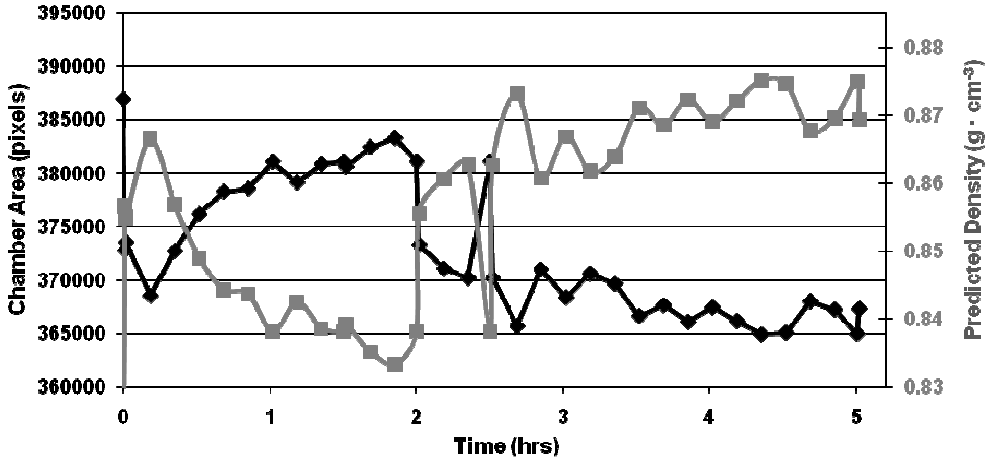

Experiments with talc as both fibers and plates

Experiment 08-29-07: prograde density = 0.76, retrograde density =0.74

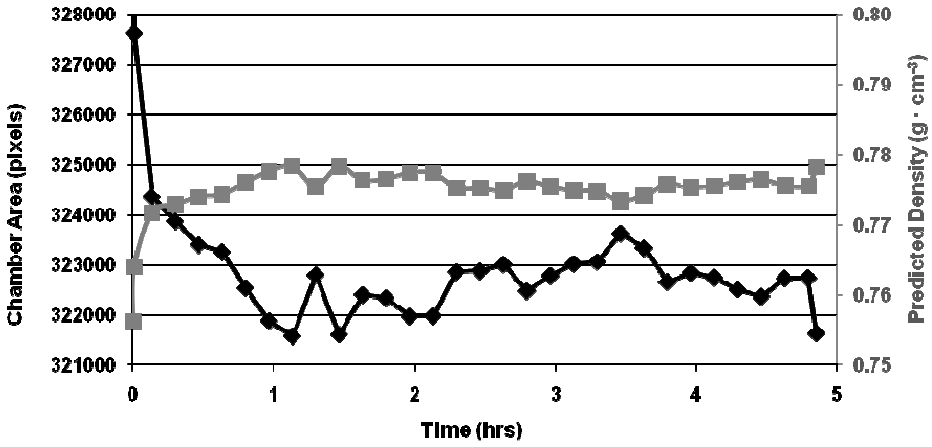

Experiment 02-24-07: prograde density = 0.61, retrograde density =0.54

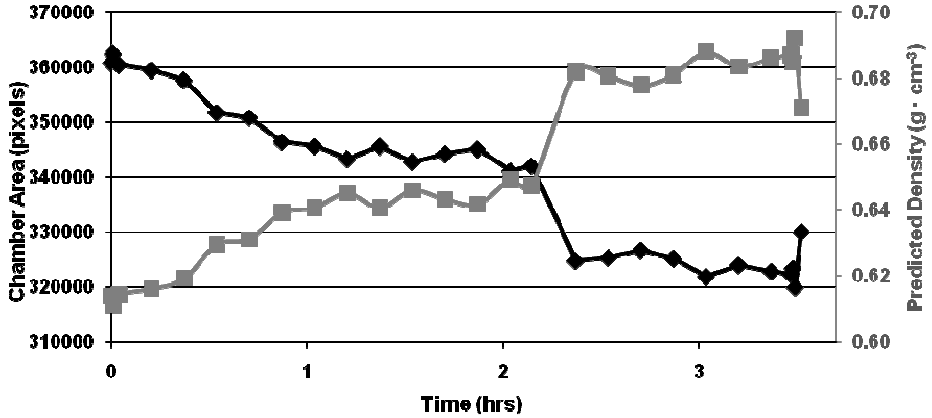

Experiment 08-25-09: prodgrade density = 0.86, retrograde density = 0.81

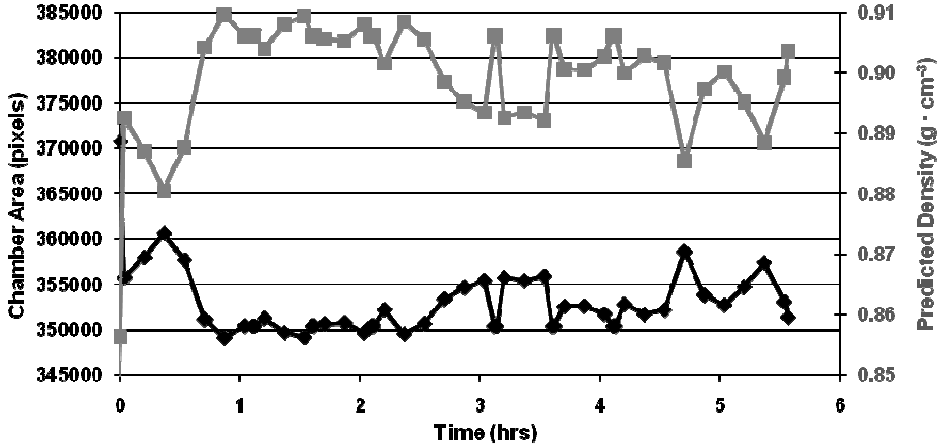

Experiments with talc dominantly fibrous

Experiment 09-05-07: prograde density = 0.96, retrograde density 0.39

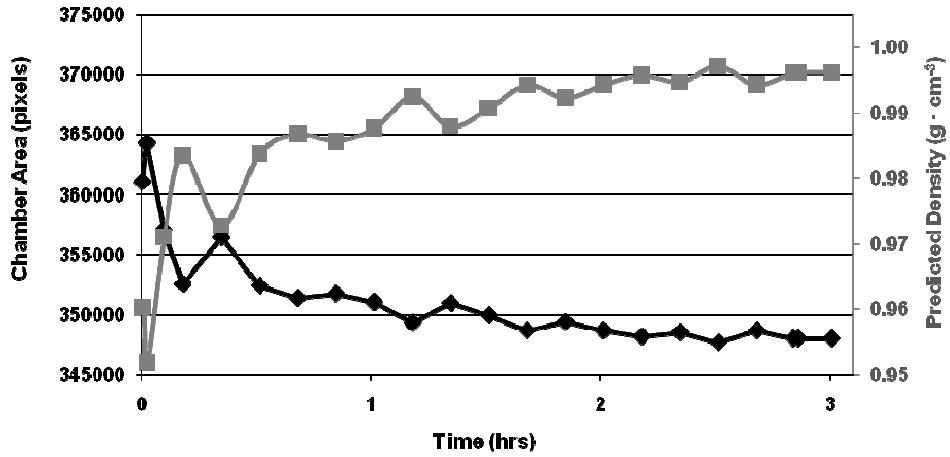

Experiment 06-10-07: prograde density = 0.57, retrograde density =0.73

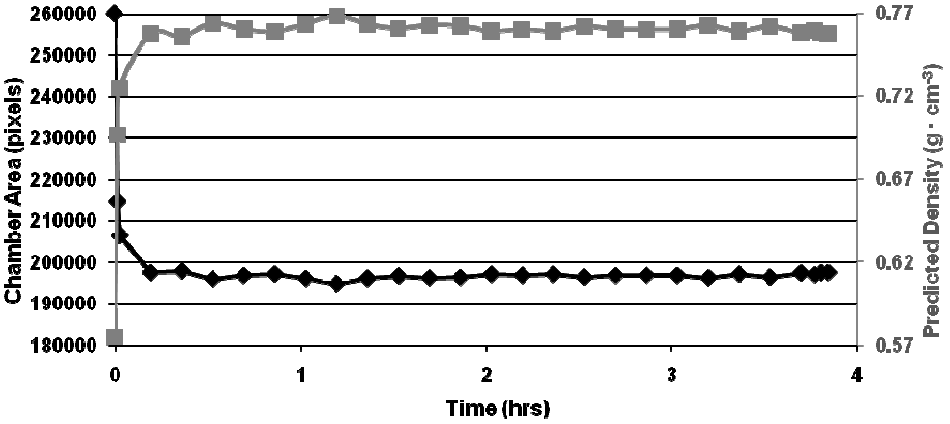

Experiment 12-02-09: prodgrade density = 0.88, retrograde density = 0.87

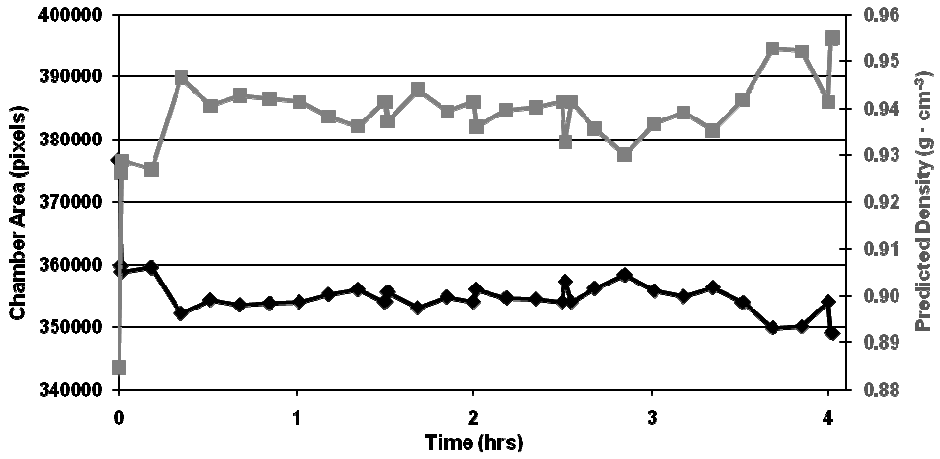

Experiment 03-02-10: prodgrade density = 0.85, retrograde density = 0.88

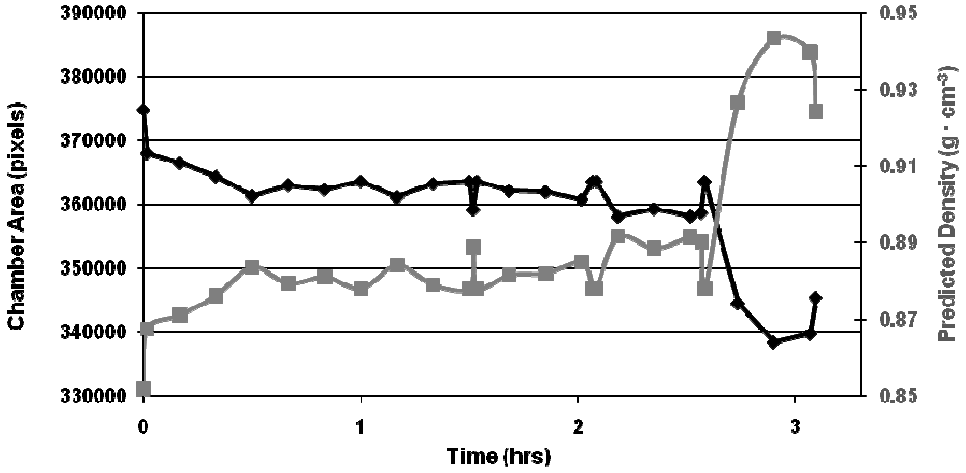

Appendix B – Supplementary Data for Chapter Three

This appendix contains supplementary materials for experiments presented in Chapter three. It is subdivided into three sections: B-1. Data tables for *in situ* mass loss determinations; B-2. *In-situ* photomicrographs of experiments; and B-3. Post-experiment secondary electron images.

B-1. Data Tables for *In Situ* Mass Loss Determination

Measurements and results from *in situ* mass loss determinations made via visual analysis of screen capture images from experiment videos. Each row of data is specific to the screen capture image acquired at the indicated time into the experiment. See the text of the document for additional explanation of the methodology. To conserve space, the following abbreviations have been used:

Column 1: *t from T_H (hrs)* - time into the experiment the screen capture image was acquired in relation to the time of the homogenization temperature, just before the initial rise in temperature.

Column 2: *T (°C)* - temperature of the cell in degrees Celsius.

Column 3: *$\rho\uparrow$ ($g \cdot cm^{-3}$), P($\rho\uparrow$) (MPa)* - $\rho\uparrow$ is the density of the fluid given by the prograde liquid-vapor homogenization determined at the beginning of the experiment. P($\rho\uparrow$) is the pressure (in MPa) determined by using the isochoric relationships of pure water for the prograde homogenization density (Wagner and Pruss, 2002).

Column 4: *$\rho\downarrow$ ($g \cdot cm^{-3}$), P($\rho\downarrow$) (MPa)* - $\rho\downarrow$ is the density of the fluid given by the retrograde liquid-vapor homogenization determined at the end of the experiment. P($\rho\downarrow$) is the pressure (in MPa) determined by the using the isochoric relationships of pure water for the retrograde homogenization density (Wagner and Pruss, 2002).

Column 5 & 6: *Chamber Vol. (μm^3), CV* - volume of the chamber, determined by measuring the cross-sectional area of the chamber aperture and multiplying by the thickness of the rhenium foil. Cross-sectional area measurements were made in triplicate, the coefficient of variation (CV) has been provided. The chamber volume was assumed to be constant after the first hour.

Column 7 & 8: *Qtz Vol. (μm^3), CV* - volume of the quartz grain, determined by measuring the cross-sectional area of the quartz grain and by treating it as an idealized 2:1 ellipse to find the two primary axes of the ellipse. The volume of the ellipsoid was determined by assuming the third axis as equal to the short axis of the ellipse.

Column 9 & 10: *Ol Vol. (μm^3), ($\rho\uparrow$), ($\rho\downarrow$)* - volume of the olivine grain. Initial measurements were made at the time of prograde homogenization and volume calculations followed the procedure described for quartz. After homogenization, olivine volume was assumed to decrease by the amount necessary to produce the calculated volume of talc grown, and is dependent on the density of the fluid (therefore the estimated volume of olivine is provided for both prograde and retrograde densities).

Page 2 of the data tables:

Column 11 & 12: *App. m*SiO_2 *(mol* SiO_2*/kg* H_2O*), (ρ↑), (ρ↓)* - the apparent concentration of silica in solution (molality). Moles of silica were determined by measuring the amount of quartz volume decrease from its size at the time of prograde homogenization. The mass of water was determined by measuring the volume of the chamber and subtracting the volumes of the quartz and olivine grains at the time of prograde homogenization and, as reactions progressed, subtracting the amount of water consumed during the production of talc. The mass of water in the cell will vary with the determined densities, therefore it is provided for the prograde and retrograde densities.

Column 13 & 14: *App. m*SiO_2 *- Qtz Sat. (mol* SiO_2*/kg* H_2O*), (ρ↑), (ρ↓)* - the concentration of silica in excess of quartz saturation determined by subtracting the calculated molality of quartz saturation (following the method of Manning, 1994) from the apparent molality of silica.

Column 15 & 16: *Tlc produced (mol), (ρ↑), (ρ↓)* - the estimated amount of talc grown (in moles) determined by assuming all silica in excess of quartz saturation is consumed in the following reaction: 3Ol + 5Qtz + 2 H_2O = 2Tlc.

Column 17 & 18: *Tlc growth rate (mol · sec*$^{-1}$ *), (ρ↑), (ρ↓)* - talc growth rate in moles per second calculated by determining the amount of moles of talc produced in between each screen capture image and dividing by the time change. At the bottom of the columns, the maximum growth rate of the experiment is reported (*Max Growth Rates)*, not inclusive of what may be interpreted as growth upon quench.

Column 19 & 20: *Tlc growth rate (mol · sec*$^{-1}$ *· m*$^{-2}$*), (ρ↑), (ρ↓)* - talc growth rate in moles per second per unit area of growth surfaces calculated from changes between each screen capture image. Growth surface areas are determined by adding the surface areas of the olivine grain and the wall of the gasket (these locations are normally the only areas where talc grows); these values are semi-quantitative.

Experiment 06-09-07

t from T_H (hrs)	**T** (°C)	**ρ↑** = 0.705 ($g \cdot cm^{-3}$) **P** (ρ↑) (MPa)	**ρ↓** = 0.818 ($g \cdot cm^{-3}$) **P** (ρ↓) (MPa)	**Chamber Vol.** (μm^3)	CV	**Qtz Vol.** (μm^3)	CV	**Ol Vol.** (μm^3) ρ↑	ρ↓
-0.04	300.9	9	95	1.83E+07	0.29%	5.39E+05	1.47%	6.11E+05	6.11E+05
0.00	444.5	155	303	1.78E+07	0.10%	6.55E+05	0.64%	6.11E+05	6.11E+05
0.01	655.4	374	596	1.54E+07	0.35%	5.28E+05	0.95%	6.11E+05	6.11E+05
0.07	653.1	371	593	1.52E+07	0.29%	4.13E+05	0.78%	5.55E+05	5.78E+05
0.16	654.6	373	595	1.54E+07	0.68%	3.93E+05	0.99%	5.46E+05	5.69E+05
0.32	650.1	368	589	1.51E+07	0.28%	3.86E+05	0.39%	5.40E+05	5.63E+05
0.49	657.5	376	599	1.53E+07	0.20%	3.71E+05	0.73%	5.35E+05	5.58E+05
0.66	650.0	368	589	1.52E+07	0.39%	3.71E+05	0.65%	5.33E+05	5.56E+05
0.82	656.6	375	598	1.54E+07	0.16%	3.58E+05	0.82%	5.29E+05	5.52E+05
0.99	655.9	374	597	1.53E+07	0.12%	3.57E+05	0.38%	5.28E+05	5.51E+05
1.16	655.9	374	597	1.53E+07	0.12%	3.56E+05	1.45%	5.27E+05	5.51E+05
1.32	652.6	371	593	1.53E+07	0.12%	3.60E+05	0.50%	5.28E+05	5.52E+05
1.49	654.2	373	595	1.53E+07	0.12%	3.56E+05	0.31%	5.27E+05	5.50E+05
1.66	654.7	373	596	1.53E+07	0.12%	3.54E+05	1.17%	5.26E+05	5.49E+05
1.82	656.1	374	597	1.53E+07	0.12%	3.51E+05	0.41%	5.25E+05	5.48E+05
1.99	656.3	375	598	1.53E+07	0.12%	3.50E+05	0.84%	5.25E+05	5.48E+05
2.16	652.9	371	593	1.53E+07	0.12%	3.50E+05	0.22%	5.24E+05	5.47E+05
2.32	655.2	374	596	1.53E+07	0.12%	3.39E+05	0.44%	5.19E+05	5.42E+05
2.49	655.4	374	596	1.53E+07	0.12%	3.37E+05	0.40%	5.18E+05	5.41E+05
2.66	653.9	372	594	1.53E+07	0.12%	3.35E+05	0.70%	5.16E+05	5.40E+05
2.82	654.3	373	595	1.53E+07	0.12%	3.33E+05	0.80%	5.15E+05	5.39E+05
2.99	655.1	373	596	1.53E+07	0.12%	3.25E+05	1.13%	5.12E+05	5.35E+05
3.12	655.2	374	596	1.53E+07	0.12%	3.25E+05	0.35%	5.11E+05	5.35E+05
3.24	234.4	1	3	1.53E+07	0.12%	n/a	n/a	n/a	n/a

Experiment 06-09-07 (cont.)

App. $mSiO_2$ (mol SiO_2 / kg H_2O)		App. $mSiO_2$ - Qtz Sat (mol SiO_2 / kg H_2O)		Tlc produced (mol)		Tlc growth rate (mol · sec^{-1})		Tlc growth rate (mol · sec^{-1} · m^{-2})	
ρ↑	ρ↓	ρ↑	ρ↓	ρ↑	ρ↓	ρ↑	ρ↓	ρ↑	ρ↓
0.00	0.00	0.00	0.00	0.00E+00	0.00E+00	0.00E+00	0.00E+00	0.00E+00	0.00E+00
0.00	0.00	0.00	0.00	0.00E+00	0.00E+00	0.00E+00	0.00E+00	0.00E+00	0.00E+00
0.56	0.48	0.00	0.00	0.00E+00	0.00E+00	0.00E+00	0.00E+00	0.00E+00	0.00E+00
1.07	0.92	0.49	0.25	1.94E-09	1.16E-09	8.60E-12	5.12E-12	3.36E-05	2.00E-05
1.14	0.98	0.56	0.31	2.25E-09	1.45E-09	1.03E-12	9.86E-13	4.02E-06	3.83E-06
1.20	1.03	0.62	0.36	2.46E-09	1.68E-09	3.37E-13	3.81E-13	1.32E-06	1.49E-06
1.25	1.07	0.65	0.39	2.63E-09	1.83E-09	2.91E-13	2.41E-13	1.14E-06	9.39E-07
1.25	1.08	0.67	0.41	2.70E-09	1.92E-09	1.14E-13	1.53E-13	4.47E-07	5.96E-07
1.29	1.11	0.70	0.43	2.84E-09	2.03E-09	2.36E-13	1.90E-13	9.16E-07	7.37E-07
1.30	1.12	0.71	0.44	2.88E-09	2.07E-09	5.93E-14	6.65E-14	2.31E-07	2.59E-07
1.30	1.12	0.71	0.44	2.90E-09	2.09E-09	3.15E-14	3.14E-14	1.23E-07	1.22E-07
1.29	1.11	0.70	0.44	2.85E-09	2.06E-09	-7.16E-14	-5.64E-14	-2.79E-07	-2.19E-07
1.30	1.12	0.72	0.45	2.90E-09	2.10E-09	7.94E-14	7.17E-14	3.09E-07	2.79E-07
1.31	1.13	0.73	0.45	2.94E-09	2.14E-09	6.41E-14	6.17E-14	2.49E-07	2.40E-07
1.32	1.14	0.73	0.46	2.98E-09	2.17E-09	6.40E-14	5.80E-14	2.49E-07	2.26E-07
1.33	1.14	0.74	0.46	2.99E-09	2.18E-09	1.64E-14	1.50E-14	6.37E-08	5.83E-08
1.33	1.14	0.74	0.47	3.02E-09	2.22E-09	4.91E-14	6.39E-14	1.91E-07	2.49E-07
1.37	1.18	0.79	0.51	3.19E-09	2.39E-09	2.91E-13	2.80E-13	1.13E-06	1.09E-06
1.38	1.19	0.79	0.51	3.22E-09	2.41E-09	4.49E-14	4.34E-14	1.75E-07	1.69E-07
1.39	1.20	0.81	0.52	3.27E-09	2.47E-09	8.21E-14	8.89E-14	3.20E-07	3.46E-07
1.40	1.21	0.82	0.53	3.31E-09	2.50E-09	6.75E-14	6.51E-14	2.63E-07	2.53E-07
1.43	1.23	0.85	0.56	3.43E-09	2.63E-09	2.06E-13	2.02E-13	8.01E-07	7.85E-07
1.44	1.24	0.85	0.56	3.44E-09	2.64E-09	2.06E-14	2.00E-14	8.00E-08	7.76E-08
1.00	0.86	0.91	0.76	3.66E-09	3.54E-09	5.45E-13	2.20E-12	2.12E-06	8.55E-06
						Max Growth Rates			
						8.60E-12	5.12E-12		

Experiment 07-09-07

$\rho\uparrow = 0.696$ $\rho\downarrow = 0.858$ ($g \cdot cm^{-3}$)

t from T_H (hrs)	**T** (°C)	**P** ($\rho\uparrow$) (MPa)	**P** ($\rho\downarrow$)	**Chamber Vol.** (μm^3)	CV	**Qtz Vol.** (μm^3)	CV	**Ol Vol.** (μm^3) $\rho\uparrow$	$\rho\downarrow$
0.00	305.2	10	160	1.37E+07	0.15%	5.21E+05	0.29%	5.07E+05	5.07E+05
0.01	549.6	255	546	1.15E+07	0.48%	4.97E+05	0.24%	5.07E+05	5.07E+05
0.03	550.7	256	548	1.13E+07	0.47%	4.81E+05	0.31%	5.07E+05	5.07E+05
0.20	550.5	255	548	1.13E+07	0.44%	4.52E+05	0.35%	5.05E+05	5.07E+05
0.37	547.5	252	543	1.13E+07	0.18%	4.42E+05	0.44%	5.00E+05	5.07E+05
0.53	553.2	258	552	1.12E+07	0.21%	4.34E+05	0.33%	4.96E+05	5.07E+05
0.70	551.5	256	549	1.12E+07	0.39%	4.29E+05	0.95%	4.93E+05	5.07E+05
0.87	557.8	263	559	1.13E+07	0.30%	4.11E+05	0.62%	4.85E+05	5.03E+05
1.03	548.1	253	544	1.12E+07	0.40%	4.08E+05	0.35%	4.82E+05	4.99E+05
1.20	547.0	252	542	1.12E+07	0.40%	4.02E+05	0.67%	4.79E+05	4.96E+05
1.37	548.8	254	545	1.12E+07	0.40%	4.00E+05	0.48%	4.78E+05	4.95E+05
1.53	555.0	260	555	1.12E+07	0.40%	3.96E+05	0.53%	4.77E+05	4.94E+05
1.70	549.5	255	546	1.12E+07	0.40%	3.96E+05	0.68%	4.76E+05	4.93E+05
1.87	551.2	256	549	1.12E+07	0.40%	3.89E+05	0.44%	4.73E+05	4.90E+05
2.03	551.0	256	549	1.12E+07	0.40%	3.88E+05	0.38%	4.72E+05	4.89E+05
2.20	551.8	257	550	1.12E+07	0.40%	3.85E+05	1.20%	4.71E+05	4.88E+05
2.37	550.4	255	548	1.12E+07	0.40%	3.85E+05	1.15%	4.71E+05	4.88E+05
2.53	549.4	254	546	1.12E+07	0.40%	3.77E+05	0.29%	4.67E+05	4.84E+05
2.70	549.4	254	546	1.12E+07	0.40%	3.79E+05	0.60%	4.67E+05	4.84E+05
2.87	548.3	253	544	1.12E+07	0.40%	3.82E+05	1.06%	4.69E+05	4.86E+05
3.03	549.6	255	550	1.12E+07	0.40%	3.79E+05	0.59%	4.68E+05	4.85E+05
3.20	550.1	255	547	1.12E+07	0.40%	3.81E+05	0.23%	4.69E+05	4.86E+05
3.37	549.1	254	546	1.12E+07	0.40%	3.79E+05	0.21%	4.68E+05	4.85E+05
3.53	550.7	256	548	1.12E+07	0.40%	3.81E+05	0.96%	4.69E+05	4.86E+05
3.70	550.7	256	548	1.12E+07	0.40%	3.82E+05	0.51%	4.69E+05	4.86E+05
3.87	549.3	254	546	1.12E+07	0.40%	3.85E+05	1.24%	4.71E+05	4.88E+05
4.03	546.2	251	541	1.12E+07	0.40%	3.86E+05	0.42%	4.71E+05	4.88E+05
4.20	548.1	253	544	1.12E+07	0.40%	3.84E+05	0.26%	4.70E+05	4.87E+05
4.37	547.9	253	544	1.12E+07	0.40%	3.90E+05	0.81%	4.73E+05	4.90E+05
4.53	547.4	252	543	1.12E+07	0.40%	3.91E+05	0.38%	4.74E+05	4.91E+05
4.70	547.1	252	543	1.12E+07	0.40%	3.92E+05	0.87%	4.74E+05	4.91E+05
4.87	549.2	254	546	1.12E+07	0.40%	3.95E+05	0.13%	4.76E+05	4.93E+05
5.03	550.9	256	548	1.12E+07	0.40%	3.90E+05	0.30%	4.73E+05	4.90E+05
5.20	550.8	256	548	1.12E+07	0.40%	3.85E+05	0.68%	4.71E+05	4.88E+05
5.37	550.0	255	547	1.12E+07	0.40%	3.85E+05	0.86%	4.71E+05	4.88E+05
5.53	549.6	255	546	1.12E+07	0.40%	3.88E+05	0.75%	4.72E+05	4.89E+05

5.70	550.9	256	548	1.12E+07	0.40%	3.92E+05	1.00%	4.74E+05	4.91E+05
5.87	553.2	258	552	1.12E+07	0.40%	3.89E+05	0.78%	4.73E+05	4.90E+05
5.93	552.0	257	550	1.12E+07	0.40%	3.90E+05	0.73%	4.73E+05	4.91E+05
5.99	203.5	1	2	1.12E+07	0.40%	3.89E+05	0.25%	4.45E+05	4.49E+05

Experiment 07-09-07 (cont.)

App. $mSiO_2$ (mol SiO_2 / kg H_2O)		App. $mSiO_2$ - Qtz Sat (mol SiO_2 / kg H_2O)		Tlc produced (mol)		Tlc growth rate (mol · sec^{-1})		Tlc growth rate (mol · sec^{-1} · m^{-2})	
ρ↑	ρ↓	ρ↑	ρ↓	ρ↑	ρ↓	ρ↑	ρ↓	ρ↑	ρ↓
0.00	0.00	0.00	0.00	0.00E+00	0.00E+00	0.00E+00	0.00E+00	0.00E+00	0.00E+00
0.15	0.12	0.00	0.00	0.00E+00	0.00E+00	0.00E+00	0.00E+00	0.00E+00	0.00E+00
0.24	0.20	0.00	0.00	0.00E+00	0.00E+00	0.00E+00	0.00E+00	0.00E+00	0.00E+00
0.42	0.34	0.01	0.00	4.20E-11	0.00E+00	7.00E-14	0.00E+00	3.16E-07	0.00E+00
0.48	0.39	0.08	0.00	2.36E-10	0.00E+00	3.24E-13	0.00E+00	1.46E-06	0.00E+00
0.54	0.44	0.13	0.00	3.71E-10	0.00E+00	2.25E-13	0.00E+00	1.02E-06	0.00E+00
0.57	0.46	0.16	0.00	4.55E-10	0.00E+00	1.39E-13	0.00E+00	6.29E-07	0.00E+00
0.67	0.55	0.26	0.04	7.38E-10	1.37E-10	4.72E-13	2.28E-13	2.13E-06	1.03E-06
0.69	0.56	0.29	0.07	8.31E-10	2.52E-10	1.55E-13	1.92E-13	7.01E-07	8.67E-07
0.73	0.59	0.33	0.10	9.40E-10	3.63E-10	1.82E-13	1.86E-13	8.25E-07	8.41E-07
0.74	0.60	0.34	0.11	9.71E-10	3.90E-10	5.10E-14	4.43E-14	2.31E-07	2.00E-07
0.76	0.62	0.35	0.12	1.01E-09	4.18E-10	6.95E-14	4.60E-14	3.14E-07	2.08E-07
0.77	0.62	0.36	0.13	1.04E-09	4.57E-10	4.47E-14	6.48E-14	2.02E-07	2.93E-07
0.81	0.66	0.40	0.16	1.16E-09	5.70E-10	1.96E-13	1.89E-13	8.87E-07	8.56E-07
0.82	0.66	0.41	0.17	1.18E-09	5.90E-10	3.32E-14	3.39E-14	1.50E-07	1.53E-07
0.83	0.67	0.42	0.18	1.22E-09	6.35E-10	7.78E-14	7.42E-14	3.52E-07	3.36E-07
0.83	0.67	0.43	0.18	1.23E-09	6.41E-10	5.15E-15	1.07E-14	2.33E-08	4.82E-08
0.88	0.71	0.47	0.22	1.37E-09	7.85E-10	2.37E-13	2.40E-13	1.07E-06	1.09E-06
0.87	0.71	0.47	0.21	1.35E-09	7.63E-10	-3.79E-14	-3.74E-14	-1.71E-07	-1.69E-07
0.85	0.69	0.45	0.20	1.30E-09	7.18E-10	-7.96E-14	-7.53E-14	-3.60E-07	-3.41E-07
0.87	0.70	0.46	0.21	1.33E-09	7.46E-10	5.15E-14	4.66E-14	2.33E-07	2.11E-07
0.86	0.69	0.45	0.20	1.30E-09	7.14E-10	-5.13E-14	-5.26E-14	-2.32E-07	-2.38E-07
0.87	0.70	0.46	0.21	1.34E-09	7.52E-10	6.09E-14	6.40E-14	2.75E-07	2.90E-07
0.86	0.70	0.45	0.20	1.30E-09	7.16E-10	-5.48E-14	-6.05E-14	-2.48E-07	-2.74E-07
0.85	0.69	0.45	0.20	1.28E-09	6.97E-10	-3.10E-14	-3.13E-14	-1.40E-07	-1.41E-07
0.83	0.67	0.43	0.18	1.23E-09	6.50E-10	-8.47E-14	-7.89E-14	-3.83E-07	-3.57E-07
0.82	0.67	0.42	0.18	1.22E-09	6.45E-10	-1.98E-14	-8.47E-15	-8.98E-08	-3.83E-08
0.84	0.68	0.43	0.19	1.25E-09	6.68E-10	4.59E-14	3.88E-14	2.08E-07	1.76E-07
0.80	0.65	0.40	0.16	1.16E-09	5.77E-10	-1.54E-13	-1.52E-13	-6.95E-07	-6.90E-07
0.79	0.64	0.39	0.15	1.13E-09	5.49E-10	-4.76E-14	-4.57E-14	-2.16E-07	-2.07E-07
0.79	0.64	0.39	0.15	1.11E-09	5.36E-10	-2.38E-14	-2.26E-14	-1.08E-07	-1.02E-07
0.77	0.62	0.37	0.13	1.05E-09	4.71E-10	-1.00E-13	-1.08E-13	-4.53E-07	-4.88E-07
0.80	0.65	0.40	0.16	1.15E-09	5.59E-10	1.53E-13	1.47E-13	6.93E-07	6.64E-07
0.83	0.67	0.42	0.18	1.22E-09	6.38E-10	1.31E-13	1.31E-13	5.92E-07	5.91E-07
0.83	0.67	0.42	0.18	1.22E-09	6.37E-10	-3.30E-15	-3.50E-16	-1.49E-08	-1.59E-09
0.82	0.66	0.41	0.17	1.18E-09	6.01E-10	-6.24E-14	-6.07E-14	-2.82E-07	-2.75E-07
0.79	0.64	0.38	0.15	1.11E-09	5.21E-10	-1.29E-13	-1.33E-13	-5.82E-07	-6.02E-07

0.81	0.66	0.40	0.16	1.15E-09	5.61E-10	7.47E-14	6.59E-14	3.38E-07	2.98E-07
0.80	0.65	0.40	0.16	1.14E-09	5.53E-10	-4.94E-14	-3.32E-14	-2.24E-07	-1.50E-07
0.81	0.65	0.73	0.56	2.11E-09	1.99E-09	4.09E-12	6.10E-12	1.85E-05	2.76E-05
						Max Growth Rates			
						4.72E-13	2.40E-13		

Experiment 08-23-07

$\rho\uparrow = 0.731$ $\rho\downarrow = 0.480$ $(g \cdot cm^{-3})$

t from T_H (hrs)	**T** (°C)	**P** ($\rho\uparrow$) (MPa)	**P** ($\rho\downarrow$)	**Chamber Vol.** (μm^3)	CV	**Qtz Vol.** (μm^3)	CV	**Ol Vol.** (μm^3) $\rho\uparrow$	$\rho\downarrow$
0.00	290.5	8	19	1.88E+07	0.18%	1.17E+06	0.94%	1.11E+06	1.11E+06
0.01	559.7	310	116	1.88E+07	0.07%	1.09E+06	0.80%	1.11E+06	1.11E+06
0.07	557.0	307	115	1.87E+07	0.30%	1.13E+06	0.31%	1.11E+06	1.11E+06
0.24	558.9	309	116	1.87E+07	0.25%	1.12E+06	0.35%	1.11E+06	1.11E+06
0.40	559.8	310	116	1.87E+07	0.21%	1.09E+06	0.36%	1.11E+06	1.10E+06
0.57	559.1	310	116	1.86E+07	0.20%	1.08E+06	0.18%	1.11E+06	1.09E+06
0.74	560.0	311	116	1.87E+07	0.07%	1.08E+06	0.30%	1.11E+06	1.09E+06
0.90	559.2	310	116	1.86E+07	0.06%	1.07E+06	0.16%	1.11E+06	1.09E+06
1.07	557.7	308	115	1.86E+07	0.06%	1.07E+06	0.09%	1.11E+06	1.09E+06
1.24	560.8	311	117	1.86E+07	0.06%	1.07E+06	0.68%	1.11E+06	1.09E+06
1.40	557.1	307	115	1.86E+07	0.06%	1.07E+06	0.23%	1.11E+06	1.09E+06
1.57	557.9	308	115	1.86E+07	0.06%	1.06E+06	0.26%	1.11E+06	1.08E+06
1.74	558.5	309	116	1.86E+07	0.06%	1.06E+06	0.41%	1.11E+06	1.08E+06
1.90	561.0	312	117	1.86E+07	0.06%	1.06E+06	0.40%	1.11E+06	1.08E+06
2.07	560.0	311	116	1.86E+07	0.06%	1.05E+06	0.05%	1.11E+06	1.08E+06
2.24	561.9	313	117	1.86E+07	0.06%	1.05E+06	0.32%	1.11E+06	1.08E+06
2.40	559.6	310	116	1.86E+07	0.06%	1.05E+06	0.35%	1.11E+06	1.08E+06
2.57	561.1	312	117	1.86E+07	0.06%	1.05E+06	0.34%	1.11E+06	1.08E+06
2.74	561.0	312	117	1.86E+07	0.06%	1.06E+06	0.15%	1.11E+06	1.08E+06
2.90	560.0	311	116	1.86E+07	0.06%	1.06E+06	0.22%	1.11E+06	1.08E+06
3.07	561.6	312	117	1.86E+07	0.06%	1.06E+06	0.17%	1.11E+06	1.08E+06
3.24	557.6	308	115	1.86E+07	0.06%	1.05E+06	0.68%	1.11E+06	1.08E+06
3.35	558.8	309	116	1.86E+07	0.06%	1.07E+06	0.19%	1.11E+06	1.09E+06
3.36	361.9	87	20	1.86E+07	0.06%	n/a	n/a	n/a	n/a

Experiment 08-23-07 (cont.)

App. $mSiO_2$ (mol SiO_2 / kg H_2O)		App. $mSiO_2$ - Qtz Sat (mol SiO_2 / kg H_2O)		Tlc produced (mol)		Tlc growth rate (mol · sec^{-1})		Tlc growth rate (mol · sec^{-1} · m^{-2})	
ρ↑	ρ↓	ρ↑	ρ↓	ρ↑	ρ↓	ρ↑	ρ↓	ρ↑	ρ↓
0.00	0.00	0.00	0.00	0.00E+00	0.00E+00	0.00E+00	0.00E+00	0.00E+00	0.00E+00
0.28	0.43	0.00	0.13	0.00E+00	4.16E-10	0.00E+00	9.24E-12	0.00E+00	3.09E-05
0.15	0.23	0.00	0.00	0.00E+00	0.00E+00	0.00E+00	-2.02E-12	0.00E+00	-6.77E-06
0.17	0.26	0.00	0.00	0.00E+00	0.00E+00	0.00E+00	0.00E+00	0.00E+00	0.00E+00
0.29	0.45	0.00	0.15	0.00E+00	4.72E-10	0.00E+00	7.86E-13	0.00E+00	2.64E-06
0.33	0.50	0.00	0.21	0.00E+00	6.47E-10	0.00E+00	2.91E-13	0.00E+00	9.78E-07
0.33	0.50	0.00	0.20	0.00E+00	6.48E-10	0.00E+00	2.99E-15	0.00E+00	1.00E-08
0.34	0.51	0.00	0.22	0.00E+00	6.88E-10	0.00E+00	6.67E-14	0.00E+00	2.24E-07
0.34	0.51	0.00	0.22	0.00E+00	6.98E-10	0.00E+00	1.54E-14	0.00E+00	5.19E-08
0.36	0.54	0.00	0.25	0.00E+00	7.74E-10	0.00E+00	1.28E-13	0.00E+00	4.30E-07
0.37	0.56	0.00	0.27	0.00E+00	8.47E-10	0.00E+00	1.20E-13	0.00E+00	4.04E-07
0.39	0.60	0.00	0.30	0.00E+00	9.60E-10	0.00E+00	1.89E-13	0.00E+00	6.35E-07
0.39	0.60	0.00	0.31	0.00E+00	9.68E-10	0.00E+00	1.26E-14	0.00E+00	4.23E-08
0.41	0.62	0.00	0.32	0.00E+00	1.02E-09	0.00E+00	8.15E-14	0.00E+00	2.74E-07
0.41	0.62	0.00	0.33	0.00E+00	1.04E-09	0.00E+00	3.25E-14	0.00E+00	1.09E-07
0.41	0.63	0.00	0.33	0.00E+00	1.05E-09	0.00E+00	2.40E-14	0.00E+00	8.06E-08
0.41	0.63	0.00	0.34	0.00E+00	1.06E-09	0.00E+00	1.61E-14	0.00E+00	5.42E-08
0.42	0.64	0.00	0.34	0.00E+00	1.07E-09	0.00E+00	1.58E-14	0.00E+00	5.31E-08
0.39	0.60	0.00	0.30	0.00E+00	9.43E-10	0.00E+00	-2.10E-13	0.00E+00	-7.07E-07
0.39	0.60	0.00	0.30	0.00E+00	9.44E-10	0.00E+00	1.59E-15	0.00E+00	5.34E-09
0.38	0.58	0.00	0.28	0.00E+00	8.78E-10	0.00E+00	-1.11E-13	0.00E+00	-3.72E-07
0.42	0.65	0.00	0.35	0.00E+00	1.11E-09	0.00E+00	3.90E-13	0.00E+00	1.31E-06
0.35	0.53	0.00	0.23	0.00E+00	7.35E-10	0.00E+00	-8.94E-13	0.00E+00	-3.00E-06
n/a	n/a	n/a	n/a	n/a	n/a	n/a	n/a	n/a	n/a

Max Growth Rates	
0.00E+00	9.24E-12

Experiment 08-29-07

$\rho\uparrow = 0.756$ $\rho\downarrow = 0.740$ ($g \cdot cm^{-3}$)

t from T_H (hrs)	**T** (°C)	**P** ($\rho\uparrow$) (MPa)	**P** ($\rho\downarrow$)	**Chamber Vol.** (μm^3)	CV	**Qtz Vol.** (μm^3)	CV	**Ol Vol.** (μm^3) $\rho\uparrow$	$\rho\downarrow$
-0.04	275.8	6	7	1.75E+07	0.26%	9.11E+05	0.50%	7.09E+05	7.09E+05
0.00	283.3	14	7	1.76E+07	0.56%	9.20E+05	0.35%	7.09E+05	7.09E+05
0.01	601.0	397	370	1.74E+07	0.27%	8.57E+05	0.31%	7.09E+05	7.09E+05
0.13	598.7	394	367	1.72E+07	0.21%	8.35E+05	0.62%	7.09E+05	7.09E+05
0.30	603.2	400	372	1.72E+07	0.11%	8.25E+05	1.19%	7.09E+05	7.09E+05
0.47	598.4	394	367	1.72E+07	0.47%	8.20E+05	0.62%	7.09E+05	7.09E+05
0.63	597.0	392	365	1.72E+07	0.13%	7.86E+05	0.17%	7.09E+05	7.09E+05
0.80	597.4	393	366	1.71E+07	0.31%	7.78E+05	1.12%	7.07E+05	7.04E+05
0.97	594.6	390	363	1.71E+07	0.09%	7.75E+05	0.61%	7.05E+05	7.02E+05
1.13	602.6	399	372	1.71E+07	0.09%	7.59E+05	0.44%	6.99E+05	6.96E+05
1.30	601.7	398	371	1.71E+07	0.09%	7.53E+05	0.50%	6.96E+05	6.93E+05
1.47	598.8	395	367	1.71E+07	0.09%	7.39E+05	0.66%	6.88E+05	6.85E+05
1.63	599.6	396	368	1.71E+07	0.09%	7.26E+05	0.55%	6.81E+05	6.78E+05
1.80	598.9	395	367	1.71E+07	0.09%	7.24E+05	0.19%	6.80E+05	6.77E+05
1.97	597.2	393	366	1.71E+07	0.09%	7.15E+05	0.13%	6.75E+05	6.72E+05
2.13	599.3	395	368	1.71E+07	0.09%	7.14E+05	0.56%	6.75E+05	6.72E+05
2.30	599.7	396	368	1.71E+07	0.09%	6.97E+05	0.69%	6.67E+05	6.64E+05
2.47	598.9	395	367	1.71E+07	0.09%	6.94E+05	0.50%	6.65E+05	6.62E+05
2.63	601.0	397	370	1.71E+07	0.09%	6.88E+05	0.27%	6.62E+05	6.59E+05
2.80	599.4	395	368	1.71E+07	0.09%	6.79E+05	0.79%	6.57E+05	6.54E+05
2.97	598.8	395	367	1.71E+07	0.09%	6.76E+05	0.60%	6.56E+05	6.53E+05
3.13	601.2	397	370	1.71E+07	0.09%	6.49E+05	0.35%	6.42E+05	6.39E+05
3.30	598.9	395	367	1.71E+07	0.09%	6.44E+05	0.72%	6.40E+05	6.37E+05
3.47	602.1	398	371	1.71E+07	0.09%	6.32E+05	0.93%	6.34E+05	6.31E+05
3.63	599.1	395	368	1.71E+07	0.09%	6.20E+05	0.64%	6.27E+05	6.24E+05
3.80	601.9	398	371	1.71E+07	0.09%	6.15E+05	0.30%	6.26E+05	6.22E+05
3.97	600.6	397	369	1.71E+07	0.09%	6.01E+05	0.16%	6.18E+05	6.15E+05
4.13	600.3	396	369	1.71E+07	0.09%	5.97E+05	1.69%	6.16E+05	6.13E+05
4.30	598.8	395	367	1.71E+07	0.09%	5.91E+05	0.71%	6.12E+05	6.09E+05
4.47	598.9	395	367	1.71E+07	0.09%	5.81E+05	0.14%	6.08E+05	6.05E+05
4.63	599.7	396	368	1.71E+07	0.09%	5.76E+05	0.84%	6.05E+05	6.02E+05
4.80	594.1	389	362	1.71E+07	0.09%	5.67E+05	0.94%	5.99E+05	5.96E+05
4.86	593.7	389	362	1.71E+07	0.09%	5.62E+05	0.50%	5.96E+05	5.93E+05
4.87	280.5	11	7	1.71E+07	0.09%	5.71E+05	0.32%	5.48E+05	5.47E+05
4.99	283.2	14	7	1.71E+07	0.09%	n/a	n/a	n/a	n/a

Experiment 08-29-07 (cont.)

App. $mSiO_2$ (mol SiO_2 / kg H_2O)		App. $mSiO_2$ - Qtz Sat (mol SiO_2 / kg H_2O)		Tlc produced (mol)		Tlc growth rate (mol · sec^{-1})		Tlc growth rate (mol · sec^{-1} · m^{-2})	
ρ↑	ρ↓	ρ↑	ρ↓	ρ↑	ρ↓	ρ↑	ρ↓	ρ↑	ρ↓
0.00	0.00	0.00	0.00	0.00E+00	0.00E+00	0.00E+00	0.00E+00	0.00E+00	0.00E+00
0.00	0.00	0.00	0.00	0.00E+00	0.00E+00	0.00E+00	0.00E+00	0.00E+00	0.00E+00
0.23	0.24	0.00	0.00	0.00E+00	0.00E+00	0.00E+00	0.00E+00	0.00E+00	0.00E+00
0.32	0.32	0.00	0.00	0.00E+00	0.00E+00	0.00E+00	0.00E+00	0.00E+00	0.00E+00
0.35	0.36	0.00	0.00	0.00E+00	0.00E+00	0.00E+00	0.00E+00	0.00E+00	0.00E+00
0.37	0.38	0.00	0.00	0.00E+00	0.00E+00	0.00E+00	0.00E+00	0.00E+00	0.00E+00
0.50	0.51	0.00	0.00	0.00E+00	1.09E-11	0.00E+00	1.81E-14	0.00E+00	6.62E-08
0.53	0.54	0.01	0.04	6.13E-11	1.63E-10	1.02E-13	2.54E-13	3.74E-07	9.28E-07
0.54	0.56	0.03	0.05	1.43E-10	2.43E-10	1.36E-13	1.34E-13	4.96E-07	4.88E-07
0.60	0.62	0.08	0.10	3.58E-10	4.62E-10	3.59E-13	3.64E-13	1.31E-06	1.33E-06
0.62	0.64	0.10	0.12	4.57E-10	5.60E-10	1.64E-13	1.64E-13	6.00E-07	5.98E-07
0.68	0.69	0.15	0.18	7.33E-10	8.35E-10	4.60E-13	4.58E-13	1.68E-06	1.68E-06
0.72	0.74	0.20	0.23	9.57E-10	1.06E-09	3.74E-13	3.74E-13	1.37E-06	1.37E-06
0.73	0.75	0.21	0.24	1.00E-09	1.11E-09	7.91E-14	7.86E-14	2.89E-07	2.87E-07
0.76	0.78	0.25	0.27	1.17E-09	1.27E-09	2.74E-13	2.73E-13	1.00E-06	1.00E-06
0.77	0.78	0.25	0.27	1.16E-09	1.27E-09	-9.10E-15	-7.83E-15	-3.33E-08	-2.86E-08
0.83	0.85	0.31	0.34	1.45E-09	1.55E-09	4.80E-13	4.81E-13	1.76E-06	1.76E-06
0.84	0.86	0.32	0.35	1.52E-09	1.62E-09	1.07E-13	1.07E-13	3.92E-07	3.90E-07
0.86	0.88	0.34	0.37	1.61E-09	1.71E-09	1.57E-13	1.58E-13	5.73E-07	5.78E-07
0.90	0.92	0.38	0.41	1.78E-09	1.88E-09	2.87E-13	2.86E-13	1.05E-06	1.05E-06
0.91	0.93	0.39	0.42	1.84E-09	1.94E-09	9.60E-14	9.56E-14	3.51E-07	3.50E-07
1.01	1.03	0.48	0.52	2.29E-09	2.40E-09	7.59E-13	7.60E-13	2.77E-06	2.78E-06
1.02	1.04	0.50	0.53	2.39E-09	2.49E-09	1.52E-13	1.51E-13	5.56E-07	5.51E-07
1.07	1.09	0.54	0.58	2.58E-09	2.69E-09	3.29E-13	3.31E-13	1.20E-06	1.21E-06
1.11	1.14	0.59	0.63	2.82E-09	2.92E-09	3.88E-13	3.86E-13	1.42E-06	1.41E-06
1.13	1.15	0.60	0.64	2.87E-09	2.98E-09	9.59E-14	9.77E-14	3.51E-07	3.57E-07
1.18	1.21	0.66	0.69	3.13E-09	3.24E-09	4.34E-13	4.34E-13	1.59E-06	1.59E-06
1.19	1.22	0.67	0.71	3.20E-09	3.31E-09	1.17E-13	1.17E-13	4.27E-07	4.27E-07
1.22	1.24	0.70	0.73	3.33E-09	3.43E-09	2.02E-13	2.01E-13	7.37E-07	7.34E-07
1.25	1.28	0.73	0.77	3.49E-09	3.59E-09	2.71E-13	2.71E-13	9.90E-07	9.90E-07
1.27	1.30	0.75	0.79	3.57E-09	3.68E-09	1.45E-13	1.45E-13	5.29E-07	5.31E-07
1.30	1.33	0.79	0.83	3.78E-09	3.89E-09	3.50E-13	3.46E-13	1.28E-06	1.27E-06
1.32	1.35	0.81	0.85	3.87E-09	3.97E-09	4.14E-13	4.14E-13	1.52E-06	1.51E-06
1.29	1.32	1.16	1.19	5.54E-09	5.57E-09	3.28E-11	3.13E-11	1.20E-04	1.14E-04
n/a	n/a	n/a	n/a	n/a	n/a	n/a	n/a	n/a	n/a
						Max Growth Rates			
						7.59E-13	7.60E-13		

Experiment 02-24-08

$\rho\uparrow = 0.614$ $\rho\downarrow = 0.538$ $(g \cdot cm^{-3})$

t from T_H (hrs)	**T** (°C)	**P** ($\rho\uparrow$) (MPa)	**P** ($\rho\downarrow$) (MPa)	**Chamber Vol.** (μm^3)	CV	**Qtz Vol.** (μm^3)	CV	**Ol Vol.** (μm^3) $\rho\uparrow$	$\rho\downarrow$
-0.08	334.9	12	6	1.93E+07	0.51%	1.35E+06	1.24%	1.21E+06	1.21E+06
-0.02	336.2	13	7	1.92E+07	0.17%	1.53E+06	0.69%	1.21E+06	1.21E+06
0.00	343.6	18	7	1.92E+07	0.18%	1.53E+06	0.25%	1.21E+06	1.21E+06
0.01	549.9	180	135	1.92E+07	0.28%	1.53E+06	0.41%	1.21E+06	1.21E+06
0.04	548.2	179	134	1.91E+07	0.37%	1.51E+06	0.71%	1.21E+06	1.21E+06
0.21	549.5	180	135	1.91E+07	0.01%	1.51E+06	0.57%	1.21E+06	1.21E+06
0.37	549.9	180	135	1.90E+07	0.17%	1.49E+06	0.65%	1.21E+06	1.21E+06
0.54	549.3	180	135	1.87E+07	0.09%	1.46E+06	0.31%	1.21E+06	1.20E+06
0.71	550.8	181	136	1.86E+07	0.11%	1.46E+06	0.26%	1.21E+06	1.20E+06
0.87	551.4	181	136	1.84E+07	0.32%	1.44E+06	0.38%	1.20E+06	1.19E+06
1.04	549.3	180	135	1.83E+07	0.47%	1.43E+06	0.98%	1.19E+06	1.19E+06
1.21	548.6	179	134	1.83E+07	0.47%	1.43E+06	0.22%	1.19E+06	1.18E+06
1.37	547.9	178	134	1.83E+07	0.47%	1.43E+06	0.42%	1.19E+06	1.18E+06
1.54	549.9	180	135	1.83E+07	0.47%	1.43E+06	0.18%	1.20E+06	1.19E+06
1.71	547.7	178	134	1.83E+07	0.47%	1.43E+06	0.10%	1.20E+06	1.19E+06
1.87	548.5	179	134	1.83E+07	0.47%	1.42E+06	0.41%	1.19E+06	1.18E+06
2.04	549.2	179	135	1.83E+07	0.47%	1.43E+06	0.34%	1.20E+06	1.19E+06
2.15	547.4	178	133	1.83E+07	0.47%	1.44E+06	0.28%	1.20E+06	1.19E+06
2.37	546.4	177	133	1.83E+07	0.47%	1.44E+06	0.28%	1.20E+06	1.19E+06
2.54	554.3	184	138	1.83E+07	0.47%	1.44E+06	0.28%	1.20E+06	1.19E+06
2.71	546.7	177	133	1.83E+07	0.47%	1.44E+06	0.28%	1.20E+06	1.19E+06
2.87	546.5	177	133	1.83E+07	0.47%	1.44E+06	0.28%	1.20E+06	1.19E+06
3.04	545.3	176	132	1.83E+07	0.47%	1.44E+06	0.28%	1.20E+06	1.19E+06
3.21	544.9	176	132	1.83E+07	0.47%	1.44E+06	0.28%	1.20E+06	1.19E+06
3.37	544.2	175	131	1.83E+07	0.47%	1.44E+06	0.28%	1.20E+06	1.19E+06
3.47	544.8	176	138	1.83E+07	0.47%	1.44E+06	0.28%	1.20E+06	1.19E+06
3.48	487.9	130	96	1.83E+07	0.47%	1.44E+06	0.25%	1.19E+06	1.18E+06
3.49	351.9	24	15	1.83E+07	0.47%	1.44E+06	0.36%	1.18E+06	1.17E+06
3.53	180.0	1	1	1.83E+07	0.47%	1.37E+06	0.51%	1.13E+06	1.13E+06

Experiment 02-24-08 (cont.)

App. $mSiO_2$ (mol SiO_2 / kg H_2O)		App. $mSiO_2$ - Qtz Sat (mol SiO_2 / kg H_2O)		Tlc produced (mol)		Tlc growth rate (mol · sec^{-1})		Tlc growth rate (mol · sec^{-1} · m^{-2})	
ρ↑	ρ↓	ρ↑	ρ↓	ρ↑	ρ↓	ρ↑	ρ↓	ρ↑	ρ↓
0.00	0.00	0.00	0.00	0.00E+00	0.00E+00	0.00E+00	0.00E+00	0.00E+00	0.00E+00
0.00	0.00	0.00	0.00	0.00E+00	0.00E+00	0.00E+00	0.00E+00	0.00E+00	0.00E+00
0.00	0.00	0.00	0.00	0.00E+00	0.00E+00	0.00E+00	0.00E+00	0.00E+00	0.00E+00
0.02	0.02	0.00	0.00	0.00E+00	0.00E+00	0.00E+00	0.00E+00	0.00E+00	0.00E+00
0.10	0.11	0.00	0.00	0.00E+00	0.00E+00	0.00E+00	0.00E+00	0.00E+00	0.00E+00
0.12	0.14	0.00	0.00	0.00E+00	0.00E+00	0.00E+00	0.00E+00	0.00E+00	0.00E+00
0.20	0.22	0.00	0.00	0.00E+00	0.00E+00	0.00E+00	0.00E+00	0.00E+00	0.00E+00
0.32	0.37	0.00	0.05	0.00E+00	1.70E-10	0.00E+00	2.83E-13	0.00E+00	9.39E-07
0.34	0.39	0.00	0.07	0.00E+00	2.39E-10	0.00E+00	1.16E-13	0.00E+00	3.87E-07
0.43	0.49	0.06	0.17	2.49E-10	5.64E-10	4.16E-13	5.41E-13	1.39E-06	1.81E-06
0.47	0.53	0.11	0.22	4.19E-10	7.31E-10	2.83E-13	2.78E-13	9.47E-07	9.29E-07
0.49	0.56	0.13	0.24	5.07E-10	8.17E-10	1.45E-13	1.44E-13	4.86E-07	4.82E-07
0.49	0.56	0.13	0.24	5.15E-10	8.25E-10	1.36E-14	1.24E-14	4.54E-08	4.16E-08
0.46	0.53	0.10	0.21	3.95E-10	7.08E-10	-1.99E-13	-1.96E-13	-6.65E-07	-6.54E-07
0.46	0.52	0.10	0.20	3.82E-10	6.91E-10	-2.29E-14	-2.70E-14	-7.65E-08	-9.02E-08
0.51	0.58	0.15	0.26	5.79E-10	8.90E-10	3.28E-13	3.30E-13	1.10E-06	1.10E-06
0.45	0.52	0.09	0.20	3.62E-10	6.73E-10	-3.61E-13	-3.60E-13	-1.21E-06	-1.20E-06
0.44	0.51	0.09	0.19	3.35E-10	6.44E-10	-6.96E-14	-7.50E-14	-2.33E-07	-2.51E-07
0.44	0.51	0.09	0.19	3.41E-10	6.49E-10	8.14E-15	6.29E-15	2.72E-08	2.10E-08
0.44	0.51	0.08	0.18	2.99E-10	6.17E-10	-6.98E-14	-5.40E-14	-2.34E-07	-1.80E-07
0.44	0.51	0.09	0.19	3.38E-10	6.46E-10	6.39E-14	4.94E-14	2.14E-07	1.65E-07
0.44	0.51	0.09	0.19	3.39E-10	6.47E-10	1.69E-15	1.31E-15	5.65E-09	4.37E-09
0.44	0.51	0.09	0.19	3.44E-10	6.52E-10	9.28E-15	7.17E-15	3.10E-08	2.40E-08
0.44	0.51	0.09	0.19	3.46E-10	6.53E-10	2.53E-15	1.95E-15	8.45E-09	6.53E-09
0.44	0.51	0.09	0.19	3.50E-10	6.56E-10	6.73E-15	5.20E-15	2.25E-08	1.74E-08
0.44	0.51	0.09	0.19	3.47E-10	6.53E-10	-8.41E-15	-6.50E-15	-2.81E-08	-2.17E-08
0.43	0.50	0.15	0.25	5.85E-10	8.30E-10	5.96E-12	4.42E-12	1.99E-05	1.48E-05
0.42	0.48	0.27	0.34	1.03E-09	1.17E-09	1.12E-11	8.38E-12	3.74E-05	2.80E-05
0.75	0.86	0.69	0.81	2.69E-09	2.74E-09	1.46E-11	1.38E-11	4.87E-05	4.63E-05
						Max Growth Rates			
						1.46E-11	1.38E-11		

Experiment 08-27-08

$\rho\uparrow$ = 0.822 $\rho\downarrow$ = 0.818 ($g \cdot cm^{-3}$)

t from T_H (hrs)	**T** (°C)	**P** ($\rho\uparrow$) (MPa)	**P** ($\rho\downarrow$)	**Chamber Vol.** (μm^3)	CV	**Qtz Vol.** (μm^3)	CV	**Ol Vol.** (μm^3) $\rho\uparrow$	$\rho\downarrow$
-0.51	254.0	31	28	1.50E+07	0.21%	1.11E+06	0.15%	4.98E+05	4.98E+05
-0.38	450.6	317	311	1.46E+07	0.14%	1.11E+06	0.44%	4.98E+05	4.98E+05
0.00	222.3	3	3	1.45E+07	0.29%	1.15E+06	0.98%	4.98E+05	4.98E+05
0.03	560.1	473	465	1.45E+07	0.30%	1.14E+06	0.42%	4.98E+05	4.98E+05
0.05	564.4	479	471	1.45E+07	0.47%	1.14E+06	0.03%	4.98E+05	4.98E+05
0.22	564.5	479	471	1.45E+07	0.26%	1.13E+06	0.34%	4.98E+05	4.98E+05
0.39	559.2	472	464	1.45E+07	0.34%	1.13E+06	0.13%	4.98E+05	4.98E+05
0.55	559.4	472	464	1.44E+07	0.10%	1.12E+06	0.66%	4.98E+05	4.98E+05
0.72	563.7	478	470	1.45E+07	0.20%	1.11E+06	0.07%	4.98E+05	4.98E+05
0.89	561.1	475	467	1.44E+07	0.25%	1.09E+06	0.53%	4.98E+05	4.98E+05
1.05	565.0	480	472	1.44E+07	0.15%	1.09E+06	0.33%	4.98E+05	4.98E+05
1.22	566.4	482	474	1.44E+07	0.15%	1.08E+06	0.19%	4.98E+05	4.98E+05
1.39	564.6	479	471	1.44E+07	0.15%	1.08E+06	0.35%	4.98E+05	4.98E+05
1.55	565.1	480	472	1.44E+07	0.15%	1.08E+06	0.14%	4.98E+05	4.98E+05
1.72	564.4	479	471	1.44E+07	0.15%	1.07E+06	0.25%	4.98E+05	4.98E+05
1.89	565.7	481	473	1.44E+07	0.15%	1.06E+06	0.16%	4.98E+05	4.98E+05
2.05	564.9	480	472	1.44E+07	0.15%	1.06E+06	0.49%	4.98E+05	4.98E+05
2.22	567.1	483	475	1.44E+07	0.15%	1.06E+06	0.25%	4.98E+05	4.98E+05
2.39	565.1	480	472	1.44E+07	0.15%	1.06E+06	0.14%	4.98E+05	4.98E+05
2.55	564.0	479	471	1.44E+07	0.15%	1.05E+06	0.10%	4.98E+05	4.98E+05
2.65	563.6	478	470	1.44E+07	0.15%	1.05E+06	0.24%	4.98E+05	4.98E+05
2.67	229.7	3	3	1.44E+07	0.15%	1.08E+06	0.33%	4.75E+05	4.75E+05
2.76	137.2	1	1	1.44E+07	0.15%	1.04E+06	0.85%	4.51E+05	4.51E+05

Experiment 08-27-08 (cont.)

App. $mSiO_2$ (mol SiO_2 / kg H_2O)		App. $mSiO_2$ - Qtz Sat (mol SiO_2 / kg H_2O)		Tlc produced (mol)		Tlc growth rate (mol · sec^{-1})		Tlc growth rate (mol · sec^{-1} · m^{-2})	
ρ↑	ρ↓	ρ↑	ρ↓	ρ↑	ρ↓	ρ↑	ρ↓	ρ↑	ρ↓
0.00	0.00	0.00	0.00	0.00E+00	0.00E+00	0.00E+00	0.00E+00	0.00E+00	0.00E+00
0.00	0.00	0.00	0.00	0.00E+00	0.00E+00	0.00E+00	0.00E+00	0.00E+00	0.00E+00
0.00	0.00	0.00	0.00	0.00E+00	0.00E+00	0.00E+00	0.00E+00	0.00E+00	0.00E+00
0.03	0.03	0.00	0.00	0.00E+00	0.00E+00	0.00E+00	0.00E+00	0.00E+00	0.00E+00
0.04	0.04	0.00	0.00	0.00E+00	0.00E+00	0.00E+00	0.00E+00	0.00E+00	0.00E+00
0.06	0.06	0.00	0.00	0.00E+00	0.00E+00	0.00E+00	0.00E+00	0.00E+00	0.00E+00
0.06	0.06	0.00	0.00	0.00E+00	0.00E+00	0.00E+00	0.00E+00	0.00E+00	0.00E+00
0.12	0.13	0.00	0.00	0.00E+00	0.00E+00	0.00E+00	0.00E+00	0.00E+00	0.00E+00
0.17	0.17	0.00	0.00	0.00E+00	0.00E+00	0.00E+00	0.00E+00	0.00E+00	0.00E+00
0.24	0.24	0.00	0.00	0.00E+00	0.00E+00	0.00E+00	0.00E+00	0.00E+00	0.00E+00
0.26	0.26	0.00	0.00	0.00E+00	0.00E+00	0.00E+00	0.00E+00	0.00E+00	0.00E+00
0.26	0.26	0.00	0.00	0.00E+00	0.00E+00	0.00E+00	0.00E+00	0.00E+00	0.00E+00
0.26	0.26	0.00	0.00	0.00E+00	0.00E+00	0.00E+00	0.00E+00	0.00E+00	0.00E+00
0.30	0.30	0.00	0.00	0.00E+00	0.00E+00	0.00E+00	0.00E+00	0.00E+00	0.00E+00
0.31	0.32	0.00	0.00	0.00E+00	0.00E+00	0.00E+00	0.00E+00	0.00E+00	0.00E+00
0.37	0.37	0.00	0.00	0.00E+00	0.00E+00	0.00E+00	0.00E+00	0.00E+00	0.00E+00
0.37	0.37	0.00	0.00	0.00E+00	0.00E+00	0.00E+00	0.00E+00	0.00E+00	0.00E+00
0.38	0.38	0.00	0.00	0.00E+00	0.00E+00	0.00E+00	0.00E+00	0.00E+00	0.00E+00
0.38	0.38	0.00	0.00	0.00E+00	0.00E+00	0.00E+00	0.00E+00	0.00E+00	0.00E+00
0.41	0.42	0.00	0.00	0.00E+00	0.00E+00	0.00E+00	0.00E+00	0.00E+00	0.00E+00
0.38	0.39	0.00	0.00	0.00E+00	0.00E+00	0.00E+00	0.00E+00	0.00E+00	0.00E+00
0.29	0.29	0.19	0.19	7.89E-10	7.93E-10	8.97E-12	9.01E-12	3.65E-05	3.67E-05
0.43	0.43	0.38	0.38	1.59E-09	1.59E-09	2.41E-12	2.40E-12	9.80E-06	9.78E-06
						Max Growth Rates			
						8.97E-12	9.01E-12		

Experiment 09-05-07

$\rho\uparrow = 0.955$ $\rho\downarrow = 0.391$ ($g \cdot cm^{-3}$)

t from T_H (hrs)	**T** (°C)	**P** ($\rho\uparrow$) (MPa)	**P** ($\rho\downarrow$)	**Chamber Vol.** (μm^3)	CV	**Qtz Vol.** (μm^3)	CV	**Ol Vol.** (μm^3) $\rho\uparrow$	$\rho\downarrow$
-0.07	95.2	1	1	1.96E+07	0.03%	9.05E+05	2.04%	6.75E+05	6.75E+05
0.00	114.5	17	1	1.92E+07	0.13%	1.07E+06	0.22%	6.75E+05	6.75E+05
0.02	638.8	1029	119	1.93E+07	0.45%	9.11E+05	1.69%	6.75E+05	6.21E+05
0.09	639.9	1031	120	1.90E+07	0.17%	9.56E+05	0.23%	6.75E+05	6.44E+05
0.18	641.0	1033	120	1.87E+07	0.35%	9.23E+05	1.04%	6.75E+05	6.27E+05
0.34	641.3	1034	120	1.89E+07	0.61%	9.03E+05	0.43%	6.75E+05	6.17E+05
0.51	638.8	1029	119	1.87E+07	0.36%	8.66E+05	0.22%	6.75E+05	5.97E+05
0.68	635.2	1022	118	1.87E+07	0.52%	8.22E+05	0.52%	6.75E+05	5.74E+05
0.84	637.7	1027	119	1.87E+07	0.44%	8.05E+05	0.74%	6.75E+05	5.66E+05
1.01	638.2	1028	119	1.86E+07	0.26%	7.83E+05	0.55%	6.71E+05	5.55E+05
1.18	638.8	1029	119	1.86E+07	0.26%	7.62E+05	0.55%	6.61E+05	5.44E+05
1.34	638.8	1029	119	1.86E+07	0.26%	7.53E+05	0.14%	6.56E+05	5.39E+05
1.51	639.4	1030	120	1.86E+07	0.26%	7.42E+05	0.82%	6.51E+05	5.34E+05
1.68	639.1	1030	119	1.86E+07	0.26%	7.10E+05	0.04%	6.35E+05	5.17E+05
1.84	640.0	1031	120	1.86E+07	0.26%	7.05E+05	0.31%	6.33E+05	5.15E+05
2.01	642.8	1036	121	1.86E+07	0.26%	6.81E+05	0.07%	6.22E+05	5.02E+05
2.18	638.4	1028	119	1.86E+07	0.26%	6.73E+05	0.32%	6.16E+05	4.98E+05
2.34	635.1	1022	118	1.86E+07	0.26%	6.60E+05	0.26%	6.07E+05	4.91E+05
2.51	634.8	1022	118	1.86E+07	0.26%	6.49E+05	0.34%	6.02E+05	4.86E+05
2.68	640.9	1033	120	1.86E+07	0.26%	6.37E+05	0.22%	5.99E+05	4.80E+05
2.84	639.7	1031	120	1.86E+07	0.26%	6.26E+05	0.49%	5.93E+05	4.74E+05
2.86	375.1	522	22	1.86E+07	0.26%	n/a	n/a	n/a	n/a
3.00	156.1	89	1	1.86E+07	0.26%	n/a	n/a	n/a	n/a

Experiment 09-05-07 (cont.)

App. *m*SiO_2 (mol SiO_2 / kg H_2O)		**App. *m*SiO_2 - Qtz Sat** (mol SiO_2 / kg H_2O)		**Tlc produced** (mol)		**Tlc growth rate** (mol · sec^{-1})		**Tlc growth rate** (mol · sec^{-1} · m^{-2})	
ρ↑	ρ↓	ρ↑	ρ↓	ρ↑	ρ↓	ρ↑	ρ↓	ρ↑	ρ↓
0.00	0.00	0.00	0.00	0.00E+00	0.00E+00	0.00E+00	0.00E+00	0.00E+00	0.00E+00
0.00	0.00	0.00	0.00	0.00E+00	0.00E+00	0.00E+00	0.00E+00	0.00E+00	0.00E+00
0.40	0.99	0.00	0.67	0.00E+00	1.86E-09	0.00E+00	2.59E-11	0.00E+00	9.03E-05
0.30	0.72	0.00	0.40	0.00E+00	1.08E-09	0.00E+00	-2.92E-12	0.00E+00	-1.03E-05
0.39	0.95	0.00	0.62	0.00E+00	1.67E-09	0.00E+00	1.95E-12	0.00E+00	6.90E-06
0.44	1.06	0.00	0.74	0.00E+00	2.01E-09	0.00E+00	5.74E-13	0.00E+00	2.02E-06
0.54	1.32	0.00	1.00	0.00E+00	2.68E-09	0.00E+00	1.11E-12	0.00E+00	3.94E-06
0.66	1.61	0.00	1.29	0.00E+00	3.47E-09	0.00E+00	1.31E-12	0.00E+00	4.65E-06
0.70	1.71	0.00	1.39	0.00E+00	3.75E-09	0.00E+00	4.66E-13	0.00E+00	1.65E-06
0.76	1.86	0.02	1.54	1.27E-10	4.14E-09	2.12E-13	6.51E-13	7.53E-07	2.31E-06
0.82	2.00	0.07	1.68	4.85E-10	4.51E-09	5.97E-13	6.20E-13	2.12E-06	2.20E-06
0.84	2.05	0.10	1.73	6.45E-10	4.67E-09	2.66E-13	2.63E-13	9.43E-07	9.32E-07
0.87	2.12	0.12	1.80	8.19E-10	4.85E-09	2.90E-13	3.08E-13	1.03E-06	1.09E-06
0.96	2.33	0.21	2.01	1.39E-09	5.43E-09	9.59E-13	9.65E-13	3.40E-06	3.42E-06
0.97	2.36	0.22	2.04	1.45E-09	5.51E-09	1.01E-13	1.23E-13	3.57E-07	4.35E-07
1.03	2.52	0.28	2.19	1.84E-09	5.93E-09	6.35E-13	7.07E-13	2.25E-06	2.51E-06
1.05	2.57	0.31	2.25	2.04E-09	6.08E-09	3.49E-13	2.51E-13	1.24E-06	8.89E-07
1.09	2.65	0.35	2.34	2.33E-09	6.32E-09	4.68E-13	4.00E-13	1.66E-06	1.42E-06
1.11	2.72	0.38	2.40	2.52E-09	6.51E-09	3.18E-13	3.11E-13	1.13E-06	1.10E-06
1.14	2.79	0.40	2.47	2.62E-09	6.70E-09	1.69E-13	3.17E-13	6.00E-07	1.12E-06
1.17	2.87	0.43	2.54	2.83E-09	6.90E-09	3.74E-13	3.50E-13	1.33E-06	1.24E-06
n/a	n/a	n/a	n/a	n/a	n/a	n/a	n/a	n/a	n/a
n/a	n/a	n/a	n/a	n/a	n/a	n/a	n/a	n/a	n/a
						Max Growth Rates			
						9.59E-13	2.59E-11		

Experiment 06-10-07

$\rho\uparrow = 0.575$ $\rho\downarrow = 0.725$ ($g \cdot cm^{-3}$)

t from T_H (hrs)	**T** (°C)	**P** ($\rho\uparrow$) (MPa)	**P** ($\rho\downarrow$)	**Chamber Vol.** (μm^3)	CV	**Qtz Vol.** (μm^3)	CV	**Ol Vol.** (μm^3) $\rho\uparrow$	$\rho\downarrow$
-0.03	347.2	17	67	1.37E+07	0.40%	6.12E+05	0.40%	6.32E+05	6.32E+05
0.00	363.9	25	85	1.38E+07	0.18%	6.10E+05	0.41%	6.32E+05	6.32E+05
0.02	653.9	227	405	1.14E+07	0.73%	4.71E+05	1.29%	5.94E+05	6.13E+05
0.03	655.6	229	406	1.10E+07	0.91%	4.32E+05	0.78%	5.73E+05	5.91E+05
0.20	653.4	227	404	1.05E+07	0.76%	4.24E+05	1.18%	5.67E+05	5.84E+05
0.36	656.0	229	407	1.05E+07	0.30%	4.15E+05	0.10%	5.63E+05	5.80E+05
0.53	653.4	227	404	1.04E+07	0.59%	4.07E+05	1.06%	5.59E+05	5.76E+05
0.70	656.7	229	408	1.04E+07	0.08%	4.02E+05	0.75%	5.56E+05	5.73E+05
0.86	654.0	228	405	1.05E+07	0.26%	3.99E+05	1.17%	5.54E+05	5.72E+05
1.03	655.7	229	406	1.04E+07	0.11%	4.04E+05	0.87%	5.57E+05	5.74E+05
1.20	654.5	228	405	1.04E+07	0.11%	3.90E+05	0.91%	5.50E+05	5.67E+05
1.36	654.8	228	406	1.04E+07	0.11%	3.92E+05	0.52%	5.51E+05	5.68E+05
1.53	656.9	230	408	1.04E+07	0.11%	4.05E+05	0.74%	5.58E+05	5.75E+05
1.70	652.7	227	403	1.04E+07	0.11%	4.23E+05	0.71%	5.66E+05	5.84E+05
1.86	657.2	230	408	1.04E+07	0.11%	4.40E+05	0.92%	5.75E+05	5.93E+05
2.03	653.2	227	404	1.04E+07	0.11%	4.53E+05	0.61%	5.82E+05	5.99E+05
2.20	654.8	228	406	1.04E+07	0.11%	4.59E+05	0.75%	5.85E+05	6.02E+05
2.36	656.8	229	408	1.04E+07	0.11%	4.59E+05	0.56%	5.85E+05	6.02E+05
2.53	656.3	229	407	1.04E+07	0.11%	4.68E+05	0.87%	5.90E+05	6.07E+05
2.70	653.6	227	404	1.04E+07	0.11%	4.68E+05	0.86%	5.89E+05	6.07E+05
2.86	654.8	228	406	1.04E+07	0.11%	4.73E+05	0.42%	5.92E+05	6.09E+05
3.03	653.4	227	404	1.04E+07	0.11%	4.61E+05	1.08%	5.86E+05	6.03E+05
3.20	654.3	228	405	1.04E+07	0.11%	4.55E+05	0.89%	5.83E+05	6.00E+05
3.36	655.9	229	407	1.04E+07	0.11%	4.63E+05	1.45%	5.87E+05	6.04E+05
3.53	656.0	229	407	1.04E+07	0.11%	4.60E+05	1.31%	5.86E+05	6.03E+05
3.70	655.3	228	406	1.04E+07	0.11%	4.36E+05	0.74%	5.73E+05	5.90E+05
3.77	656.2	229	407	1.04E+07	0.11%	4.27E+05	1.41%	5.69E+05	5.86E+05
3.80	284.4	1	8	1.04E+07	0.11%	4.61E+05	0.82%	5.62E+05	5.65E+05
3.84	202.5	1	1	1.04E+07	0.11%	n/a	n/a	n/a	n/a

Experiment 06-10-07 (cont.)

App. mSiO$_2$ (mol SiO$_2$ / kg H$_2$O)		**App. mSiO$_2$ - Qtz Sat** (mol SiO$_2$ / kg H$_2$O)		**Tlc produced** (mol)		**Tlc growth rate** (mol · sec^{-1})		**Tlc growth rate** (mol · sec^{-1} · m^{-2})	
ρ↑	ρ↓	ρ↑	ρ↓	ρ↑	ρ↓	ρ↑	ρ↓	ρ↑	ρ↓
n/a	n/a	n/a	n/a	n/a	n/a	n/a	n/a	n/a	n/a
0.00	0.00	0.00	0.00	0.00E+00	0.00E+00	0.00E+00	0.00E+00	0.00E+00	0.00E+00
1.03	0.82	0.55	0.22	1.30E-09	6.49E-10	2.20E-11	1.10E-11	9.69E-05	4.83E-05
1.38	1.09	0.89	0.48	2.02E-09	1.39E-09	1.68E-11	1.73E-11	7.52E-05	7.72E-05
1.51	1.20	1.03	0.60	2.23E-09	1.64E-09	3.47E-13	4.06E-13	1.58E-06	1.85E-06
1.58	1.25	1.10	0.65	2.38E-09	1.78E-09	2.48E-13	2.45E-13	1.13E-06	1.11E-06
1.66	1.31	1.17	0.71	2.52E-09	1.92E-09	2.30E-13	2.32E-13	1.05E-06	1.06E-06
1.69	1.34	1.21	0.74	2.62E-09	2.02E-09	1.61E-13	1.63E-13	7.32E-07	7.45E-07
1.71	1.36	1.23	0.76	2.67E-09	2.07E-09	8.25E-14	7.80E-14	3.75E-07	3.55E-07
1.68	1.33	1.19	0.73	2.57E-09	1.98E-09	-1.52E-13	-1.51E-13	-6.95E-07	-6.89E-07
1.80	1.42	1.31	0.82	2.83E-09	2.23E-09	4.26E-13	4.29E-13	1.95E-06	1.96E-06
1.78	1.41	1.29	0.81	2.79E-09	2.19E-09	-6.57E-14	-6.64E-14	-3.00E-07	-3.03E-07
1.68	1.33	1.19	0.72	2.56E-09	1.96E-09	-3.86E-13	-3.92E-13	-1.76E-06	-1.79E-06
1.53	1.21	1.05	0.61	2.25E-09	1.66E-09	-5.11E-13	-4.96E-13	-2.33E-06	-2.27E-06
1.40	1.11	0.91	0.50	1.95E-09	1.35E-09	-5.07E-13	-5.20E-13	-2.32E-06	-2.37E-06
1.29	1.02	0.81	0.42	1.73E-09	1.14E-09	-3.68E-13	-3.54E-13	-1.68E-06	-1.62E-06
1.24	0.98	0.75	0.38	1.61E-09	1.02E-09	-1.89E-13	-1.93E-13	-8.61E-07	-8.83E-07
1.24	0.98	0.75	0.38	1.61E-09	1.02E-09	-5.98E-17	-6.20E-15	-2.73E-10	-2.83E-08
1.17	0.92	0.68	0.32	1.45E-09	8.56E-10	-2.70E-13	-2.67E-13	-1.23E-06	-1.22E-06
1.17	0.93	0.68	0.32	1.46E-09	8.74E-10	2.25E-14	3.12E-14	1.03E-07	1.42E-07
1.13	0.90	0.65	0.29	1.38E-09	7.87E-10	-1.42E-13	-1.45E-13	-6.49E-07	-6.64E-07
1.23	0.97	0.74	0.37	1.59E-09	1.00E-09	3.53E-13	3.56E-13	1.61E-06	1.63E-06
1.27	1.01	0.79	0.40	1.69E-09	1.09E-09	1.58E-13	1.55E-13	7.22E-07	7.06E-07
1.21	0.96	0.72	0.35	1.55E-09	9.51E-10	-2.33E-13	-2.37E-13	-1.06E-06	-1.08E-06
1.23	0.97	0.74	0.37	1.59E-09	9.95E-10	7.37E-14	7.31E-14	3.37E-07	3.34E-07
1.43	1.13	0.94	0.53	2.02E-09	1.43E-09	7.20E-13	7.20E-13	3.29E-06	3.29E-06
1.50	1.18	1.01	0.58	2.17E-09	1.57E-09	5.52E-13	5.43E-13	2.52E-06	2.48E-06
1.23	0.97	1.13	0.85	2.41E-09	2.28E-09	1.88E-12	5.55E-12	8.59E-06	2.53E-05
n/a	n/a	n/a	n/a	n/a	n/a	n/a	n/a	n/a	n/a
						Max Growth Rates			
						2.20E-11	1.73E-11		

B-2. *In Situ* Photomicrographs of Experiments

This appendix provides photomicrographs of experiments. The photomicrographs are screen capture images acquired from videos of experiments; each image has a horizontal field of view of 590 µm. Most photomicrographs are sets of four images taken during the following event during the experiment: the time of prograde homogenization, the first visible appear of fibers (1^{st} fibers), and the time of retrograde homogenization. Each image has the time (t) and temperature (T) labeled as well as the mineral phases present (i.e., Ol - olivine, Qtz - quartz).

Experiment: 06-09-07 – plate dominated

Just after Prograde Homogenization

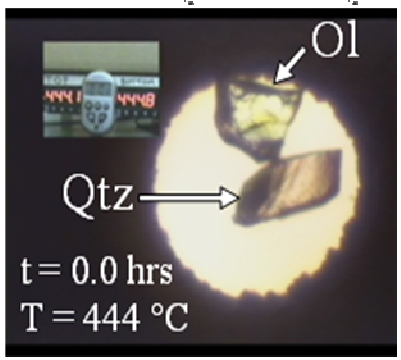

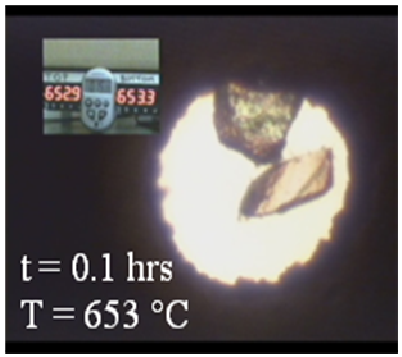

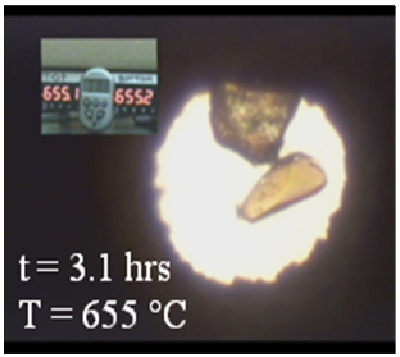

Retrograde Homogenization

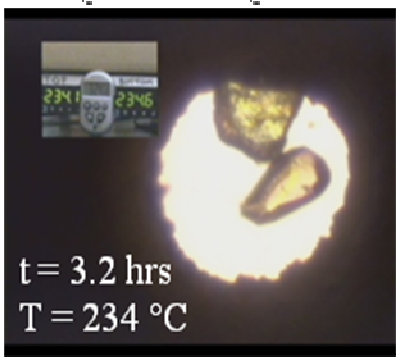

Experiment: 07-09-07 – plate dominated

Prograde Homogenization

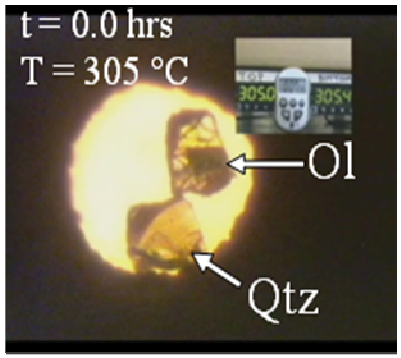

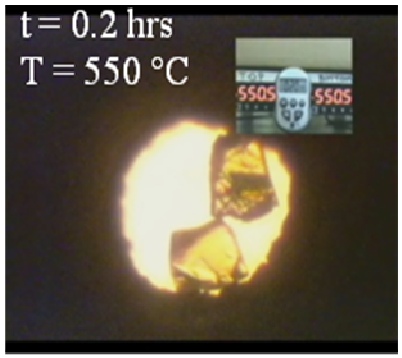

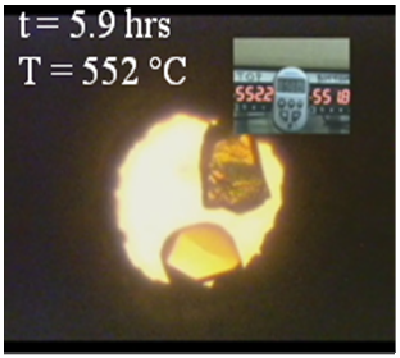

Retrograde Homogenization

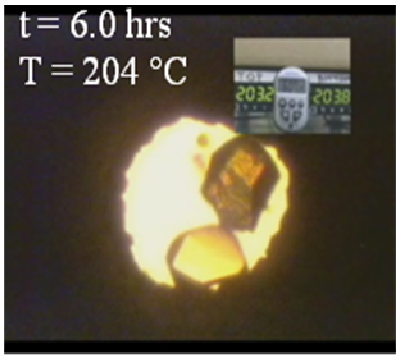

Experiment: 08-23-07 – both plates and fibers present

Prograde Homogenization

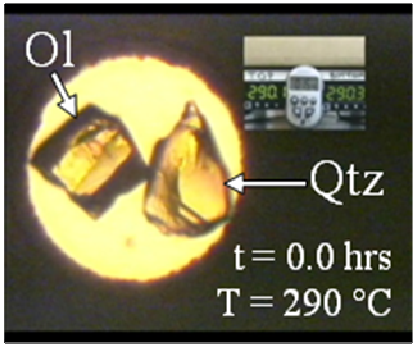

1st fibers

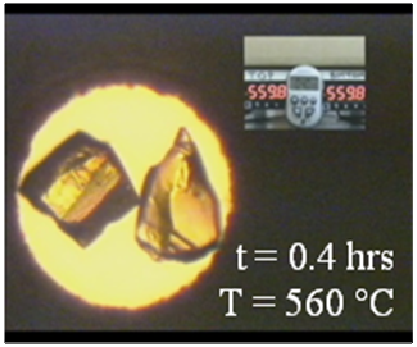

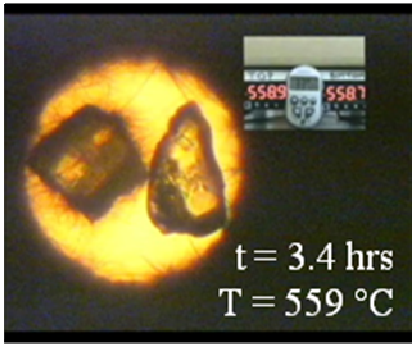

Retrograde Homogenization

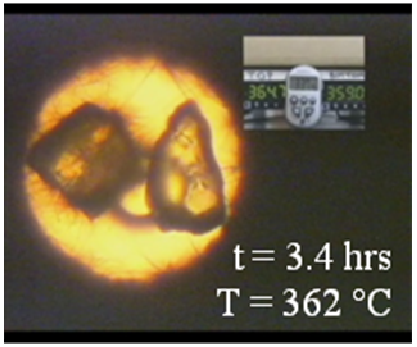

Experiment: 02-24-08 – both plates and fibers present

Homogenization

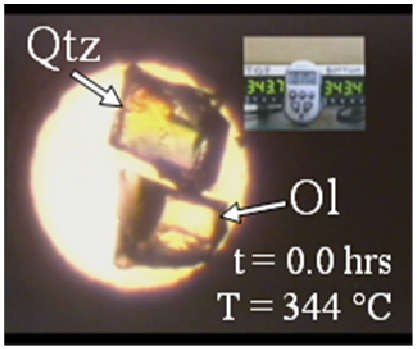

1st fibers

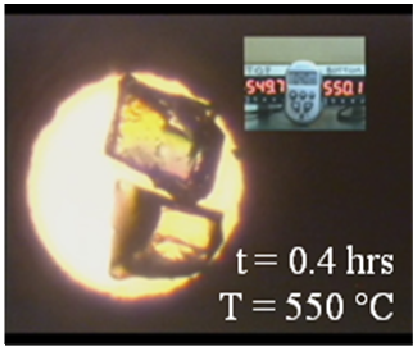

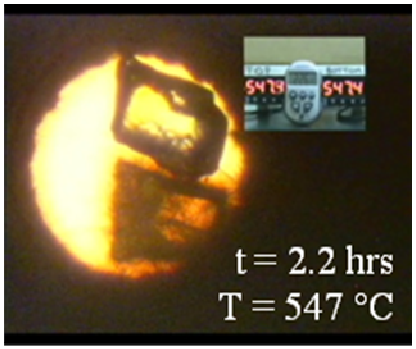

Retrograde Homogenization

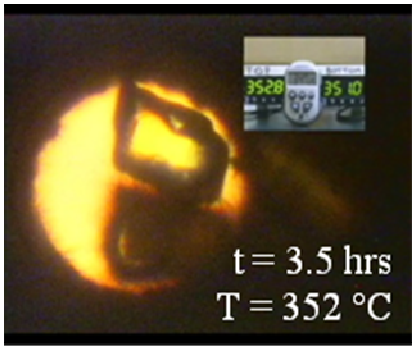

Experiment: 08-27-08 – both plates and fibers present

Prograde Homogenization | 1st fibers | Retrograde Homogenization

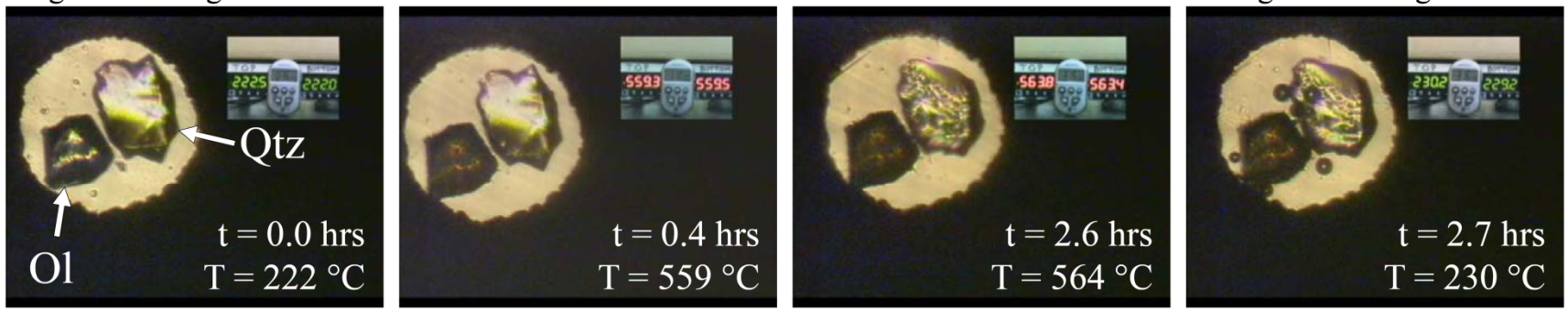

Experiment: 09-05-07 – fiber dominated

Prograde Homogenization | 1st fibers | Retrograde Homogenization

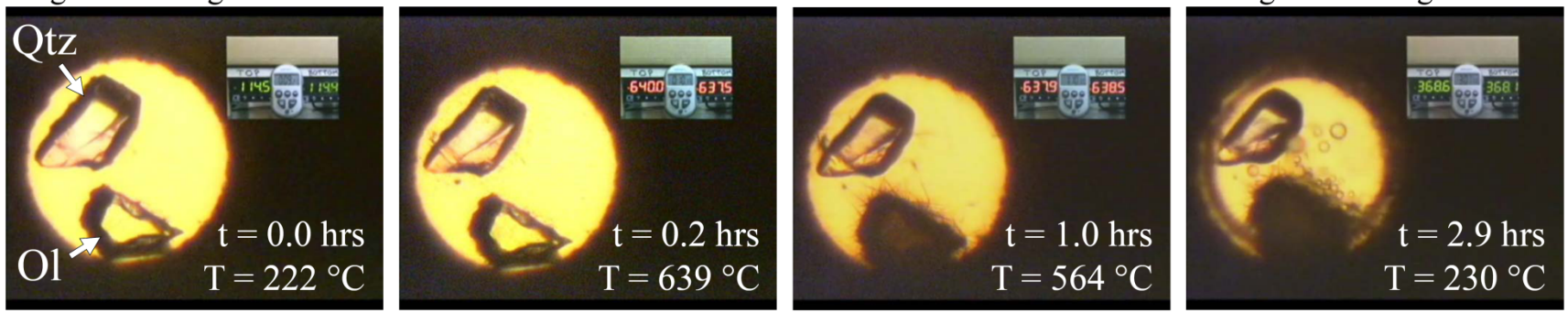

Experiment: 06-10-07 – fiber dominated

Prograde Homogenization

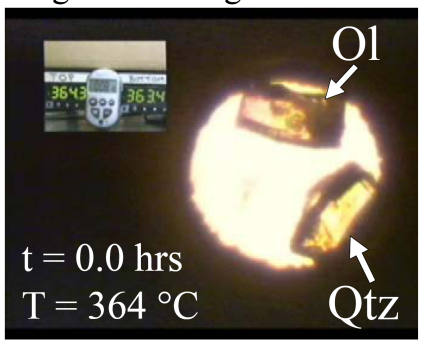

1st fibers

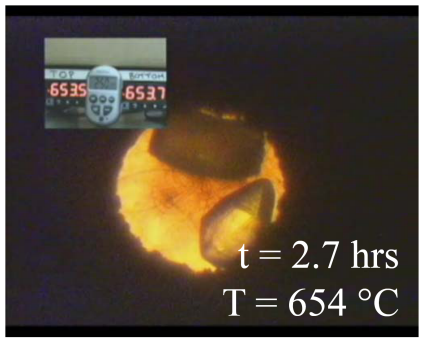

Retrograde Homogenization

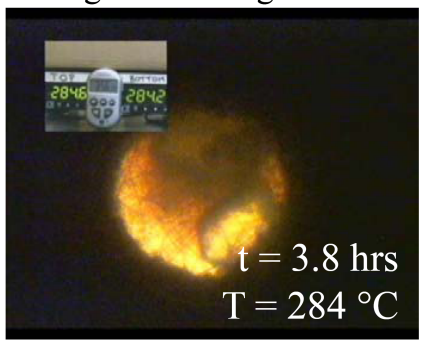

B-3. Post-experiment Secondary Electron Images

This appendix provides secondary electron images of post-experiment reaction products collect on a JEOL JXA-8900 electron probe microanalyzer. Each image is accompanied by a scale and a short description of the phases present. Phase identification was determined by SR-XRD and energy dispersive spectroscopy.

Experiment: Run 18 – plate dominated

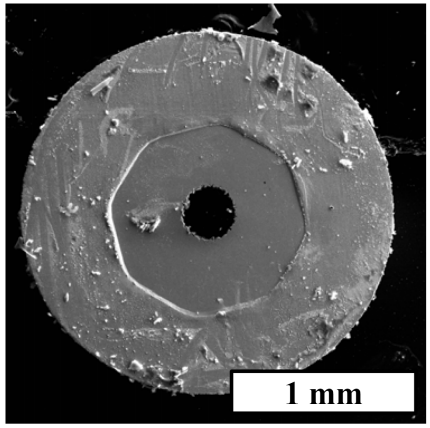

view of full gasket

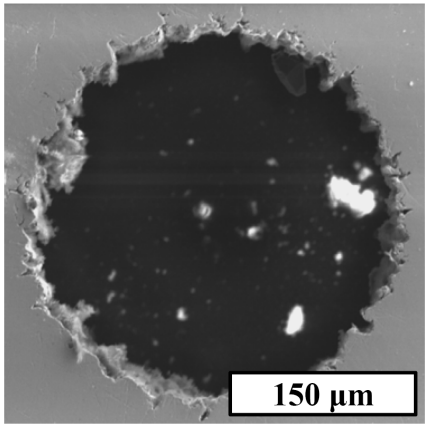

view of empty gasket aperture

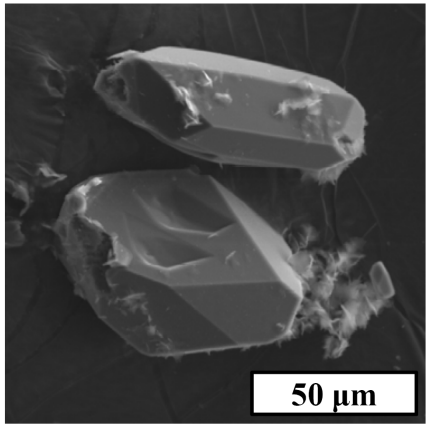

quartz grains on carbon tape

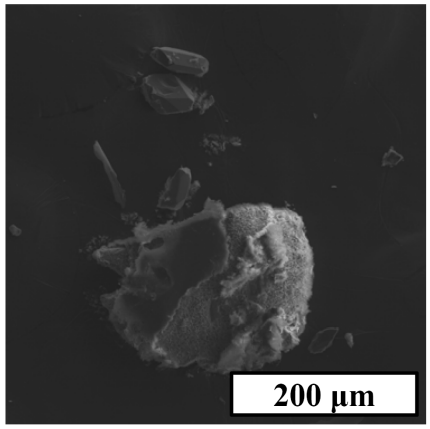

talc plates and fibers on olivine and quartz on carbon tape

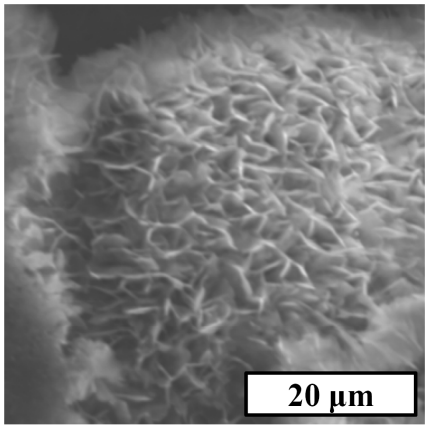

talc plates on olivine

Experiment: Run 23 – plate dominated

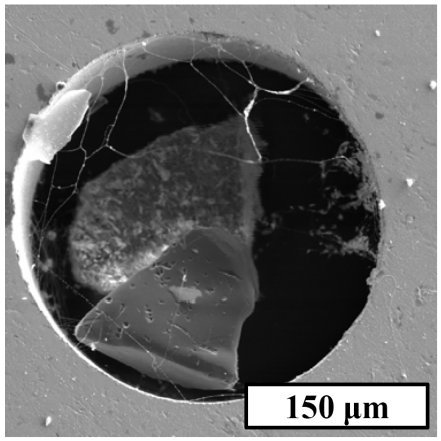

view of gasket aperture

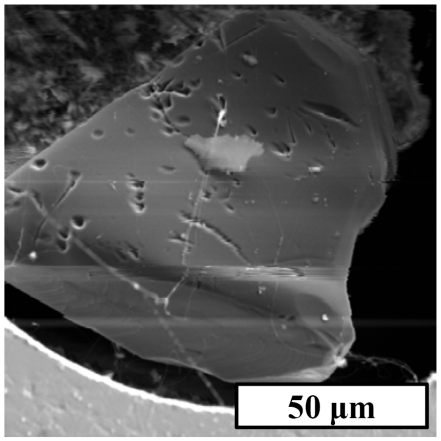

etch pits on quartz

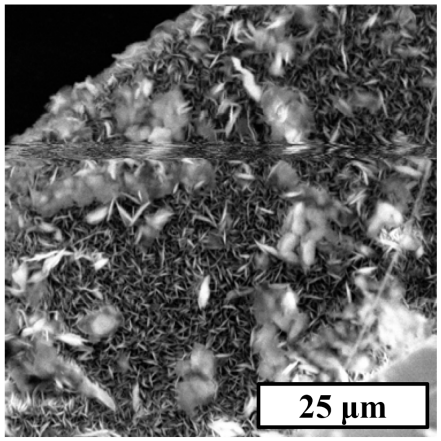

talc plates on olivine

Experiment: 08-23-07 – both plates and fibers present

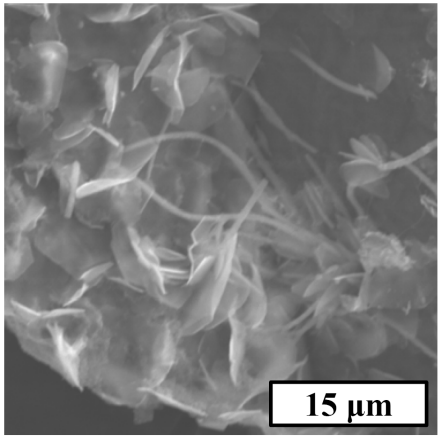

talc plates and fibers on olivine

Experiment: Run 13 – both plates and fibers present

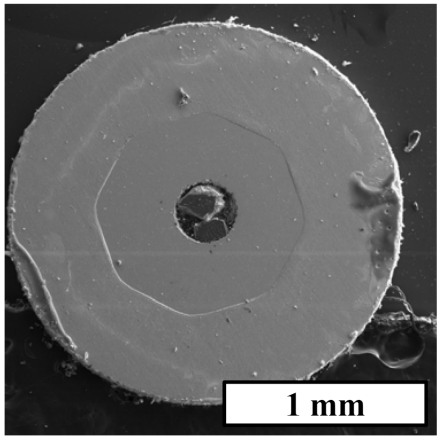

view of full gasket

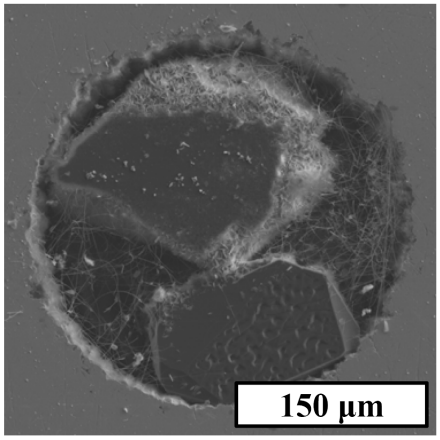

view of gasket aperture

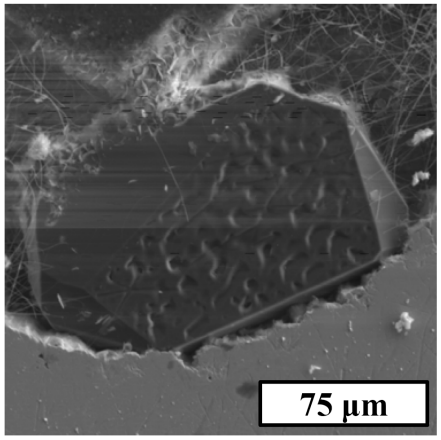

etch pits where quartz was in contact with the diamond

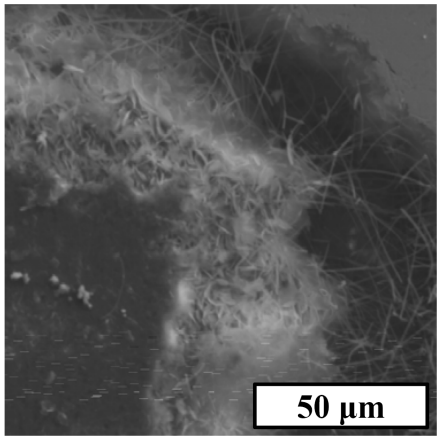

talc plates and fibers on olivine

Experiment: Run 11 – both plates and fibers present

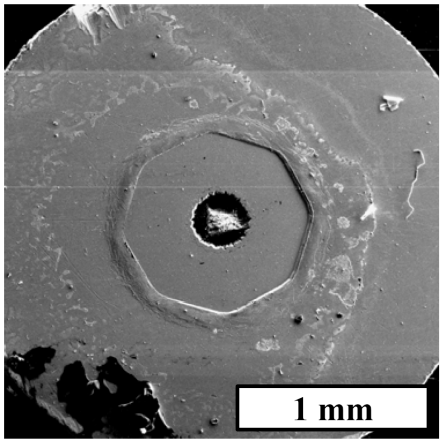

view of full gasket

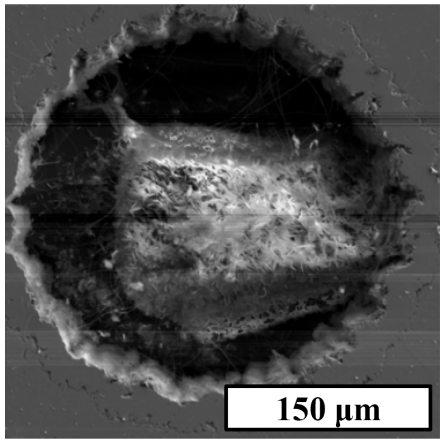

view of gasket aperture

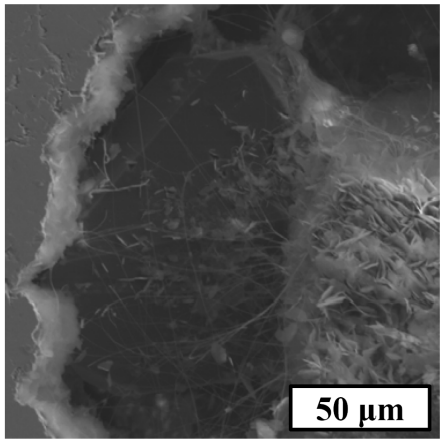

quartz and talc plates and fibers

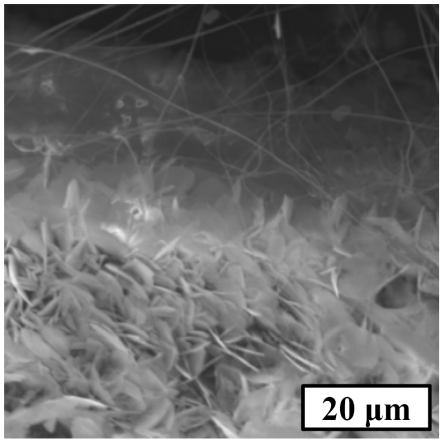

talc plates and fibers on olivine

Experiment: 06-10-07 – fiber dominated

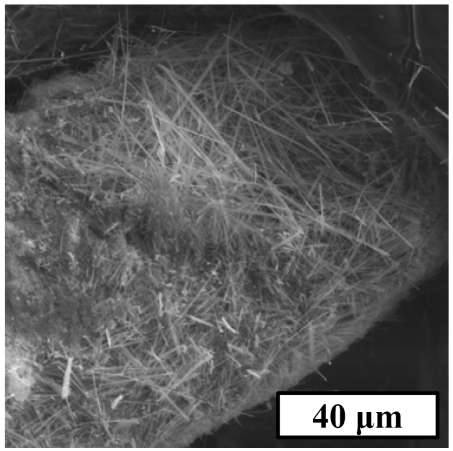

talc fibers on olivine

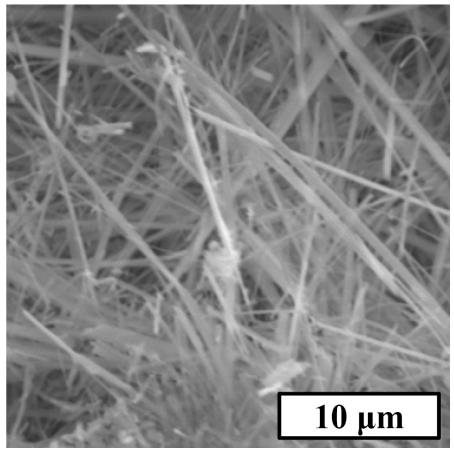

talc fibers on olivine

B-4. Synchrotron Radiation X-ray Diffraction Plates for 'Run 11'

This appendix provides some of the plates produced during synchrotron radiation x-ray diffraction analysis of an experiment (Run 11). The starting materials for this experiment were olivine + quartz + water. The experiment was held at two isothermal temperature steps: first at 600 °C for 1.82 hours and second at 650 °C for 0.75 hours). The four plates presented are the raw data collected as represented in the program Fit2d® by an inverse grey scale and the labeled by time and experimental temperature at collection.

Spectra: Run 11_001
Collection time: 0.00 hours
Temperature: 400 °C

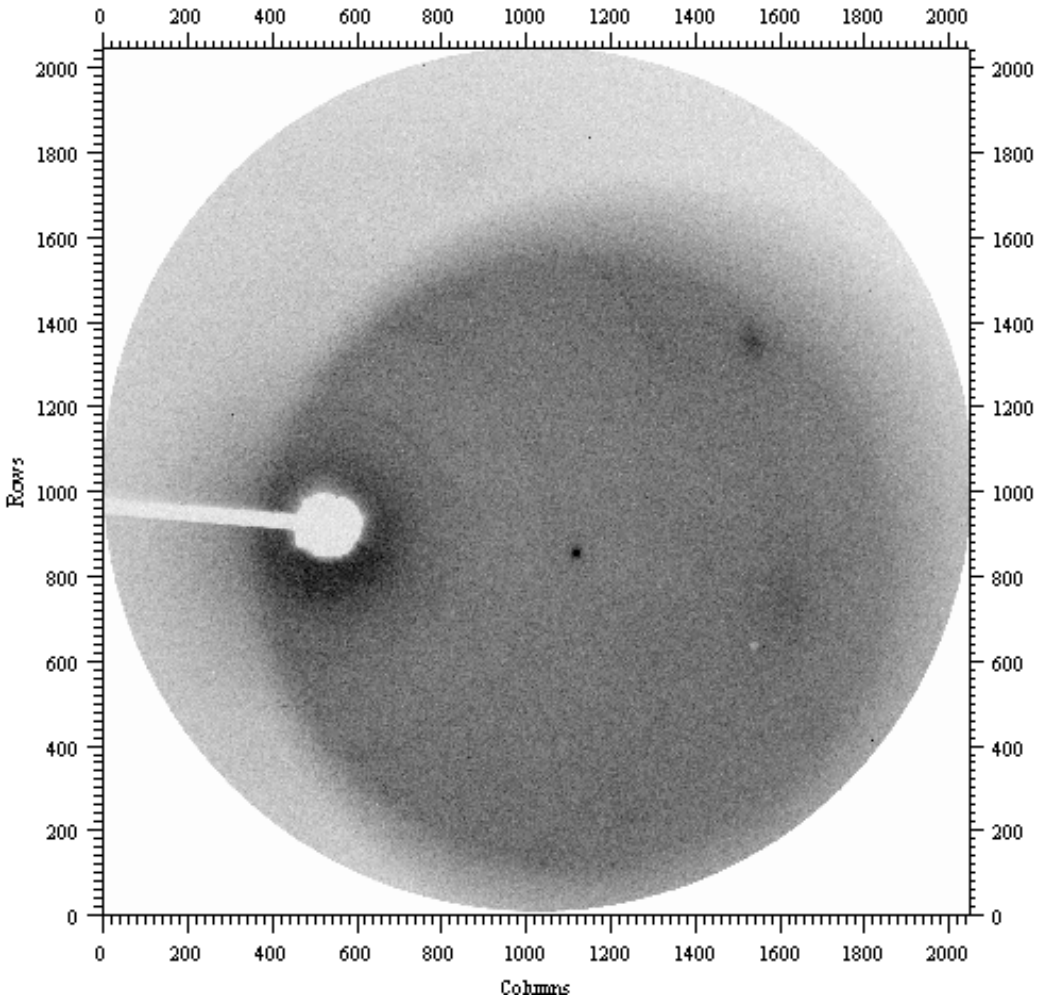

Spectra: Run 11_014
Collection time: 1.00 hours
Temperature: 600 °C

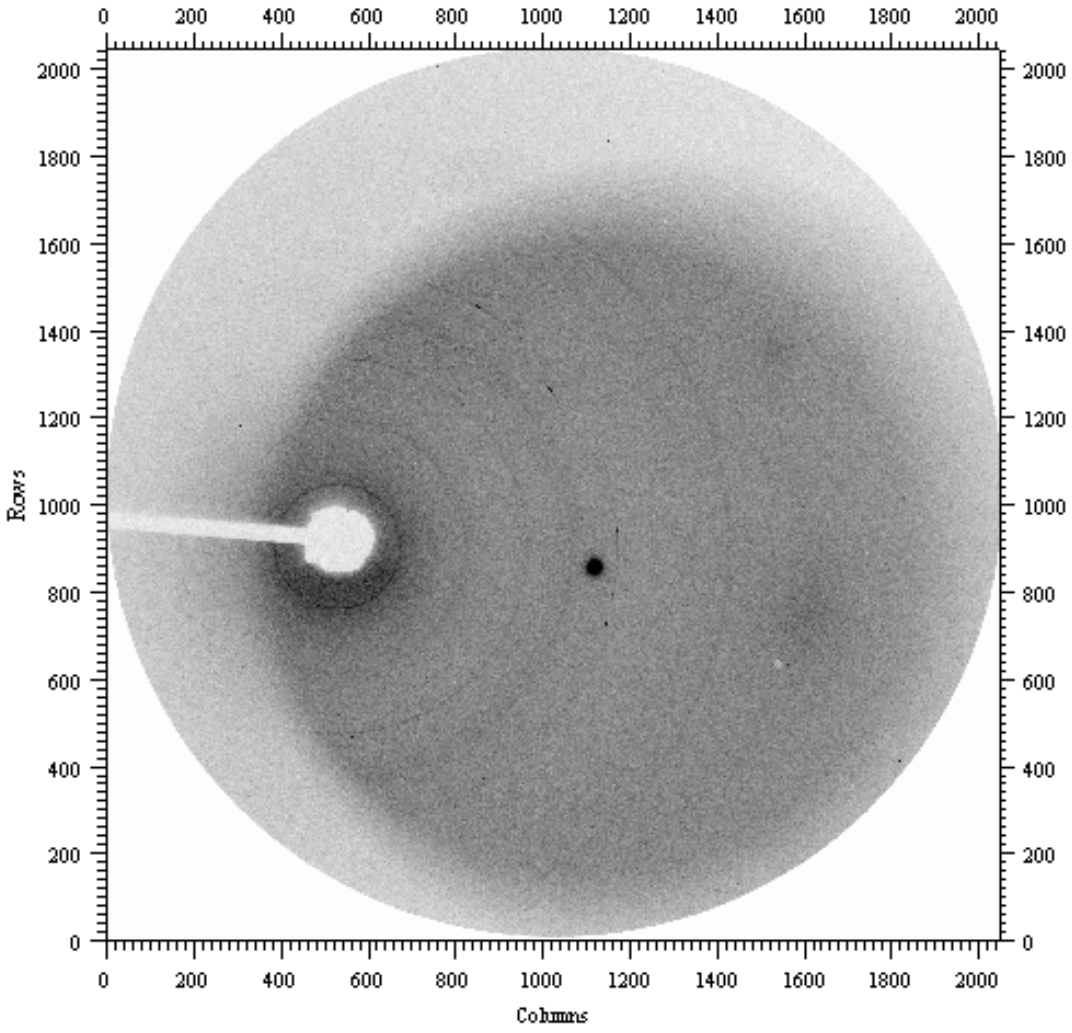

Spectra: Run 11_022
Collection time: 1.84 hours
Temperature: 600 °C

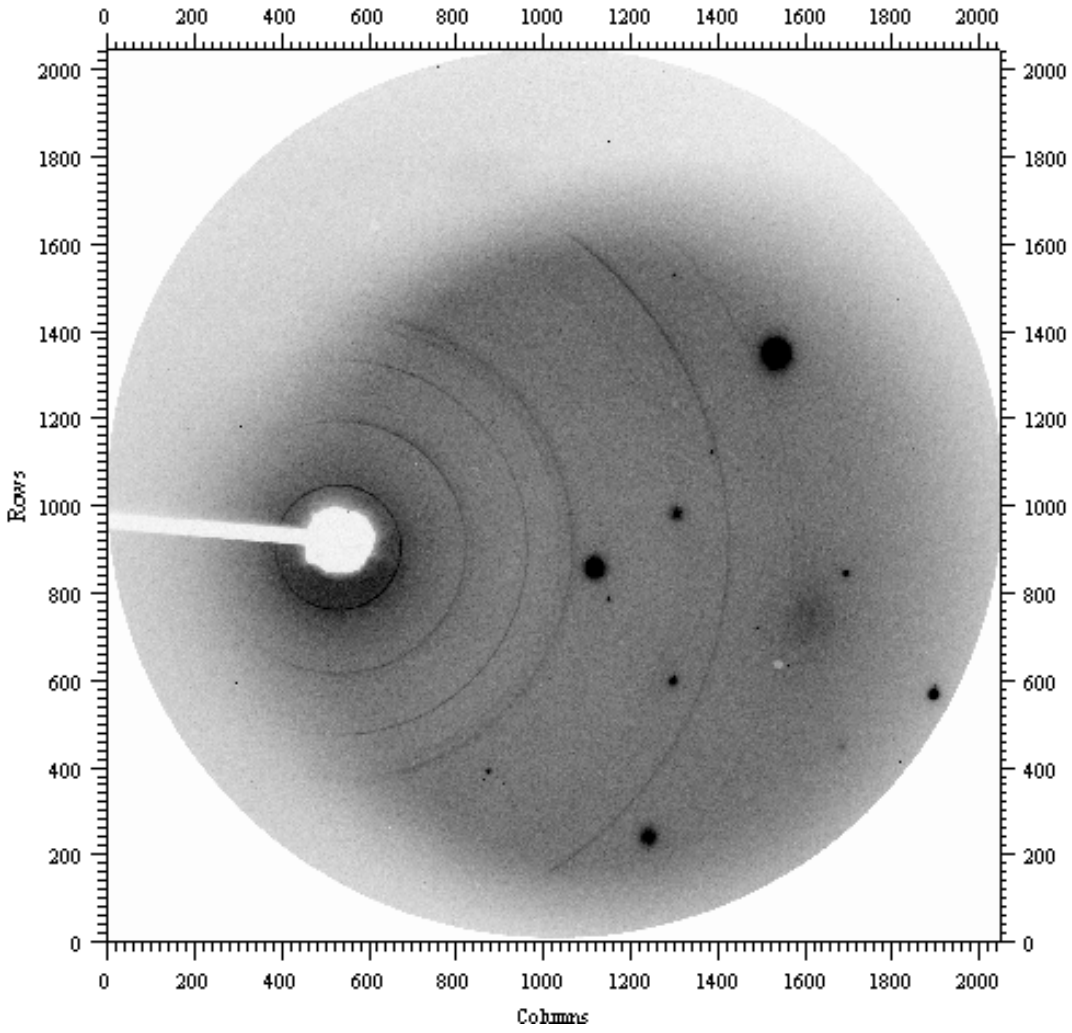

Spectra: Run 11_028
Collection time: 2.59 hours
Temperature: 650 °C

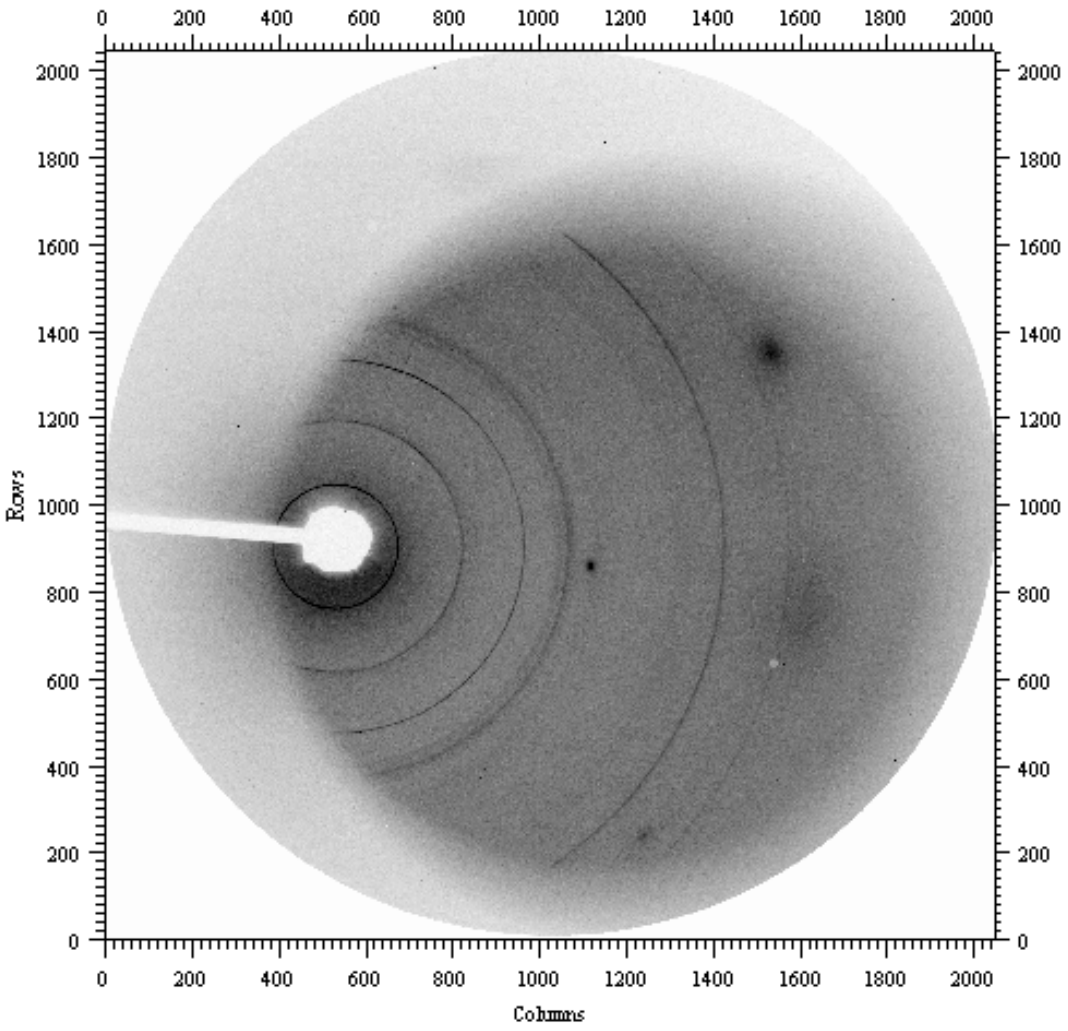

Appendix C – Supplementary Data for Chapter Four

This appendix contains supplementary materials for experiments presented in Chapter Three. It is subdivided into three sections: C-1. Data tables for *in situ* mass loss determinations; C-2. *In-situ* photomicrographs of experiments; and C-3. Post-experiment secondary electron images.

C-1. Data Tables for *In Situ* Mass Loss Determination

Measurements and results from *in situ* mass loss determinations made via visual analysis of screen capture images from experiment videos. Each row of data is specific to the screen capture image acquired at the indicated time into the experiment. See the text of the document for additional explanation of the methodology. To conserve space, the following abbreviations have been used:

Column 1: *t from T_H (hrs)* - time into the experiment the screen capture image was acquired in relation to the time of the homogenization temperature, just before the initial rise in temperature.

Column 2: *T (°C)* - temperature of the cell in degrees Celsius.

Column 3: *$\rho\uparrow$ ($g \cdot cm^{-3}$), P($\rho\uparrow$) (MPa)* - $\rho\uparrow$ is the density of the fluid given by the prograde liquid-vapor homogenization determined at the beginning of the experiment. P($\rho\uparrow$) is the pressure (in MPa) determined by using the isochoric relationships of pure water for the prograde homogenization density (Wagner and Pruss, 2002).

Column 4: *$\rho\downarrow$ ($g \cdot cm^{-3}$), P($\rho\downarrow$) (MPa)* - $\rho\downarrow$ is the density of the fluid given by the retrograde liquid-vapor homogenization determined at the end of the experiment. P($\rho\downarrow$) is the pressure (in MPa) determined by the using the isochoric relationships of pure water for the retrograde homogenization density (Wagner and Pruss, 2002).

Column 5 & 6: *Chamber Vol. (μm^3), CV* - volume of the chamber, determined by measuring the cross-sectional area of the chamber aperture and multiplying by the thickness of the rhenium foil. Cross-sectional area measurements were made in triplicate, the coefficient of variation (CV) has been provided. The chamber volume was assumed to be constant after the first hour.

Column 7 & 8: *Qtz Vol. (μm^3), CV* - volume of the quartz grain, determined by measuring the cross-sectional area of the quartz grain and by treating it as an idealized 2:1 ellipse to find the two primary axes of the ellipse. The volume of the ellipsoid was determined by assuming the third axis as equal to the short axis of the ellipse.

Column 9 & 10: *Mgs Vol. (μm^3), ($\rho\uparrow$), ($\rho\downarrow$)* - volume of the magnesite grain. Initial measurements were made at the time of prograde homogenization. The cross-sectional area of the magnesite grain was treated as an idealized 2:1 ellipse to find the two primary axes of the ellipse. The volume was determined by assuming the third axis as being equal to 50 µm based on a natural parting in the starting materials, and treating the magnesite grain as an elliptical cylinder. After homogenization, magnesite volume was assumed to decrease by the amount necessary to produce the estimated amount of talc grown. The estimated amount talc growth will vary depending on the density of the fluid, therefore the estimated volume of magnesite is provided for both prograde and retrograde densities.

Page 2 of the data tables:

Column 11 & 12: *App. m*SiO_2 *(mol SiO_2/kg H_2O+CO_2), (ρ↑), (ρ↓)* - the apparent concentration of silica in solution (molality). Moles of silica were determined by measuring the amount of quartz volume decrease from its size at the time of prograde homogenization. The mass of water was determined by measuring the volume of the chamber and subtracting the volumes of the quartz and magnesite grains at the time of prograde homogenization and, as reactions progressed, subtracting the amount of water consumed during the production of talc. The mass of carbon dioxide is determined by the assumed amount of magnesite decarbonation necessary to produce the estimated amount of talc grown. The masses of water and carbon dioxide in the cell will vary with the determined densities, therefore it is provided for the prograde and retrograde densities.

Column 13 & 14: *App. m*SiO_2 *- Qtz Sat. (mol SiO_2/kg H_2O+CO_2), (ρ↑), (ρ↓)* - the concentration of silica in excess of quartz saturation determined by subtracting the calculated molality of quartz saturation (following the method of Akinfiev and Diamond, 2009) from the apparent molality of silica.

Column 15 & 16: *Tlc produced (mol), (ρ↑), (ρ↓)* - the estimated amount of talc grown (in moles) determined by assuming all silica in excess of quartz saturation is consumed in the following reaction: $3Mgs + 4Qtz + 1H_2O = 1Tlc + 3CO_2$.

Column 17 & 18: *Tlc growth rate (mol · sec^{-1}), (ρ↑), (ρ↓)* - talc growth rate in moles per second calculated by determining the amount of moles of talc produced in between each screen capture image divided by the time change. At the bottom of the columns, the maximum growth rate of the experiment is reported (*Max Growth Rates)*, not inclusive of what may be interpreted as growth upon quench.

Column 19 & 20: *Tlc growth rate (mol · sec^{-1} · m^{-2}), (ρ↑), (ρ↓)* - talc growth rate in moles per second per unit area of growth surfaces calculated from changes between each screen capture image. Growth surface areas are determined by adding the surface areas of the magnesite grain and the wall of the gasket (these locations are normally the only areas where talc grows); values are semi-quantitative.

Column 21 & 22: *Carbon Dioxide (mole percent), (ρ↑), (ρ↓)* - mole percent of carbon dioxide. The mole percent of carbon dioxide is determined by the calculated amount of magnesite decarbonation necessary to produce the calculated volume of talc grown.

Experiment 11-04-09

$\rho\uparrow = 0.821$ $\rho\downarrow = 0.677$ ($g \cdot cm^{-3}$)

t from T_H (hrs)	**T** (°C)	**P** ($\rho\uparrow$) (MPa)	**P** ($\rho\downarrow$)	**Chamber Vol.** (μm^3)	CV	**Qtz Vol.** (μm^3)	CV	**Mgs Vol.** (μm^3) $\rho\uparrow$	$\rho\downarrow$
0.00	227.8	2	2	1.23E+07	0.32%	6.90E+05	0.62%	2.18E+06	2.18E+06
0.01	464.4	333	151	1.19E+07	0.30%	6.26E+05	0.34%	2.18E+06	2.18E+06
0.02	464.2	332	150	1.19E+07	0.40%	5.70E+05	0.25%	2.14E+06	2.14E+06
0.19	472.4	345	158	1.17E+07	0.14%	4.82E+05	2.19%	2.05E+06	2.07E+06
0.35	466.1	335	152	1.19E+07	0.17%	4.28E+05	3.48%	2.00E+06	2.03E+06
0.52	461.5	328	148	1.20E+07	0.14%	3.64E+05	2.08%	1.94E+06	1.98E+06
0.69	466.6	336	153	1.20E+07	0.49%	3.56E+05	2.25%	1.94E+06	1.97E+06
0.85	464.6	333	151	1.21E+07	0.37%	3.17E+05	3.26%	1.90E+06	1.94E+06
1.02	464.9	333	151	1.21E+07	0.43%	3.08E+05	2.37%	1.89E+06	1.94E+06
1.19	465.2	334	151	1.21E+07	0.43%	2.99E+05	2.27%	1.88E+06	1.93E+06
1.35	457.5	323	144	1.21E+07	0.43%	2.60E+05	2.64%	1.84E+06	1.90E+06
1.50	461.2	331	149	1.21E+07	0.43%	2.05E+05	2.64%	1.78E+06	1.85E+06
1.52	511.8	400	196	1.21E+07	0.43%	1.72E+05	1.70%	1.78E+06	1.84E+06
1.69	514.7	404	199	1.21E+07	0.43%	1.32E+05	2.86%	1.74E+06	1.80E+06
1.85	516.7	407	201	1.21E+07	0.43%	8.86E+04	3.08%	1.70E+06	1.77E+06
2.00	518.9	413	205	1.21E+07	0.43%	6.52E+04	3.08%	1.68E+06	1.75E+06
2.02	562.1	470	244	1.21E+07	0.43%	2.50E+04	2.19%	1.65E+06	1.73E+06
2.19	561.7	470	244	1.21E+07	0.43%	0.00E+00	0.00%	1.63E+06	1.71E+06
2.35	566.3	476	249	1.21E+07	0.43%	0.00E+00	0.00%	1.63E+06	1.71E+06
2.50	568.4	483	253	1.21E+07	0.43%	0.00E+00	0.00%	1.63E+06	1.71E+06
2.52	611.6	539	292	1.21E+07	0.43%	0.00E+00	0.00%	1.65E+06	1.73E+06
2.69	611.2	538	291	1.21E+07	0.43%	0.00E+00	0.00%	1.65E+06	1.73E+06
2.85	611.2	538	291	1.21E+07	0.43%	0.00E+00	0.00%	1.65E+06	1.73E+06
3.02	609.4	536	289	1.21E+07	0.43%	0.00E+00	0.00%	1.65E+06	1.73E+06
3.19	612.6	540	292	1.21E+07	0.43%	0.00E+00	0.00%	1.65E+06	1.73E+06
3.35	613.0	540	293	1.21E+07	0.43%	0.00E+00	0.00%	1.65E+06	1.73E+06
3.52	614.0	542	294	1.21E+07	0.43%	0.00E+00	0.00%	1.65E+06	1.73E+06
3.69	613.3	541	293	1.21E+07	0.43%	0.00E+00	0.00%	1.65E+06	1.73E+06
3.85	613.9	542	294	1.21E+07	0.43%	0.00E+00	0.00%	1.65E+06	1.73E+06
4.02	462.2	329	149	1.21E+07	0.43%	0.00E+00	0.00%	1.59E+06	1.68E+06
4.19	465.9	335	152	1.21E+07	0.43%	0.00E+00	0.00%	1.60E+06	1.69E+06
4.35	460.9	328	147	1.21E+07	0.43%	0.00E+00	0.00%	1.60E+06	1.69E+06
4.52	463.3	331	147	1.21E+07	0.43%	0.00E+00	0.00%	1.60E+06	1.69E+06
4.69	461.9	329	148	1.21E+07	0.43%	0.00E+00	0.00%	1.60E+06	1.69E+06
4.85	461.1	328	147	1.21E+07	0.43%	0.00E+00	0.00%	1.60E+06	1.69E+06
5.01	462.5	330	149	1.21E+07	0.43%	0.00E+00	0.00%	1.60E+06	1.69E+06
5.02	301.5	97	9	1.21E+07	0.43%	0.00E+00	0.00%	1.60E+06	1.69E+06

Experiment 11-04-09 (cont.)

(Max. Growth Rate in Bold)

App. *m*SiO_2 (mol SiO_2 / kg H_2O+CO_2)		***m*SiO_2 - Qtz Sat** (mol SiO_2 / kg H_2O+CO_2)		**Tlc produced** (mol)		**Tlc growth rate** (mol · sec^{-1})		**Tlc growth rate** (mol · sec^{-1} · m^{-2})		**Carbon Dioxide** (mole percent)	
ρ↑	ρ↓	ρ↑	ρ↓	ρ↑	ρ↓	ρ↑	ρ↓	ρ↑	ρ↓	ρ↑	ρ↓
0.00	0.00	0.00	0.00	0.00E+00	0.00E+00	0.00E+00	0.00E+00	0.00E+00	0.00E+00	0.00%	0.00%
0.36	0.46	0.00	0.02	0.00E+00	0.00E+00	0.00E+00	0.00E+00	0.00E+00	0.00E+00	0.00%	0.00%
0.68	0.86	0.27	0.34	5.28E-10	5.30E-10	**1.76E-11**	**1.77E-11**	6.47E-05	6.49E-05	0.37%	0.37%
1.18	1.49	0.76	0.83	1.51E-09	1.32E-09	1.64E-12	1.31E-12	6.04E-06	4.84E-06	1.04%	0.90%
1.49	1.88	1.04	1.11	2.08E-09	1.79E-09	9.50E-13	7.84E-13	3.49E-06	2.88E-06	1.43%	1.22%
1.85	2.34	1.39	1.47	2.82E-09	2.39E-09	1.23E-12	1.01E-12	4.52E-06	3.68E-06	1.94%	1.62%
1.90	2.39	1.42	1.50	2.89E-09	2.46E-09	1.23E-13	1.06E-13	4.49E-07	3.87E-07	1.99%	1.66%
2.12	2.68	1.63	1.71	3.33E-09	2.82E-09	7.34E-13	6.08E-13	2.68E-06	2.22E-06	2.29%	1.90%
2.17	2.74	1.67	1.75	3.42E-09	2.89E-09	1.39E-13	1.19E-13	5.08E-07	4.34E-07	2.34%	1.94%
2.22	2.80	1.71	1.80	3.52E-09	2.98E-09	1.68E-13	1.40E-13	6.13E-07	5.10E-07	2.41%	2.00%
2.44	3.09	1.92	2.01	3.98E-09	3.36E-09	7.65E-13	6.34E-13	2.80E-06	2.32E-06	2.72%	2.24%
2.76	3.48	2.24	2.31	4.67E-09	3.90E-09	1.28E-12	1.01E-12	4.69E-06	3.69E-06	3.18%	2.59%
2.94	3.71	2.27	2.39	4.76E-09	4.05E-09	1.48E-12	2.42E-12	5.42E-06	8.86E-06	3.24%	2.68%
3.17	4.00	2.48	2.60	5.24E-09	4.44E-09	7.95E-13	6.58E-13	2.90E-06	2.40E-06	3.56%	2.93%
3.42	4.32	2.69	2.81	5.72E-09	4.85E-09	7.97E-13	6.82E-13	2.91E-06	2.49E-06	3.88%	3.18%
3.55	4.48	2.79	2.91	5.95E-09	5.05E-09	4.34E-13	3.78E-13	1.58E-06	1.38E-06	4.03%	3.31%
3.78	4.77	2.90	3.04	6.21E-09	5.31E-09	4.34E-12	4.23E-12	1.58E-05	1.55E-05	4.20%	3.47%
3.92	4.95	3.02	3.16	6.49E-09	5.55E-09	4.69E-13	3.97E-13	1.71E-06	1.45E-06	4.39%	3.61%
3.92	4.95	3.01	3.15	6.47E-09	5.53E-09	-4.18E-14	-2.92E-14	-1.53E-07	-1.07E-07	4.37%	3.60%
3.92	4.95	3.00	3.15	6.45E-09	5.52E-09	-3.75E-14	-2.68E-14	-1.37E-07	-9.79E-08	4.36%	3.59%
3.92	4.95	2.90	3.07	6.22E-09	5.35E-09	-3.84E-12	-2.68E-12	-1.40E-05	-9.80E-06	4.21%	3.50%
3.92	4.95	2.91	3.07	6.23E-09	5.36E-09	2.65E-14	1.35E-14	9.67E-08	4.91E-08	4.22%	3.50%
3.92	4.95	2.91	3.07	6.23E-09	5.36E-09	1.23E-15	1.70E-15	4.49E-09	6.20E-09	4.22%	3.50%
3.92	4.95	2.91	3.07	6.23E-09	5.36E-09	3.35E-16	1.78E-16	1.23E-09	6.50E-10	4.22%	3.50%
3.92	4.95	2.91	3.07	6.24E-09	5.37E-09	1.64E-14	1.15E-14	6.00E-08	4.19E-08	4.22%	3.51%
3.92	4.95	2.90	3.07	6.22E-09	5.36E-09	-3.13E-14	-2.16E-14	-1.14E-07	-7.89E-08	4.21%	3.50%
3.92	4.95	2.90	3.07	6.22E-09	5.36E-09	-2.93E-16	-6.42E-16	-1.07E-09	-2.34E-09	4.21%	3.50%
3.92	4.95	2.90	3.07	6.22E-09	5.35E-09	-9.63E-15	-6.68E-15	-3.52E-08	-2.44E-08	4.21%	3.50%
3.92	4.95	2.90	3.07	6.22E-09	5.36E-09	7.34E-15	4.99E-15	2.68E-08	1.82E-08	4.21%	3.50%
3.92	4.95	3.21	3.32	6.94E-09	5.85E-09	1.19E-12	8.29E-13	4.34E-06	3.03E-06	4.68%	3.80%
3.92	4.95	3.17	3.30	6.86E-09	5.81E-09	-1.23E-13	-6.87E-14	-4.49E-07	-2.51E-07	4.63%	3.77%
3.92	4.95	3.17	3.29	6.85E-09	5.81E-09	-1.20E-14	-1.17E-14	-4.39E-08	-4.28E-08	4.62%	3.77%
3.92	4.95	3.18	3.30	6.87E-09	5.82E-09	3.35E-14	2.35E-14	1.22E-07	8.59E-08	4.64%	3.78%
3.92	4.95	3.17	3.30	6.86E-09	5.81E-09	-1.84E-14	-1.24E-14	-6.72E-08	-4.52E-08	4.63%	3.77%
3.92	4.95	3.18	3.30	6.87E-09	5.82E-09	1.05E-14	7.02E-15	3.83E-08	2.56E-08	4.63%	3.78%
3.92	4.95	3.18	3.30	6.87E-09	5.82E-09	4.83E-15	3.56E-15	1.77E-08	1.30E-08	4.64%	3.78%
3.92	4.95	3.17	3.30	6.87E-09	5.81E-09	-1.18E-13	-8.17E-14	-4.31E-07	-2.99E-07	4.63%	3.77%

Experiment 08-06-10

$\rho\uparrow = 0.804$ $\rho\downarrow = 0.884$ ($g \cdot cm^{-3}$)

t from T_H (hrs)	**T** (°C)	**P** ($\rho\uparrow$) (MPa)	**P** ($\rho\downarrow$) (MPa)	**Chamber Vol.** (μm^3)	CV	**Qtz Vol.** (μm^3)	CV	**Mgs Vol.** (μm^3) $\rho\uparrow$	$\rho\downarrow$
-0.01	244.8	4	103	1.82E+07	0.15%	2.68E+05	0.10%	1.30E+06	1.30E+06
0.00	247.2	4	107	1.82E+07	0.12%	2.65E+05	0.63%	1.30E+06	1.30E+06
0.02	465.8	307	479	1.63E+07	0.15%	2.13E+05	0.73%	1.31E+06	1.31E+06
0.17	467.4	309	481	1.62E+07	0.33%	1.25E+05	0.89%	1.27E+06	1.29E+06
0.33	465.6	307	478	1.60E+07	0.30%	9.17E+04	0.82%	1.24E+06	1.25E+06
0.50	466.1	307	479	1.59E+07	0.14%	6.95E+04	0.07%	1.22E+06	1.23E+06
0.67	465.3	306	478	1.59E+07	0.17%	5.54E+04	0.30%	1.20E+06	1.22E+06
0.83	466.4	308	480	1.59E+07	0.24%	4.52E+04	0.46%	1.20E+06	1.21E+06
1.00	465.1	306	478	1.59E+07	0.06%	3.81E+04	0.78%	1.19E+06	1.20E+06
1.17	462.6	302	473	1.59E+07	0.06%	3.21E+04	0.38%	1.18E+06	1.19E+06
1.33	464.1	304	476	1.59E+07	0.06%	2.64E+04	0.43%	1.18E+06	1.19E+06
1.50	463.2	303	474	1.59E+07	0.06%	2.34E+04	1.05%	1.17E+06	1.18E+06
1.52	516.0	375	562	1.59E+07	0.06%	6.06E+03	1.54%	1.18E+06	1.19E+06
1.63	514.9	374	560	1.59E+07	0.06%	0.00E+00	0.00%	1.17E+06	1.19E+06
1.67	515.4	375	561	1.59E+07	0.06%	0.00E+00	0.00%	1.17E+06	1.19E+06
1.74	181.7	1	1	1.59E+07	0.06%	0.00E+00	0.00%	1.08E+06	1.06E+06

Experiment 08-06-10 (cont.)

App. $mSiO_2$ (mol SiO_2 / kg H_2O+CO_2)		$mSiO_2$ - Qtz Sat (mol SiO_2 / kg H_2O+CO_2)		Tlc produced (mol)		Tlc growth rate (mol · sec^{-1})		Tlc growth rate (mol · sec^{-1} · m^{-2})		Carbon Dioxide (mole percent)	
ρ↑	ρ↓	ρ↑	ρ↓	ρ↑	ρ↓	ρ↑	ρ↓	ρ↑	ρ↓	ρ↑	ρ↓
0.00	0.00	0.00	0.00	0.00E+00	0.00E+00	0.00E+00	0.00E+00	0.00E+00	0.00E+00	0.00%	0.00%
0.00	0.00	0.00	0.00	0.00E+00	0.00E+00	0.00E+00	0.00E+00	0.00E+00	0.00E+00	0.00%	0.00%
0.17	0.16	0.00	0.00	0.00E+00	0.00E+00	0.00E+00	0.00E+00	0.00E+00	0.00E+00	0.00%	0.00%
0.46	0.42	0.13	0.06	4.25E-10	2.19E-10	7.87E-13	4.06E-13	2.63E-06	1.36E-06	0.17%	0.09%
0.57	0.52	0.24	0.17	8.01E-10	6.35E-10	6.27E-13	6.93E-13	2.10E-06	2.32E-06	0.32%	0.26%
0.65	0.59	0.31	0.24	1.04E-09	9.01E-10	4.04E-13	4.43E-13	1.36E-06	1.49E-06	0.42%	0.36%
0.69	0.63	0.36	0.29	1.20E-09	1.08E-09	2.66E-13	2.93E-13	8.92E-07	9.82E-07	0.49%	0.43%
0.73	0.66	0.39	0.32	1.31E-09	1.19E-09	1.79E-13	1.95E-13	6.02E-07	6.54E-07	0.53%	0.48%
0.75	0.68	0.41	0.35	1.39E-09	1.29E-09	1.39E-13	1.54E-13	4.66E-07	5.17E-07	0.56%	0.52%
0.77	0.70	0.44	0.37	1.47E-09	1.37E-09	1.31E-13	1.47E-13	4.38E-07	4.95E-07	0.59%	0.55%
0.79	0.72	0.45	0.39	1.53E-09	1.43E-09	9.31E-14	9.93E-14	3.13E-07	3.33E-07	0.62%	0.57%
0.80	0.73	0.46	0.40	1.57E-09	1.48E-09	6.52E-14	6.98E-14	2.19E-07	2.34E-07	0.63%	0.59%
0.85	0.78	0.44	0.36	1.49E-09	1.34E-09	-1.21E-12	-2.27E-12	-4.06E-06	-7.61E-06	0.60%	0.54%
0.87	0.80	0.46	0.38	1.57E-09	1.42E-09	1.78E-13	1.99E-13	5.97E-07	6.68E-07	0.63%	0.57%
0.87	0.80	0.46	0.38	1.57E-09	1.42E-09	-3.05E-14	-3.78E-14	-1.02E-07	-1.27E-07	0.63%	0.57%
0.87	0.80	0.79	0.77	2.70E-09	2.91E-09	4.10E-12	5.38E-12	1.38E-05	1.81E-05	1.08%	1.15%
						Max Growth Rate					
						7.87E-13	6.93E-13				

Experiment 08-25-09

$\rho\uparrow = 0.856$ $\rho\downarrow = 0.812$ ($g \cdot cm^{-3}$)

t from T_H (hrs)	**T** (°C)	**P** ($\rho\uparrow$) (MPa)	**P** ($\rho\downarrow$)	**Chamber Vol.** (μm^3)	CV	**Qtz Vol.** (μm^3)	CV	**Mgs Vol.** (μm^3) $\rho\uparrow$	$\rho\downarrow$
-0.02	207.1	1	1	1.20E+07	0.12%	1.35E+06	0.74%	1.20E+06	1.20E+06
0.00	214.1	13	3	1.18E+07	0.13%	1.37E+06	0.46%	1.20E+06	1.20E+06
0.03	461.6	406	315	1.13E+07	0.44%	1.27E+06	0.80%	1.17E+06	1.17E+06
0.20	464.9	411	320	1.14E+07	0.21%	1.27E+06	0.62%	1.17E+06	1.17E+06
0.37	465.5	410	321	1.15E+07	0.22%	1.25E+06	1.27%	1.16E+06	1.15E+06
0.53	463.6	409	318	1.14E+07	0.21%	1.23E+06	0.06%	1.14E+06	1.14E+06
0.70	463.6	409	318	1.12E+07	0.30%	1.20E+06	0.79%	1.11E+06	1.11E+06
0.87	466.0	412	321	1.11E+07	0.10%	1.17E+06	0.30%	1.08E+06	1.09E+06
1.03	464.9	411	320	1.12E+07	0.28%	1.16E+06	1.00%	1.08E+06	1.08E+06
1.10	464.2	410	319	1.12E+07	0.28%	1.16E+06	1.03%	1.07E+06	1.07E+06
1.12	513.6	489	388	1.12E+07	0.28%	1.14E+06	0.57%	1.07E+06	1.07E+06
1.20	516.2	490	391	1.12E+07	0.28%	1.12E+06	0.50%	1.05E+06	1.06E+06
1.37	512.3	484	386	1.12E+07	0.28%	1.11E+06	0.40%	1.04E+06	1.05E+06
1.53	518.0	493	394	1.12E+07	0.28%	1.11E+06	0.71%	1.04E+06	1.04E+06
1.60	518.0	493	394	1.12E+07	0.28%	1.11E+06	0.25%	1.04E+06	1.05E+06
1.61	563.2	562	456	1.12E+07	0.28%	1.08E+06	0.48%	1.03E+06	1.03E+06
1.70	565.6	566	459	1.12E+07	0.28%	1.06E+06	0.81%	1.01E+06	1.02E+06
1.87	563.7	563	457	1.12E+07	0.28%	1.05E+06	0.22%	1.00E+06	1.01E+06
2.03	565.5	566	459	1.12E+07	0.28%	1.04E+06	1.24%	9.95E+05	1.00E+06
2.09	566.3	567	460	1.12E+07	0.28%	1.03E+06	0.74%	9.90E+05	9.96E+05
2.11	616.3	642	528	1.12E+07	0.28%	9.88E+05	0.25%	9.66E+05	9.72E+05
2.20	614.6	639	525	1.12E+07	0.28%	9.29E+05	0.25%	9.09E+05	9.18E+05
2.37	612.7	637	523	1.12E+07	0.28%	7.27E+05	0.14%	7.09E+05	7.25E+05
2.53	613.5	638	524	1.12E+07	0.28%	6.32E+05	0.89%	6.27E+05	6.46E+05
2.70	617.2	643	529	1.12E+07	0.28%	5.76E+05	0.94%	5.78E+05	5.99E+05
2.87	615.4	641	527	1.12E+07	0.28%	5.06E+05	0.31%	5.12E+05	5.34E+05
3.03	614.6	639	525	1.12E+07	0.28%	4.49E+05	0.60%	4.59E+05	4.83E+05
3.12	615.4	641	527	1.12E+07	0.28%	3.96E+05	0.43%	4.08E+05	4.34E+05
3.13	666.5	716	594	1.12E+07	0.28%	3.35E+05	1.06%	3.78E+05	4.03E+05
3.20	666.6	716	594	1.12E+07	0.28%	3.02E+05	0.48%	3.46E+05	3.72E+05
3.37	666.4	716	594	1.12E+07	0.28%	2.84E+05	0.88%	3.31E+05	3.58E+05
3.53	666.3	716	594	1.12E+07	0.28%	2.81E+05	1.13%	3.30E+05	3.57E+05
3.60	665.7	715	593	1.12E+07	0.28%	2.68E+05	1.11%	3.16E+05	3.43E+05
3.62	714.3	785	657	1.12E+07	0.28%	1.99E+05	0.04%	2.72E+05	2.99E+05
3.70	718.3	791	662	1.12E+07	0.28%	1.53E+05	0.62%	2.28E+05	2.56E+05
3.87	715.5	787	658	1.12E+07	0.28%	1.12E+05	1.07%	1.92E+05	2.22E+05
4.03	718.3	791	662	1.12E+07	0.28%	8.78E+04	2.67%	1.70E+05	1.99E+05

4.11	717.0	789	660	1.12E+07	0.28%	5.99E+04	1.49%	1.44E+05	1.75E+05
4.13	763.1	854	719	1.12E+07	0.28%	0.00E+00	0.00	1.12E+05	1.42E+05
4.20	766.5	859	724	1.12E+07	0.28%	0.00E+00	0.00	1.17E+05	1.47E+05
4.37	771.1	866	729	1.12E+07	0.28%	0.00E+00	0.00	1.19E+05	1.48E+05
4.53	763.1	854	719	1.12E+07	0.28%	0.00E+00	0.00	1.22E+05	1.51E+05
4.70	462.4	407	316	1.12E+07	0.28%	0.00E+00	0.00	-4.49E+04	-2.61E+03
4.87	463.7	409	318	1.12E+07	0.28%	0.00E+00	0.00	-1.50E+04	2.37E+04
5.03	466.0	412	321	1.12E+07	0.28%	0.00E+00	0.00	-1.97E+04	1.98E+04
5.20	462.0	406	316	1.12E+07	0.28%	0.00E+00	0.00	-1.80E+04	2.12E+04
5.37	463.2	408	317	1.12E+07	0.28%	0.00E+00	0.00	-1.98E+04	1.96E+04
5.53	462.4	407	316	1.12E+07	0.28%	0.00E+00	0.00	-1.91E+04	2.03E+04
5.57	236.6	48	4	1.12E+07	0.28%	0.00E+00	0.00	-1.95E+04	1.99E+04

Experiment 08-25-09 (cont.)

App. $mSiO_2$ (mol SiO_2 / kg H_2O+CO_2)		$mSiO_2$ - Qtz Sat (mol SiO_2 / kg H_2O+CO_2)		Tlc produced (mol)		Tlc growth rate (mol · sec^{-1})		Tlc growth rate (mol · sec^{-1} · m^{-2})		Carbon Dioxide (mole percent)	
ρ↑	ρ↓	ρ↑	ρ↓	ρ↑	ρ↓	ρ↑	ρ↓	ρ↑	ρ↓	ρ↑	ρ↓
0.00	0.00	0.00	0.00	0.0E+00	0.00E+00	0.00E+00	0.00E+00	0.00E+00	0.00E+00	0.00%	0.00%
0.00	0.00	0.00	0.00	0.0E+00	0.00E+00	0.00E+00	0.00E+00	0.00E+00	0.00E+00	0.00%	0.00%
0.60	0.63	0.19	0.21	3.8E-10	3.92E-10	3.15E-12	3.27E-12	1.47E-05	1.52E-05	0.25%	0.26%
0.59	0.63	0.18	0.20	3.7E-10	3.82E-10	-1.79E-14	-1.76E-14	-8.32E-08	-8.19E-08	0.24%	0.25%
0.68	0.72	0.27	0.28	5.3E-10	5.36E-10	2.70E-13	2.57E-13	1.25E-06	1.19E-06	0.35%	0.36%
0.77	0.82	0.35	0.37	7.1E-10	7.03E-10	2.93E-13	2.78E-13	1.36E-06	1.30E-06	0.47%	0.47%
0.96	1.01	0.53	0.55	1.1E-09	1.05E-09	6.04E-13	5.74E-13	2.83E-06	2.69E-06	0.71%	0.69%
1.12	1.18	0.68	0.70	1.4E-09	1.35E-09	5.25E-13	5.00E-13	2.46E-06	2.35E-06	0.92%	0.89%
1.17	1.24	0.73	0.74	1.5E-09	1.43E-09	1.46E-13	1.40E-13	6.85E-07	6.57E-07	0.98%	0.94%
1.20	1.27	0.76	0.77	1.5E-09	1.49E-09	2.64E-13	2.51E-13	1.24E-06	1.18E-06	1.02%	0.98%
1.31	1.38	0.77	0.79	1.6E-09	1.53E-09	4.94E-13	5.99E-13	2.32E-06	2.81E-06	1.04%	1.00%
1.39	1.47	0.85	0.87	1.7E-09	1.68E-09	5.42E-13	5.09E-13	2.54E-06	2.38E-06	1.14%	1.10%
1.47	1.55	0.92	0.94	1.9E-09	1.82E-09	2.40E-13	2.34E-13	1.13E-06	1.09E-06	1.24%	1.19%
1.47	1.55	0.92	0.95	1.9E-09	1.84E-09	2.93E-14	2.70E-14	1.37E-07	1.26E-07	1.25%	1.20%
1.48	1.56	0.92	0.94	1.9E-09	1.82E-09	-7.51E-14	-6.71E-14	-3.52E-07	-3.14E-07	1.24%	1.19%
1.63	1.72	0.98	1.01	2.0E-09	1.95E-09	2.15E-12	2.18E-12	1.01E-05	1.02E-05	1.32%	1.28%
1.74	1.84	1.08	1.10	2.2E-09	2.15E-09	6.62E-13	6.31E-13	3.10E-06	2.96E-06	1.46%	1.40%
1.80	1.90	1.12	1.15	2.3E-09	2.25E-09	1.65E-13	1.58E-13	7.72E-07	7.43E-07	1.52%	1.46%
1.85	1.95	1.17	1.20	2.4E-09	2.34E-09	1.71E-13	1.63E-13	8.03E-07	7.65E-07	1.59%	1.53%
1.89	1.99	1.20	1.23	2.5E-09	2.41E-09	3.12E-13	3.01E-13	1.46E-06	1.41E-06	1.63%	1.57%
2.15	2.27	1.33	1.37	2.8E-09	2.69E-09	4.76E-12	4.73E-12	2.23E-05	2.22E-05	1.82%	1.74%
2.48	2.62	1.64	1.67	3.4E-09	3.33E-09	2.02E-12	1.93E-12	9.45E-06	9.03E-06	2.25%	2.14%
3.60	3.80	2.67	2.71	5.8E-09	5.59E-09	3.94E-12	3.77E-12	1.84E-05	1.77E-05	3.77%	3.51%
4.13	4.36	3.07	3.11	6.7E-09	6.52E-09	1.60E-12	1.55E-12	7.48E-06	7.26E-06	4.37%	4.05%
4.44	4.69	3.30	3.34	7.3E-09	7.08E-09	9.65E-13	9.35E-13	4.52E-06	4.38E-06	4.74%	4.38%
4.84	5.10	3.61	3.66	8.1E-09	7.84E-09	1.31E-12	1.27E-12	6.12E-06	5.93E-06	5.22%	4.81%
5.15	5.44	3.86	3.90	8.7E-09	8.45E-09	1.04E-12	1.01E-12	4.89E-06	4.74E-06	5.61%	5.15%
5.45	5.75	4.08	4.13	9.3E-09	9.02E-09	1.97E-12	1.91E-12	9.22E-06	8.95E-06	5.98%	5.47%
5.79	6.10	4.22	4.28	9.7E-09	9.39E-09	6.02E-12	6.14E-12	2.82E-05	2.88E-05	6.20%	5.67%
5.97	6.30	4.36	4.42	1.0E-08	9.75E-09	1.57E-12	1.51E-12	7.35E-06	7.07E-06	6.43%	5.87%
6.07	6.41	4.42	4.48	1.0E-08	9.92E-09	2.92E-13	2.87E-13	1.37E-06	1.34E-06	6.54%	5.96%
6.09	6.42	4.43	4.48	1.0E-08	9.94E-09	1.98E-14	2.02E-14	9.28E-08	9.46E-08	6.54%	5.97%
6.16	6.50	4.49	4.55	1.0E-08	1.01E-08	7.08E-13	6.85E-13	3.32E-06	3.21E-06	6.65%	6.05%
6.55	6.91	4.68	4.75	1.1E-08	1.06E-08	8.60E-12	8.65E-12	4.03E-05	4.05E-05	6.96%	6.33%
6.80	7.18	4.87	4.94	1.1E-08	1.11E-08	1.72E-12	1.66E-12	8.08E-06	7.80E-06	7.27%	6.60%
7.03	7.42	5.02	5.09	1.2E-08	1.15E-08	6.93E-13	6.81E-13	3.25E-06	3.19E-06	7.53%	6.81%
7.17	7.56	5.11	5.18	1.2E-08	1.18E-08	4.48E-13	4.36E-13	2.10E-06	2.04E-06	7.69%	6.95%

7.32	7.72	5.21	5.29	1.2E-08	1.21E-08	1.10E-12	1.08E-12	5.15E-06	5.05E-06	7.87%	7.10%
7.65	8.08	5.35	5.43	1.3E-08	1.25E-08	6.29E-12	6.46E-12	2.95E-05	3.03E-05	8.09%	7.30%
7.65	8.08	5.32	5.40	1.3E-08	1.24E-08	-2.19E-13	-2.26E-13	-1.03E-06	-1.06E-06	8.06%	7.27%
7.65	8.08	5.31	5.39	1.3E-08	1.24E-08	-2.93E-14	-2.59E-14	-1.37E-07	-1.21E-07	8.05%	7.26%
7.65	8.08	5.30	5.38	1.3E-08	1.24E-08	-5.76E-14	-5.35E-14	-2.70E-07	-2.51E-07	8.03%	7.24%
7.65	8.08	5.99	6.04	1.5E-08	1.42E-08	3.27E-12	3.01E-12	1.53E-05	1.41E-05	9.19%	8.15%
7.65	8.08	5.85	5.90	1.4E-08	1.39E-08	-5.87E-13	-5.16E-13	-2.75E-06	-2.42E-06	8.98%	8.00%
7.65	8.08	5.87	5.92	1.4E-08	1.39E-08	9.29E-14	7.64E-14	4.35E-07	3.58E-07	9.02%	8.02%
7.65	8.08	5.86	5.92	1.4E-08	1.39E-08	-3.35E-14	-2.84E-14	-1.57E-07	-1.33E-07	9.00%	8.02%
7.65	8.08	5.87	5.93	1.4E-08	1.39E-08	3.52E-14	3.17E-14	1.65E-07	1.48E-07	9.02%	8.02%
7.65	8.08	5.87	5.92	1.4E-08	1.39E-08	-1.45E-14	-1.30E-14	-6.82E-08	-6.08E-08	9.01%	8.02%
7.65	8.08	5.87	5.92	1.4E-08	1.39E-08	4.19E-14	3.75E-14	1.96E-07	1.76E-07	9.01%	8.02%
						Max Growth Rate					
						8.60E-12	8.65E-12				

Experiment 05-11-10

$\rho\uparrow = 0.799$ $\rho\downarrow = 0.600$ ($g \cdot cm^{-3}$)

t from T_H (hrs)	**T** (°C)	**P** ($\rho\uparrow$) (MPa)	**P** ($\rho\downarrow$) (MPa)	**Chamber Vol.** (μm^3)	CV	**Qtz Vol.** (μm^3)	CV	**Mgs Vol.** (μm^3) $\rho\uparrow$	$\rho\downarrow$
0.00	247.8	4	4	1.14E+07	0.09%	4.96E+05	0.68%	1.16E+06	1.16E+06
0.01	461.8	294	102	1.14E+07	0.36%	4.61E+05	0.42%	1.16E+06	1.16E+06
0.17	464.3	297	104	1.14E+07	0.26%	3.78E+05	0.60%	1.11E+06	1.10E+06
0.33	463.4	296	104	1.15E+07	0.20%	2.83E+05	0.45%	1.02E+06	1.03E+06
0.50	460.6	292	102	1.15E+07	0.32%	2.33E+05	1.99%	9.68E+05	9.96E+05
0.67	464.1	297	104	1.14E+07	0.06%	2.16E+05	2.32%	9.54E+05	9.85E+05
0.83	464.2	297	104	1.14E+07	0.33%	2.10E+05	1.78%	9.49E+05	9.81E+05
1.00	465.0	298	105	1.14E+07	0.10%	2.06E+05	0.39%	9.45E+05	9.78E+05
1.17	464.0	297	104	1.14E+07	0.10%	1.84E+05	3.53%	9.24E+05	9.61E+05
1.33	467.0	301	106	1.14E+07	0.10%	1.58E+05	3.05%	9.00E+05	9.42E+05
1.50	466.4	300	106	1.14E+07	0.10%	1.38E+05	1.86%	8.79E+05	9.27E+05
1.52	512.9	363	141	1.14E+07	0.10%	1.26E+05	3.26%	8.82E+05	9.23E+05
1.67	515.8	367	144	1.14E+07	0.10%	7.55E+04	1.75%	8.32E+05	8.83E+05
1.83	518.2	370	145	1.14E+07	0.10%	3.11E+04	4.65%	7.90E+05	8.50E+05
2.00	518.8	371	146	1.14E+07	0.10%	0.00E+00	0.00%	7.62E+05	8.26E+05
2.02	564.5	432	181	1.14E+07	0.10%	0.00E+00	0.00%	7.77E+05	8.34E+05
2.04	340.3	127	15	1.14E+07	0.10%	0.00E+00	0.00%	7.22E+05	8.09E+05

Experiment 05-11-10 (cont.)

App. $mSiO_2$ (mol SiO_2 / kg H_2O+CO_2)		$mSiO_2$ - Qtz Sat (mol SiO_2 / kg H_2O+CO_2)		Tlc produced (mol)		Tlc growth rate (mol · sec^{-1})		Tlc growth rate (mol · sec^{-1} · m^{-2})		Carbon Dioxide (mole percent)	
ρ↑	ρ↓	ρ↑	ρ↓	ρ↑	ρ↓	ρ↑	ρ↓	ρ↑	ρ↓	ρ↑	ρ↓
0.00	0.00	0.00	0.00	0.00E+00	0.00E+00	0.00E+00	0.00E+00	0.00E+00	0.00E+00	0.00%	0.00%
0.20	0.27	0.00	0.02	0.00E+00	2.30E-11	0.00E+00	5.75E-13	0.00E+00	2.70E-06	0.00%	0.02%
0.67	0.90	0.34	0.48	6.78E-10	7.22E-10	1.21E-12	1.24E-12	5.66E-06	5.84E-06	0.47%	0.50%
1.21	1.61	0.87	1.01	1.75E-09	1.54E-09	1.78E-12	1.36E-12	8.34E-06	6.38E-06	1.20%	1.05%
1.50	1.99	1.14	1.28	2.31E-09	1.98E-09	9.39E-13	7.31E-13	4.40E-06	3.43E-06	1.59%	1.34%
1.59	2.12	1.22	1.36	2.47E-09	2.11E-09	2.75E-13	2.24E-13	1.29E-06	1.05E-06	1.70%	1.43%
1.63	2.17	1.25	1.39	2.54E-09	2.16E-09	1.08E-13	8.57E-14	5.07E-07	4.03E-07	1.74%	1.46%
1.65	2.20	1.27	1.41	2.58E-09	2.20E-09	6.88E-14	5.57E-14	3.24E-07	2.62E-07	1.77%	1.48%
1.77	2.36	1.39	1.53	2.83E-09	2.39E-09	4.15E-13	3.24E-13	1.95E-06	1.53E-06	1.94%	1.61%
1.92	2.56	1.52	1.67	3.12E-09	2.62E-09	4.80E-13	3.85E-13	2.26E-06	1.81E-06	2.13%	1.76%
2.03	2.71	1.64	1.77	3.36E-09	2.80E-09	4.10E-13	2.93E-13	1.93E-06	1.38E-06	2.30%	1.88%
2.10	2.79	1.62	1.80	3.32E-09	2.84E-09	-6.62E-13	6.48E-13	-3.11E-06	3.05E-06	2.27%	1.90%
2.39	3.18	1.89	2.07	3.92E-09	3.31E-09	1.10E-12	8.71E-13	5.16E-06	4.10E-06	2.67%	2.21%
2.64	3.51	2.11	2.30	4.40E-09	3.70E-09	8.13E-13	6.61E-13	3.82E-06	3.11E-06	3.00%	2.46%
2.81	3.75	2.26	2.45	4.74E-09	3.98E-09	5.66E-13	4.62E-13	2.66E-06	2.17E-06	3.22%	2.63%
2.81	3.75	2.18	2.40	4.56E-09	3.89E-09	-3.05E-12	-1.48E-12	-1.43E-05	-6.95E-06	3.10%	2.58%
2.81	3.75	2.46	2.56	5.21E-09	4.19E-09	8.62E-12	3.95E-12	4.06E-05	1.86E-05	3.53%	2.76%
						Max Growth Rate					
						1.78E-12	1.36E-12				

Experiment 12-02-09

$\rho\uparrow = 0.885$ $\rho\downarrow = 0.873$ ($g \cdot cm^{-3}$)

t from T_H (hrs)	**T** (°C)	**P** ($\rho\uparrow$) (MPa)	**P** ($\rho\downarrow$) (MPa)	**Chamber Vol.** (μm^3)	CV	**Qtz Vol.** (μm^3)	CV	**Mgs Vol.** (μm^3) $\rho\uparrow$	$\rho\downarrow$
-0.03	180.6	1	1	1.21E+07	0.18%	6.55E+05	0.63%	1.35E+06	1.35E+06
0.00	198.3	28	10	1.20E+07	0.06%	6.67E+05	0.33%	1.35E+06	1.35E+06
0.01	457.6	464	439	1.15E+07	0.92%	6.24E+05	1.20%	1.35E+06	1.35E+06
0.02	460.5	469	443	1.14E+07	0.13%	5.23E+05	0.65%	1.29E+06	1.29E+06
0.18	464.7	476	450	1.15E+07	0.28%	3.81E+05	0.56%	1.15E+06	1.16E+06
0.35	464.0	475	449	1.12E+07	0.27%	3.73E+05	1.16%	1.15E+06	1.16E+06
0.52	461.3	470	445	1.13E+07	0.56%	3.71E+05	1.19%	1.15E+06	1.15E+06
0.68	465.6	477	452	1.13E+07	0.60%	3.62E+05	1.74%	1.14E+06	1.14E+06
0.85	464.0	475	449	1.13E+07	0.42%	3.46E+05	0.68%	1.13E+06	1.13E+06
1.02	465.2	477	451	1.13E+07	0.65%	3.27E+05	1.09%	1.11E+06	1.11E+06
1.18	465.2	477	451	1.13E+07	0.65%	3.23E+05	0.94%	1.11E+06	1.11E+06
1.35	467.0	480	454	1.13E+07	0.65%	3.10E+05	0.85%	1.09E+06	1.10E+06
1.50	462.1	476	445	1.13E+07	0.65%	3.05E+05	0.74%	1.09E+06	1.09E+06
1.52	512.7	555	528	1.13E+07	0.65%	2.78E+05	0.42%	1.08E+06	1.08E+06
1.68	512.3	555	527	1.13E+07	0.65%	2.52E+05	2.23%	1.06E+06	1.06E+06
1.85	516.8	562	534	1.13E+07	0.65%	2.40E+05	1.42%	1.04E+06	1.05E+06
2.00	517.5	568	534	1.13E+07	0.65%	2.35E+05	1.53%	1.04E+06	1.04E+06
2.02	563.1	637	608	1.13E+07	0.65%	1.98E+05	1.34%	1.03E+06	1.03E+06
2.18	566.1	642	613	1.13E+07	0.65%	1.76E+05	2.28%	1.00E+06	1.01E+06
2.35	565.2	641	611	1.13E+07	0.65%	1.51E+05	1.94%	9.82E+05	9.85E+05
2.50	564.8	645	609	1.13E+07	0.65%	1.42E+05	1.21%	9.74E+05	9.77E+05
2.52	613.2	717	686	1.13E+07	0.65%	1.17E+05	2.62%	9.72E+05	9.75E+05
2.55	613.3	723	685	1.13E+07	0.65%	1.15E+05	1.48%	9.70E+05	9.73E+05
2.68	616.3	722	691	1.13E+07	0.65%	7.92E+04	2.11%	9.35E+05	9.38E+05
2.85	615.4	721	690	1.13E+07	0.65%	4.07E+04	2.53%	9.00E+05	9.04E+05
3.02	612.0	715	684	1.13E+07	0.65%	2.16E+04	5.95%	8.83E+05	8.87E+05
3.18	615.2	720	689	1.13E+07	0.65%	1.96E+03	5.46%	8.63E+05	8.67E+05
3.35	614.7	720	690	1.13E+07	0.65%	3.74E+02	9.08%	8.64E+05	8.68E+05
3.52	615.6	721	690	1.13E+07	0.65%	0.00E+00	0.00%	8.64E+05	8.68E+05
3.68	614.1	719	688	1.13E+07	0.65%	0.00E+00	0.00%	8.64E+05	8.68E+05
3.85	613.9	718	687	1.13E+07	0.65%	0.00E+00	0.00%	8.63E+05	8.67E+05
4.00	614.9	725	687	1.13E+07	0.65%	0.00E+00	0.00%	8.63E+05	8.67E+05
4.02	224.6	68	53	1.13E+07	0.65%	0.00E+00	0.00%	8.64E+05	8.68E+05
4.03	189.3	10	1	1.13E+07	0.65%	0.00E+00	0.00%	7.37E+05	7.44E+05

Experiment 12-02-09 (cont.)

App. $mSiO_2$ (mol SiO_2 / kg H_2O+CO_2)		$mSiO_2$ - Qtz Sat (mol SiO_2 / kg H_2O+CO_2)		Tlc produced (mol)		Tlc growth rate (mol · sec^{-1})		Tlc growth rate (mol · sec^{-1} · m^{-2})		Carbon Dioxide (mole percent)	
ρ↑	ρ↓	ρ↑	ρ↓	ρ↑	ρ↓	ρ↑	ρ↓	ρ↑	ρ↓	ρ↑	ρ↓
0.00	0.00	0.00	0.00	0.00E+00	0.00E+00	0.00E+00	0.00E+00	0.00E+00	0.00E+00	0.00%	0.00%
0.00	0.00	0.00	0.00	0.00E+00	0.00E+00	0.00E+00	0.00E+00	0.00E+00	0.00E+00	0.00%	0.00%
0.22	0.22	0.00	0.00	0.00E+00	0.00E+00	0.00E+00	0.00E+00	0.00E+00	0.00E+00	0.00%	0.00%
0.72	0.73	0.32	0.33	7.22E-10	7.23E-10	4.82E-11	4.82E-11	2.15E-04	2.16E-04	0.44%	0.44%
1.43	1.45	1.01	1.02	2.31E-09	2.29E-09	2.64E-12	2.61E-12	1.18E-05	1.17E-05	1.39%	1.36%
1.47	1.49	1.02	1.02	2.32E-09	2.30E-09	2.17E-14	2.31E-14	9.74E-08	1.04E-07	1.40%	1.37%
1.48	1.50	1.03	1.03	2.35E-09	2.33E-09	5.03E-14	4.96E-14	2.26E-07	2.22E-07	1.41%	1.38%
1.52	1.54	1.07	1.08	2.46E-09	2.44E-09	1.81E-13	1.79E-13	8.13E-07	8.02E-07	1.48%	1.44%
1.61	1.63	1.15	1.15	2.63E-09	2.61E-09	2.80E-13	2.77E-13	1.26E-06	1.24E-06	1.58%	1.54%
1.70	1.72	1.23	1.24	2.84E-09	2.81E-09	3.49E-13	3.45E-13	1.57E-06	1.55E-06	1.70%	1.66%
1.72	1.75	1.25	1.26	2.88E-09	2.85E-09	6.92E-14	6.87E-14	3.11E-07	3.08E-07	1.73%	1.68%
1.78	1.81	1.31	1.32	3.03E-09	3.00E-09	2.57E-13	2.39E-13	1.16E-06	1.07E-06	1.82%	1.76%
1.81	1.83	1.33	1.33	3.06E-09	3.04E-09	5.39E-14	7.17E-14	2.42E-07	3.22E-07	1.83%	1.79%
1.94	1.97	1.38	1.38	3.18E-09	3.16E-09	2.01E-12	2.02E-12	9.03E-06	9.08E-06	1.91%	1.86%
2.07	2.10	1.49	1.50	3.47E-09	3.44E-09	4.78E-13	4.72E-13	2.14E-06	2.12E-06	2.08%	2.02%
2.14	2.17	1.55	1.56	3.60E-09	3.57E-09	2.25E-13	2.23E-13	1.01E-06	1.00E-06	2.16%	2.09%
2.16	2.19	1.56	1.57	3.64E-09	3.61E-09	5.84E-14	5.84E-14	2.62E-07	2.62E-07	2.17%	2.11%
2.34	2.38	1.64	1.65	3.83E-09	3.80E-09	3.27E-12	3.28E-12	1.47E-05	1.47E-05	2.29%	2.22%
2.45	2.49	1.74	1.75	4.08E-09	4.05E-09	4.10E-13	4.05E-13	1.84E-06	1.82E-06	2.43%	2.36%
2.58	2.61	1.85	1.85	4.34E-09	4.30E-09	4.36E-13	4.31E-13	1.96E-06	1.94E-06	2.59%	2.50%
2.62	2.66	1.89	1.89	4.44E-09	4.40E-09	1.82E-13	1.80E-13	8.16E-07	8.08E-07	2.64%	2.56%
2.75	2.79	1.89	1.90	4.46E-09	4.43E-09	3.88E-13	4.45E-13	1.74E-06	2.00E-06	2.66%	2.57%
2.76	2.80	1.90	1.91	4.48E-09	4.45E-09	1.64E-13	1.59E-13	7.36E-07	7.15E-07	2.67%	2.58%
2.94	2.98	2.07	2.08	4.90E-09	4.86E-09	8.69E-13	8.59E-13	3.90E-06	3.86E-06	2.91%	2.81%
3.13	3.17	2.23	2.24	5.31E-09	5.26E-09	6.84E-13	6.78E-13	3.07E-06	3.04E-06	3.15%	3.03%
3.22	3.27	2.31	2.32	5.51E-09	5.47E-09	3.37E-13	3.34E-13	1.51E-06	1.50E-06	3.27%	3.14%
3.32	3.37	2.40	2.41	5.75E-09	5.70E-09	3.99E-13	3.95E-13	1.79E-06	1.77E-06	3.41%	3.27%
3.33	3.38	2.39	2.40	5.73E-09	5.68E-09	-3.16E-14	-3.02E-14	-1.42E-07	-1.36E-07	3.40%	3.26%
3.33	3.38	2.39	2.41	5.74E-09	5.69E-09	1.49E-14	1.46E-14	6.71E-08	6.55E-08	3.40%	3.26%
3.33	3.38	2.39	2.40	5.73E-09	5.69E-09	-1.02E-14	-9.96E-15	-4.59E-08	-4.47E-08	3.40%	3.26%
3.33	3.38	2.40	2.41	5.74E-09	5.70E-09	1.54E-14	1.50E-14	6.92E-08	6.74E-08	3.40%	3.27%
3.33	3.38	2.40	2.41	5.74E-09	5.70E-09	1.46E-15	1.46E-15	6.57E-09	6.54E-09	3.40%	3.27%
3.33	3.38	2.39	2.40	5.74E-09	5.69E-09	-1.02E-13	-9.92E-14	-4.57E-07	-4.46E-07	3.40%	3.26%
3.33	3.38	2.96	2.97	7.23E-09	7.15E-09	4.27E-11	4.17E-11	1.92E-04	1.87E-04	4.26%	4.04%
						Max Growth Rate					
						4.82E-11	4.82E-11				

Experiment 03-02-10

$\rho\uparrow = 0.852$ $\rho\downarrow = 0.876$ ($g \cdot cm^{-3}$)

t from T_H (hrs)	**T** (°C)	**P** ($\rho\uparrow$) (MPa)	**P** ($\rho\downarrow$)	**Chamber Vol.** (μm^3)	CV	**Qtz Vol.** (μm^3)	CV	**Mgs Vol.** (μm^3) $\rho\uparrow$	$\rho\downarrow$
-0.01	208.7	1	1	1.20E+07	0.15%	5.88E+05	0.24%	1.52E+06	1.52E+06
0.00	213.4	6	36	1.19E+07	0.08%	5.86E+05	0.46%	1.52E+06	1.52E+06
0.02	464.8	400	456	1.17E+07	0.22%	5.39E+05	0.18%	1.52E+06	1.52E+06
0.17	463.8	399	451	1.17E+07	0.29%	4.53E+05	0.26%	1.46E+06	1.46E+06
0.33	465.0	401	453	1.16E+07	0.05%	4.21E+05	0.81%	1.43E+06	1.43E+06
0.50	464.0	400	451	1.15E+07	0.48%	3.91E+05	0.61%	1.40E+06	1.40E+06
0.67	464.1	400	451	1.16E+07	0.24%	3.75E+05	0.81%	1.39E+06	1.39E+06
0.83	465.4	402	454	1.15E+07	0.45%	3.50E+05	0.16%	1.37E+06	1.36E+06
1.00	462.7	398	449	1.16E+07	0.28%	3.40E+05	0.53%	1.36E+06	1.35E+06
1.17	458.9	392	443	1.16E+07	0.28%	3.32E+05	0.81%	1.35E+06	1.35E+06
1.33	459.2	392	443	1.16E+07	0.28%	3.20E+05	1.07%	1.34E+06	1.33E+06
1.50	460.6	394	446	1.16E+07	0.28%	3.06E+05	0.43%	1.32E+06	1.32E+06
1.52	460.4	394	445	1.16E+07	0.28%	3.03E+05	1.17%	1.32E+06	1.32E+06
1.53	512.2	473	533	1.16E+07	0.28%	2.81E+05	1.13%	1.31E+06	1.31E+06
1.68	512.8	475	530	1.16E+07	0.28%	2.74E+05	0.19%	1.31E+06	1.31E+06
1.85	513.7	476	532	1.16E+07	0.28%	2.56E+05	0.30%	1.29E+06	1.29E+06
2.02	514.1	477	533	1.16E+07	0.28%	2.43E+05	1.07%	1.28E+06	1.28E+06
2.07	514.8	477	538	1.16E+07	0.28%	2.33E+05	0.88%	1.27E+06	1.27E+06
2.08	563.2	550	615	1.16E+07	0.28%	2.14E+05	0.55%	1.27E+06	1.27E+06
2.18	565.2	554	614	1.16E+07	0.28%	2.00E+05	0.93%	1.25E+06	1.25E+06
2.35	566.4	556	616	1.16E+07	0.28%	1.84E+05	0.66%	1.24E+06	1.24E+06
2.52	568.8	560	620	1.16E+07	0.28%	1.64E+05	0.86%	1.22E+06	1.22E+06
2.57	561.6	549	608	1.16E+07	0.28%	1.63E+05	0.17%	1.22E+06	1.22E+06
2.58	613.3	625	694	1.16E+07	0.28%	1.41E+05	0.14%	1.22E+06	1.21E+06
2.73	618.0	633	696	1.16E+07	0.28%	2.44E+04	3.38%	1.10E+06	1.10E+06
2.90	615.3	629	692	1.16E+07	0.28%	0.00E+00	0.00%	1.08E+06	1.08E+06
3.07	612.0	624	687	1.16E+07	0.28%	0.00E+00	0.00%	1.08E+06	1.08E+06
3.09	190.2	1	1	1.16E+07	0.28%	0.00E+00	0.00%	9.79E+05	9.66E+05

Experiment 03-02-10 (cont.)

App. $mSiO_2$ (mol SiO_2 / kg H_2O+CO_2)		$mSiO_2$ - Qtz Sat (mol SiO_2 / kg H_2O+CO_2)		Tlc produced (mol)		Tlc growth rate (mol · sec^{-1})		Tlc growth rate (mol · sec^{-1} · m^{-2})		Carbon Dioxide (mole percent)	
ρ↑	ρ↓	ρ↑	ρ↓	ρ↑	ρ↓	ρ↑	ρ↓	ρ↑	ρ↓	ρ↑	ρ↓
0.00	0.00	0.00	0.00	0.00E+00	0.00E+00	0.00E+00	0.00E+00	0.00E+00	0.00E+00	0.00%	0.00%
0.00	0.00	0.00	0.00	0.00E+00	0.00E+00	0.00E+00	0.00E+00	0.00E+00	0.00E+00	0.00%	0.00%
0.25	0.24	0.00	0.00	0.00E+00	0.00E+00	0.00E+00	0.00E+00	0.00E+00	0.00E+00	0.00%	0.00%
0.70	0.68	0.35	0.33	7.45E-10	7.24E-10	1.38E-12	1.34E-12	5.87E-06	5.70E-06	0.48%	0.46%
0.87	0.84	0.51	0.49	1.09E-09	1.08E-09	5.72E-13	5.87E-13	2.44E-06	2.50E-06	0.70%	0.68%
1.03	1.00	0.67	0.65	1.43E-09	1.43E-09	5.68E-13	5.83E-13	2.43E-06	2.49E-06	0.91%	0.90%
1.11	1.08	0.74	0.72	1.60E-09	1.60E-09	2.77E-13	2.84E-13	1.18E-06	1.21E-06	1.02%	1.01%
1.24	1.21	0.87	0.85	1.87E-09	1.88E-09	4.62E-13	4.73E-13	1.97E-06	2.02E-06	1.19%	1.19%
1.29	1.26	0.92	0.90	1.99E-09	2.00E-09	1.95E-13	2.01E-13	8.33E-07	8.57E-07	1.27%	1.26%
1.33	1.30	0.96	0.95	2.09E-09	2.10E-09	1.60E-13	1.65E-13	6.82E-07	7.04E-07	1.33%	1.32%
1.40	1.36	1.03	1.01	2.23E-09	2.25E-09	2.36E-13	2.41E-13	1.01E-06	1.03E-06	1.42%	1.41%
1.47	1.43	1.10	1.07	2.38E-09	2.39E-09	2.52E-13	2.44E-13	1.07E-06	1.04E-06	1.51%	1.50%
1.49	1.45	1.10	1.09	2.40E-09	2.42E-09	3.69E-13	5.10E-13	1.57E-06	2.17E-06	1.53%	1.52%
1.60	1.56	1.14	1.12	2.48E-09	2.49E-09	1.33E-12	1.20E-12	5.68E-06	5.10E-06	1.58%	1.56%
1.64	1.60	1.17	1.15	2.56E-09	2.57E-09	1.40E-13	1.44E-13	5.96E-07	6.12E-07	1.63%	1.61%
1.74	1.69	1.26	1.24	2.76E-09	2.78E-09	3.34E-13	3.42E-13	1.42E-06	1.46E-06	1.75%	1.73%
1.81	1.76	1.33	1.31	2.91E-09	2.93E-09	2.51E-13	2.57E-13	1.07E-06	1.09E-06	1.85%	1.83%
1.86	1.81	1.37	1.35	3.01E-09	3.04E-09	5.82E-13	5.94E-13	2.48E-06	2.53E-06	1.91%	1.89%
1.96	1.91	1.39	1.36	3.04E-09	3.05E-09	4.49E-13	2.82E-13	1.91E-06	1.20E-06	1.93%	1.90%
2.03	1.98	1.45	1.42	3.19E-09	3.21E-09	4.12E-13	4.22E-13	1.76E-06	1.80E-06	2.02%	1.99%
2.12	2.06	1.53	1.50	3.36E-09	3.39E-09	2.96E-13	3.02E-13	1.26E-06	1.29E-06	2.13%	2.10%
2.22	2.16	1.62	1.59	3.58E-09	3.60E-09	3.52E-13	3.59E-13	1.50E-06	1.53E-06	2.26%	2.23%
2.23	2.17	1.63	1.60	3.61E-09	3.64E-09	1.80E-13	1.93E-13	7.67E-07	8.22E-07	2.28%	2.25%
2.34	2.28	1.65	1.61	3.64E-09	3.66E-09	5.81E-13	3.79E-13	2.48E-06	1.62E-06	2.31%	2.27%
2.96	2.88	2.22	2.19	5.00E-09	5.05E-09	2.52E-12	2.57E-12	1.07E-05	1.10E-05	3.15%	3.08%
3.09	3.00	2.31	2.27	5.22E-09	5.27E-09	3.62E-13	3.69E-13	1.54E-06	1.57E-06	3.28%	3.21%
3.09	3.00	2.31	2.27	5.22E-09	5.27E-09	2.01E-15	3.28E-15	8.59E-09	1.40E-08	3.28%	3.21%
3.09	3.00	2.80	2.79	6.43E-09	6.58E-09	1.27E-11	1.37E-11	5.43E-05	5.85E-05	4.02%	3.95%
						Max Growth Rate					
						2.52E-12	2.57E-12				

Experiment 06-23-10

$\rho\uparrow = 0.901$ $\rho\downarrow = 0.823$ ($g \cdot cm^{-3}$)

t from T_H (hrs)	**T** (°C)	**P** ($\rho\uparrow$) (MPa)	**P** ($\rho\downarrow$)	**Chamber Vol.** (μm^3)	CV	**Qtz Vol.** (μm^3)	CV	**Mgs Vol.** (μm^3) $\rho\uparrow$	$\rho\downarrow$
-0.01	165.1	1	1	7.84E+06	0.13%	7.81E+05	0.05%	7.76E+05	7.76E+05
0.00	186.5	34	1	7.85E+06	0.20%	7.80E+05	0.28%	7.76E+05	7.76E+05
0.03	460.0	516	334	7.84E+06	0.31%	6.58E+05	0.23%	6.94E+05	6.94E+05
0.19	464.7	525	341	7.72E+06	0.60%	4.61E+05	0.58%	4.98E+05	5.13E+05
0.36	467.0	529	344	7.67E+06	0.25%	3.79E+05	0.69%	4.26E+05	4.45E+05
0.53	467.2	529	344	7.74E+06	0.18%	3.37E+05	0.55%	3.89E+05	4.09E+05
0.69	460.5	517	335	7.70E+06	0.31%	3.10E+05	0.61%	3.62E+05	3.84E+05
0.86	465.7	526	342	7.69E+06	0.32%	2.85E+05	0.64%	3.39E+05	3.62E+05
1.03	465.7	527	342	7.66E+06	0.15%	2.62E+05	0.98%	3.17E+05	3.41E+05
1.19	464.7	525	341	7.66E+06	0.15%	2.27E+05	0.23%	2.81E+05	3.08E+05
1.36	465.7	526	342	7.66E+06	0.15%	2.17E+05	0.30%	2.75E+05	3.02E+05
1.53	466.7	528	344	7.66E+06	0.15%	2.00E+05	0.74%	2.53E+05	2.86E+05
1.54	513.9	609	411	7.66E+06	0.15%	1.86E+05	0.11%	2.56E+05	2.81E+05
1.69	515.7	612	414	7.66E+06	0.15%	1.75E+05	0.28%	2.44E+05	2.71E+05
1.86	512.7	607	410	7.66E+06	0.15%	1.74E+05	0.99%	2.44E+05	2.71E+05
2.03	513.7	609	411	7.66E+06	0.15%	1.68E+05	1.03%	2.38E+05	2.65E+05
2.04	563.1	693	481	7.66E+06	0.15%	1.57E+05	0.60%	2.39E+05	2.65E+05
2.19	560.8	689	478	7.66E+06	0.15%	1.47E+05	0.97%	2.28E+05	2.54E+05
2.36	566.6	698	486	7.66E+06	0.15%	1.38E+05	0.67%	2.20E+05	2.47E+05
2.53	563.6	693	482	7.66E+06	0.15%	1.36E+05	0.63%	2.19E+05	2.45E+05
2.54	613.3	776	551	7.66E+06	0.15%	1.20E+05	0.30%	2.16E+05	2.40E+05
2.69	615.6	780	554	7.66E+06	0.15%	1.22E+05	0.95%	2.19E+05	2.44E+05
2.86	614.8	778	553	7.66E+06	0.15%	1.27E+05	0.69%	2.24E+05	2.48E+05
3.03	614.2	777	552	7.66E+06	0.15%	1.30E+05	0.97%	2.26E+05	2.51E+05
3.19	612.6	775	550	7.66E+06	0.15%	1.35E+05	0.85%	2.31E+05	2.55E+05
3.36	614.8	778	553	7.66E+06	0.15%	1.35E+05	0.86%	2.31E+05	2.55E+05
3.53	613.9	777	552	7.66E+06	0.15%	1.28E+05	0.20%	2.24E+05	2.48E+05
3.69	616.5	781	555	7.66E+06	0.15%	1.19E+05	0.50%	2.15E+05	2.40E+05
3.86	614.1	777	552	7.66E+06	0.15%	1.10E+05	0.77%	2.06E+05	2.32E+05
4.03	615.1	779	553	7.66E+06	0.15%	1.09E+05	0.61%	2.06E+05	2.31E+05
4.06	615.1	779	553	7.66E+06	0.15%	1.12E+05	1.01%	2.09E+05	2.34E+05
4.10	229.9	109	3	7.66E+06	0.15%	1.41E+05	0.98%	1.66E+05	2.05E+05

Experiment 06-23-10 (cont.)

App. $mSiO_2$ (mol SiO_2 / kg H_2O+CO_2)		$mSiO_2$ - Qtz Sat (mol SiO_2 / kg H_2O+CO_2)		Tlc produced (mol)		Tlc growth rate (mol · sec^{-1})		Tlc growth rate (mol · sec^{-1} · m^{-2})		Carbon Dioxide (mole percent)	
ρ↑	ρ↓	ρ↑	ρ↓	ρ↑	ρ↓	ρ↑	ρ↓	ρ↑	ρ↓	ρ↑	ρ↓
0.00	0.00	0.00	0.00	0.00E+00	0.00E+00	0.00E+00	0.00E+00	0.00E+00	0.00E+00	0.00%	0.00%
0.00	0.00	0.00	0.00	0.00E+00	0.00E+00	0.00E+00	0.00E+00	0.00E+00	0.00E+00	0.00%	0.00%
0.95	1.04	0.59	0.64	8.50E-10	8.56E-10	9.45E-12	9.52E-12	5.70E-05	5.74E-05	0.81%	0.81%
2.47	2.71	2.08	2.13	3.16E-09	2.99E-09	3.84E-12	3.55E-12	2.33E-05	2.16E-05	2.95%	2.72%
3.11	3.41	2.58	2.65	4.00E-09	3.79E-09	1.41E-12	1.33E-12	8.59E-06	8.11E-06	3.72%	3.40%
3.43	3.76	2.84	2.91	4.45E-09	4.20E-09	7.37E-13	6.94E-13	4.47E-06	4.21E-06	4.12%	3.75%
3.65	3.99	3.03	3.10	4.77E-09	4.50E-09	5.35E-13	5.00E-13	3.25E-06	3.04E-06	4.41%	4.00%
3.84	4.21	3.18	3.25	5.03E-09	4.76E-09	4.43E-13	4.21E-13	2.69E-06	2.56E-06	4.65%	4.21%
4.02	4.40	3.33	3.40	5.30E-09	5.01E-09	4.41E-13	4.15E-13	2.68E-06	2.53E-06	4.89%	4.41%
4.29	4.70	3.56	3.63	5.71E-09	5.40E-09	6.90E-13	6.50E-13	4.20E-06	3.95E-06	5.25%	4.73%
4.37	4.78	3.60	3.68	5.79E-09	5.47E-09	1.27E-13	1.24E-13	7.72E-07	7.53E-07	5.32%	4.79%
4.50	4.92	3.74	3.79	6.04E-09	5.66E-09	4.23E-13	3.15E-13	2.57E-06	1.92E-06	5.55%	4.94%
4.61	5.05	3.72	3.82	6.01E-09	5.71E-09	-4.54E-13	8.53E-13	-2.77E-06	5.19E-06	5.52%	4.98%
4.70	5.14	3.80	3.89	6.15E-09	5.83E-09	2.59E-13	2.28E-13	1.58E-06	1.39E-06	5.64%	5.08%
4.70	5.15	3.80	3.89	6.16E-09	5.84E-09	4.66E-15	5.26E-15	2.84E-08	3.20E-08	5.65%	5.08%
4.75	5.20	3.84	3.93	6.23E-09	5.90E-09	1.14E-13	1.08E-13	6.93E-07	6.58E-07	5.71%	5.13%
4.83	5.29	3.83	3.93	6.21E-09	5.91E-09	-2.91E-13	1.12E-13	-1.77E-06	6.80E-07	5.69%	5.14%
4.91	5.37	3.90	4.00	6.34E-09	6.03E-09	2.44E-13	2.23E-13	1.49E-06	1.35E-06	5.81%	5.23%
4.98	5.46	3.95	4.05	6.43E-09	6.12E-09	1.51E-13	1.50E-13	9.21E-07	9.11E-07	5.89%	5.31%
5.00	5.47	3.96	4.06	6.45E-09	6.14E-09	3.32E-14	2.89E-14	2.02E-07	1.76E-07	5.91%	5.32%
5.12	5.61	3.98	4.10	6.49E-09	6.20E-09	5.92E-13	9.99E-13	3.60E-06	6.08E-06	5.94%	5.37%
5.11	5.59	3.96	4.07	6.45E-09	6.16E-09	-7.03E-14	-6.99E-14	-4.28E-07	-4.25E-07	5.90%	5.34%
5.07	5.55	3.93	4.04	6.39E-09	6.11E-09	-9.33E-14	-8.88E-14	-5.68E-07	-5.40E-07	5.85%	5.30%
5.04	5.52	3.91	4.02	6.36E-09	6.07E-09	-5.34E-14	-5.13E-14	-3.25E-07	-3.12E-07	5.83%	5.27%
5.00	5.48	3.88	3.99	6.31E-09	6.02E-09	-9.16E-14	-8.81E-14	-5.57E-07	-5.36E-07	5.78%	5.23%
5.01	5.48	3.88	4.00	6.31E-09	6.02E-09	4.02E-15	5.56E-15	2.45E-08	3.38E-08	5.78%	5.23%
5.06	5.53	3.92	4.04	6.39E-09	6.10E-09	1.35E-13	1.27E-13	8.24E-07	7.71E-07	5.85%	5.29%
5.13	5.61	3.98	4.10	6.49E-09	6.20E-09	1.67E-13	1.61E-13	1.02E-06	9.80E-07	5.94%	5.37%
5.20	5.69	4.04	4.15	6.60E-09	6.30E-09	1.78E-13	1.66E-13	1.08E-06	1.01E-06	6.03%	5.45%
5.21	5.70	4.04	4.16	6.60E-09	6.30E-09	8.12E-15	9.84E-15	4.94E-08	5.99E-08	6.04%	5.45%
5.18	5.68	4.02	4.13	6.56E-09	6.27E-09	-3.30E-13	-3.13E-13	-2.01E-06	-1.90E-06	6.00%	5.42%
4.96	5.43	4.29	4.34	7.08E-09	6.62E-09	3.41E-12	2.33E-12	2.08E-05	1.42E-05	6.45%	5.69%
						Max Growth Rate					
						9.45E-12	9.52E-12				

C-2. *In Situ* Photomicrographs of Experiments

This appendix provides photomicrographs of experiments. The photomicrographs are screen capture images acquired from videos of experiments; each image has a horizontal field of view of 590 µm. Most photomicrographs are sets of four images taken during the following event during the experiment: the time of prograde homogenization, the first visible appear of fibers (1^{st} fibers), the moment when quartz appears to be completely dissolved (Qtz gone), and the time of retrograde homogenization. Each image has the time (t) and temperature (T) labeled as well as the mineral phases present (i.e., Mgs - magnesite, Qtz - quartz).

Experiment: 11-04-09 – plate dominated

Prograde Homogenization

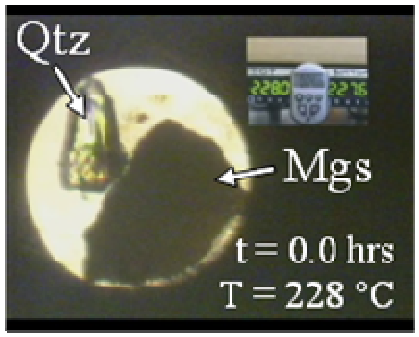

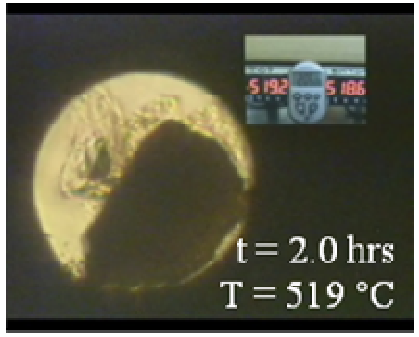

Qtz gone

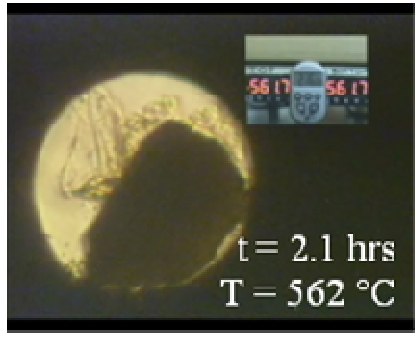

Retrograde Homogenization

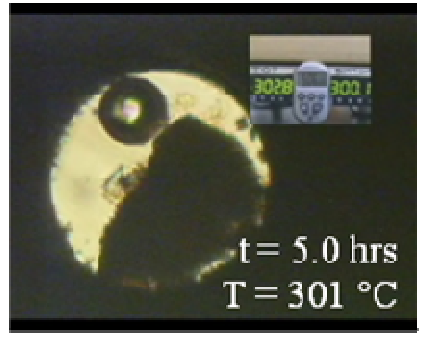

Experiment : 08-06-10 – plate dominated

Prograde Homogenization

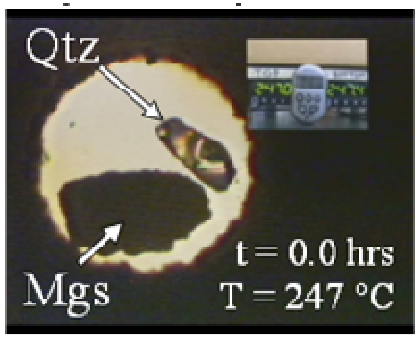

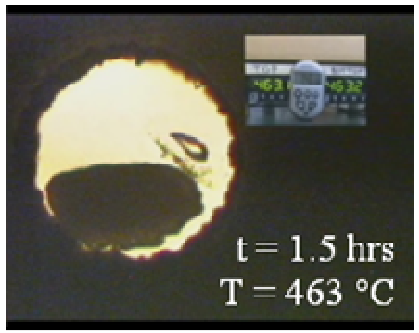

Qtz gone

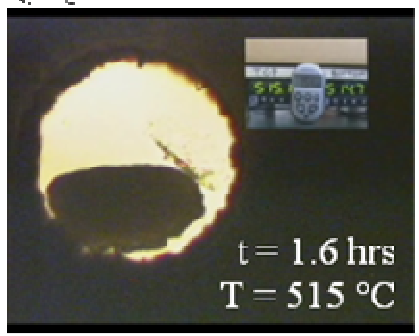

Retrograde Homogenization

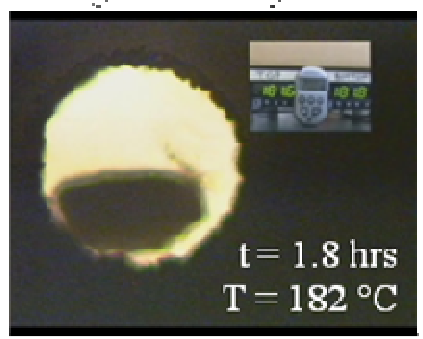

Experiment: 03-02-10 – both plates and fibers present

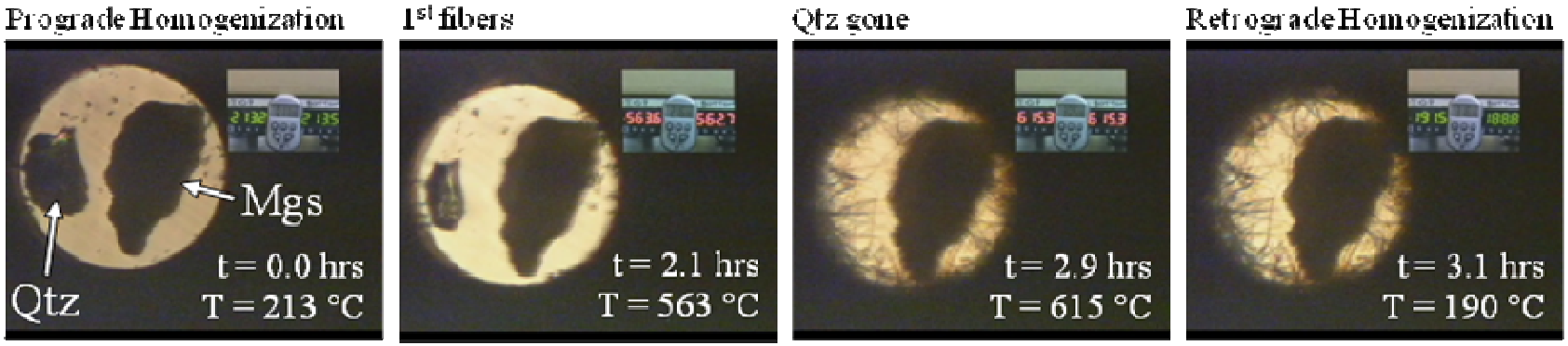

Experiment: 12-02-09 – both plates and fibers present

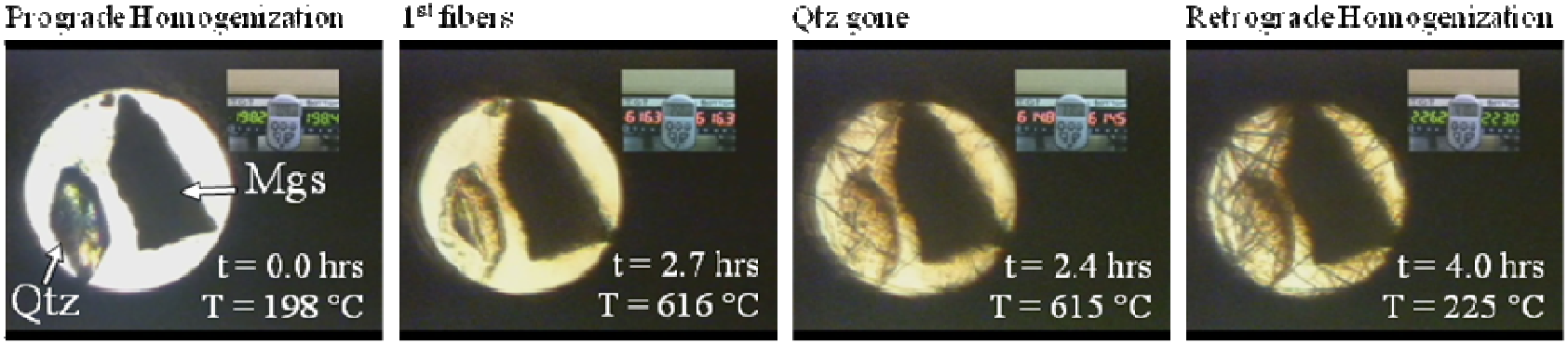

Experiment: 06-23-10 – both plates and fibers present

Prograde Homogenization

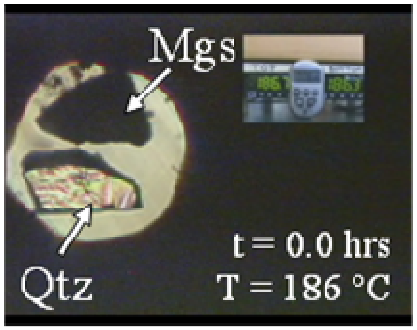

1st fibers

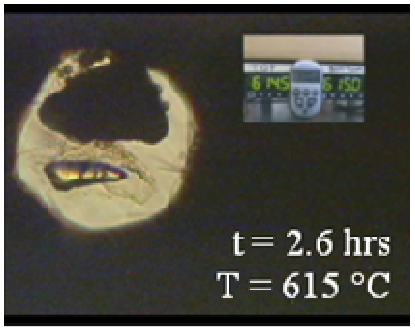

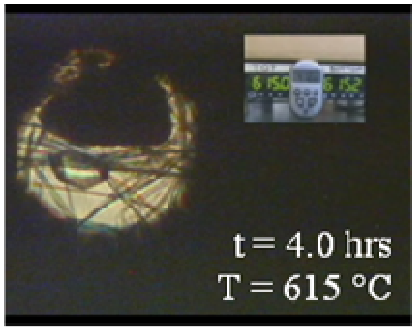

Retrograde Homogenization

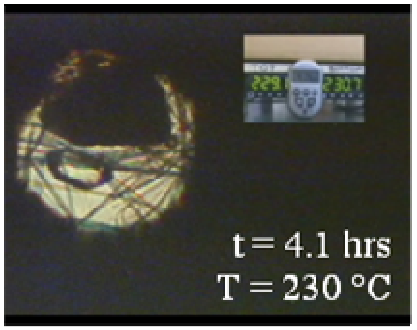

Experiment: 08-25-09 – fiber dominated

Homogenization

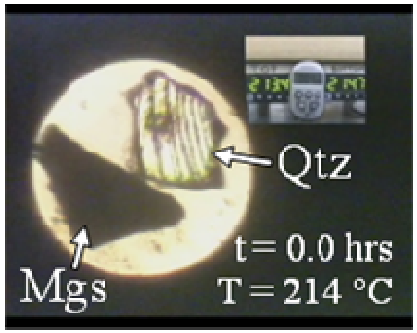

1st fibers

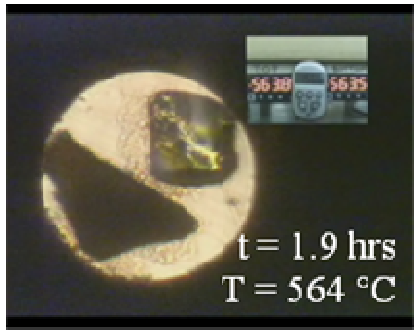

Qtz gone

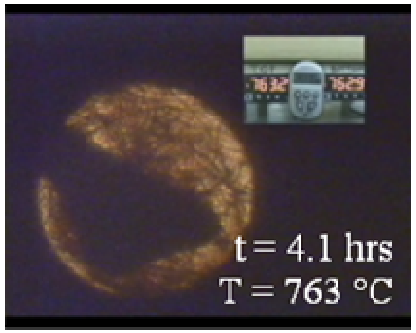

Retrograde Homogenization

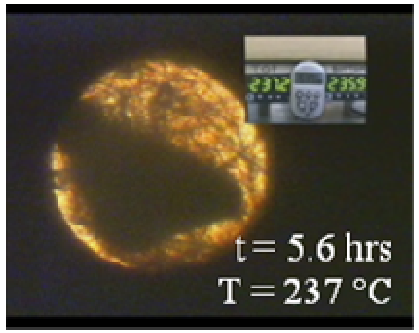

Experiment: 05-11-10 – fiber dominated

Homogenization

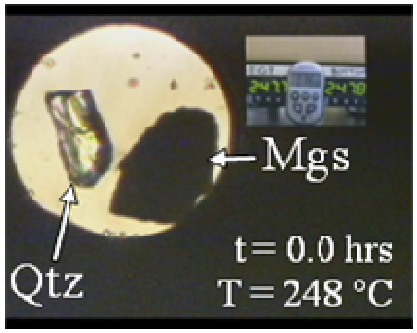

1st fibers

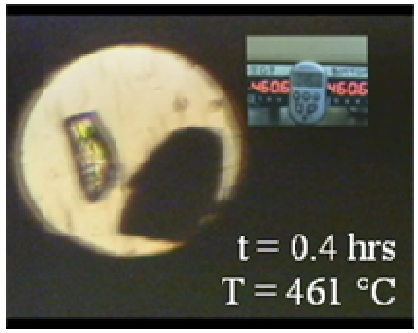

Qtz gone

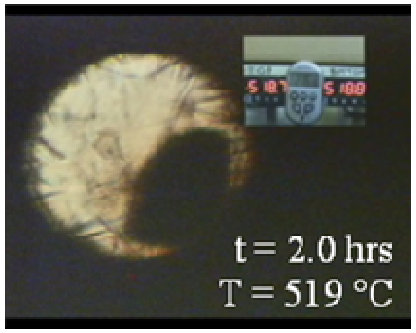

Retrograde Homogenization

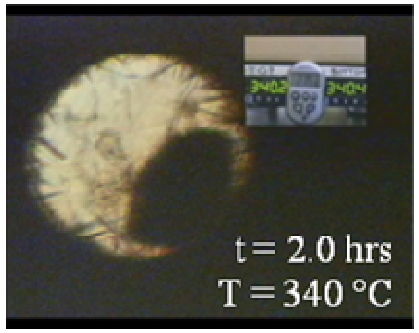

C-3. Post-experiment Secondary Electron Images

This appendix provides secondary electron images of post-experiment reaction products collect on a JEOL JXA-8900 electron probe microanalyzer. Each image is accompanied by a scale and a short description of the phases present. Phase identification was determined by SR-XRD and energy dispersive spectroscopy.

Experiment: 11-04-09 – plate dominated

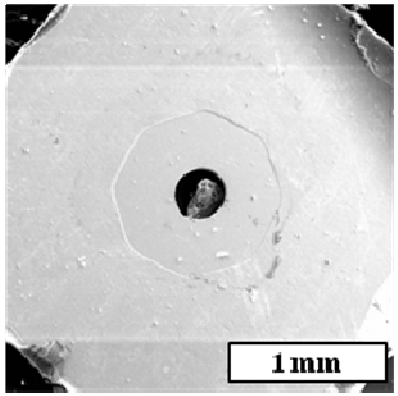

view of full gasket

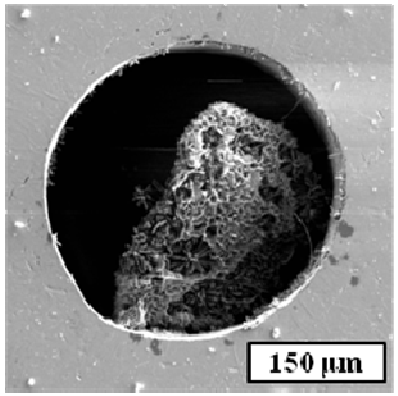

view of gasket aperture

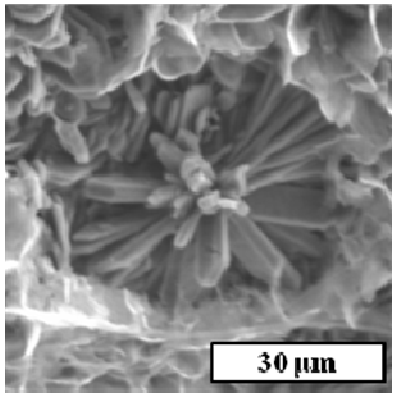

forsterite floret surrounded by talc plates

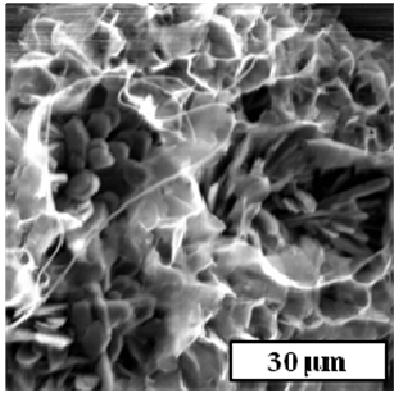

forsterite floret surrounded by talc plates

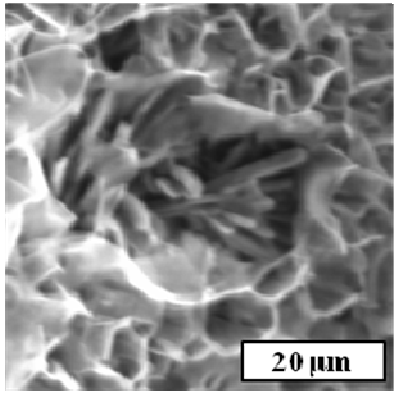

forsterite floret surrounded by talc plates

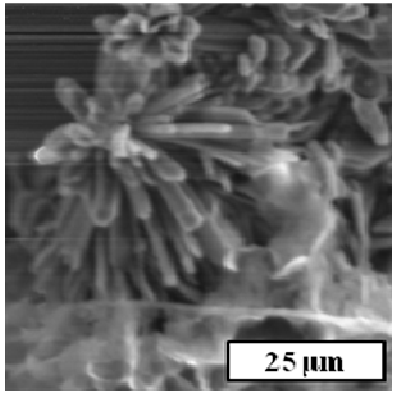

forsterite floret surrounded by talc plates

Experiment: 11-04-09 – plate dominated **(cont.)**

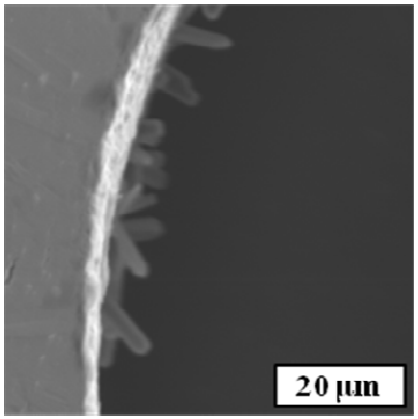

forsterite on gasket wall

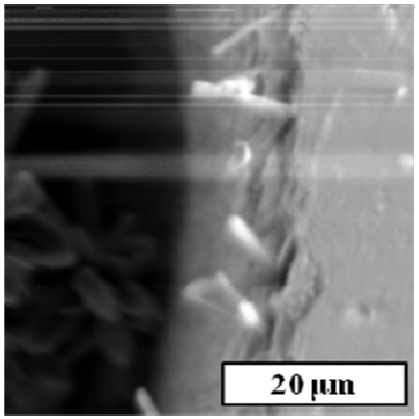

forsterite on gasket wall

Experiment: 08-06-10 – plate dominated

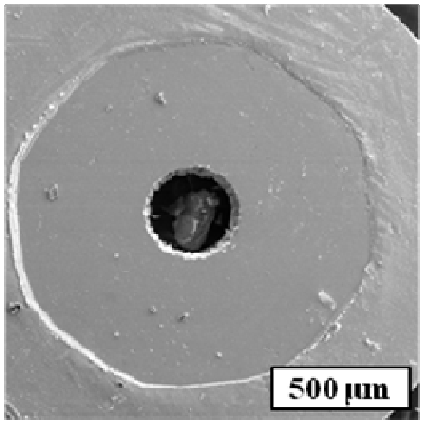

view of full gasket

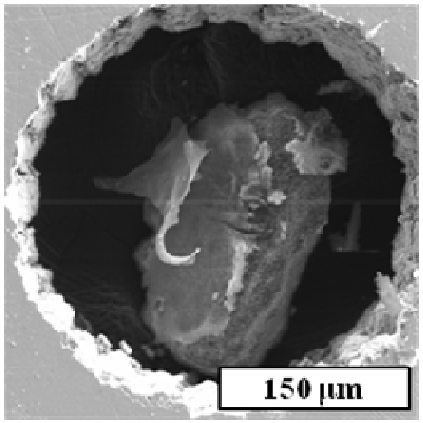

view of gasket aperture

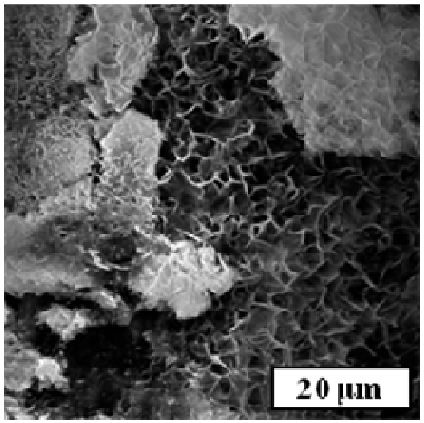

talc plates on magnesite with a rind from where the magnesite was in contact with the diamond

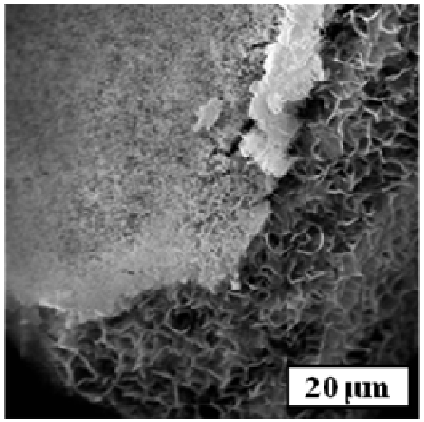

talc plates on magnesite and the rind

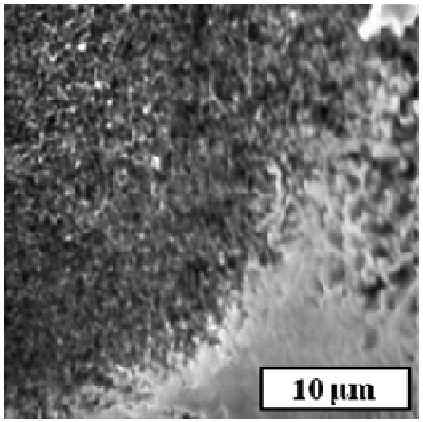

the rind on the magnesite

Experiment: Run 27 – plate dominated

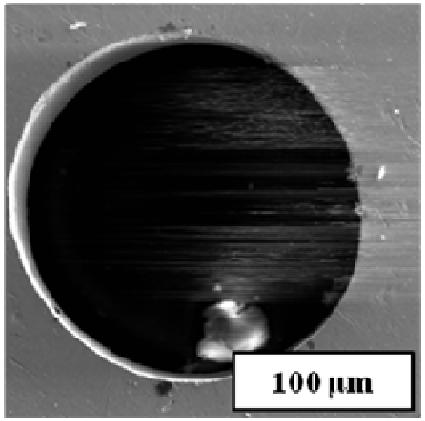

view of gasket aperture

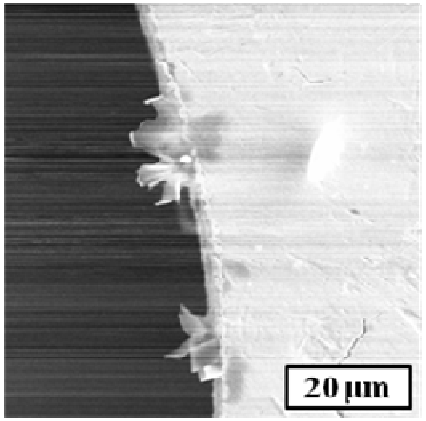

talc plates on the gasket wall

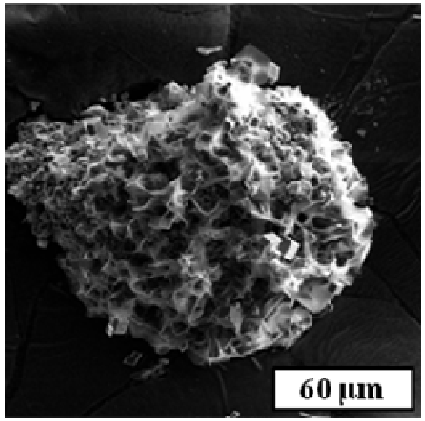

talc plates and reprecipitated magnesite

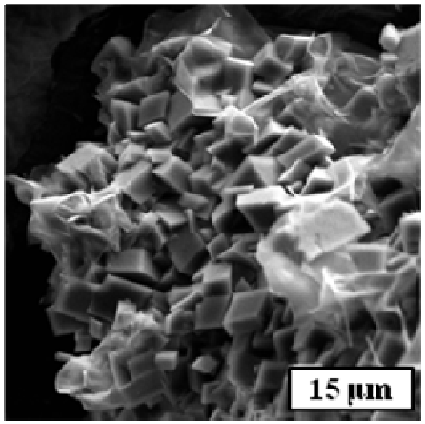

talc plates and magnesite rhombahedra

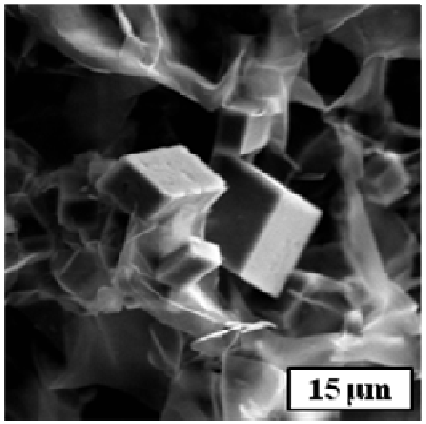

talc plates and magnesite rhombahedra

Experiment: Run 32 – plate dominated

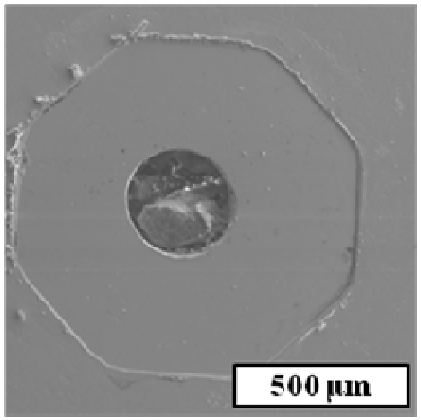

view of full gasket

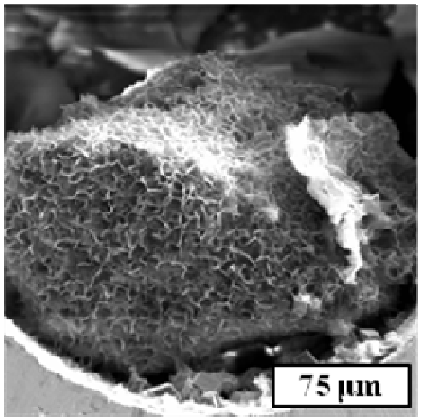

talc plates on magnesite

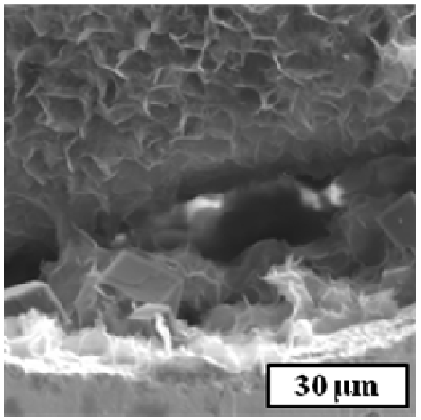

talc plates on magnesite and magnesite rhombahedra on wall

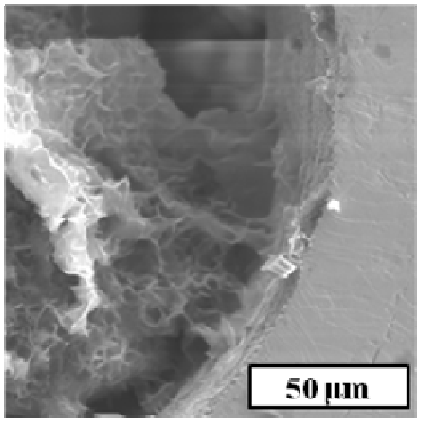

talc plates on magnesite and magnesite rhombahedra on wall

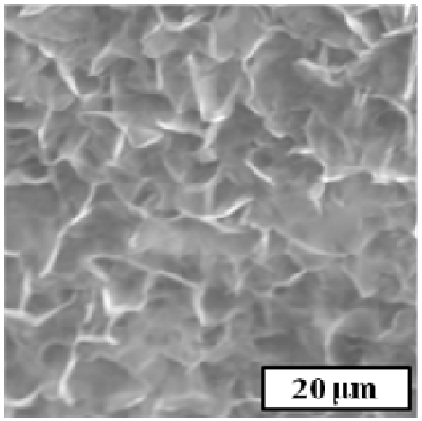

talc plates on magnesite

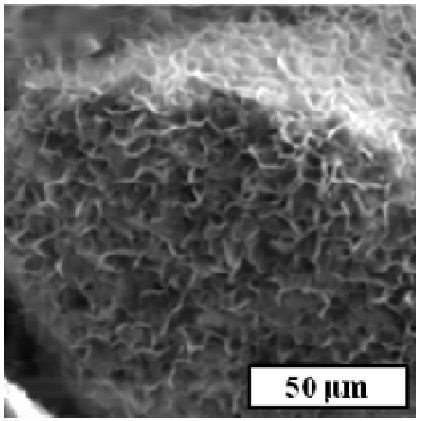

talc plates on magnesite

Experiment: Run 33 – plate dominated

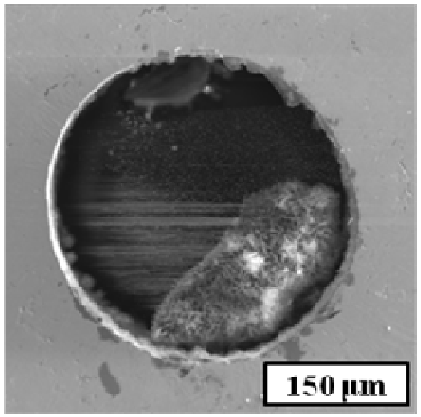

view of gasket aperture

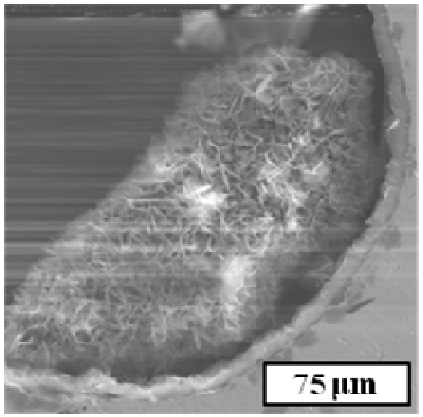

talc plates on magnesite

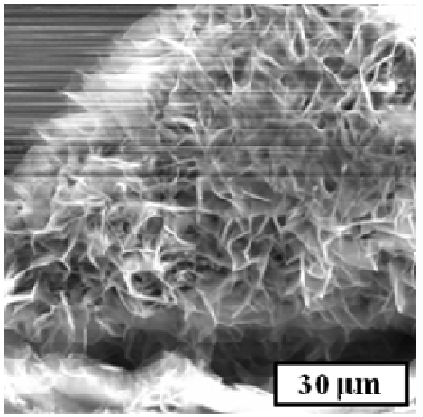

talc plates on magnesite

Experiment: Run 37 – plate dominated

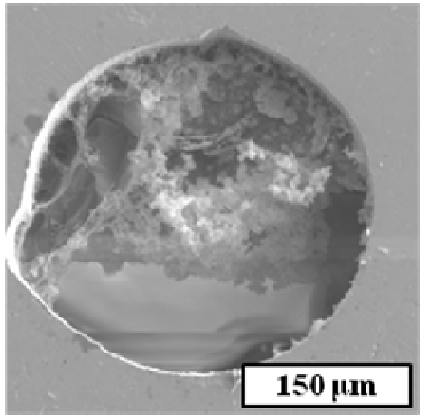

view of gasket aperture

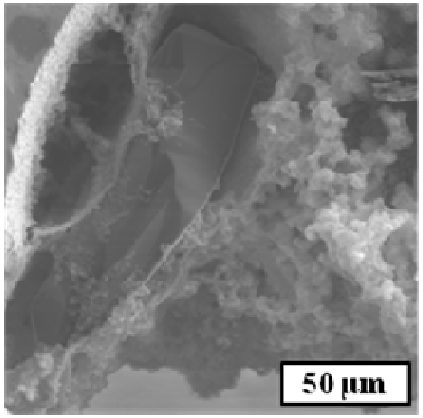

quartz and talc plates on magnesite

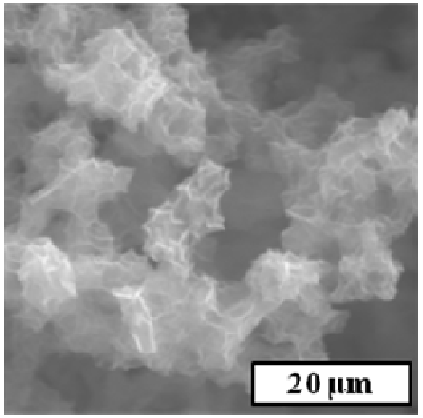

talc plates on magnesite

Experiment: 08-25-09 fiber dominated

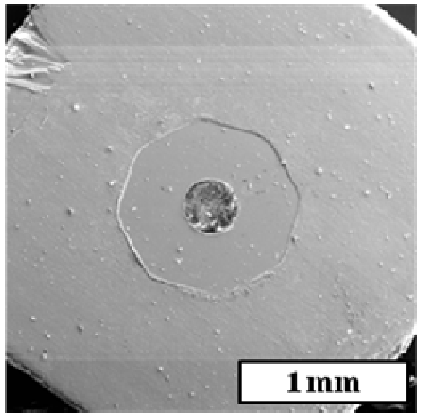

view of full gasket

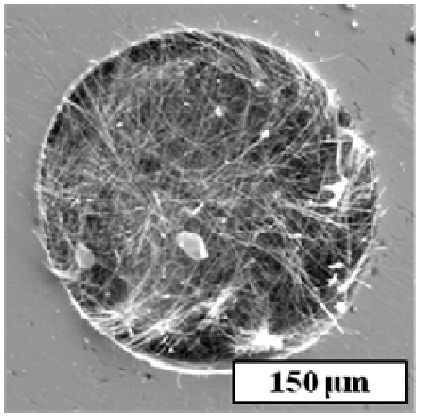

view of gasket aperture

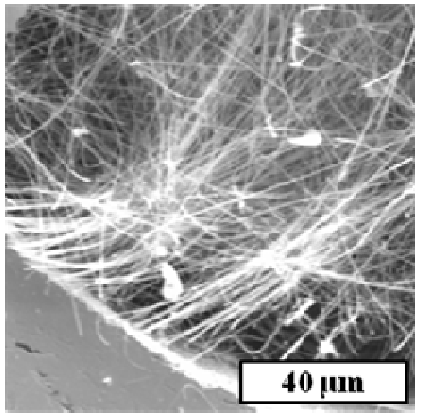

talc fibers on magnesite

Experiment: 05-11-10 – fiber dominated

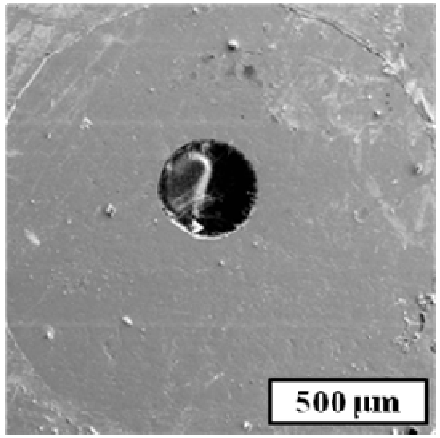

view of full gasket

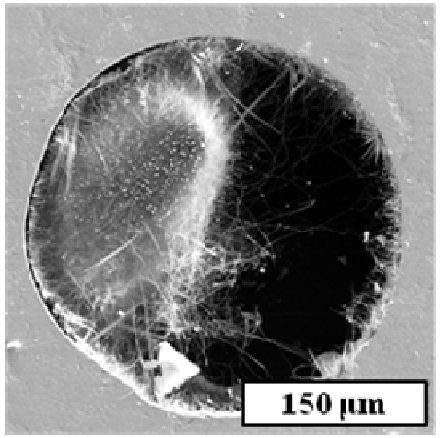

view of gasket aperture

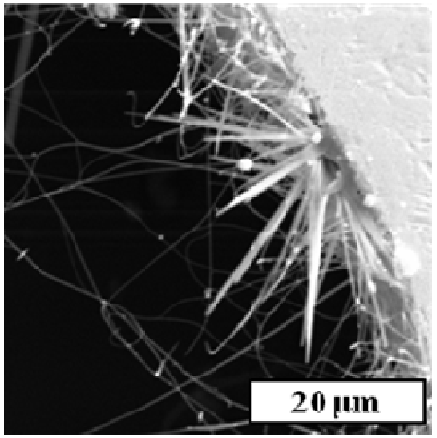

talc fibers radiating from the gasket wall

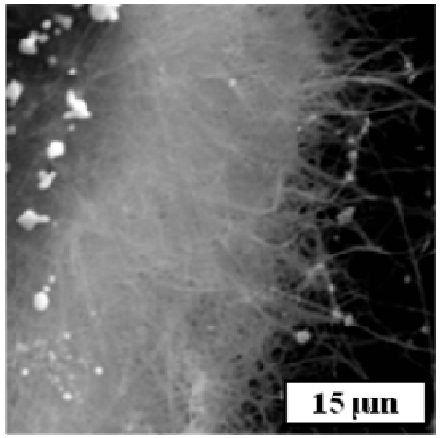

talc fibers on magnesite

Experiment: 12-02-09 both plates and fibers present

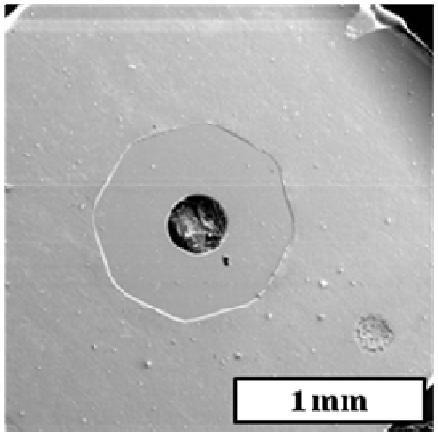

view of full gasket

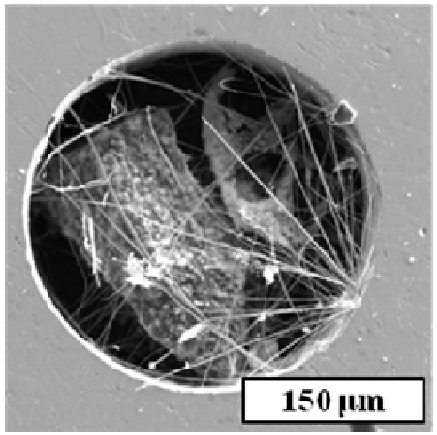

view of gasket aperture

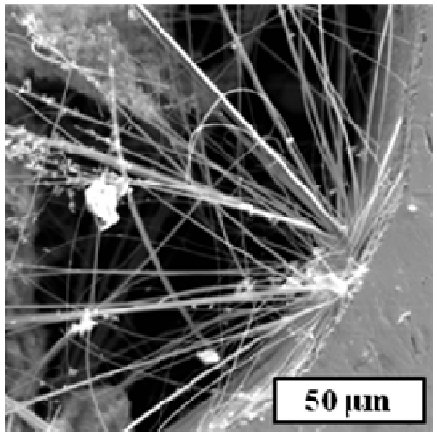

talc fibers radiating from the gasket wall

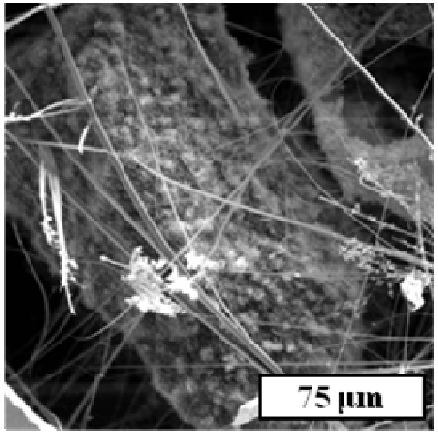

talc plates and fibers on magnesite

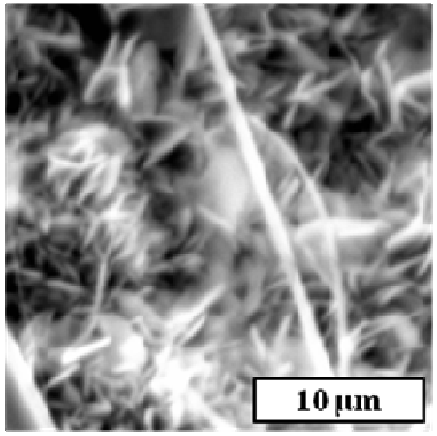

talc plates and fibers on magnesite

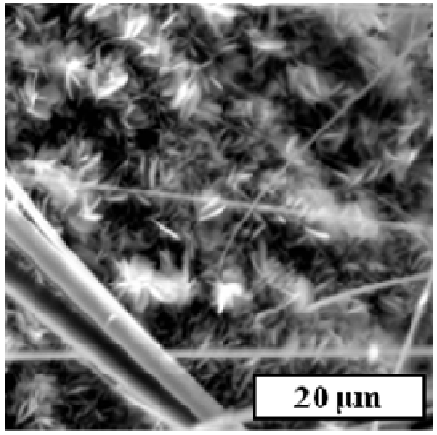

talc plates and fibers on magnesite

Experiment: 03-02-10 both plates and fibers present

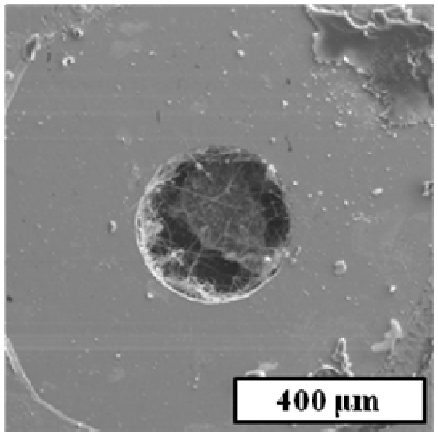

view of full gasket

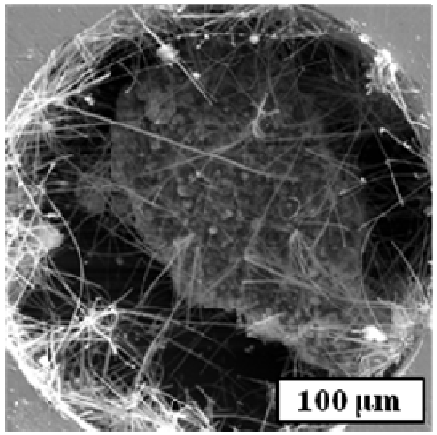

view of gasket aperture

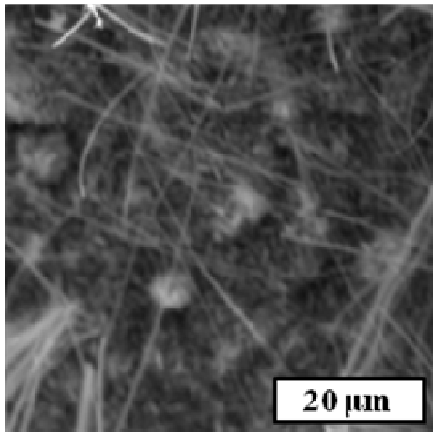

talc plates and fibers on magnesite

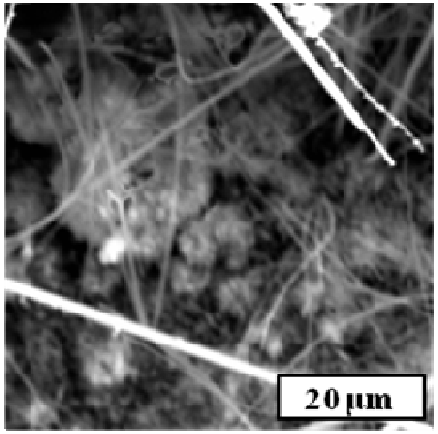

talc plates and fibers on magnesite

Experiment: 06-23-10 – both plates and fibers present

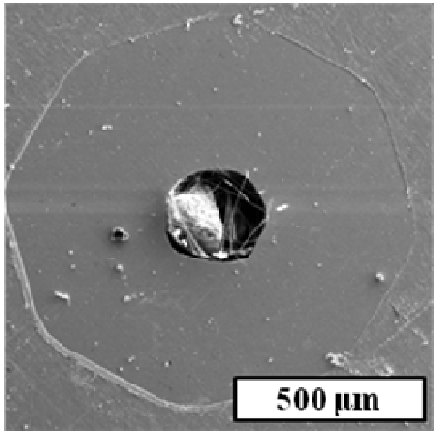

view of full gasket

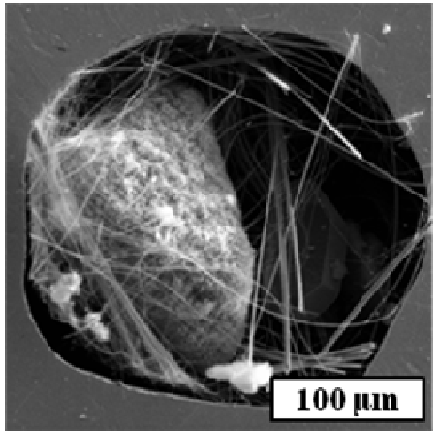

view of gasket aperture

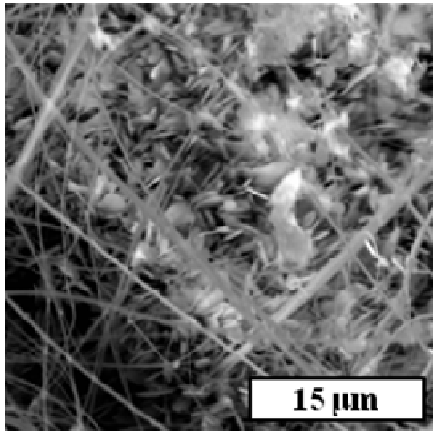

talc plates and fibers on magnesite

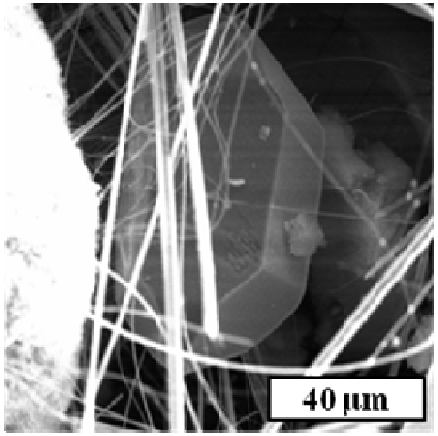

quartz with talc fibers

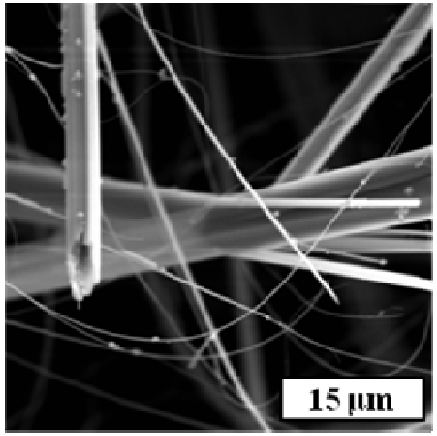

talc fibers

Experiment: Run 36 both plates and fibers present

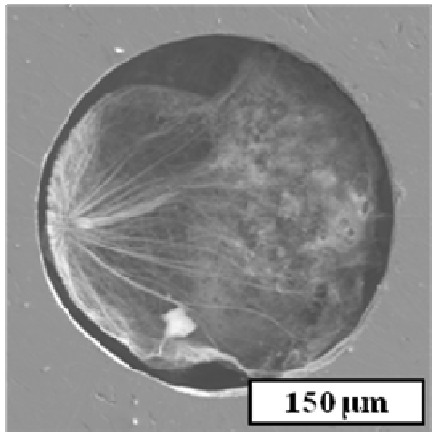

view of gasket aperture

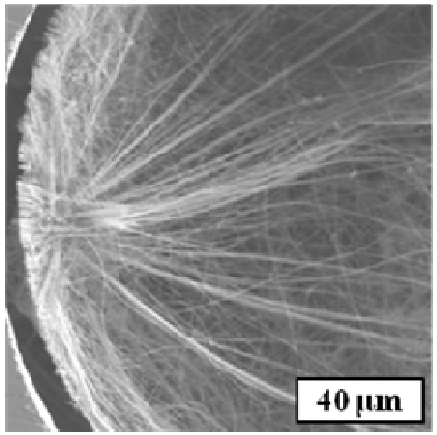

talc fibers radiating from the gasket wall

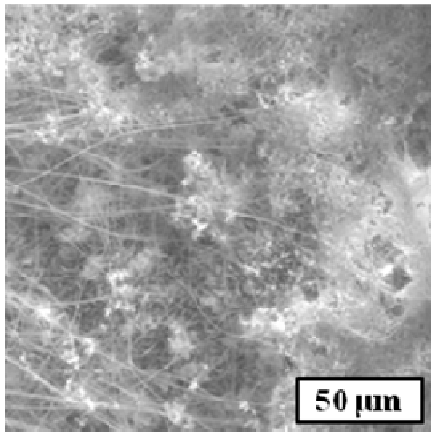

talc plates and fibers on magnesite

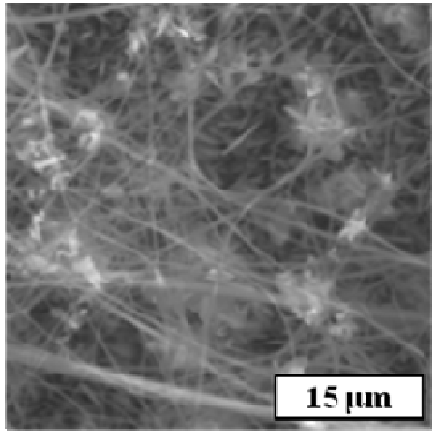

talc plates and fibers on magnesite

C-4. Synchrotron Radiation X-ray Diffraction Plates for 'Run 27'

This appendix provides some of the plates produced during synchrotron radiation x-ray diffraction analysis of an experiment (Run 27). The starting materials for this experiment were magnesite + quartz + water. The experiment was held at five isothermal temperature steps: (1) 465 °C for 1.5 hours, (2) 515 °C for 0.50 hours, (3) 565 °C for 0.50 hours (4) 615 °C for 1.50 hours and (5) 465 °C for 1.00 hours. The four plates presented are the raw data collected as represented in the program Fit2d® by an inverse grey scale and the labeled by time and experimental temperature at collection.

Spectra: Run 27_002
Collection time: 0.00 hours
Temperature: 25 °C

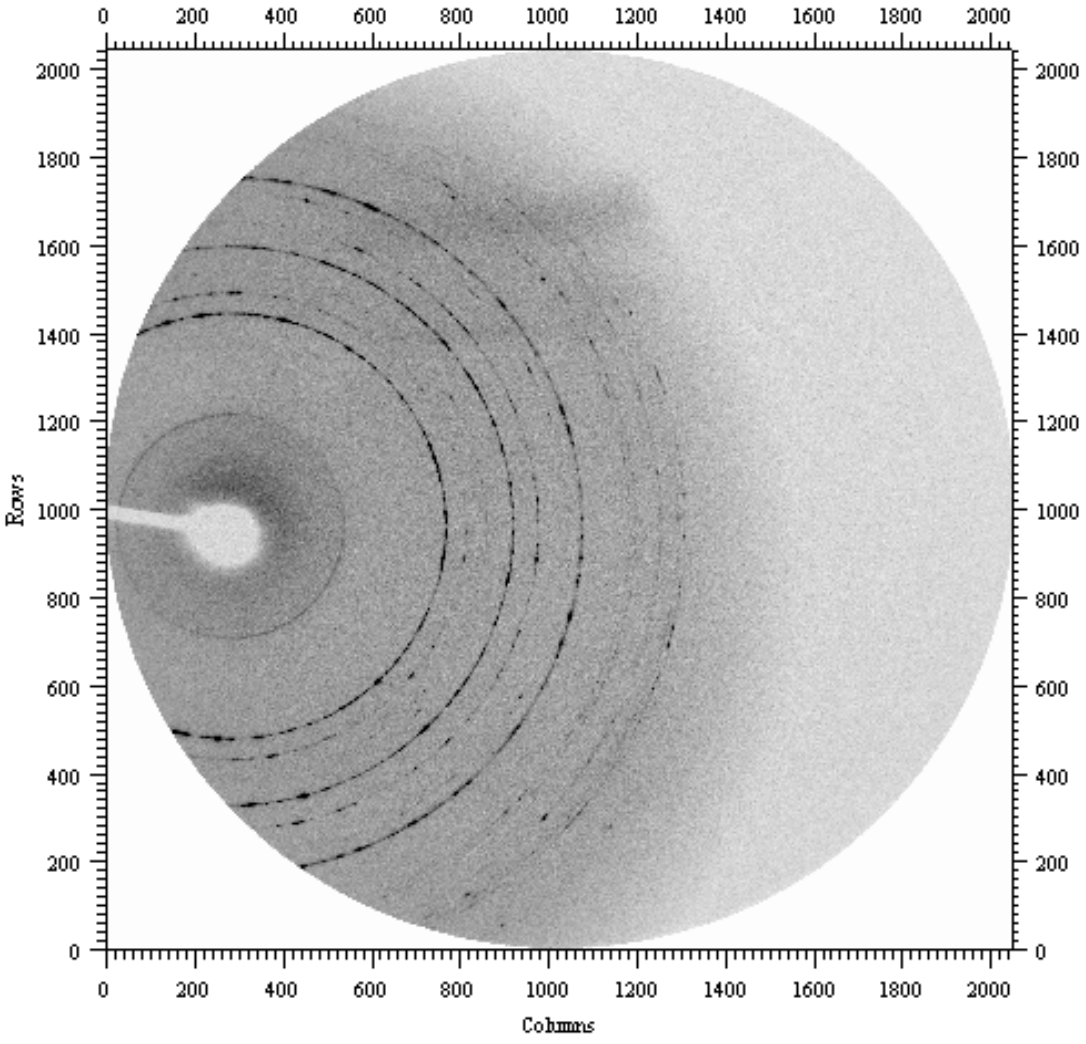

Spectra: Run 27_054
Collection time: 2.00 hours
Temperature: 515 °C

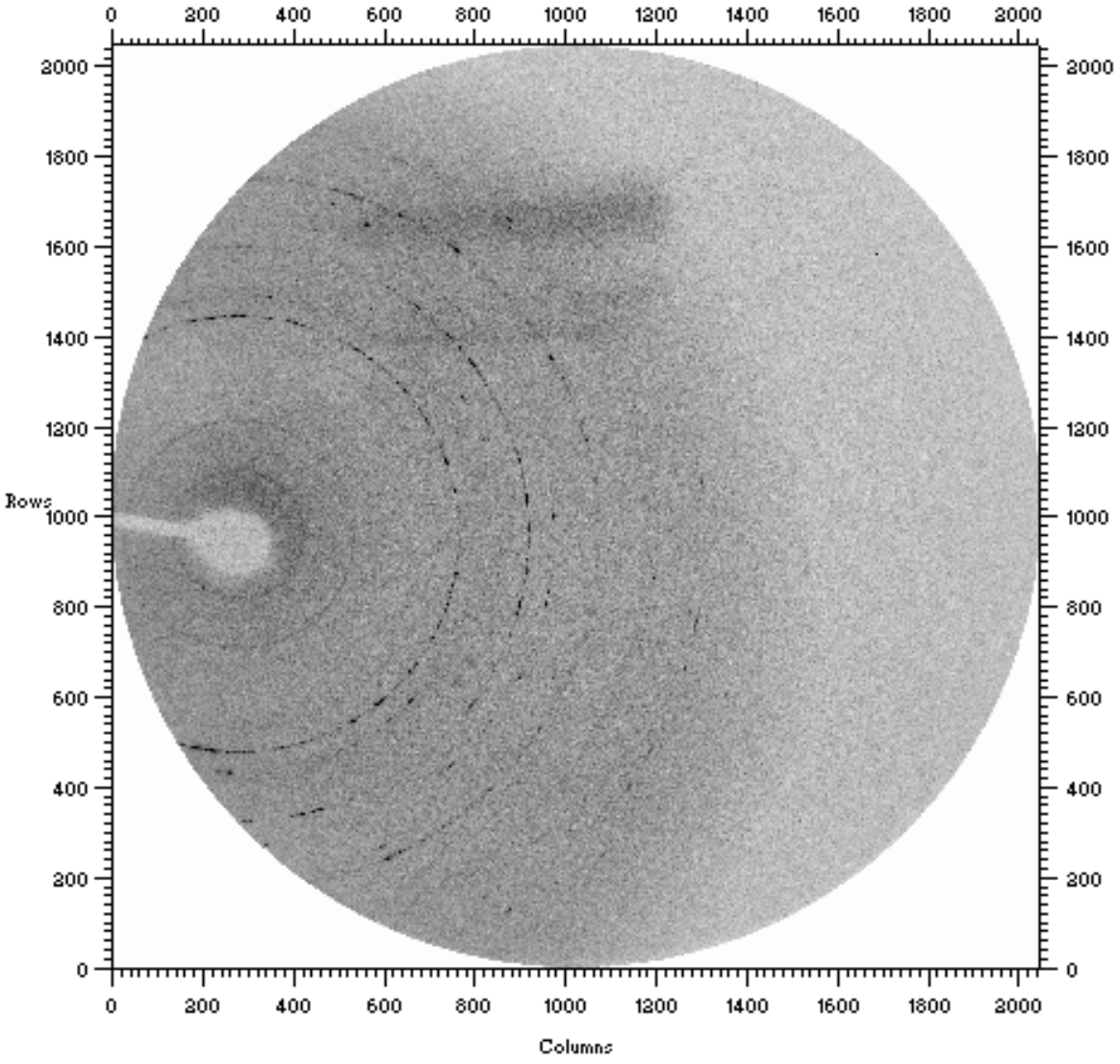

Spectra: Run 27_109
Collection time: 4.00 hours
Temperature: 615 °C

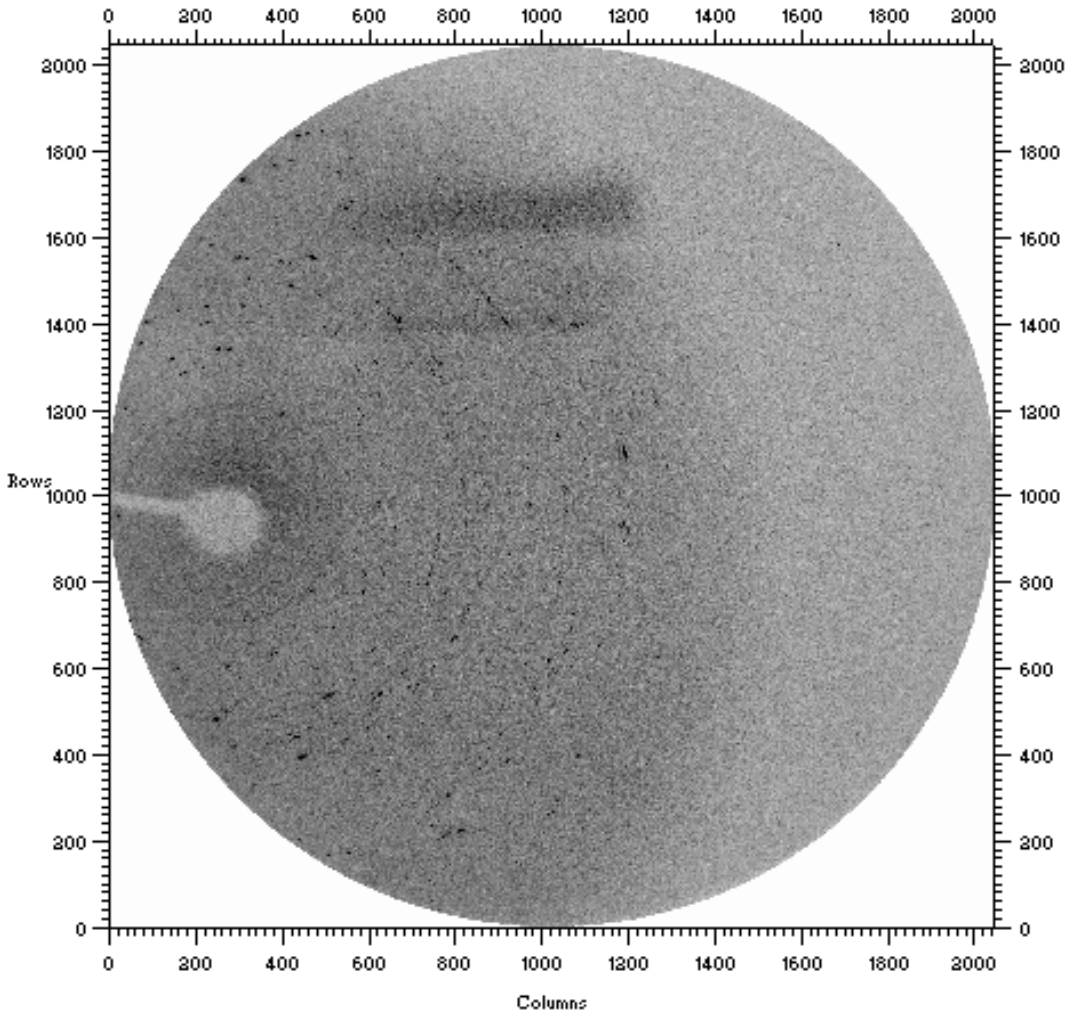

Spectra: Run 27_150
Collection time: 5.64 hours
Temperature: 465 °C

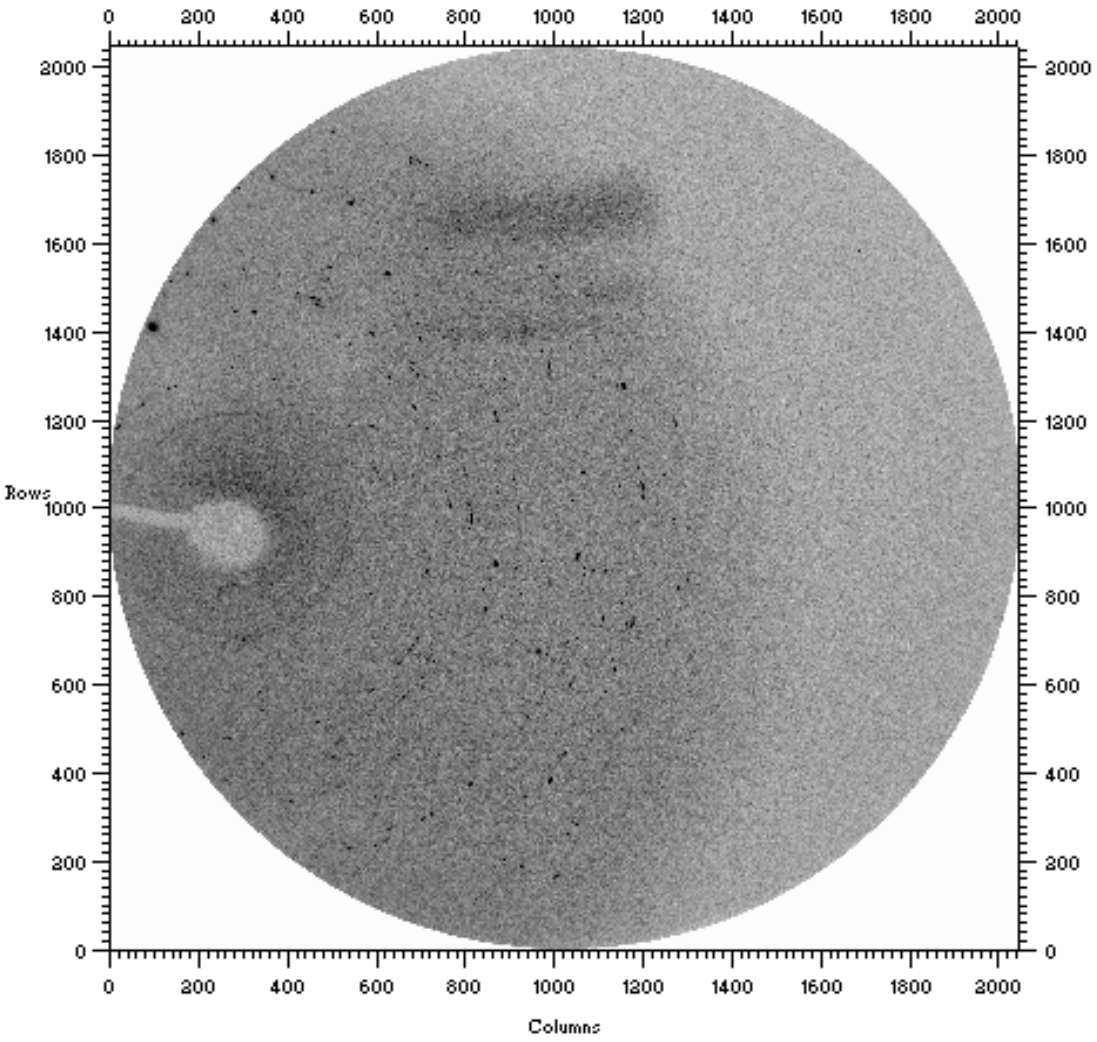

Appendix D – Videos of Experiments

Videos accompanying the data and images have been provided via electronic supplementary material (videos provided are listed below). All videos have been condensed (sped up so that 1 second of video time equals 8.6 minutes of actual time). The field of view for all videos is 590 μm across the horizontal. See the text for additional discussion.

Ol+Qtz+Fluid Experiments

Experiment	**Starting Materials**
Plate dominated experiments	
06-09-07	Ol+Qtz+0.1m*m*HCl
07-09-07	Ol+Qtz+0.1m*m*HCl
Experiments resulting in both plates and fibers	
08-23-07	Ol+Qtz+0.1m*m*HCl
08-29-07	Ol+Qtz+0.1m*m*HCl
02-24-08	Ol+Qtz+0.1m*m*HCl
08-27-08	Ol+Qtz+10m*m*HCl
Fiber dominated experiments	
09-05-07	Ol+Qtz+H_2O
06-10-07	Ol+Qtz+0.1m*m*HCl

Mgs+Qtz+H_2O Experiments

Experiment	**Starting Materials**
Plate dominated experiments	
11-04-09	Mgs+Qtz+H_2O
08-06-10	Mgs+Qtz+H_2O
Experiments resulting in both plates and fibers	
12-02-09	Mgs+Qtz+H_2O
03-02-10	Mgs+Qtz+H_2O
06-23-10	Mgs+Qtz+H_2O
Fiber dominated experiments	
08-25-09	Mgs+Qtz+H_2O
05-11-10	Mgs+Qtz+H_2O

References

Abu-Jaber, N. S. and Kimberley, M. M. (1992) Origin of ultramafic-hosted vein magnesite deposits. Ore Geology Reviews, 7, 155-191.

Aharon, P. (1988) A stable-isotope study of magnesites from the Rum Jungle Uranium Field, Australia: Implications for the origin of strata-bound massive magnesites. Chemical Geology, 69, 127-145.

Ahn, J. H. and Busek, P. R. (1991) Microstructures and fiber-formation mechanisms of crocidolite asbestos. American Mineralogist, 76, 1467-1478.

Andreani, M., Mével, C., Boullier, A.-M., and Escartin, J. (2007) Dynamic control on serpentine crystallization in veins: constraints on hydration processes in oceanic peridotites. Geochemistry Geophysics and Geosystems, 8, Q02012, doi:10.1029/2006GC001373.

Akinfiev, N. N. and Diamond, L. W. (2009) A simple predictive model of quartz solubility in water–salt–CO_2 systems at temperatures up to 1000 °C and pressures up to 1000 MPa. Geochimica et Cosmochimica Acta, 73, 1597-1608.

Aranovich, L. and Newton, R. (1999) Experimental determination of CO_2-H_2O activity-composition relations at 600-1000 °C and 6-14 kbar by reversed decarbonation and dehydration reactions. American Mineralogist, 84, 1319-1332.

Audétat, A. and Keppler, H. (2005) Solubility of rutile in subduction zone fluids, as determined by experiments in the hydrothermal diamond anvil cell. Earth and Planetary Science Letters, 232, 393-402.

Bailey, K. F., Kelse, J., Wylie, A. G. and Lee, R. J. (2003) The asbestiform and nonasbestiform mineral growth habit and their relationship to cancer studies: A pictorial presentation. Report for R. J. Lee Group, Inc., Monroeville, Pennsylvania, April 2003.

Bakker, R. J. (2003) Package FLUIDS 1. Computer programs for analysis of fluid inclusion data and for modeling bulk fluid properties. Chemical Geology, 194, 3-23.

Bassett, W. A., Shen, A. H., Bucknum, M., and Chou I-M. (1993) A new diamond anvil cell for hydrothermal studies to 10 GPa and -190°C to 1100°C: Reviews of Scientific Instruments, 64, 2340-2345.

Bassett, W. A., Wu, T. C., Chou, I-M., Haselton, H. T., Jr., Frantz, J., Mysen, B. O., Huang, W. L., Sharma, K., and Schiferl, D. (1996) The hydrothermal diamond anvil cell (HDAC) and its applications. In: "Mineral Spectroscopy: A Tribute to Roger G. Burns", M.D. Dyar, C. McCammon, and M.W. Schaefer eds., The Geochemical Society Special Publication, 5, 261-272.

Bassett, W. A. (2003) High pressure-temperature aqueous systems in the hydrothermal diamond anvil cell (HDAC). European Journal of Mineralogy, 15, 773 – 780.

Beard, M. E., Crankshaw, O. S., Ennis, J. T. and Moore, C. E. (2001) Analysis for crayons for asbestos and other fibrous materials, and recommendations for improved analytical definitions (informal report). Research Triangle Institute, Center for Environmental Measurements and Quality Assurance, Earth and Mineral Sciences Department, Research Triangle Park, North Carolina, 23 pp., appendices A-H.

Becker, H. and Altherr, R. (1992) Evidence from ultra-high-pressure marble for recycling of sediments into the mantle. Nature, 358, 745-748.

Berman, R. G., Engi, M., Greenwood, H. J., and Brown, T. H. (1986) Derivation of internally-consistent thermodynamic data by the technique of mathematical programming: a review with application to the system MgO-SiO_2-H_2O. Journal of Petrology, 27, 1331-1364.

Biellmann, C., Gillet, P., Guyot, F., Peyronneau, J., and Reynard, B. (1993) Experimental evidence for carbonate stability in the Earth's lower mantle. Earth and Planetary Science Letters, 118, 31–41.

Bose, K. and Ganguly, J. (1994) Thermogravitmetric study of the dehydration kinetics of talc. American Mineralogist, 79, 692-699.

Bowen, N. L. and Tuttle, O. F. (1949) The system MgO-SiO_2-H_2O. Bulletin of the Geological Society of America, 60, 439-460.

Bricker, O. P., Nesbitt, H. W., and Gunter, W. D. (1973) The stability of talc. American Mineralogist, 58, 64-72.

Brindley, G. W. and Hayami, R. (1963) Kinetics and mechanisms of dehydration and recrystallization of serpentine I. Clays and Clay Minerals, 12, 49-54.

Burchard, M., Zaitsev, A. M., and Maresch, W. V. (2003) Extending the pressure and temperature limits of the hydrothermal diamond anvil cells. Review of Scientific Instruments, 74, 1263 – 1266.

Cama, J., Ganor, J., Ayora, C. and Lasaga, A. C. (2000) Smectite dissolution kinetics at 80°C and pH 8.8. Geochimica et Cosmochimica Acta, 64, 2701–2717.

Chernosky, J. V., Jr. (1976) The stability of anthophyllite- A reevaluation based on new experimental data. American Mineralogist, 61, 1145-1155.

Chernosky, J. V., Jr. and Autio, L. K. (1979) The stability of anthophyllite in the presence of quartz. American Mineralogist, 64, 294-303.

Chernosky, J. V., Jr., Day, H. W. and Caruso, L. J. (1985) Equilibria in the system MgO-SiO_2-H_2O: experimental determination of the stability of Mg-anthophyllite. American Mineralogist, 70, 223-236.

Christian, J. W. (2002) The Theory of Transforamtions in Metals and Alloys. Pergamon Press, New York, 1200 pgs.

Chou, I-M. (2007) Pressure calibrants in the hydrothermal diamond anvil cell. International Geology Review, 49, 289-300.

Davidson, L. E. Shaw, S. and Benning, L.G. (2008) Kinetics and mechanisms of schwertmannite transformation to goethite and hematite under alkaline conditions. American Mineralogist, 93, 1326-1337.

Day, H. W. and Halbach, H. (1979) The stability field of anthophyllite: the effect of experimental uncertainty on permissible phase diagram topologies. American Mineralogist, 64, 809-823.

Day, H. W., Chernosky, J. V. and Kumin, H. J. (1985) Equilibria in the system MgO-SiO_2-H_2O: a thermodynamic analysis. American Mineralogist, 70, 223-236.

Dungan, M. A. (1977) Metastability in serpentine-olivine equilibria. American Mineralogist, 62, 1018-1029.

Evans, B. W. and Trommsdorff, V. (1974) Stability of enstatite + talc, and CO_2-metasomatism of metaperidotite, Val d'Efra, Lepontine Alps. American Journal of Science, 274, 274-296.

Evans, B. W. (1977) Metamorphism of Alpine peridotite and serpentinite. Annual Reviews Earth and Planetary Sciences, 5, 397-447.

Ferrari, M. and Viti, C. (2010) Retrograde hydration sequence in disordered Mg-amphiboles: A TEM investigation. American Mineralogist, 95, 81-91.

Fiquet, G., Guyot, F., Kunz, M., Matas, J., Andrault, D., and Hanfland, M. (2002) Structural refinements of magnesite at very high pressure. American Mineralogist, 87, 1261-1265.

Frantz, J. D. and Popp, R. K. (1979) Mineral-solution equilibria - I. An experimental study of complexing and thermodynamic properties of aqueous $MgCl_2$ in the system MgO-SiO_2-H_2O-HCl. Geochimica et Cosmochimica Acta, 43, 1223-1239.

Fyfe, W. S. (1962) On the relative stability of talc, anthophyllite, and enstatite. American Journal of Science, 260, 460-466.

Gerya, T., Maresch, W. V., Buchard, M., Zakhartchouk, V., Doltsinis, N. L. and Fockenberg, T. (2005) Thermodynamic modeling of solubility and speciation of silica in H_2O-SiO_2 fluid up to 1300°C and 20 kbar based on the chain reaction formalism. European Journal of Mineralogy, 17, 269-283.

Gillet, P. (1993) Stability of magnesite ($MgCO_3$) at mantle pressure and temperature conditions: A Raman spectroscopy study. American Mineralogist, 78, 1328-1331.

Greenwood, H. J. (1963) The synthesis and stability of anthophyllite. Journal of Petrology, 4, 317-351.

Greenwood, H. J. (1967) Mineral equilibria in the system MgO-SiO_2-H_2O-CO_2, in Researches in Geochemistry, Abelson, P. ed.: New York, London, Syndey, John Wiley and Sons, p. 542-567.

Greenwood, H. J. (1971) Anthophyllite. Corrections and comments on its stability. American Journal of Science, 270, 151-154.

Greenwood, W. S. (1998) A mineralogical analysis of fibrous talc. University of Maryland, College Park, MS Thesis, 162 pp.

Gross, J. (2009) Mineral solubility measurements at high pressures: Redesigning the hydrothermal diamond anvil cell, crystal volume computations and birefringence mapping. Ph.D. Dissertation, Ruhr-University of Bochum, 232 pgs.

Haselton, H. T., Jr., Chou, I-M., Shen, A. H., and Bassett, W. A. (1995) Techniques for determining pressure in the hydrothermal diamond-anvil cell: The behavior of ice polymorphs (I, III, V, VI): American Mineralogist, 80, 1302 – 1306.

Hemingway, B. S. (1991) Thermodynamic properties of anthophyllite and talc: Corrections and discussion of calorimetric data. American Mineralogist, 76, 1589-1596.

Hemley, J. J., Montoya, J. W., Christ, C. L. and Hostetler, P. B. (1977a) Mineral equilibria in the MgO-SiO_2-H_2O system: I talc-chrysotile-olivine-brucite stability relations. American Journal of Science, 277, 322-351.

Hemley, J. J., Montoya, J. W., Shaw, D. R. and Luce, R. W. (1977b) Mineral equilibria in the MgO-SiO_2-H_2O system: II talc-antigorite-olivine-anthophyllite-enstatite stability relations and some geologic implication in the systems. American Journal of Science, 277, 353-383.

Huang, W. L., Bassett, W. A., Wu, T. C. (1994) Dehydration and hydration of montmorillonite at elevated temperatures and pressures monitored using synchrotron radiation. American Mineralogist, 79, 683-691.

Isshiki, M., Irifune, T., Hirose, K., Ono, S., Ohishi, Y., Watanuki, T., Nishibori, E., Takata, M., and Sakata, M. (2004) Stability of magnesite and its high-pressure form in the lowermost mantle. Nature, 427, 60-63.

Jamieson, J. C., Lawason, A. W., Nachtrieb, N. D. (1959) New Device for obtaining X-ray diffraction patterns from substance exposed to high pressure. Review of Scientific Instruments, 30, 1016-1019.

Janecky, D. R. and Seyfried, W. E., Jr. (1986) Hydrothermal serpentinization of peridotite within the oceanic crust: Experimental investigations of mineralogy and major element chemistry. Geochimica et Cosmochimica Acta, 50, 1357-1378.

Johannes, W. (1969) An experimental investigation of the system MgO-SiO_2-H_2O-CO_2. American Journal of Science, 267, 1083-1104.

Johannes, W. and Holtz F. (1996) Petrogenesis and Experimental Petrology of Granitic Rocks. Springer-Verlag, Berlin. 335 p.

Katsura, T., Tsuchida, Y., Ito, E., Yagi, T., Utsumi, W., and Akimoto, S. (1991) Stability of magnesite under the lower mantle conditions. Proceedings of the Japan Academy, 67, 57-60.

Kennedy, G. C. (1950) A portion of the system silica-water. Economic Geology, 45, 629–653.

Lasaga, A. C. (1998) Kinetic theory in the Earth Sciences. Princeton University Press, Princeton, New Jersey, 811 pgs.

Leake, B. E. et al. (1997) Nomenclature of amphiboles: Report of the subcommittee on amphiboles of the international mineralogical association, Commission on New Minerals and Mineral Names. Canadian Mineralogist, 35, 219-246.

Lide, D. R. (2000) CRC Handbook of Chemistry and Physics (81st Edition). CRC Press, Boca Raton, FL

Litasov, K. D., Fei, Y. W., Ohtani, E., Kuribayashi, T., and Funakoshi, K. (2008) Thermal equation of state of magnesite to 32GPa and 2073K. Physics of the Earth and Planetary interiors, 168, 191-203.

MacAdam, W. I. (1886) On the analysis of talc used in papermaking. Mineralogical Society of London, 7, 75.

Manning, C. E. (1994) The solubility of quartz in H_2O in the lower crust and upper mantle. Geochimica et Cosmochimica Acta, 58, 4831-4839.

Manning, C. E., Wilke, M., Schmidt, C. and Cauzid, J. (2008) Rutile solubility in albite-H_2O and $Na_2Si_3O_7$-H_2O at high temperatures and pressures by in-situ synchrotron micro-XRF. Earth and Planetary Science Letters, 272, 730-737.

Martin, B. and Fyfe, W. S. (1970) Some experimental and theoretical observations of kinetics of hydration reactions with particular reference to serpentinization. Chemical Geology, 6, 185-202.

Matthews, W. and Davis, W. J. (1999) A practical image analysis technique for estimating the weight of abraded mineral fractions used in U-Pb age dating. In: Radiogenic Age and Isotopic Studies: Report 12, Current Research 1999-F, Geological Survey of Canada, 1-7.

Menary, J. W., Ubbelohde, A. R., and Woodward, I. (1951) The thermal transition in caesium chloride in relation to crystal structure. Proceedings of the Royal Society of London. Series A, 208, 158-169.

Merrill, L. and W. A. Bassett (1974) Miniature diamond anvil pressure cell for single crystal x-ray diffraction studies. Review of Scientific Instruments, 45, 290-294.

Molina, J. and Poli, S. (2000) Carbonate stability and fluid composition in subducted oceanic crust: and experimental study on the H_2O-CO_2 -bearing basalts. Earth and Planetary Science Letters, 176, 295-310.

Moody, Judith (1976) An experimental study on the serpentinization of iron-bearing olivines. Canadian Mineralogist, 14, 462-478.

Mysen, B. O. (2009) Solution mechanisms of silicate in aqueous fluid and H_2O in coexisting silicate melts determined in-situ at high pressure and high temperature. Geochimica et Cosmochimica Acta, 73, 5748-5763.

Mysen, B. O. (2010) Speciation and mixing behavior of silica-saturated aqueous fluid at high temperature and pressure. American Mineralogist, 95, 1807-1816.

Newton, R. C. and Manning, C. E. (2000) Quartz solubility in H_2O-NaCl and H_2O-CO_2 solutions at deep crust-upper mantle pressures and temperatures: 2-15 kbar and 500-900 °C. Geochimica et Cosmochimica Acta, 64, 2993-3005.

Newton, R. C. and Manning, C. E. (2002) Solubility of silica in equilibrium with enstatite, olivine, and H_2O at deep crust/upper mantle pressures and temperatures and an activity-concentration model for polymerization of aqueous silica. Geochimica et Cosmochimica Acta, 66, 4165-4176.

Newton, R. C. and Manning, C. E. (2009) Hydration state and activity of aqueous silica in H_2O-CO_2 fluids at high pressure and temperature. American Mineralogist, 94, 1287-1290.

Normand, C., Williams-Jones, A. E., Martin, R. F., and Hojatollah, V. (2002) Hydrothermal alteration of olivine in a flow-through autoclave: Nucleation and growth of serpentine phases. American Mineralogist, 87, 1699-1709.

Oelkers, E. H., Gislason, S. R., and Matter, J. (2008) Mineral carbonation of CO_2. Elements, 4, 333-337.

Palekar, L. D., Sponer, C. M. and Coffin, D. L. (1979) Influence of crystallization habit of minerals on *in vitro* cytotoxicity. Annals of the New York Academy of Sciences, 330, 673–686.

Pawley, A. R. (1998) The reaction talc + olivine = enstatite + H_2O: New experimental results and petrological implications. American Mineralogist, 83, 51-57.

Phillips, A. H. and Hess, H. H. (1936) Metamorphic differentiation at contacts between serpentine and siliceous country rocks. American Mineralogist, 21, 333-362.

Pohl, W. (1990) Genesis of magnesite deposits – models and trends. Geologische Rundschau, 79, 291-299.

Read, H. H. (1934) On zoned associations of antigorite, talc, actinolite, chlorite, and biotite in Unst, Shetland Islands. Mineralogical Magazine, 145, 519-540.

Ross, M., Smith, W. L., and Ashton, W. H. (1968) Triclinic talc and associated amphiboles from Gouverneur mining district, New York. American Mineralogist, 53, 751-769.

Rudnick, R., McDonough, W., and O'Connell, R. (1998) Thermal structure, thickness and composition of continental lithosphere, Chemical Geology, Special issue: Geochemical Earth Reference Model, 145, 399-416.

Sanford, R. F. (1981) Mineralogical and chemical effects of hydration reactions and applications to serpentinization. American Mineralogist, 66, 290-297.

Sanford, R. F. (1982) Growth of ultramafic reaction zones in greenschist to amphibolite facies metamorphism. American Journal of Science, 282, 543-616.

Schmidt, C. and Ziemann, M. A. (2000) In-situ Raman spectroscopy of quartz: A pressure sensor for hydrothermal diamond-anvil cell experiments at elevated temperatures. American Mineralogist, 85, 1725 – 1734.

Shen, A. H., Bassett, W. A., and Chou, I-M. (1993) The α-β quartz transition observed at simultaneous high temperatures and high pressures in a diamond-anvil cell by laser interferometry: American Mineralogist, 78, 694 – 698.

Skorodumova, N. V., Belonoshko, A. B., Huang, L., Ahuja, R., and Johansson, B. (2005) Stability of the $MgCO_3$ structures under lower mantle conditions. American Mineralogist, 90, 1008-1011.

Stein, C. (1995) Heat flow of the earth, American Geophysical Union Reference Shelf. 1, pp. 144–158.

Stemple, I. S. and Brindley, G. W. (1960) A structural study of talc and talc-tremolite relations. Journal of the American Ceramic Society, 43, 34-42.

Takafuji, N., Fujino, K., Nagai, T., Seto, Y., and Haname, D. (2006) Decarbonation reaction of magnesite in subducting slabs at the lower mantle. Physics and Chemistry of Minerals, 33, 651-654.

Takesue, M., Shimoyama, K., Murakami, S., Hakuta, Y., Hayashi, H., and Smith, R. L., Jr. (2007) Phase formation of Mn-doped zinc silicate in water at high-temperatures and high-pressures. Journal of Supercritical Fluids, 43, 214-221.

Van Gosen, B. S., Lowers, H. A., Sutley, S. J. and Gent, C. A. (2004) Using the geologic setting of talc deposits as an indicator of amphibole asbestos content. Environmental Geology, 45, 920-939.

Van Valkenburg, A. (1964) Diamond high pressure windows. Diamond Research, 1964, 17-20.

Van Valkenburg, A., Mao, H. K., and Bell, P. M. (1971) Solubility of minerals at high water pressures. Carnegie Institution of Washington, Year Book, 70, 233-237.

Veblen, D. R. (1980) Anthophyllite asbestos: microstructures, intergrown sheet silicates, and mechanisms of fiber formation. American Mineralogist, 65, 1075-1086.

Virta, R. L. (2002) Talc and Pyrophyllite. U.S. Geological Survey, Mineral Commodity Summaries, January 2002

Wagner, W. and Pruss, A. (2002) The IAPWS formulation 1995 for the thermodynamic properties of ordinary water substance for general and scientific use. Journal of Physical Chemistry Reference Data, 31, 387–535.

Walker, J. S. and Zoltai, T. (1979) A comparison of asbestos fibers with synthetic crystals known as “whiskers.” Annals of the New York Academy of Sciences 330, 687–704.

Wang, H. M., Henderson, G. S., and Brenan, J. M. (2004) Measuring quartz solubility by in-situ weight-loss determination using a hydrothermal diamond cell. Geochimica et Cosmochimica Acta, 68, 5197–5204.

Wegner, W. W. and Ernst, W. G. (1983) Experimentally determined hydration and dehydration reaction rates in the system MgO-SiO_2-H_2O. American Journal of Science, 283-A, 151-180.

Weir, C. F., Lippincott, E. R., Van Valkenberg, A., and Bunting, E. N. (1959) Infrared studies in the 1- to 15-micron region to 30,000 atmospheres. Journal of Research of the National Bureau of Standards, 65A, 55-62.

Wylie, A. G. and Huggins, C. W. (1980) Characteristics of a potassian winchite – Asbestos from the Allamoore talc district, Texas. Canadian Mineralogist, 18, 101-107.

Wylie, A. G., Skinner, H. C. W., Marsh, J., Snyder, H., Garzione, C., Hodkinson, D., Winters, R. and Mossman, B. T. (1997) Mineralogical features associated with cytotoxic and proliferative effects of fibrous talc and asbestos on rodent tracheal epithelial and pleural mesothelial cells. Toxicology and Applied Pharmacology, 147, 143-150.

Wylie, A. G. and Verkouteren, J. R. (2000) Amphibole asbestos from Libby, Montana: Aspects of nomenclature. American Mineralogist, 85, 1540-1542.

Zen, E-an (1971) Comments on the thermodynamic constants and hydrothermal stability relations of anthophyllite. American Journal of Science, 270, 136-150.

Zen, E-an and Chernosky, J. V., Jr., (1976) Correlated free energy values of anthophyllite, brucite, clinochysotile, enstatite, olivine, quartz, and talc. American Mineralogist, 61, 1156-1166.

Zoltai, T. (1981) Amphibole asbestos mineralogy. In: Veblen, D. R. (ed.), Amphiboles and other hydrous pyriboles: mineralogy. Mineralogical Society of America, Washington, D. C., Reviews in Mineralogy, 9A, 237-278.

Zotov, N. and Keppler, H. (2002) Silica speciation in aqueous fluids at high pressures and high temperatures. Chemical Geology, 184, 71-82.

Ryan J. Kerrigan

EDUCATION:

University of Maryland **September 2005 – January 2011**
College Park, MD

Doctor of Philosophy: Geology
Thesis Title: Reaction rates and textural development of hydrolysis reactions in the system MgO-SiO_2-H_2O.
Advisors: Dr. Philip Candela and Dr. Philip Piccoli

University of Minnesota **September 2002 – December 2004**
Minneapolis, MN

Master of Science: Geology
Thesis Title: The relation of sulfur speciation and color in lazurite solid solution.
Advisor: Dr. James H. Stout

Bridgewater State College **September 1996 – May 2002**
Bridgewater, MA

Bachelor of Science: Geology
Bachelor of Arts: Chemistry
Minor: Geography
Undergraduate Thesis Title: Investigations of hourglass inclusions in selenite.
Advisors: Dr. Chifuru Noda and Dr. Peter Saccocia

TEACHING EXPERIENCE:

Awards:

– 2008-09 Center for Teaching Excellence, University of Maryland, Distinguished Teaching Assistant
– 2007-08 College of Computer, Mathematics and Physical Science Outstanding Teaching Assistant
– 2007-08 Center for Teaching Excellence, University of Maryland, Distinguished Teaching Assistant

Head TA/Coordinator of Teaching Assistants:

– Physical Geology Laboratory (UMD – GEOL 110**)** 4 semesters
Duties include: Organization and coordination for up to 12 sections of GEOL 110, curriculum development and implementation, field trip organization, website maintenance and conflict resolution.
– Volcanoes of the Earth Laboratory (UMN – GEO 1011**)** 1 semester
Duties include: Organization of all labs, curriculum development and implementation, procurement and manufacturing of materials required for labs.

Teaching Assistantships:

– Physical Geology Laboratory (UMD – GEOL 110) 6 semesters
– Igneous and Metamorphic Petrology Lab. (UMD – GEOL 443) 4 semesters
– Mineralogy Laboratory (UMD – GEOL 322) 2 semesters
– Physical Oceanography Laboratory (UMN – GEO 1006) 2 semesters
– Introductory Field Camp, Dillon MT. (UMN – GEO 3911) 1 semester
– The Dynamic Earth Laboratory (UMN – GEO 1001) 1 semester
– Volcanoes of the Earth Laboratory (UMN – GEO 1011**)** 1 semester

Guest Lecturing:

– Petrology (UMD – GEOL 422) March, 2010, Topic: magma generation in the mantle.
– Thermodynamics of Geological Processes (UMD – GEOL 614) October, 2009, Topic: experimental petrology by using the diamond anvil cell.
– Petrology (UMD – GEOL 422) April, 2009, Topic: the metamorphism of mafic rocks.

RESEARCH EXPERIENCE:

Research Assistantships:

– Mineralogy research, Supervisor – Dr. James H. Stout 2 semesters
– Electron Microprobe Laboratory, Supervisor – Ellery Frahm 1 semester

Doctoral Research: Department of Geology, University of Maryland, 2005-2010 (research advisors: Dr. Philip A. Candela and Dr. Philip M. Piccoli)

– Experimentation with the hydrothermal diamond anvil cell for investigations related to phase equilibria and kinetics.
– Analysis of materials using powder and single crystal x-ray diffraction.
– Index of refraction determination with spindle stage instrumentation.
– Electron diffraction and imaging of fibrous materials using transmission electron microscopy.
– Energy dispersive spectroscopy and imaging using the electron probe microanalyzer.
– Integrating hydrothermal diamond anvil cell experiments with synchrotron radiation x-ray diffraction analysis: Experienced User at the National Synchrotron Light Source – Brookhaven National Laboratory and the Advanced Photon Source – Argonne National Laboratory.
– Imaging analysis to determine in-situ mass loss of reactants and run products.

Masters Research: Department of Geology and Geophysics, University of Minnesota, 2002-2004 (research advisor: Dr. James H. Stout)

– Geologic mapping of igneous plutons and associated skarn ore deposits within Gunnison National Forest.
– Use of lapidary equipment, making thin sections from samples collected.
– Wavelength dispersive spectroscopy, valence state determination and imaging using the electron probe microanalyzer.
– Valance state determinations using x-ray photoelectron spectroscopy

Research Interests:

– Thermodynamics and kinetics of water/rock interactions during hydrothermal alteration
– Use of synchrotron radiation-based techniques to address problems related to kinetics
– Understanding the necessary conditions for the development of particular mineral habits and rock textures
– Relating lab-based thermodynamic and kinetic experiments to field observations
– Thermodynamics and kinetics of reactions of CO_2-rich fluids with mafic minerals with application to carbon sequestration
– Pedagogy of effectively training scientists and exposing non-geologists to the wonders of our Earth

PUBLICATIONS:

Kerrigan, R. J., Candela, P. A. and Piccoli, P. M. (2010) *Olivine + Quartz + Water ± HCl at mid-crustal conditions in the hydrothermal diamond anvil cell: Controls on the growth of fibrous talc,* To be submitted to American Mineralogist (near submission).

Kerrigan, R. J., Candela, P. A. and Piccoli, P. M. (2010) *Magnesite decarbonation and talc growth in the presence of silica-rich water at mid-crustal conditions: Kinetics determined by in-situ reactant mass loss*, To be submitted to American Mineralogist (near submission).

ABSTRACTS:

Kerrigan, R. J., Candela, P. A. and Piccoli, P. M. (2009) *In-situ synchrotron radiation x-ray diffraction and visual imaging study of magnesite + quartz + water at mid-crustal temperatures and pressures*, Eos Trans. AGU 90(52), Fall Meeting Suppl., Abstract V43B-2244 (Poster).

Kerrigan, R. J., Candela, P. A., Piccoli, P. M. and Wylie, A. G. (2007) *Growth of Fibrous Talc and Anthophyllite in the Hydrothermal Diamond Anvil Cell*, Eos Trans. AGU 88(52), Fall Meeting Suppl., Abstract V12A-07 (Presentation).

Maglio, S. J., Frank, M. R., Aarestad, B., Scott, H., Huggins, S., Kerrigan, R., Prakapenka, V. and Kuznetsov, A. (2007) *An experimental study in the Mg_2SiO_4 - $Fe_{1-X}S$ - H_2O System: Implications for Ganymede's interior*. GSA Abstracts with Programs, 39, No. 6, 571

Proposals:

Kerrigan, R. J., Candela, P. A. and Piccoli, P. M. *Magnesite decarbonation and growth of fibrous talc through hydrothermal reactions: kinetics, textures and the global carbon cycle.* National Synchrotron Light Source – Brookhaven National Laboratory. Submitted August 2009, accepted September 2009.

Kerrigan, R. J., Candela, P. A. and Piccoli, P. M. *Hydrothermal reactions kinetics and fibrous mineral development in a non-equilibrium KFMASH (K_2O-FeO-MgO-Al_2O_3-SiO_2-H_2O) system under greenschist*

to amphibolite facies metamorphic conditions. National Synchrotron Light Source – Brookhaven National Laboratory. Submitted June 2009, accepted July 2009.

Kerrigan, R. J., Candela, P. A. and Piccoli, P. M. *A study of olivine hydration reaction kinetics.* National Synchrotron Light Source – Brookhaven National Laboratory. Submitted August 2008, accepted September 2008.

Kerrigan, R. J. and Stout, J. H. *Chemical Characterization of Lazurite by X-ray Photoelectron Spectroscopy.* Center for Microanalysis of Materials, University of Illinois, Urbana-Champagne (CMM-UIUC). Submitted August 2003, accepted September 2003

WORKSHOPS:

Geology and Geophysics Applied to Industry: *An American Association of Petroleum Geologists short course*. Convener: Fred Schroeder, University of Maryland, College Park, MD, March 19, 2010.

Pursuing an Academic Career: *An On the Cutting Edge Workshop for Graduate Students and Post-docs*. Co-Conveners: Jon Lewis and Rachel Beane, Northeast – Southeast Regional Geological Society of America Meeting, Baltimore, MD, March 13, 2010.

COMMUNITY OUTREACH:

– Guest lecturer **August 2010**

Provided a geomaterials lecture for high school students as part of the University of Maryland's College Preparation Workshop Series.

– Volunteer tutor and mentor **Sept. 2006 – June 2010**

Community Club, New York Avenue Presbyterian Church, Washington, D.C. *Duties include:* weekly meetings with Washington, D.C. high school students for mentoring and tutoring in all subjects.

– Volunteer tour guide for Maryland Day **April 2006 – April 2009**

University of Maryland, Department of Geology, College Park, MD, 20742.

Duties include: providing interpretive tours for the general public of the University of Maryland's Geology Museum for the annual Maryland Day event.

– Guest lecturer **Aug. 2007, Aug. 2009**

Provided a geology lecture for kindergarten students.

– Guest lecturer **October 2004**

Provided a 'Rocks, minerals and gems' lecture for the Minnesota Mineral Club.

PROFESSIONAL AFFILIATIONS:

– American Geophysical Union - Since 2001
– Geological Society of America - Since 2001
– Mineralogical Society of America - Since 2001
– National Association of Geoscience Teachers - Since 2007